

Technische Universität München
Institut für Energietechnik

Fachgebiet für Thermofluiddynamik

Nonlinear Aeroacoustic Characterization of Resonators

Kilian H. Förner

Vollständiger Abdruck der von der Fakultät für Maschinenwesen der
Technischen Universität München zur Erlangung des akademischen
Grades eines

DOKTOR – INGENIEURS

genehmigten Dissertation.

Vorsitzender:

Prof. Rafael Macián-Juan, Ph. D.

Prüfer der Dissertation:

Prof. Wolfgang Polifke, Ph. D.

Prof. Dr. Ines Lopez Arteaga

TU Eindhoven/Niederlande und

KTH Royal Institute of Technology/Schweden

Die Dissertation wurde am 11. Mai 2017 bei der Technischen Universität München
eingereicht und durch die Fakultät für Maschinenwesen am 4. Sept. 2017 angenommen.

Abstract

The present thesis addresses the nonlinear damping behavior of acoustic resonators—such as quarter-wave and Helmholtz resonators—originating from flow separation at the edges of the resonators in the presence of high acoustic amplitudes. In particular, it focuses on the following aspects: high-fidelity fluid dynamic simulations, gathering in-depth knowledge about the mechanisms involved and data-based reduced-order modeling.

Compressible fluid dynamic simulations are conducted for the nonlinear aeroacoustic characterization. These simulations are acoustically excited at an inlet boundary with the Navier-Stokes characteristics boundary condition. The computational setup is successfully validated against experiments for various test cases. In addition, a novel methodology applying incompressible flow simulations is developed and cross-validated against compressible simulations.

The validated compressible computational setup is employed as a powerful tool to investigate nonlinear effects in detail. The effects of the resonator edge contour on the damping behavior are analyzed. It is demonstrated that a blunt edge reduces the flow separation at the leading edge significantly, resulting in a reduction of the nonlinear resistance. Furthermore, the scattering to higher harmonics is investigated in the nonlinear regime. For the Helmholtz resonator, a pattern in the spectrum of the scattered wave is found, where only the odd harmonics are present. A quasi-steady analysis identifies the flow symmetry during the inflow and the outflow phase as the reason for this pattern. Accordingly, the pattern becomes weaker for a Helmholtz resonator with an asymmetric neck and vanishes totally for a quarter-wave resonator. Moreover, it is shown that the overall scattering to higher harmonics remains on minor and moderate levels for the Helmholtz and quarter-wave resonator, respectively.

Data-based reduced-order modeling of the dynamics of resonators forms the core of the thesis. For that purpose, system identification techniques are applied on broadband input/output data from a fluid dynamic simulation. The linear dynamics are reproduced very accurately by an estimated linear autoregressive model. Such a model can be represented as a digital filter with an infinite number of filter coefficients. Since the autoregressive model exhibits a moderate number of free model parameters, it is robust against over-fitting. This methodology is extended into the nonlinear regime. A novel gray-box model structure, named local-linear neuro-fuzzy network, is proposed along with a procedure for a bias-free identification. This model—defined in the time domain—reproduces the nonlinear dynamics accurately in a robust manner by an estimation based on data from a single simulation. Since this model is very flexible and can be evaluated efficiently,

it can be employed as an acoustic boundary condition in other fluid dynamic or aeroacoustic simulations for the assessment of the nonlinear stability of the overall system. Moreover, the efficient and robust nonlinear characterization makes this approach feasible to support the resonator design in an early stage of development.

Kurzfassung

Die vorliegende Arbeit befasst sich mit den nichtlinearen Dämpfungseigenschaften akustischer Resonatoren wie z.B. $\lambda/4$ - und Helmholtzresonatoren, die aufgrund von Strömungsablösung an den Resonatorkanten bei hohen akustischen Amplituden auftreten. Insbesondere werden folgende Aspekte betrachtet: die akkurate strömungsmechanische Simulation, die Vertiefung des Kenntnisstandes über die auftretenden Mechanismen und die datengestützte Generierung von Modellen reduzierter Ordnung.

Für die nichtlineare aeroakustische Charakterisierung werden kompressible strömungsmechanische Simulationen durchgeführt. Diese Simulationen werden am Einlass, an dem die Navier-Stokes-Characteristics-Randbedingung implementiert ist, akustisch angeregt. Das numerische Setup wird erfolgreich anhand von Experimenten für verschiedene Testfälle validiert. Zudem wird eine neue Methode, basierend auf inkompressiblen Simulationen, entwickelt und an kompressiblen Simulationen validiert.

Das validierte kompressible Setup wird eingesetzt, um nichtlineare Effekte im Detail zu untersuchen. Zunächst wird die Auswirkung der Resonatorkantenkontur auf die Dämpfungseigenschaften analysiert. Es wird gezeigt, dass eine stumpfe Kante die Strömungsablösung an der Vorderkante erheblich reduziert, was zu einer Verringerung des nichtlinearen Widerstandes führt. Zudem wird die Streuung in Oberschwingungen im nichtlinearen Regime untersucht. Für den Helmholtzresonator wird ein Muster im Spektrum der reflektierten Welle sichtbar, in dem ausschließlich die ungeradzahligen Oberschwingungen vorhanden sind. Als Ursache hierfür wird in einer quasi-stationären Analyse die Strömungssymmetrie während der Ein- und Ausströmphase ermittelt. Dementsprechend wird das Muster für einen Helmholtzresonator mit einem asymmetrischen Hals schwächer und verschwindet vollständig für einen $\lambda/4$ -Resonator. Darüber hinaus wird gezeigt, dass die gesamte Streuung zu Oberschwingungen auf kleinem Niveau für den Helmholtzresonator bzw. einem moderaten für den $\lambda/4$ -Resonator verbleibt.

Die datengestützte Modellierung der Resonatordynamik bildet den Kern dieser Arbeit. Hierfür werden Systemidentifikationstechniken auf breitbandige Ein- und Ausgangsdaten einer strömungsmechanischen Simulation angewendet. Die lineare Dynamik wird durch ein geschätztes lineares autoregressives Modell sehr genau wiedergegeben. Ein solches Modell kann als digitaler Filter mit unendlich vielen Filterkoeffizienten dargestellt werden. Da das autoregressive Modell nur eine geringe Anzahl an freien Modellparametern aufweist, ist es robust gegenüber Over-Fitting. Diese Methodik wird in das nichtlineare Regime ausgedehnt. Eine neue Gray-Box-Modellstruktur, ein sogenanntes lokal-lineares Neuro-Fuzzy-

Netzwerk, wird zusammen mit einer Prozedur für eine biasfreie Identifikation entwickelt. Dieses im Zeitbereich definierte Modell reproduziert robust die nichtlineare Dynamik basierend auf Daten einer einzigen Simulation. Aufgrund seiner Flexibilität und effizienten Auswertbarkeit kann es als akustische Randbedingung in strömungsmechanischen oder aeroakustischen Simulationen zur Beurteilung der nichtlinearen Stabilität des Gesamtsystems eingesetzt werden. Darüber hinaus kann dieser Ansatz durch die effiziente und robuste nichtlineare Charakterisierung den Auslegungsprozess von Resonatoren bereits zu einem frühen Entwicklungsstadium unterstützen.

Vorwort

Die vorliegende Arbeit entstand am Fachgebiet für Thermofluidodynamik der Technischen Universität München während meiner Tätigkeit als wissenschaftlicher Mitarbeiter. Diese wurde durch die Deutsche Forschungsgemeinschaft (DFG) im Rahmen des Sonderforschungsbereichs Transregio 40 (TRR40) gefördert und das Leibniz-Rechenzentrum (LRZ) gewährte Zugang zu seinen Rechenclustern.

Ein herzliches Dankeschön möchte ich meinem Doktorvater Wolfgang Polifke aussprechen für die Möglichkeit am Fachgebiet für Thermofluidodynamik zu arbeiten und diese Dissertation anzufertigen. Hierbei wurden mir viele Freiräume gelassen, aber zur gegebenen Zeit stand er mir fachlich immer hilfreich zur Seite. In den vielen gemeinsamen Montagsmeetings und Mittagessen schätzte ich den angenehmen Rahmen, in dem neben fachlichen Themen auch Zeit für Alltägliches oder Privates war. Zudem bin ich froh, dass mir problemlos ermöglicht wurde meine berufliche Tätigkeit gut mit meiner Familie zu vereinbaren. Ines Lopez Arteaga danke ich für die Übernahme des Koreferates und Herrn Prof. Dr. Macián-Juan für seine Tätigkeit als Prüfungsvorsitzender.

Für die gute Atmosphäre am Fachgebiet für Thermofluidodynamik und am Lehrstuhl für Thermodynamik bedanke ich mich bei allen Kolleginnen und Kollegen. Ich genoss es, mir das Büro mit Thomas teilen zu dürfen, der immer wieder erster Ansprechpartner bei Fragen und Problemen war. Für die hervorragende thematische Einarbeitung möchte ich meinem TRR40-Vorgänger Alejandro Danke sagen. Stellvertretend für alle Kolleginnen und Kollegen, mit denen ich viele konstruktive Gespräche führte, will ich hier Armin, Carlo, Sebastian, Stefan Jaensch, Thomas Emmert und meinen TRR40-Nachfolger Simon nennen. Zudem bereitete mir die Zusammenarbeit mit Studenten immer Freude, wo ich hier stellvertretend Daniel erwähnen möchte, der es am längsten mit mir ausgehalten hat. Für die Unterstützung bei allem Organisatorischen will ich mich beim Sekretariatsteam, allen voran beim guten T(F)D-Geist Helga, bedanken. Im Kollegium erlebten wir neben all dem Fachlichen auch privat viel miteinander. Ich werde mich immer gerne an unsere Einstands-, Doktor-, und First-Fire-Feiern sowie die vielen Aktivitäten erinnern; wie Fußballspielen, Skifahren, Grillen, Kneipentouren, Betriebsausflüge, . . .

Über meinen Forschungsaufenthalt an der TU Eindhoven bin ich ebenfalls froh. Die fachlichen und persönlichen Gespräche mit meinen Gastgebern Sjoerd Rienstra und Deepesh waren sehr bereichernd. Zudem freut es mich, hier Ines Lopez Arteaga und Muttalip kennengelernt zu haben. Im Gegenzug konnte ich Jonathan für seinen Forschungsaufenthalt an der TUM beherbergen, woraus eine sehr fruchtbare wissenschaftliche Zusammenarbeit und Freundschaft entstanden ist.

Zu guter Letzt will ich mich bei meiner Familie bedanken: Angefangen bei meinen Eltern, die mich während meines ganzen Ausbildungsweges unterstützten. Und natürlich bei meiner Frau Iris, die immer für mich da war, wenn ich sie brauchte, und mit der ich in dieser Zeit eine wunderbare Familie gründen konnte. DANKE!

Contents

1	Introduction	1
2	Fluid Dynamic and Acoustic Background	5
2.1	Working Principle and Types of Resonators	5
2.2	Governing Equations	7
2.3	Impedance and Reflection Coefficient	10
2.4	Impedance and Reflection Coefficient Describing Functions	13
2.5	1-D Modeling Approaches	14
3	Numerical Assessment of Thermoacoustic Stability	21
3.1	Methodological Overview	21
3.2	Network Model for a Rocket Combustion Chamber	22
4	CFD Simulations of Acoustic Resonators	25
4.1	Compressible CFD Simulations	25
4.2	Incompressible CFD Simulations	29
5	Aeroacoustic Characterization of Nonlinear Effects by Harmonic Probing	31
5.1	Influence of Edge Shape on the Flow Separation and the Damping Behavior	31
5.2	Scattering to Higher Harmonics	32
6	Aeroacoustic Characterization by Data-Based Reduced-Order Modeling	35
6.1	Linear System Identification and Prediction Error Method	36
6.2	Linear Aeroacoustic Characterization of Resonators	37
6.3	Nonlinear Aeroacoustic Characterization of Resonators	38
7	Summary and Conclusion	41
7.1	Mapping the Influence of Acoustic Resonators on Rocket Engine Combustion Stability	43
7.2	Determination of Acoustic Impedance for Helmholtz Resonators Through Incompressible Unsteady Flow Simulations	44
7.3	On the Non-Linear Influence of the Edge Geometry on Vortex Shedding in Helmholtz Resonators	44
7.4	Scattering to Higher Harmonics for Quarter-Wave and Helmholtz Resonators	45

CONTENTS

- 7.5 Aeroacoustic Characterization of Helmholtz Resonators in the Linear Regime with System Identification 46
- 7.6 Nonlinear Aeroacoustic Characterization of Helmholtz Resonators with a Local-Linear Neuro-Fuzzy Model 47

- Bibliography** **49**

- List of Figures** **61**

- Supervised Students** **63**

- A Reproduction of Papers** **65**

 - A.1 Mapping the Influence of Acoustic Resonators on Rocket Engine Combustion Stability 66
 - A.2 Determination of Acoustic Impedance for Helmholtz Resonators Through Incompressible Unsteady Flow Simulations 74
 - A.3 On the Non-Linear Influence of the Edge Geometry on Vortex Shedding in Helmholtz Resonators 83
 - A.4 Scattering to Higher Harmonics for Quarter-Wave and Helmholtz Resonators 91
 - A.5 Aeroacoustic Characterization of Helmholtz Resonators in the Linear Regime with System Identification 102
 - A.6 Nonlinear Aeroacoustic Characterization of Helmholtz Resonators with a Local-Linear Neuro-Fuzzy Model 110

1 Introduction

Acoustic resonators are used as sound absorbers in various technical applications. For instance, they are implemented to reduce sound emissions to the environment or to suppress thermoacoustic oscillations [1]. Combustion systems, such as domestic heaters, gas turbines or rocket engines, may suffer from so-called thermoacoustic instabilities [2]. These instabilities can occur due to the feedback of the combustion process and the acoustics within the system. By a fluctuating heat release from the combustion, the gaseous volume is thermally expanded in an unsteady manner which produces sound. This sound is reflected at the combustion chamber boundaries and, in turn, influences the combustion process itself. In the case of an instability, this feedback may lead to very high amplitudes. In the worst case, these high amplitudes can damage or even destroy the combustion system. Among other arrangements to weaken this feedback, acoustic resonators are implemented in the walls of the combustion chamber [3, Chp. 8]. Exemplarily, an L-shape quarter-wave resonator mounted in the Vulcain 2, the main stage engine of the Ariane 5 rocket, is shown in Fig. 1.1a.

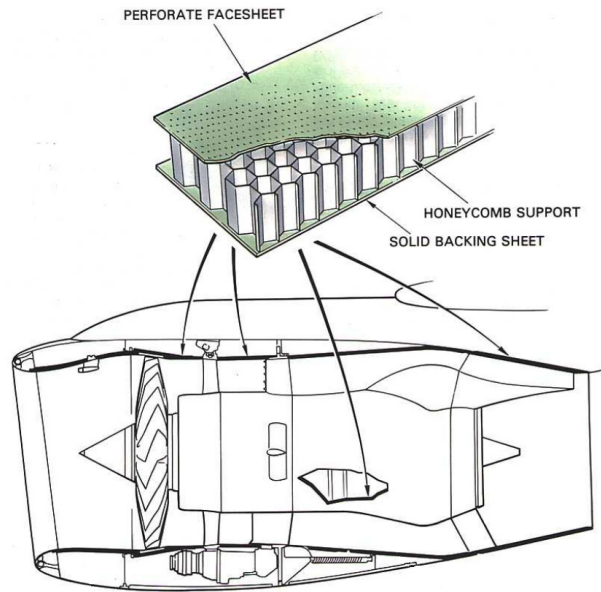
Prominent examples of resonators employed for the reduction of sound emissions are found in aero-engines [4, Chp. 19]. Several sound sources are present in such an engine, where fan noise is dominant in modern devices. Regularities for sound emissions are continuously intensified to protect humans and animals from the harmful effects of noise [4, Chp. 19]. Acoustic liners, which can be considered as an array of Helmholtz resonators, are commonly placed in the inlet and the exhaust duct to meet these regulations. Figures 1.1b presents the placement of such liners in an engine.

To determine the sound emissions or the thermoacoustic stability of a system equipped with resonators, a model for their dynamics is needed. Such a model is often provided in terms of the impedance. The impedance relates, by definition, the local fluctuating acoustic pressure to the local acoustic velocity in a linear fashion. However, at high acoustic amplitudes, resonators do not behave in a linear manner due to flow separation at their edges. When the analysis is performed in the frequency or the Laplace domain, the linearity of the models considered is required. Hence, often local-linear models are constructed, where correction parameters are incorporated into the impedance model emulating the nonlinear influence. A local-linear model is valid for a specific amplitude range, for which the correction parameters are set. Accordingly, such a model cannot be used in the time domain when amplitudes change dynamically. However, a model accounting for dynamical changes is needed for a rigorous nonlinear analysis of systems in the time domain.

This dissertation addresses the nonlinear damping effects present in acoustic resonators. In particular, it focuses on high-fidelity computational fluid dynamics (CFD) simulations of the resonator dynamics including nonlinear phenomena, on deepening the knowledge of the nonlinear mechanisms, and on their data-based reduced-order modeling. CFD simula-



(a) L-shaped quarter-wave resonator in a Vulcain 2 engine.¹



(b) Liners in an aero-engine (taken from [4, Chp. 19]).

Figure 1.1: Resonators in technical applications.

tions have proven their capability of reproducing the physics accurately. Thus, a validated simulation setup can be a powerful tool to study aspects of the nonlinear interactions. In the present thesis, the impact of the edge shape on the damping characteristics and the scattering to higher harmonics is investigated in detail using this tool. The findings are consolidated by analytic considerations aligned with flow visualizations. The potential of CFD simulations is also employed to generate models of the resonator dynamics. Existing models are mainly based on first principles in combination with some correction terms. These correction terms are adjudicated by correlation analysis of experimental data. When the set of correlation parameters is determined correctly, the harmonic behavior of the resonator can be described well for a fixed amplitude of excitation. In this thesis, a data-based modeling approach is pursued. Based on the input/output data of a simulation, a reduced-order model (ROM) is estimated using system identification (SI) techniques. ROMs are generated in both the linear and the nonlinear regime. By this procedure, an efficient and robust approach is presented to generate accurate models for various resonator geometries and conditions.

The results were presented at conferences and in journals. Major publications are reproduced in the Appendix A. The present paper-based dissertation guides through these publications by summarizing the most important results, embedding them in the literature context, and, most importantly, showing the interconnections between them. The thesis is structured as follows: Section 2 lays the theoretical and terminological foundation. Different types of resonators (Sec. 2.1) as well as the fluid dynamic and acoustic governing

¹Private photography taken with permission at the museum of the DLR (Deutsches Zentrum für Luft- und Raumfahrt), Lampoldshausen (Germany).

equations (Sec. 2.2) are introduced. Modeling in terms of the reflection coefficient and the impedance (Secs. 2.3 and 2.4) as well as a 1-D quasi-steady modeling approach (Sec. 2.5) are presented. In Sec. 3, the impact of several parameters of quarter-wave resonators on the linear thermoacoustic stability of a generic rocket combustion chamber is demonstrated by a network model. The computational setup is introduced in Sec. 4. Section 5 addresses some aspects of the nonlinear behavior. The shape of the edges of resonators influences the separation behavior and, thus, the nonlinear damping characteristics as discussed in Sec. 5.1. The scattering to higher harmonics for different resonator types is considered in Sec. 5.2. Section 6 reports on data-based reduced-order modeling. After a general introduction on SI (Sec. 6.1), the linear SI approach and results for some test cases are presented in Sec. 6.2. This approach is extended into the nonlinear regime by a new gray-box model in Sec. 6.3. Finally, conclusions are given in Sec. 7. Here, also the author's contribution to the attached papers is described clearly.

2 Fluid Dynamic and Acoustic Background

This chapter introduces the essential terminology and analytical concepts of the thesis. First, the different types of resonators are introduced in Sec. 2.1. Here, the principle of the damping mechanism is also briefly described in prose. Section 2.2 presents the governing equations from fluid dynamics and sketches the derivations of the acoustic Helmholtz and wave equation. In Sec. 2.3, it is shown that the linear impact of a resonator located at the boundary of a domain can be modeled as an impedance or a reflection coefficient. Describing functions generalize these expressions for the nonlinear regime as presented in Sec. 2.4. Finally, a quasi-steady 1-D modeling approach commonly used in the literature is given in Sec. 2.5. Such a relatively simple approach can model the dynamics surprisingly well and helps to develop a clear picture of them.

2.1 Working Principle and Types of Resonators

Hard walls fully reflect an incident wave without any loss. Whereas, at an acoustic resonator, the incident wave is only partially reflected due to imposed losses there. A resonator exploits the resonance of a cavity being connected via one or several openings to the chamber. This resonance leads to high particle velocities at the opening of the cavity, which causes losses there. In general, two main types of resonators are distinguished: locally and non-locally reacting resonators. In the locally reacting case, its behavior is independent of the angle of the incident acoustic wave. This is achieved when either only one opening per cavity is present or when the openings connected via the backing volume are arranged closely to each other (in comparison to the wavelength). Otherwise, the resonator is referred to as non-locally reacting and its behavior cannot be modeled by considering only a local section of the device's surface, as sketched in Fig. 2.1a. In most technical applications, resonators can be considered as locally reacting. Hence, this thesis is restricted to that kind of resonators. Three prototypes of locally reacting resonators can be identified: the Helmholtz, the half-wave, and the quarter-wave resonator. The Helmholtz resonator, displayed in Fig. 2.1d, is named after Hermann von Helmholtz, who was the first to analyze it theoretically [6]. This resonator type has a closed cavity, which is connected to the chamber via an opening with a narrow cross-section, the so-called *neck*. The half-wave and the quarter-wave resonators consist of tubes, see Figs. 2.1b and 2.1c. The opening of such a tube resonator linked to the chamber is referred to as its *mouth*. The half-wave resonator has also an opening at the backside of the tube, while the end of the quarter-wave type is closed. The lengths of the tubes determine the eigenfrequencies of the half-wave and the quarter-wave resonators. The half and the quarter of eigenfre-

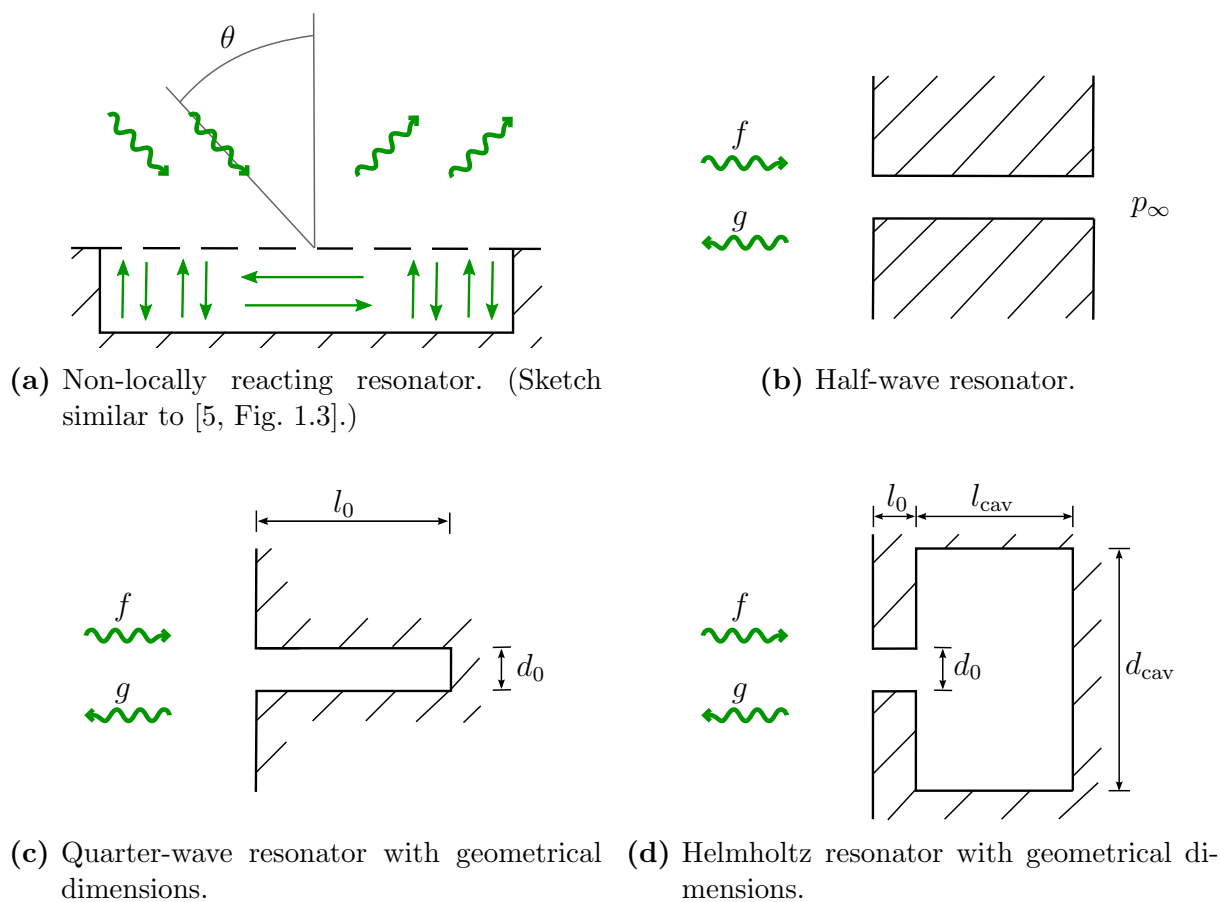


Figure 2.1: Sketches of basic resonator types with acoustic traveling f - and g -waves.

quencies' wavelengths coincide with the lengths of the tubes, which explains the naming of these resonator types. Since an open end is often difficult to realize, the quarter-wave tube and Helmholtz resonator are mainly implemented in applications. Accordingly, only those two types are considered in the present thesis.

For locally reacting resonators, Rayleigh [7] described their working principle by the analogy to a mechanical mass-spring-damper system. The mass in the neck or the mouth of the resonator corresponds to the mass in its mechanical counterpart. The imposed losses and the compressibility of the backing volume correlate with the losses of the mechanical damper and the stiffness of the spring, respectively. The external pressure driving the system corresponds to a force acting on the mechanical system. A mathematical description of this system is given in Sec. 2.5.

The losses mentioned above are caused by the fluid motion at the opening of the resonator. There are two main loss mechanisms: the thermo-viscous losses due to friction at the walls and losses due to flow separation. The former scale linearly with the particle velocity. This means that, for instance, the losses double when the velocity doubles. However, this relation is not valid for the losses caused by the flow separation. When the particle velocity at the edges of the resonator is beyond a certain level, the fluid particle cannot follow the resonator contour, the flow separates and a jet forms. The kinetic energy of that jet does not recuperate into the acoustic energy, but is transformed into vortices

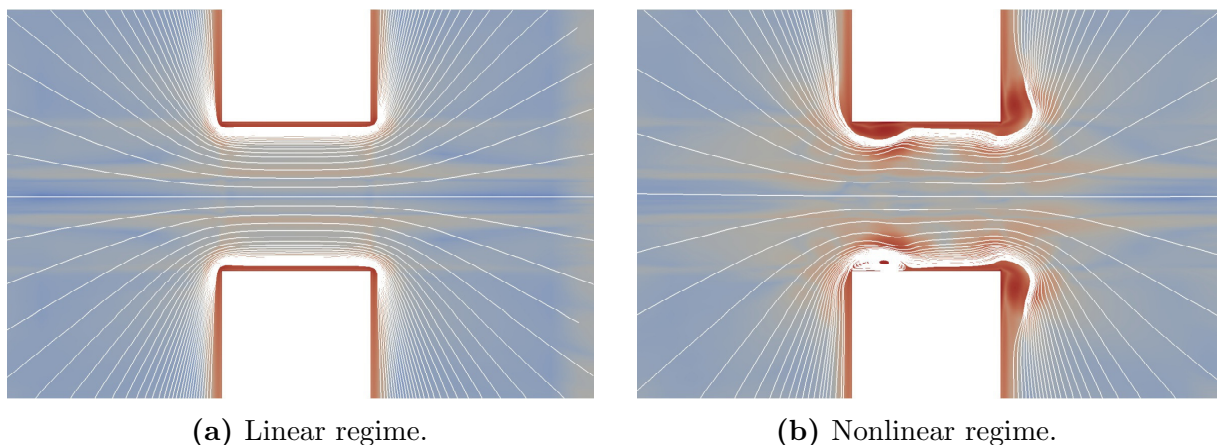


Figure 2.2: Snapshots of streamlines in the vicinity of a Helmholtz resonator neck generated with the CFD environment introduced in Chp. 4.

instead, which are finally dissipated via the turbulent cascade process. The energy which the jet carries—and thus also the acoustic loss—depends on the particle velocity in a nonlinear manner. Moreover, the level of forcing influences the induced flow at the opening of the resonator noticeably. The change of the flow characteristics impacts not only the acoustic losses as described above, but also the fluid mass taking part in the resonant flow motion. This corresponds to a variation of mass in the mass-spring-damper model and, thus, changes the eigenfrequency of the resonator. It is common to distinguish between the *linear* and the *nonlinear regime*. In the linear regime, where the acoustic forcing is sufficiently low, only the linear effects are present. The resonator is said to be operated in the nonlinear regime when the forcing is high enough to trigger nonlinear effects. Typical streamlines for both regimes are illustrated for an Helmholtz resonator in Fig. 2.2. The flow separation at the edges can clearly be seen in the nonlinear regime presented in Fig. 2.2b. In this thesis, these nonlinear effects are studied in detail (see Sec. 5) and a data-based reduced-order model for their description is developed (see Sec. 6).

2.2 Governing Equations

This thesis investigates the acoustic damping of resonators, i. e., the losses of sound propagating in a fluid when it interacts with those devices. All relevant effects are fully included in the *Navier-Stokes equations* for Newtonian, compressible fluids without external forces (see for instance the manuscript by Davidson [8]). This set of equations consists of the *continuity*, the *momentum*, and the *energy equation*. The relation between the density ρ and the velocity of the fluid u_i in space x_i and time t can be written in Einstein notation for the mass and momentum equation as:

$$\frac{d\rho}{dt} + \rho \frac{\partial u_i}{\partial x_i} = 0, \quad \text{and} \quad (2.1)$$

$$\rho \frac{du_i}{dt} = -\frac{\partial p}{\partial x_i} + \frac{\partial}{\partial x_j} \left(2\mu S_{ij} - \frac{2}{3}\mu \frac{\partial u_k}{\partial x_k} \delta_{ij} \right). \quad (2.2)$$

Above, the operator $d \cdot / dt$ denotes the material derivative $d \cdot / dt = \partial \cdot / \partial t + u_i \partial \cdot / \partial x_i$. The pressure, the viscosity, and the strain rate tensor are referred to as p , μ , and S_{ij} , respectively. The rate tensor is defined as $S_{ij} = 1/2 (\partial u_i / \partial x_j + \partial u_j / \partial x_i)$. The transport equation for the internal energy e reads as:

$$\rho \frac{de}{dt} = -p \frac{\partial u_i}{\partial x_i} + 2\mu S_{ij} S_{ij} - \frac{2}{3}\mu S_{kk} S_{ii} + \frac{\partial}{\partial x_i} \left(k_T \frac{\partial T}{\partial x_i} \right). \quad (2.3)$$

Above, the variables T and k_T stand for the temperature and the thermal conductivity, respectively. In addition to the partial differential equations (PDEs) above, two equations of state are required for a complete problem description. Here, the ideal gas law can be applied for all cases considered:

$$p = \rho R_s T, \quad (2.4)$$

where R_s is the specific gas constant. For an ideal gas, the specific internal energy e and the temperature T are linked by the relation:

$$e = \int c_v dT = \int c_p dT - \frac{p}{\rho}, \quad (2.5)$$

where c_v and c_p denote the specific heat capacities at constant specific volume and at constant pressure, respectively.

The set of equations above describes the whole physics involved. However, it is often meaningful to consider some simplification of them. Disregarding viscosity, the momentum equation (2.2) reduces to the *Euler equation*

$$\rho \frac{du_i}{dt} + \frac{\partial p}{\partial x_i} = 0. \quad (2.6)$$

If additionally the flow is assumed to be incompressible and irrotational, i.e. $\omega_i \equiv \epsilon_{ijk} \partial u_k / \partial x_j = 0^1$, it further reduces to the *incompressible Bernoulli equation*

$$\frac{\partial \phi}{\partial t} + \frac{1}{2} u_i u_i + \frac{p}{\rho} = \text{const.} \quad (2.7)$$

This equation is valid along a streamline and the variable ϕ stands for the potential of the irrotational flow $\partial \phi / \partial x_i = u_i$. It is often starting point for the analysis of so-called *acoustically compact* elements, see Sec. 2.5.

In acoustics, isentropic disturbances of flow variables are considered [9]. Hence, any varying quantity q is decomposed into its mean q_0 and its fluctuating parts q' , i.e. $q = q_0 + q'$. If the fluctuating parts are small in comparison to a suitable reference value, it is valid with only minor loss of generality to neglect higher-order products of fluctuating quantities. The continuity (2.1) and the Euler equation (2.6) for the fluctuating quantities read as

$$\frac{d_0 \rho'}{dt} + \rho_0 \frac{\partial u'_i}{\partial x_i} = 0 \quad \text{and} \quad (2.8)$$

$$\rho_0 \frac{d_0 u'_i}{dt} + \frac{\partial p'}{\partial x_i} = 0, \quad (2.9)$$

¹ ϵ_{ijk} denotes the permutation tensor defined as $\epsilon_{ijk} = \begin{cases} 1 & \text{if } (i, j, k) \in \{(1, 2, 3), (2, 3, 1), (3, 1, 2)\} \\ -1 & \text{if } (i, j, k) \in \{(3, 2, 1), (1, 3, 2), (2, 1, 3)\} \\ 0 & \text{else} \end{cases}$

where $d_0 \cdot / dt$ stands for the material derivative with respect to the mean flow $u_{0,i}$. For an isentropic compression, the fluctuating pressure p' and density ρ' are related in first order approximation as

$$p' = c_0^2 \rho' , \quad (2.10)$$

where the constant c_0 is defined as $c_0^2 = (\partial p / \partial \rho)_s$ with the index s indicating the isentropic relation. The variable c_0 is named *speed of sound*, since acoustic perturbations propagate in space with that speed, as it can be seen below in Eq. (2.12). For an ideal gas, the speed of sound is given by $c_0 = \sqrt{\gamma R_s T}$, where γ denotes the adiabatic index $\gamma = c_p / c_v$. By combination of Eqs. (2.8), (2.9) and (2.10), the so-called *wave equation* can be formulated:

$$\frac{d_0^2 p'}{dt^2} - c_0^2 \frac{\partial^2 p'}{\partial x_i \partial x_i} = 0 . \quad (2.11)$$

When the acoustic pressure p' is known, the particle velocity u'_i can be deduced from it by applying Eqs. (2.8) and (2.10).

In many applications, the sound propagates in a 1-D manner. This is, e. g., valid for plane waves in a duct with constant cross section area. Hence, a 1-D configuration is considered in the following paragraph.

The wave equation (2.11) can be factorized as

$$\left(\frac{d_0}{dt} + c_0 \frac{\partial}{\partial x} \right) \left(\frac{d_0}{dt} - c_0 \frac{\partial}{\partial x} \right) p' = 0 . \quad (2.12)$$

Each factor represents an operator known from the convection equation with the convective speeds $\pm(c_0 \mp u_0)$. In this form, it can be seen that the solution of the 1-D wave equation consists of two perturbations traveling upstream and downstream with the speed c_0 relative to the mean fluid motion. These two characteristic waves, also known as Riemann invariants, are defined as

$$f = \frac{1}{2} \left(\frac{p'}{\rho_0 c_0} + u' \right) \quad \text{and} \quad g = \frac{1}{2} \left(\frac{p'}{\rho_0 c_0} - u' \right) . \quad (2.13)$$

Accordingly, the acoustic velocity and pressure is given in terms of f and g as

$$u' = f - g \quad \text{and} \quad \frac{p'}{\rho_0 c_0} = f + g , \quad (2.14)$$

respectively.

In linear acoustics, equations are often transformed into frequency domain by the Fourier transform \mathcal{F} . Quantities in the frequency domain are indicated by $\hat{\cdot}$ and the angular frequency is denoted as ω in the following. The pressure in frequency domain \hat{p} is given by

$$\hat{p}(\omega) = \mathcal{F}\{p\}(\omega) = \int_{-\infty}^{\infty} p(t) e^{-i\omega t} dt . \quad (2.15)$$

When the pressure is determined in the frequency domain, the inverse Fourier transform \mathcal{F}^{-1} yields the corresponding value in the time domain

$$p(t) = \mathcal{F}^{-1}\{\hat{p}\}(t) = \frac{1}{2\pi} \int_{-\infty}^{\infty} \hat{p} e^{i\omega t} d\omega . \quad (2.16)$$

A quantity gained by the inverse Fourier transform is complex-valued. Without loss of generality, the real part of this quantities can be considered as the physical quantity. The 3-D wave equation (2.11) without mean flow is transformed to

$$\frac{\partial^2 \hat{p}}{\partial x_i \partial x_i} + k^2 \hat{p} = 0 \quad (2.17)$$

and is named *Helmholtz equation*. The parameter k is called *wavenumber* and is defined as $k \equiv \omega/c_0$. In a 1-D setup, the propagation of a f -wave in a duct with length l can be written in terms of the wavenumber as: $f_{\text{out}} = \exp(-ilk) f_{\text{in}}$, where $f_{\text{in/out}}$ denote the f -wave entering and leaving the duct, respectively.

2.3 Impedance and Reflection Coefficient

Solving the Helmholtz equation (2.17) on a given domain requires setting boundary conditions (BCs) on the entire boundary. For an ideal opening to the environment, no pressure fluctuations are assumed, i. e., a Dirichlet BC $\hat{p} = 0$ is set on such a boundary. At a hard wall, no wall-normal velocity fluctuations can take place, which means that the gradient of the pressure vanishes in wall-normal direction n_i . This means the Neumann BC $(\partial \hat{p} / \partial x_i) n_i = 0$ is set. In addition to these ideal cases, situations occur where the pressure and velocity fluctuations are coupled in a certain manner. This is modeled as a Robin BC with the so-called (*surface*) *impedance* Z . This quantity is defined in the frequency domain as the ratio of the pressure fluctuations \hat{p} to the wall-normal velocity fluctuation $\hat{u}_i n_i$:

$$Z(\omega) = \frac{\hat{p}(\omega)}{\hat{u}_i(\omega) n_i} . \quad (2.18)$$

Hence, the impedance describes the frequency response function for the pressure when the boundary is excited by a velocity fluctuation. Impedance values should be regarded as an “effective, averaged boundary condition the incident sound experiences rather than as a detailed quantity associated with a point measurement” [10]. The real and imaginary part of the complex valued impedance are denoted as the *resistance* and the *reactance*, respectively. It can be shown that an acoustically passive boundary exhibits a non-negative resistance $\text{Re}(Z) \geq 0$ and that the boundary absorbs sound for $\text{Re}(Z) > 0$, see Rienstra [11]. The two special cases of an ideal opening and a hard wall correspond to impedances $Z_{\text{open}} = 0$ and $|Z_{\text{wall}}| = \infty$, respectively. The impedance perceived by an acoustic wave traveling within a fluid is called *specific impedance* and is given by $\rho_0 c_0$. To allow for a more intuitive interpretation, the impedance is often normalized with respect to that specific value. The normalized impedance $z = Z/(\rho_0 c_0)$ is denoted by lower case z in the following. By a 1-D acoustic analysis [12], the impedance of a loss-free quarter-wave

tube with effective length l_e can be calculated. An f -wave is entering the tube, propagates the distance l_e along the tube, is reflected at the hard wall end (with reflection coefficient $R = 1$, see below Eq. (2.21)), and finally travels as g -wave along the tube in opposite direction. This yields the normalized impedance

$$z(\omega) = \frac{1}{\rho_0 c_0} \frac{\hat{p}}{\hat{u}} = \frac{f + g}{f - g} = \frac{1 + \exp(-i2l_e k)}{1 - \exp(-i2l_e k)} = -i \cot\left(\frac{\omega l_e}{c_0}\right), \quad (2.19)$$

where $k \equiv \omega/c_0$ denotes the wavenumber, see Eq. (2.17).

The relation between the acoustic velocity and the pressure on a boundary $Z(\omega)\hat{u}(\omega) = \hat{p}(\omega)$ can also be described in the time domain. The multiplication in the frequency domain results in a convolution (marked by the symbol $*$) of $u(t)$ with the so-called *impulse response* of the impedance $Z_t(t)$:

$$p(t) = (\mathcal{F}^{-1}\{Z\} * u)(t) = \int_{-\infty}^{\infty} Z_t(\tau) u(t - \tau) d\tau. \quad (2.20)$$

The impulse response Z_t is given by the inverse Fourier transformed impedance $Z_t(t) = \mathcal{F}^{-1}\{Z\}(t) = 1/(2\pi) \int_{-\infty}^{\infty} Z(\omega) \exp(i\omega t) d\omega$. A physical system formulated in a ‘cause and effect manner’ can be assumed to be causal, which means that its response cannot depend on future inputs. In formula, this means that $Z_t(t) = 0$ for all $t < 0$.

Another way to acoustically characterize a boundary is the ratio of the reflected acoustics (g) to the normally incident (f), see Fig. 2.1 ($\theta = 0$). This is done by the *reflection coefficient*, which is defined as

$$R(\omega) = \frac{\hat{g}(\omega)}{\hat{f}(\omega)}. \quad (2.21)$$

Its connection to the impedance is given by

$$R = \frac{z - 1}{z + 1} = \frac{Z - \rho_0 c_0}{Z + \rho_0 c_0}, \quad \text{or} \quad z = \frac{Z}{\rho_0 c_0} = \frac{1 + R}{1 - R}. \quad (2.22)$$

In the formula above, it can be observed that there are no reflections for a normalized impedance of unity, $z = 1$. A system with a normalized resistance below and above unity is referred to as *normally damped* and *over-damped*, respectively. When the plane wave is incident upon boundary with an angle θ (see Fig. 2.1a), the reflection is given by

$$R_\theta = \frac{z \cos(\theta) - 1}{z \cos(\theta) + 1}. \quad (2.23)$$

The maximal absorption is achieved for $z = 1/\cos(\theta)$ in that case.

Frequency response functions such as R and Z describe the system behavior in the Fourier domain and, thus, are valid if the system dynamics are neither decaying nor growing. In many aeroacoustic systems, this assumption applies. For instance, the sound propagation in the inlet duct of an aero-engine can be studied under this assumption, since the sound pressure does not vary on short time scales. However, this assumption is violated when the (linear) thermoacoustic stabilization of a system is studied. Here, transfer functions

in the Laplace domain have to be considered. Exemplarily shown for the pressure, the Laplace transformation \mathcal{L} is defined as:

$$P(s) = \mathcal{L}\{p\}(s) = \int_0^{\infty} p(t)e^{-st} dt . \quad (2.24)$$

Functions in the Laplace domain are denoted by an capital letter, e. g., $P(s)$ for the pressure. The complex-valued Laplace variable $s = \sigma_s + i\omega$ describes both the angular frequency ω and the growth rate σ_s of a signal. All frequency response functions defined in the Fourier domain can also be defined analogously in the Laplace domain. For instance, the impedance reads here as:

$$Z_s(s) = \frac{P(s)}{U(s)} . \quad (2.25)$$

The frequency response functions in the Fourier domain define the behavior only on the imaginary axis of the complex-valued Laplace domain. The Laplace domain representation contains additional information for the behavior of the system responding to an decaying or increasing input signal $u'(t) = \hat{u} \exp[(\sigma_s + i\omega)t]$.

The transfer behavior of any linear, time-invariant (LTI) system can fully be modeled by a transfer function in the Laplace domain. In this context, linear means that the input and the output signal (which are functions in time) can be related to each other by a linear function. Time-invariant implies that the characteristics of the system do not change in time. If the frequency response is known in the Fourier domain, say $Z(\omega)$, it generally cannot be extruded into the Laplace domain as $Z_s(s) = Z_s(\sigma_s + i\omega) \neq Z(\omega)$ for $\sigma_s \neq 0$, see Schmid *et al.* [13]. A frequency response described by a holomorphic² or meromorphic³ function can be extended to a transfer function in the Laplace domain by analytic continuation, which is by construction valid for the underlying LTI system.

In experiments, the impedance cannot be obtained directly since the velocity in the neck is difficult to measure. When there is no mean flow present, the two- or multi-microphone method offers a good possibility to determine the impedance, see for instance Temiz *et al.* [14]. Here, a sample, such as a resonator, is located at the end of a tube, the so-called *impedance tube*, which is equipped with an array of microphones. A loudspeaker placed at the other end excites this configuration harmonically. From the pressure data of the microphones, the characteristic f - and g -waves (see Eq. (2.13)) can be reconstructed. Their ratio gives the reflection coefficient R , cf. Eq. (2.21), from which the impedance can be deduced, see Eq. (2.22). However, for acoustic resonators, the transformation from the reflection coefficient R to the resistance $\text{Re}(z)$ is ill-conditioned for frequencies clearly distinct from the eigenfrequency, see Förner and Polifke [15, Sec. 3.3]. This means that even a small deviation in the reflection coefficient can lead to a huge deviation in the resistance.

In presence of *grazing flow*—a mean flow normal to the resonator opening, this impedance tube approach is difficult to realize. The in-situ method developed by Dean [16] can be applied instead under such conditions. Here, at least one microphone is mounted on the

²complex differentiable

³holomorphic except for a set of isolated points

front plate and one at the bottom of the cavity. Assuming 1-D acoustic propagation in the cavity, the impedance can be deduced from these measurements. In a supervised Semester thesis by the present author, Bambauer [17] implemented both methods in the CFD setup presented in Sec. 4.1 and showed a reasonable agreement of impedance values determined by these approaches. However, a slight discrepancy increasing with the grazing velocity was visible. Due to difficulties placing the microphone close to the sample, so-called impedance education techniques are widespread. Here, the microphones are located far away from the sample and the impedance is calculated by an inverse problem by means of CAA simulations, see for instance Zhou [5].

2.4 Impedance and Reflection Coefficient Describing Functions

As mentioned above, a resonator behaves in a linear manner only for sufficiently small particle velocities close to the edges of the opening. For larger velocities, the flow separates, leading to nonlinear effects. Sivian [18] as well as Ingård and Labate [19] were among the first discovering and modeling this nonlinear behavior. In Sec. 2.5, the impact of the separation effects on the damping characteristics is discussed in more detail. In the nonlinear regime, the system behavior cannot be modeled by a transfer function, which is by definition only valid for an LTI system. Measurements and models are nevertheless often presented in a similar fashion as so-called *describing functions*. Here, the harmonic response of the system to harmonic forcing is given in dependence on the frequency and the sound pressure level (SPL), see for instance Hersh *et al.* [20]. The SPL serves as an indicator for the strength of the acoustic signal. It is defined via the root mean square (RMS) of the acoustic pressure p_{rms} and the reference pressure $p_{\text{ref}} = 20 \mu\text{Pa}$ as

$$\text{SPL} = 20 \log_{10} \left(\frac{p_{\text{rms}}}{p_{\text{ref}}} \right) \text{ dB} . \quad (2.26)$$

However, the describing function does not describe the entire behavior of a nonlinear system.

Overall, the nonlinear behavior of an acoustic resonator manifests itself in several aspects: The most prominent nonlinear effect is that the harmonic behavior changes with the excitation amplitude. This effect is considered by the describing function approach. Hence, for many technical applications, the impedance describing function captures major parts of the dynamics if acoustic amplitudes remain constant. However, there is also scattering to higher harmonics [18, 21, 22], which cannot be modeled by the impedance describing function. This scattering is investigated both analytically and numerically by Förner *et al.* [23] for Helmholtz and quarter-wave resonators and is briefly summarized in Sec. 5.2. In presence of broadband acoustic excitation, the SPL is not a suitable quantity to correlate with nonlinear effects. Instead, the RMS of the particle velocity at the resonator opening seems to be appropriate, see Bodén [24]. Moreover, the acoustic behavior at a certain frequency can be influenced noticeably by multi-tonal excitation, which means that in the excitation signal not only a single frequency is present, but also multiples of that frequencies, see

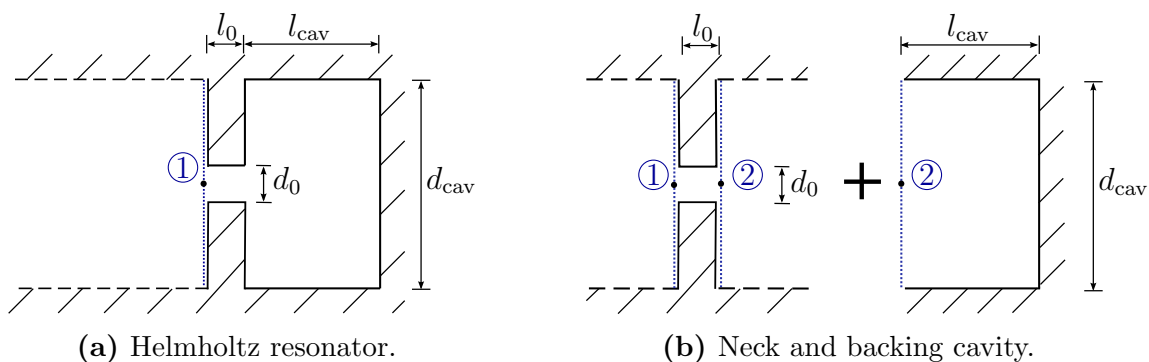


Figure 2.3: Segregation of the Helmholtz resonator into its components.

Bodén [25, 26] and Serrano *et al.* [27]. For this special type of excitation, the resistance for a specific frequency can even take negative values.

2.5 1-D Modeling Approaches

Ingard and Ising [28] suggested studying a Helmholtz resonator segregated in its neck and its backing cavity, as depicted in Fig. 2.3. For typical geometries, the neck itself is *acoustically compact*. This means that the neck is very small in comparison to the acoustic wavelength $\lambda = 2\pi c_0/\omega$, or in other words the Helmholtz number $\text{He} = l_0/\lambda \ll 1$. Here, l_0 denotes the length of the neck. In the following, its diameter is referred to as d_0 and the cylindrical cavity has the length l_{cav} and the diameter d_{cav} , as sketched in Fig. 2.3. With a compact neck, effects of compressibility do not have to be taken into account for the neck but only for the cavity (cf. Eq. (2.28) below). The compact neck is characterized in the frequency domain by the *transfer impedance*

$$Z_o = \frac{\Delta \hat{p}}{\hat{u}}, \quad (2.27)$$

where $\Delta \hat{p} = \hat{p}_1 - \hat{p}_2$ stands for the fluctuating pressure drop from position ① to ②, see Fig. 2.3b. The velocity \hat{u} refers to the cross-sectional surface averaged velocity in the duct. It is equal on both sides of the neck due to the mass conservation and the assumption of incompressibility. There are other authors using the cross-sectional surface averaged velocity in the neck u'_o instead. These two velocities are related via the porosity of the resonator plate $\sigma \equiv d_0^2/d_{\text{cav}}^2$, such that $u' = \sigma u'_o$. The surface impedance of the cylindrical cavity at position ② is given by

$$Z_{\text{cav}} = \frac{\hat{p}_2}{\hat{u}_2} = -i \frac{\rho_0 c_0^2}{l_{\text{cav}} \omega}. \quad (2.28)$$

This expression can be derived by assuming an isentropic uniform compression/expansion of the backing volume. In first order approximation (of the Laurent series), this agrees with the admittance of a quarter-wave tube given in Eq. (2.19), cf. Tournadre *et al.* [29]. Summing up both contributions yields the overall impedance Z of the resonator at the reference plane ① (cf. Fig. 2.3a)

$$Z = Z_o + Z_{\text{cav}}. \quad (2.29)$$

Thus, the knowledge of the transfer impedance of the neck allows for the full characterization of the Helmholtz resonator.

The flow through the neck can be treated as incompressible due to its acoustic compactness. For this purpose, the incompressible Bernoulli equation (2.7) is applied. By doing so, it is implicitly assumed that the flow is inviscid and does not separate. The equation is expressed in terms of fluctuating quantities in 1-D, where x denotes the axial spatial coordinate in the following. Evaluation on a streamline on two reference points on both sides of the neck gives:

$$(\phi'_2 - \phi'_1) + \frac{1}{2} (u'_2{}^2 - u'_1{}^2) + \frac{1}{\rho_0} (p'_2 - p'_1) = 0 . \quad (2.30)$$

The first term can be rewritten by introducing an effective length l_e

$$\phi'_2 - \phi'_1 = \int_1^2 u'(x) dx = \int_1^2 \frac{A_o}{A(x)} u'_o dx = u'_o l_e = \frac{u'}{\sigma} l_e . \quad (2.31)$$

Here, A_o and u'_o denote the cross section area and the velocity in the neck, respectively. The x -dependent cross section area formed by the flow path is $A(x)$. Note that the effective length equals the geometrical length of the neck l_o with an additional *end correction*, see, e. g., Ingard [30]. Due to the conservation of mass, $u_1 = u_2$ and, therefore, the second term in Eq. (2.30) vanishes. Thus, the pressure drop $\Delta p' = p'_1 - p'_2$ over the neck without losses can be expressed as:

$$\Delta p' \approx \rho_0 \frac{1}{\sigma} l_e \frac{\partial u'}{\partial t} . \quad (2.32)$$

The thermo-viscous losses along the neck walls, which are not considered in the above equation, can be included by an appropriate real-valued constant R_l (see, e. g., Bodén and Zhou [31]). When the acoustical particle displacement in the neck reaches the same order of magnitude as the neck diameter d_0 or is larger, i. e., when the *Strouhal number* $Sr = \omega d_0 \sigma / |\hat{u}|$ is small, the flow cannot follow the edge contour and separates. Thus, the flow contracts, taking less area to jet through the neck as sketched in Fig. 2.3. The ratio of the flow core area to the geometrical cross-sectional area is described by the *vena contracta factor* C_d , which is also often referred to as the *discharge coefficient* [20, 32]. In the linear regime where $Sr \gg 1$, it can be assumed $C_d \approx 1$, whereas $C_d < 1$ holds in the nonlinear regime. Besides the effects captured by the Strouhal number, also the edge shape has a strong impact on the separation process. The separation is more pronounced, the sharper the edge is [33, 34], see also Sec. 5.1. Using the contraction factor, the velocity in the neck can be expressed as $u'_o = 1/(C_d \sigma) u'$. When such a jet forms, it draws energy off the acoustics, which is dissipated in the vortex structures generated due to the separation. If it is assumed that the kinetic energy of the flow in the neck $1/2 \rho_0 (1/(C_d \sigma) \tilde{u}')^2$ is fully dissipated and does not recuperate downstream of the neck (see for instance Ingard [21]), it follows

$$\Delta p' \approx \underbrace{\rho_0 \frac{1}{\sigma} l_e \frac{\partial u'}{\partial t}}_{\text{inertia}} + \underbrace{R_l u'}_{\text{viscosity}} + \underbrace{\frac{1}{2} \rho_0 \frac{u' |u'|}{(C_d \sigma)^2}}_{\text{flow separation}} . \quad (2.33)$$

The influence of the backing volume can be inserted into Eq. (2.33). The pressure inside the cavity at location ② can be expressed as $\partial p'_2 / \partial t = \rho_0 c_0^2 u' / l_{\text{cav}}$ (cf. Eq. (2.28)). Introducing

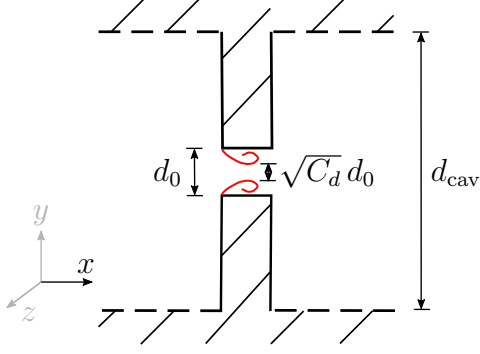


Figure 2.4: Vena contracta of the flow due to flow separation.

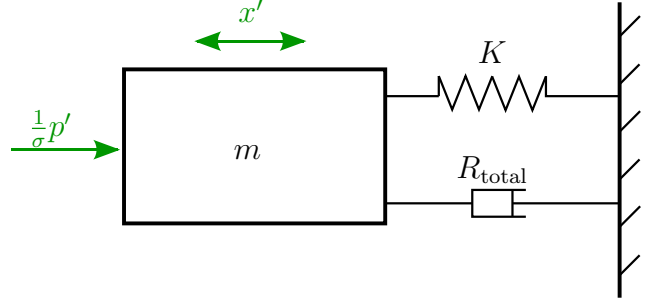


Figure 2.5: Analogy of a resonator to a mechanical mass-spring-damper system.

the particle displacement in the neck $x' = \int u' dt / \sigma$ yields (cf. Singh and Rienstra [35])

$$\frac{1}{\sigma} p' \approx \rho_0 l_e \frac{1}{\sigma} \frac{\partial^2 x'}{\partial t^2} + \left(R_l + \frac{\rho_0}{2\sigma C_d^2} \left| \frac{\partial x'}{\partial t} \right| \right) \frac{\partial x'}{\partial t} + \frac{\rho_0 c_0^2}{l_{\text{cav}}} x' . \quad (2.34)$$

By applying the crude approximation

$$\frac{\rho_0}{2\sigma C_d^2} \left| \frac{\partial x'}{\partial t} \right| \frac{\partial x'}{\partial t} \approx R_{nl} \frac{\partial x'}{\partial t} \quad (2.35)$$

(see Garrison *et al.* [36]), the total resistance is summarized in $R_{\text{total}} = R_l + R_{nl}$. Equation (2.34) can be rewritten using the constants m and K for the description of respectively the inertia effect of the mass in the opening and the compressibility of the backing volume:

$$\frac{1}{\sigma} p' \approx m \frac{\partial^2 x'}{\partial t^2} + R_{\text{total}} \frac{\partial x'}{\partial t} + K x' . \quad (2.36)$$

The ordinary differential equation (ODE) above has the same structure as an ODE modeling a mechanical mass-spring-damper system as sketched in Fig. 2.5. This provides the mathematical justification for the mechanical analogy already given in Sec. 2.1. From the study of such single degree of freedom oscillators (SDOFs), it is known that its angular eigenfrequency equals

$$\omega_{\text{eig}} = \sqrt{\frac{K}{m}} = c_0 \sqrt{\frac{\sigma}{l_e l_{\text{cav}}}} . \quad (2.37)$$

For moderate damping, the free system oscillates at its angular eigenfrequency ω_{eig} .

Equation (2.36) can be transform in the frequency and the Laplace domain, i.e. $\hat{p}(\omega) = Z(\omega)\hat{u}(\omega)$ and $P(s) = Z_s(s)U(s)$, respectively. The resulting expressions for the impedance are given by:

$$Z(\omega) = R_{\text{total}} + i \left(m \omega - \frac{K}{\omega} \right) \quad \text{and} \quad (2.38)$$

$$Z_s(s) = R_{\text{total}} + s m + \frac{1}{s} K . \quad (2.39)$$

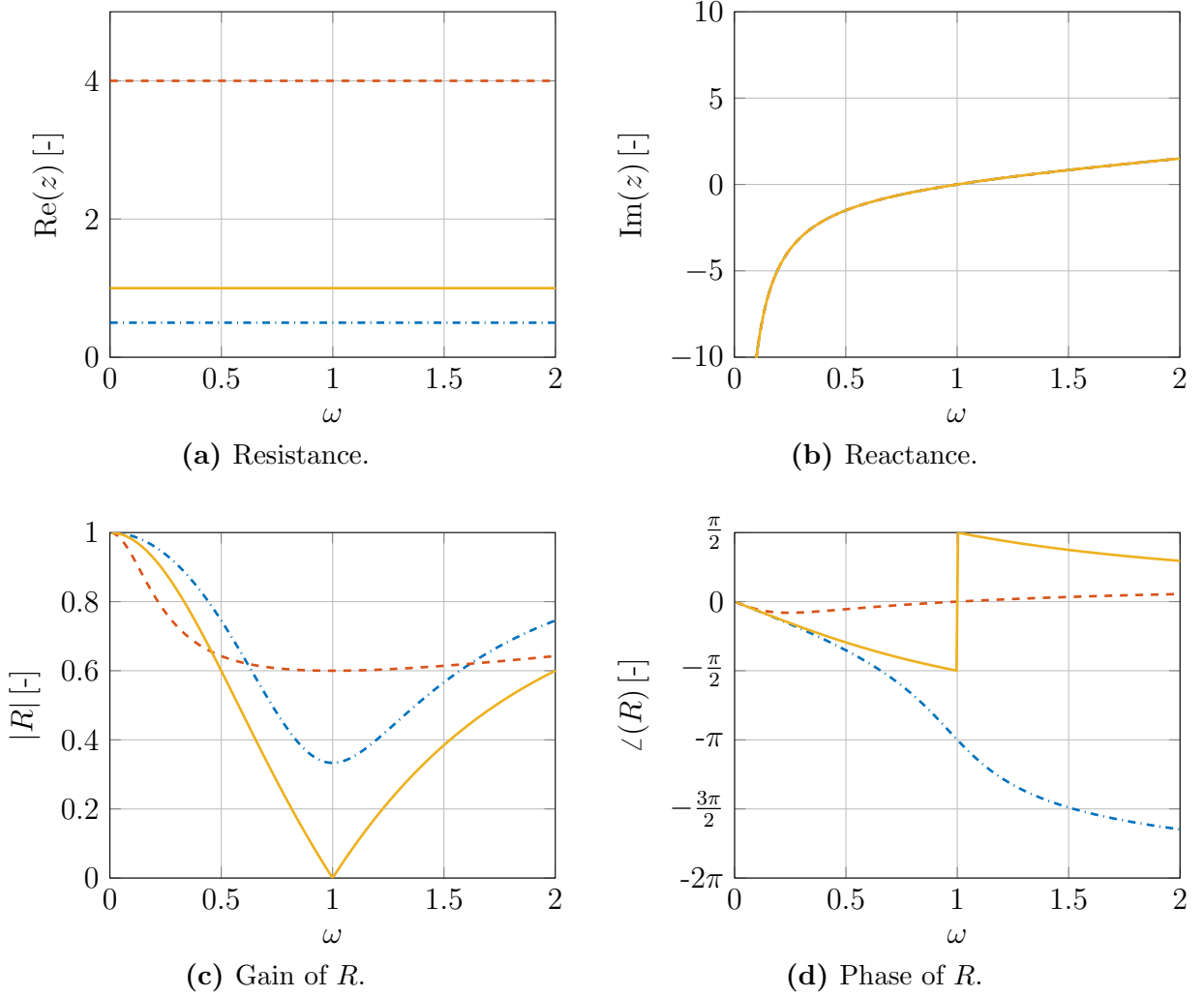


Figure 2.6: Impedance and reactance determined by the generic SDOF model in Eq. (2.38) for a normally damped \cdots , an optimally damped — , and over-damped system --- .

In the following, the dynamics of the SDOF system (2.36) are discussed in terms of the impedance and the reflection coefficient. For that purpose, generic systems with the mass $m/(\rho_0 c_0) = 1 \text{ s}$ and the compressibility constant $K/(\rho_0 c_0) = 1 \text{ s}^{-1}$ are considered. The normalized impedances z and the corresponding reflection coefficients R , determined by Eq. (2.22), are plotted in Fig. 2.6 for three cases. For these cases, different resistance values $R_{\text{total}}/(\rho_0 c_0) = \text{Re}(z) \in [0.5, 1, 4]$ are taken into account covering normally damped (\cdots for $\text{Re}(z) = 0.5$), optimally damped (— for $\text{Re}(z) = 1$), and over-damped conditions (--- for $\text{Re}(z) = 4$). For all cases, the angular eigenfrequency of the generic systems equal unity, where the reactance curves change their signs, see Fig. 2.6b. In Fig. 2.6c, it can clearly be seen that the resonator absorbs best at its eigenfrequency $\omega_{\text{eig}} = 1$, meaning that the gain of the reflection coefficient $|R|$. When the resistance $\text{Re}(z)$ increases in the normally damped regime, the absorption increases. As explained above in Sec. 2.3, the resonator dampens optimally for $\text{Re}(z) = 1$ and absorbs all incident acoustic energy at its eigenfrequency, see the — -curve in Fig. 2.6c. In the over-damped regime with $\text{Re}(z) >$

1, increasing the resistance decreases the maximal absorption, while the bandwidth of absorption is widened simultaneously, see the $---$ -curve in Fig. 2.6c. Moreover, the phase curves of the reflection coefficients $\angle R$ behave differently depending on damping regimes, see Fig. 2.6d. At the eigenfrequency, the f - and g -waves are respectively in phase for the normally damped ($\angle R \pmod{2\pi} = 0$) and in antiphase for the over-damped regime ($\angle R \pmod{2\pi} = \pi$). Far away from the eigenfrequency, R is always in phase.

Overall, the nonlinear effects for the damping behavior can be briefly be summarized like this: High acoustic amplitudes trigger flow separation at the edges. This leads to additional acoustic losses increasing the resistance. By variation of the resistance, the resonator operates either in the normally damped or the over-damped regime, resulting in the implications explained in the previous paragraph. In addition to the effects on the resistance, flow separation reduces the mass taking part in the oscillation. This corresponds to a reduction of the effective length and shifts the eigenfrequency to higher frequencies.

Semi-analytical approaches, similar to the one presented above, are followed by several authors to derive expressions for the impedance of a resonator or an orifice. Refer for instance to Rice [37], to Cummings and Eversman [38], to Elnady and Bodén [39], as well as to Hersh *et al.* [20].

A similar idea can also be employed to model the impedance of a quarter-wave resonator. Its impedance can be written as (cf. Cárdenas Miranda [40])

$$Z^{\text{QW}}(\omega) = R_l^{\text{QW}} + R_{nl}^{\text{QW}} - i\rho_0 c_0 \cot\left(\frac{\omega l_e^{\text{QW}}}{c_0}\right). \quad (2.40)$$

Also for this resonator type, the resistance consists of a linear R_l^{QW} and a nonlinear component R_{nl}^{QW} . The linear resistance originates from the friction at the wall, which is largest close to the mouth of the resonator, since here the particle velocities are highest. As in the case of the Helmholtz resonator, the additional losses of the flow separation for high velocities are collected in the term R_{nl}^{QW} . Usually, the transition from the linear to the nonlinear regime occurs for higher SPLs in comparison to a Helmholtz resonator with an eigenfrequency in the same order of magnitude, see [33, 41]. The effective length l_e^{QW} corresponds to the length of the quarter-wave tube elongated by a length correction. However, this length correction is smaller for the quarter-wave resonator in comparison to the Helmholtz resonator, since it only has to account for the fluid taking part in the oscillation in front of the one opening. The angular eigenfrequency is given by

$$\omega_{\text{eig}}^{\text{QW}} = \frac{c_0 \pi}{2l_e}. \quad (2.41)$$

The acoustic wavelength $\lambda = 2\pi c_0 / \omega_{\text{eig}}^{\text{QW}}$ corresponding to the eigenfrequency equals a quarter of the effective length l_e^{QW} of the resonator, which explains the origin of its name.

In the discussion above and also in the further course of the thesis, effects of mean flow, temperature distribution, and hot gas penetration into the resonator opening are ignored. In many technically relevant application, there is a grazing flow over the resonator. For instance, this is studied experimentally by Jones *et al.* [42] and numerically by Zhang and Bodony [43]. Summarized, the grazing flow increases the resistance, while the effective length is decreased. Resonators in gas turbines are often *purged*, which means that cool

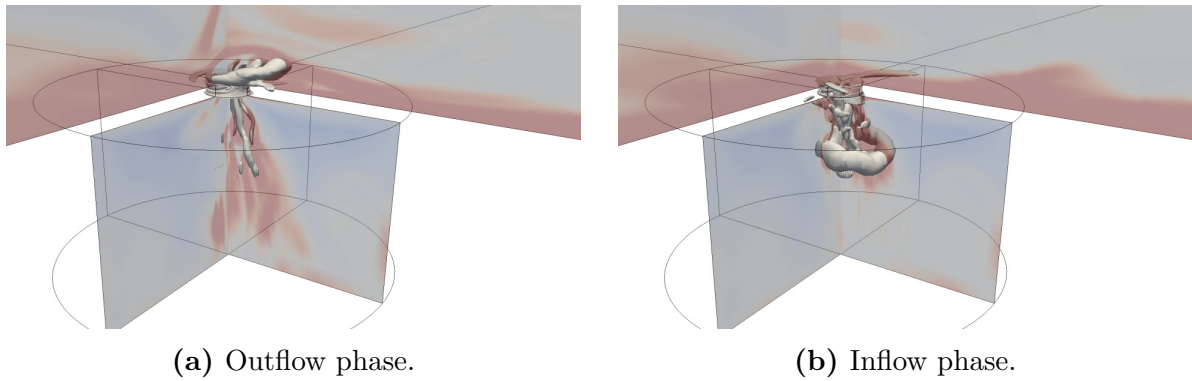


Figure 2.7: CFD simulation (cf. Chp. 4) with grazing flow (from left to right) in the nonlinear regime; vortices are visualized with the Q-criterion.

gas is injected into the backing cavity such that a mean flow directed outwards of the resonator is present. By doing so, they are guarded against the hot gas in the combustion chamber and constant working conditions are guaranteed. This increases the acoustic losses significantly, see, e. g., Eldredge and Dowling [44], Bellucci *et al.* [45], or Scarpato *et al.* [46]. When the amplitude of the acoustic excitation rises and the purging flow rate is too low, hot gas can penetrate the resonator opening. This can detune the resonator and should thus be avoided, see the studies by Ćosić *et al.* [47] and Rupp *et al.* [48]. The present thesis does not deal explicitly with these phenomena. However, the computational setup presented in Sec. 4.1 is capable of incorporating them. Figure 2.7 presents exemplarily snapshots of a simulation in the nonlinear regime with grazing flow. For details, refer to the theses, supervised by the present author, of Mayr [49] and of Bambauer [17]. The latter also shows how a Helmholtz resonator with several openings is correctly scaled to a single orifice resonator. The data-based modeling approaches in Sec. 6 can also be applied under the mentioned operating conditions.

3 Numerical Assessment of Thermoacoustic Stability

Acoustic resonators are used to suppress thermoacoustic instabilities in combustion systems. A fluctuating combustion process leads to a fluctuating thermal expansion, which, in turn, can produce acoustic sound. In 1878, Rayleigh [2] expressed this as follows: “For instability to occur, heat must be released at the moment of greatest compression.” So, if the integral over the product of the fluctuating heat release \dot{Q}' and the fluctuating pressure p' over a period T is positive, i. e.,

$$\int_0^T \dot{Q}' p' > 0 , \quad (3.1)$$

the flame acts as a sound source. The emitted sound is reflected at the boundaries of the chamber and affects the combustion process again. This closed loop process can lead to a so-called *thermoacoustic instability*. Here, the pressure amplitude can grow to high values until the combustion chamber is either destroyed or nonlinear saturation processes and interdependencies come into play. Self-excited instabilities can occur at the eigenfrequencies of the system. For an eigenfrequency, the assigned spatial distribution of the acoustic quantities, especially of the pressure, is referred to as an eigenmode.

Over the years, modeling of the mechanisms involved and their analytical and numerical evaluation became a powerful tool to study the interaction of those mechanisms and supporting the design process of combustion systems. In Sec. 3.1, a very brief, exemplary and, hence, incomplete overview of such modeling approaches is given. The study of Förner *et al.* [50] is summarized in Sec. 3.2.

3.1 Methodological Overview

There exist several approaches to determine the thermoacoustic stability of a system. Among other things, they differ in the extent to which models (instead of the full set of equations) are used to describe the involved phenomena [51]. A way to reduce the complexity is to consider linearized problems. Linearized modeling enables to determine the linear stability, i. e., predicting whether the amplitudes in the system grow or decay in the regime of small distortion from a chosen operating point. Due to this limitation, it cannot anticipate an amplitude level for linearly unstable operating conditions. In return, linear systems can be evaluated in the frequency/Laplace domain. The increased modern computational resources facilitate high-fidelity CFD simulations including nonlinear effects even for large high-complex systems. For instance, Urbano *et al.* [52] investigated

the thermoacoustic behavior of a rocket combustion chamber with multiple injectors by means of large eddy simulations. However, the computational costs of such high-fidelity simulations are not yet affordable in industrial practice. At the other end of the spectrum of modeling, there are analytical models for specific geometries. As an example, the modes of a rocket combustion chamber can be estimated by the eigenmodes in of a cylinder with an appropriate length correction for the nozzle [33]. Due to the assumptions made, such pure analytic models are often inappropriate for realistic applications. Instead, the *divide et impera* strategy is of avail in many cases [53]. Here, the overall system is segregated into sub-components. Models for those sub-components can, for instance, be derived analytically, identified experimentally or numerically. Each sub-component is modeled separately and their models are connected to a network. For such network tools, see for instance Li and Morgans [54], often a 1-D acoustic behavior is assumed at the connecting planes. Via such a 1-D interfaces, also a 3-D computational domain can be coupled to the 1-D network simulation, see for instance Huber *et al.* [55], Bellucci *et al.* [56], Kaess *et al.* [57], Schulze and Sattelmayer [58] as well as Emmert *et al.* [59]. On such a 3-D computational domains, sets of equations of different complexity can be solved. Jaensch *et al.* [60] demonstrated that any (acoustic) linear subsystem behavior can be connected to a CFD simulation as a BC on a 1-D interface using a systematic state-space approach. As an alternative to the high-fidelity CFD approach, linearized equations are often applied, as the Helmholtz, the linearized Euler, or the linearized Navier-Stokes equations, cf. Pankiewicz and Sattelmayer [61], Nicoud *et al.* [62] as well as Gikadi [63]. Besides the Helmholtz equation, such linearized equations require the mean field information, which has to be determined in an a priori CFD simulation. Accordingly, such hybrid approaches are often referred to as *CFD/CAA techniques*. In combination with an appropriate flame model, these techniques can predict the linear stability. For instance, Schulze [64] followed the CFD/CAA approach to study a rocket combustion chamber. In this study, the mode shape, which is determined in an initial CFD/CAA run, was used as an input to characterize the high-frequency response of the single flame in a high-fidelity CFD simulation. Feeding back this flame response into the CAA simulation enabled predicting the linear stability.

Overall, there exist various methods for the stability analysis of thermoacoustic systems. Resonators are employed in many relevant applications. For the stability analysis of such damped systems, all methods require an accurate model for the damping performance of resonators, if they do not resolve this behavior explicitly. Depending on the field of application, such a model must either be linear—for a linear analysis in the frequency or the time domain—or nonlinear—for a rigorous nonlinear study in the time domain. In Sec. 6, it is discussed how reduced-order models can be provided on basis of CFD simulation data. Before that, a study with a low-order network model is presented in the following section, illustrating the stabilizing impact of resonators in a combustion system.

3.2 Network Model for a Rocket Combustion Chamber

In this section, the study by Förner *et al.* [50] (reproduced in the Appendix on p. 66ff.) is briefly presented. For a generic rocket combustion chamber, an extensive parametric study

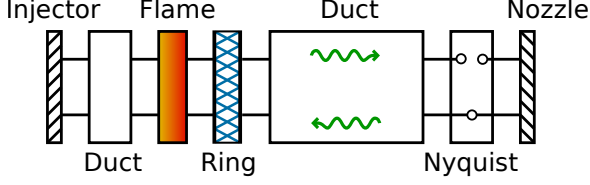


Figure 3.1: Acoustic network of a generic test chamber with resonator ring. (Reproduced from [50].)

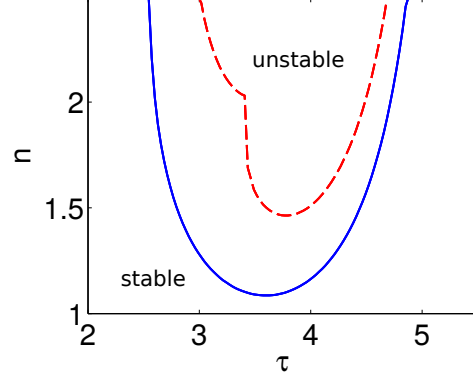


Figure 3.2: Stability map in dependency on the flame parameters n_f and τ for the undamped (blue solid) and well-tuned damped (red dashed) chamber. (Reproduced from [50].)

is conducted regarding the impact of quarter-wave resonators on the linear thermoacoustic stability. The model used is based on the network model from Cárdenas Miranda and Polifke [65]. It is defined in the frequency domain and is capable of considering both plane and non-plane modes. The modeling approach and results achieved are summarized in the following.

The main idea of this modeling approach is the segregation of the entire system into sub-components. Figure 3.1 presents the segregated combustion chamber, which is equipped with resonators. These resonators are arranged azimuthally in a ring, as it is usually done in modern rocket motors, see for instance Oswald and Farago [66]. This ring is modeled as a single element in the network.

In a cylindrical duct segment, the 3-D solution of the convected wave equation can be written in cylindrical coordinates (x, r, θ) as:

$$\begin{aligned} \frac{p'(x, r, \theta)}{c_0 \rho_0} &= \sum_{m,n} \left[J_m(\alpha_{mn}^+ r) F_{mn} e^{-ik_{mn}^+ x} + J_m(\alpha_{mn}^- r) G_{mn} e^{-ik_{mn}^- x} \right] e^{-st} e^{im\theta} \\ &= \sum_{m,n} (f_{mn} + g_{mn}) , \end{aligned} \quad (3.2)$$

where J_m denotes the first kind Bessel function of order m . As in the 1-D case, there are also waves traveling downstream f_{mn} and upstream g_{mn} . Here, these waves have an additional azimuthal order m and a radial order n . Their phase velocity is determined by their wavenumbers, where k_{mn}^\pm and α_{mn}^\pm are the axial and radial wavenumbers. The superscripts + and - denote the corresponding wavenumbers for the up- and downstream traveling waves, respectively. These numbers are linked by the *dispersion relation*

$$(\alpha_{mn}^\pm)^2 = \left(-\frac{s}{c_0} - \text{Ma} k_{mn}^\pm \right)^2 - (k_{mn}^\pm)^2 , \quad (3.3)$$

where Ma stands for the Mach number of the axial uniform flow in the cylindrical duct. Using the impedance BC at the cylinder wall, the wavenumbers can be calculated for all orders m and n . In the case of a hard wall, this is done analytically. In the resonator ring, an effective homogeneous impedance is derived. For each resonator, an impedance model as in Eq. (2.40) is incorporated into this homogeneous expression. A numerical root-finding algorithm is applied to detect the wavenumbers for the soft wall conditions. At the interconnection with the resonator ring element, a mode matching technique is employed to guarantee mass and momentum conservation over the interface, see Gabard and Astley [67]. This mode matching introduces also scattering to higher order modes at the interfaces.

The nozzle is modeled according to Bell and Zinn [68] and, at the injector plate, full reflections are imposed. For the flame considered as a thermoacoustic element of zero thickness, the well-known sensitive time lag model proposed by Crocco [69] is applied:

$$\frac{\dot{Q}'}{\dot{Q}} = n_f (1 - e^{-s\tau}) \frac{p'^u}{p^u} . \quad (3.4)$$

This $n\text{-}\tau$ model relates the relative pressure fluctuation p'^u/p^u on the cold upstream side to the relative fluctuating heat release \dot{Q}'/\dot{Q} with a time lag τ and an interaction index n_f . Using the linearized Rankine-Hugoniot equations [70], the fluctuating heat release is translated into acoustic quantities. The eigenmodes and, accordingly, the linear stability of the entire system are estimated via the Nyquist criterion applied in the Nyquist element, see Sattelmayer and Polifke [71]. Here, the network is cut (as depicted in Fig. 3.1) and the open loop transfer function is evaluated for signals with constant amplitude ($\sigma_s = 0$). This has the advantage that the transfer behavior of each element has to be known only for ω . The eigenfrequencies are estimated by the minimal distances to the critical point.

By applying this network model for a generic test chamber, it is observed that the most unstable mode is the 1T1L mode (first longitudinal mode $n = 1$ with azimuthal order $m = 1$), which is indeed typical for rocket combustion chambers [64]. By a parametric study, the optimal length and the optimal number of resonators are determined for that mode. An additional eigenmode is observed for a chamber equipped with these well-tuned resonators. Both the original and the additional mode show favorable stability properties. Resonators are often tuned—which means that their lengths are varied—with respect to the eigenfrequencies of the undamped system. However, a noticeable discrepancy between this a priori estimated length and the optimal length is observed. This highlights the necessity of analyzing the coupled system of resonators and combustion chamber in the design process. Since publication, this main conclusion obtained with the low-order network has been confirmed by the finite element simulations by Schulze *et al.* [72]. The stability map of the well-tuned and the totally undamped combustion chamber is visualized in Fig. 3.2 with respect to the flame parameters n_f and τ . The area of the linearly stable operation conditions is significantly increased by inserting the well-tuned resonator ring. Moreover, the sensitivity of the stability with respect to the nonlinear resistance of the resonators R_{nl}^{QW} is clearly pointed out in this study. This underlines the need for accurate models that describe the impact of high pressure oscillations. A method of generating data-based ROMs valid for such high pressure is presented in Sec. 6.3.

4 CFD Simulations of Acoustic Resonators

The work presented employs CFD simulation as a major tool. The computational setup is introduced in this chapter and the methodology is briefly embedded in the literature context. As acoustics is of compressible nature, a compressible solver, addressed in Sec. 4.1, is mostly applied. However, incompressible techniques can be adopted for the aeroacoustic characterization of acoustically compact elements. This is done for the Helmholtz resonator by a segregation approach, see Sec. 4.2.

4.1 Compressible CFD Simulations

Tam and co-workers were among the first to prove the potential of CFD simulations to capture the resonator dynamics. Tam and Kurbatskii [73] studied via direct numerical simulations (DNSs) the vortex shedding at a slit resonator in 2-D. In dependency on frequency and SPL, they determined the transition from the linear regime without vortex shedding to the nonlinear regime with vortex shedding. In this juncture, they showed its acoustical damping effect. These findings were validated experimentally by Tam *et al.* [74]. Tam *et al.* [75] performed DNSs on a 3-D computational domain and depicted the different structure of shed vortices in 3-D in comparison to 2-D. However, the vortex shedding remained the main source for acoustical dissipation for high SPLs also in the 3-D setup. Zhang and Bodony also followed the DNS approach in a series of papers. They investigated the flow physics in detail and demonstrated that the vortices form turbulent structures for high SPLs even for moderate Reynolds numbers based on the particle velocity [32]. Furthermore, they analyzed the impact of laminar and turbulent grazing flow on the damping behavior [43]. The effect of purging flow through an orifice was studied by means of large eddy simulations (LESs) by Mendez and Eldredge [76] as well as by Scarpato *et al.* [77]. Moreover, the linearized Navier-Stokes equations can be used to investigate the linear response of resonator, as it was done by Tournadre *et al.* [78] for the investigation of temperature effects. An alternative approach to solving the Navier-Stokes equations is the Lattice Boltzmann method, which is based on particle collision models and is promising low numerical cost, see for instance Ji and Zhao [79].

Main parts of the work presented are also based on CFD simulations. Compressible CFD simulations are performed with OpenFOAM [80] for an ideal gas with the PIMPLE algorithm, which is a combination of algorithms SIMPLE [81] and PISO [82]. This pressure-based algorithm solves the compressible Navier-Stokes equations, see Sec. 2.2, using second-order schemes in space and time. The time integration is executed implicitly by

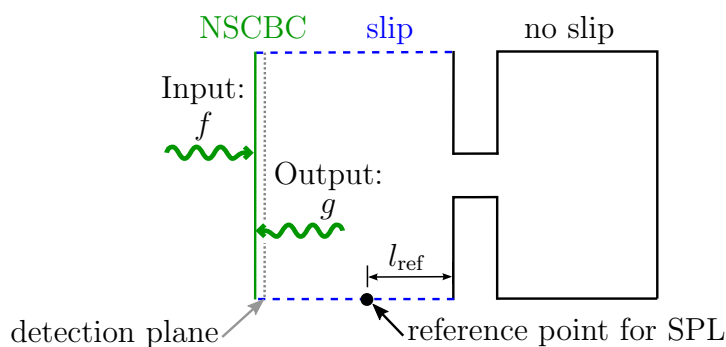


Figure 4.1: Computational domain for the Helmholtz resonator.

a backward time stepping. In principle, this scheme allows for acoustic Courant-Friedrichs-Lewy (CFL) numbers $c_0\Delta t/\Delta x$ larger than unity, where Δt and Δx denote the time step and the length interval of the computational grid, respectively. However, computational setups with acoustic CFL numbers considerably smaller than unity in the major parts of the grids are considered for the high-fidelity simulations. Resolving the acoustics correctly in the simulation requires an accurate velocity-pressure-energy coupling. In OpenFOAM, this is achieved by the convergence control with a sufficiently low threshold for the pressure residuum, which is set maximally to 1×10^{-5} . The time step is set to $\Delta t = 1 \times 10^{-6}$ s for cases with an eigenfrequency $2\pi\omega_{\text{eig}} < 1$ kHz.

Both axisymmetric 2-D and 3-D structured meshes are considered in the studies presented. The axisymmetric and 3-D meshes are generated by the OpenFOAM tool blockMesh and the commercial software ANSYS ICEM CFD, respectively. The cell sizes close to the walls at the opening of the resonator must be set fine enough to resolve the boundary layer for the frequency range of interest, which can be estimated by the Stokes length $\delta_s = 2\pi\sqrt{2\mu/(\omega\rho_0)}$. For all published results, mesh independence is achieved regarding the acoustic reflection coefficient.

For the configurations considered without mean flow, it is showed that sub-grid scale (SGS) turbulence models in LES have only a minor impact on the acoustic properties, see the supervised Master’s thesis by Qin [83]. Zhang and Bodony [32] demonstrated that flow separation leads to turbulent structures in front of the resonator opening also for rather low Reynolds numbers. However, it is checked by comparison to LES—applying, i. a., the k -equation eddy-viscosity model—that SGS modeling has only minor influence on the resulting impedances and vortex separation for the cases considered. This shows that the mesh resolution in the vicinity of the resonator opening is chosen fine enough to resolve the separation mechanism correctly even without a SGS model. Hence, good results can be achieved without SGS model, see [29, 84]. However, this might change for other circumstance, for instance, when the SPL is further increased or when a mean flow is present.

The general computational domain for the Helmholtz resonator is sketched in Fig. 4.1. For the quarter-wave resonator, the computations are set up analogously. Since the dissipation takes place at the resonator walls, a no-slip condition is used here, indicated by solid lines in the figure. A slip boundary condition is applied at the boundaries of the cylindrical domain in front of the resonator, presented with dashed lines, to exclude dissipative

effects not related to the resonator itself. At the inlet, the *Navier-Stokes characteristics boundary condition* (NSCBC), cf. Poinso and Lele [85], is utilized. This boundary condition ensures a low acoustic reflection of the outgoing g -wave at the boundary of the computational domain in the frequency range of interest. Simultaneously, an input signal can be imposed for the incoming f -wave. In the studies presented, either harmonic or broadband signals covering various SPL ranges have been applied. The broadband signals imposed are generated according to Föller and Polifke [86]. Such a signal is designed in a way that it excites the entire frequency spectrum of interest, while steep changes in the input signal are avoided, which could otherwise cause numerical difficulties. Moreover, this signal shows a low autocorrelation, which promises to improve the identification results, see Chap. 6.

Detection planes are placed in the computational domain at a sufficient distance from the resonator such that non-acoustic disturbances are absent there. Such non-acoustic disturbances are present in the vicinity of the resonator opening due to shed vortices. The resulting acoustic quantities must be independent of the position of this plane. If there is a difference noticeable at two planes close to the inlet, the computational domain has to be elongated further. At the planes, time series of the area averaged fluctuating pressure p' and velocity u' are detected. From these quantities, time series of the f - and g -waves can be computed directly, see Eq. (2.13). These time series are time-shifted with respect to each other to account for the time it takes to travel from the detection plane to the resonator and back. These corrected time series can either be used for SI in the case of a broadband excitation, or the reflection coefficient can be determined at a single frequency in case of a harmonic excitation. In the second case, the time series are cropped to an integer multiple of the excitation period $2\pi/\omega$ to avoid leakage in the discrete Fourier transform and to dispose of any transient behavior. Now, the reflection coefficient can be evaluated $R(\omega) = \hat{g}(\omega)/\hat{f}(\omega)$ and the impedance can be deduced from it, see Eq. (2.22).

In the nonlinear regime, the damping characteristics depend on the amplitude of excitation. This dependency is often described in terms of the SPL. In a 1-D duct as in computational setup, the pressure at a reference position is given by the superposition of an f - and a g -wave, $p'/(\rho_0 c_0) = f + g$ (cf. Eq. (2.14)). Using the laws for the propagation of the plane waves in the duct and the reflection with the coefficient $R(\omega, \text{SPL})$, the amplitude A_f of a harmonic input signal $f(t) = A_f \sin(\omega t)$ has to be imposed as (cf. [29])

$$A_f = 10^{\text{SPL}/20} \frac{\sqrt{2} p_{\text{ref}}}{|1 + R(\omega, \text{SPL}) \exp(-i\omega 2l_{\text{ref}}/c_0)| \rho_0 c_0} \quad (4.1)$$

to gain the desired SPL at a reference position in a distance l_{ref} from the resonator. If the reflection coefficient R —which is, in general, the case—is unknown, an iterative procedure of simulations is required to set the amplitude correctly, since its value is needed in Eq. (4.1). In the cases where the overall SPL is of minor importance, only the SPL of the incident acoustic wave is considered. This is referred to as *incident SPL*. This is also done by other authors, for instance, Tam and Kurbatskii [73] as well as Zhang and Bodony [32]. Note that in general the incident SPL and the actual total SPL differ from each other.

The solver settings are validated against measurements for several test cases. Exemplarily, this is presented in Fig. 4.2 for measurements from Hersh *et al.* [20]. The dimensions

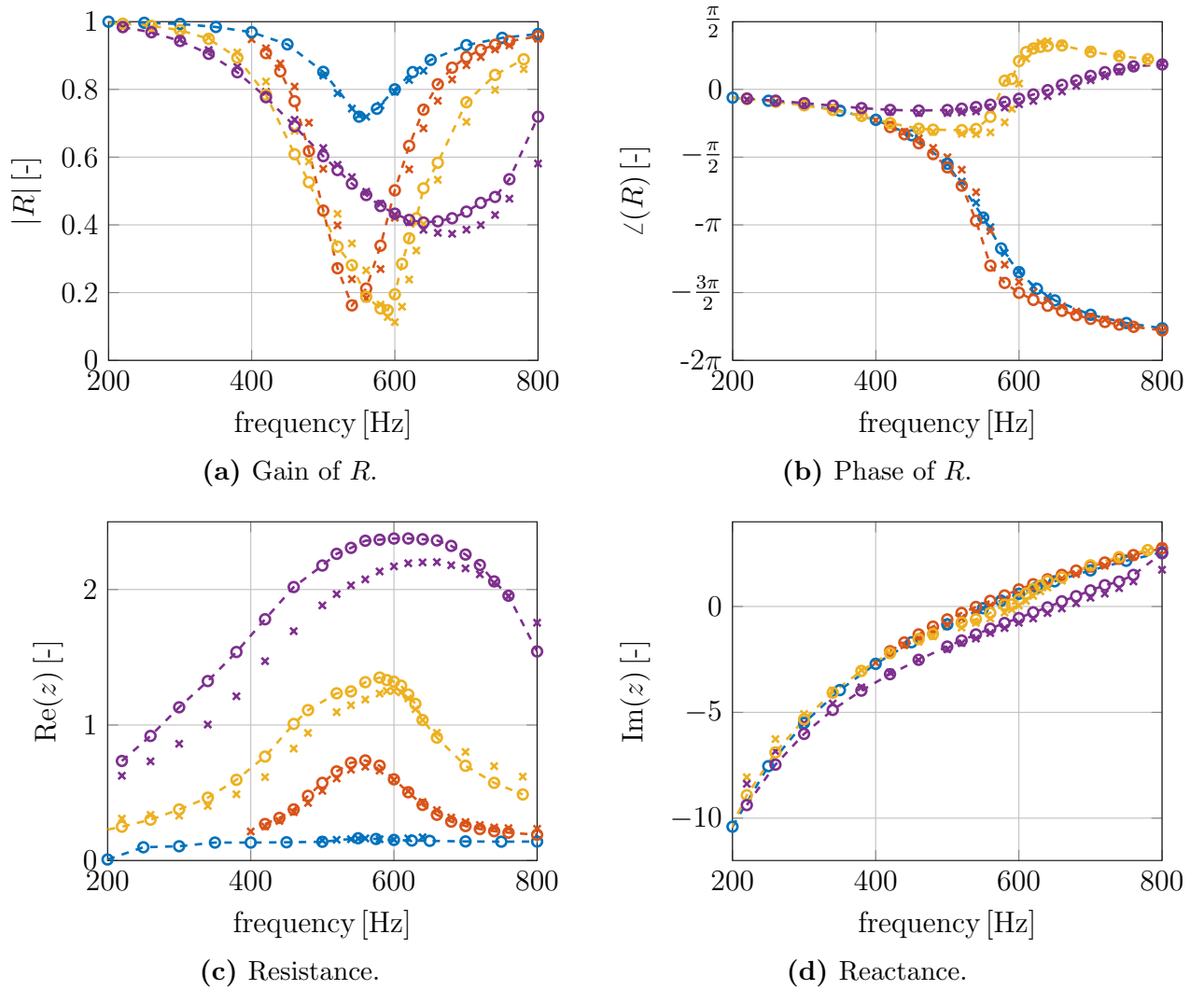


Figure 4.2: Reflection coefficient R and normalized impedance z for a configuration from [20]: Measurements (\times) from [20, Fig. 12a] and CFD simulations ($- \bullet -$) for 75 dB (\bullet), 120 dB (\circ), 130 dB (\circ), and 140 dB (\circ). (Figure is reproduced from [15]).

of this configuration are given by $l_0 = 0.159$ cm, $d_0 = 0.635$ cm, $l_{\text{cav}} = 2.54$ cm, and $d_{\text{cav}} = 5.08$ cm. Accordingly, its open area ratio $\sigma = d_0^2/d_{\text{cav}}^2$ yields 1.56 % and its eigenfrequency can be estimated around 570 Hz by Eq. (2.37) for ambient conditions and using $8/(3\pi) d_0$ as end correction [30]. The experiment has been conducted for four SPLs namely 75 dB, 120 dB, 130 dB, and 140 dB. Only the low SPL case of 75 dB is located in the linear regime. Since no reference location for the SPL is given in the paper [20], it is assumed that those values refer to the position of the front plate, i.e. $l_{\text{ref}} = 0$ (see Eq. (4.1)). The CFD simulations are performed on a 3-D grid with around 1.8 million cells. Subfigures 4.2a and 4.2b depict gain and phase of the reflection coefficient R for both the measurements [20, Fig. 12a] and the simulations. The reflection coefficient is transformed to the normalized impedance, which is shown in Subfigs. 4.2c and 4.2d. In comparison to the measurements, the numerics over-predict the resistance very slightly for the 130 dB

case and moderately for the 140 dB case. The lower resistance values in the experiment might (at least partially) originate from non-perfectly sharp edges due to manufacturing reasons, cf. Tournadre *et al.* [87]. Besides that small deviation in the resistance for high SPLs, all curves agree reasonably well. It can be concluded that the CFD setup presented is capable of capturing the acoustics in both the linear and the nonlinear regime. It is competitive against other CFD approaches [32, 75], where partially larger deviations from the experiment are present.

The expected physical behavior from the 1-D consideration in Sec. 2.5 fits well to the impedance and reflection coefficients presented in Fig. 4.2. The resistance rises with increasing SPL as seen in Fig. 4.2c. The eigenfrequency can be detected by the zero-crossing of the reactance. In Fig. 4.2d, it can be observed that the eigenfrequency shifts slightly to higher frequencies with higher SPLs. The zero-crossing of the 140 dB reactance curve is at a noticeably higher frequency in comparison to the other curves. This nonlinear behavior manifests itself in the corresponding reflection coefficient as follows (see Figs. 4.2a and 4.2b): First, the maximal absorption increases with SPL in the lower SPL range. When the normalized resistance exceeds unity, the maximal absorption decreases due to over-damping of the system, but the frequency bandwidth of high absorption becomes wider. For such an over-damped system, the phase curve differs from a normally damped system, see Fig. 4.2b. All $\angle R$ -curves show that the f - and g -waves are in phase for frequencies far away from the eigenfrequency. Close to the eigenfrequency, these waves are in antiphase for normally damped systems, whereas they are in phase for over-damped systems.

4.2 Incompressible CFD Simulations

It may be surprising for non-acousticians but incompressible CFD simulations can be employed to acoustically characterize devices that are compact (see Sec. 2.5). This means that their geometric dimensions are small in comparison to the acoustic wavelengths for the frequency range of interest. In many cases, the incompressible framework allows for a simpler and more robust simulation setup in comparison to the compressible setup. Jaensch *et al.* [88] characterized the thermoacoustic response of flames based on incompressible simulations. In the field of aeroacoustics, Martínez-Lera *et al.* [89] successfully combined incompressible CFD and vortex sound theory [90] to a two-dimensional laminar flow through a T -joint. This methodology is further improved and applied to corrugated pipes by Nakiboğlu *et al.* [91] and to a large orifice configuration with through-flow by Lacombe *et al.* [92] for whistling prediction. In contrast to those previous works, the present study focuses on both the linear and the nonlinear regime of Helmholtz resonators in absence of mean flow. This method can be extended to the case with a mean flow due to the general formulation and arguments presented by Nakiboğlu *et al.* [91] and Golliard *et al.* [93].

The study by Tournadre *et al.* [29] (reproduced in the Appendix on p. 74ff.) shows the potential of incompressible simulations to study the aeroacoustic response of a Helmholtz resonator. Here, the Helmholtz resonator is segregated into the neck and the backing volume as suggested by Ingard and Ising [28], see also Fig. 2.3 in Sec. 2.5. This study

demonstrates that this segregation approach works not only in the linear but also in the nonlinear regime if the amplitudes in the simulations are set correctly. The incompressible simulations are excited by a velocity perturbation. The nonlinear effects are triggered by the flow separation process at the neck, which is governed by the particle velocity in the neck. Hence, it is essential to set the amplitude of the velocity excitation such that the velocity in the segregated neck coincides with the velocity in the neck in the composed resonator. Therefore, the SPL in the segregated system differs in general from the SPL in the composed system. The overall impedance of the resonator is determined by assembling the neck transfer impedance and the surface impedance of the backing volume, see Eq. (2.29). Following this scaling rule, a good agreement of the incompressible simulations with both the compressible simulations and experiments can be achieved.

The advantage of the simpler incompressible simulation framework is exploited by Caeiro *et al.* [84]. In this study with a contribution of the present author, an adjoint approach is used to formulate an optimization procedure for the shape of the resonator neck. This procedure enables to determine a neck contour which exhibits a desired target impedance at a specific frequency and SPL.

5 Aeroacoustic Characterization of Nonlinear Effects by Harmonic Probing

The behavior of resonators is commonly determined by harmonic probing [20]. Here, a sinusoidal signal—with a certain frequency and amplitude—excites the device acoustically. The studies summarized in this chapter apply this technique to explore aspects of the nonlinear behavior of the resonator response. In addition, analytic considerations confirm the results. In Sec. 5.1, the impact of the edge shape of the neck on the reflection coefficient and the impedance is investigated in the nonlinear regime for Helmholtz resonators. Scattering to higher harmonics is analyzed for both Helmholtz and quarter-wave resonators in a second study presented in Sec. 5.2.

5.1 Influence of Edge Shape on the Flow Separation and the Damping Behavior

As explained above, the nonlinear effects in the resonator response originate mainly due to flow separation at the edges of the resonator. Laudien *et al.* [33] showed that the shape of the edge influences the damping performance of a resonator. Murray *et al.* [94] investigated the change of the damping performance due to the manufacturing process. They concluded that the acoustic resistance is strongly influenced by small variation of the edge shape. Earlier, Disselhorst and Wijngaarden [95] observed in a similar configuration—in an open pipe—a very significant impact of the edge shape on its acoustic behavior. For an orifice, Temiz *et al.* [96] focused on the transition behavior from the linear to the nonlinear regime and detected a strong effect of the edge shape on the damping. They related this effect to the vena contracta factor C_d (see Sec. 2.5) induced by the contour of the orifice.

Förner *et al.* [34] (reproduced in the Appendix on p. 83ff.) quantitatively investigate the impact of the edge shape of Helmholtz resonators by means of both CFD simulations and measurements. The measurements are conducted by M. A. Temiz at TU Eindhoven. Here, different samples with sharp edges and with 45°-chamfers are considered, as depicted in Fig. 5.1. The results of both methods agree qualitatively well, even though the absolute values of the resistance slightly disagree in the nonlinear regime. In spite of this noticeable deviation, the following conclusions can be drawn based on both methods: With increasing length of the chamfer, the eigenfrequency of the resonator increases. This corresponds to a reduction of the effective length, meaning that the mass taking part in the oscillation reduces with the length of the chamfer. More prominently, the nonlinear resistance is

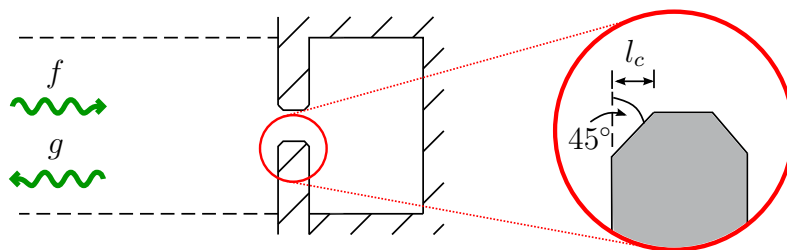


Figure 5.1: Helmholtz resonator with a chamfer of length l_c at the edges of the neck.

reduced by the presence of a chamfer. This effect is almost independent of the length of the chamfer. This behavior can be explained by studying the contraction of the jet in the neck. In the flow visualization for the sharp edge cases, a huge separation zone at the leading edge is observed, which correlates with a vena contracta factor $C_d \ll 1$. In presence of a chamfer, this zone is noticeably reduced corresponding to a contracta factor close to unity, $C_d \approx 1$. The contraction detected in the CFD simulations agrees reasonably well with the reduction in the resistance and with literature values for the static vena contracta factors [97].

5.2 Scattering to Higher Harmonics

As mentioned above, scattering to higher harmonics may take place for resonators operating in the nonlinear regime. This means that the resonator is excited harmonically at an angular frequency ω_0 ¹ and the spectrum of the response comprises of the content not only of this fundamental harmonic ω_0 , but also of the higher harmonics $n\omega_0$, ($n = 2, 3, \dots$). The scattering to higher harmonics is rarely studied in the literature for resonators. For an orifice, which is closely related to the Helmholtz resonator, this scattering was studied experimentally and analytically by Ingard and co-workers [21, 28] as well as by Cummings [22]. An *Odd-Harmonics-Only* (OHO) pattern in the higher harmonics was observed, where only the odd harmonics ($n = 1, 3, 5, \dots$) are present in the response. This observation could be explained by a quasi-steady analysis based on the Bernoulli equation, see Eq. (2.33). In a supervised thesis of the present author, Mages [98] studied this equation numerically reformulated in terms of Riemann invariants f and g . He also retrieves the OHO pattern also in this formulation of the problem.

Förner *et al.* [41] (reproduced in the Appendix on p. 91ff.) extend the quasi-steady approach from the literature [21, 22, 28] such that it can also be applied to Helmholtz resonators with an asymmetric neck, or for quarter-wave resonators. Moreover, compressible CFD simulations are conducted to study this phenomenon for the configurations mentioned. The nonlinear contribution to the pressure drop over the neck of a Helmholtz resonator can be approximated as $1/2 \rho_0 (1/(C_d \sigma) u')^2$, according to Eq. (2.33). The main impact of a one-sided chamfered neck is the different contraction of the fluid jetting through it, see Sec. 5.1. For the modeling, a constant vena contracta factor C_d^+ is as-

¹In this section, the excitation frequency is clearly marked by the subscript 0 to avoid confusion with frequency content at higher harmonics.

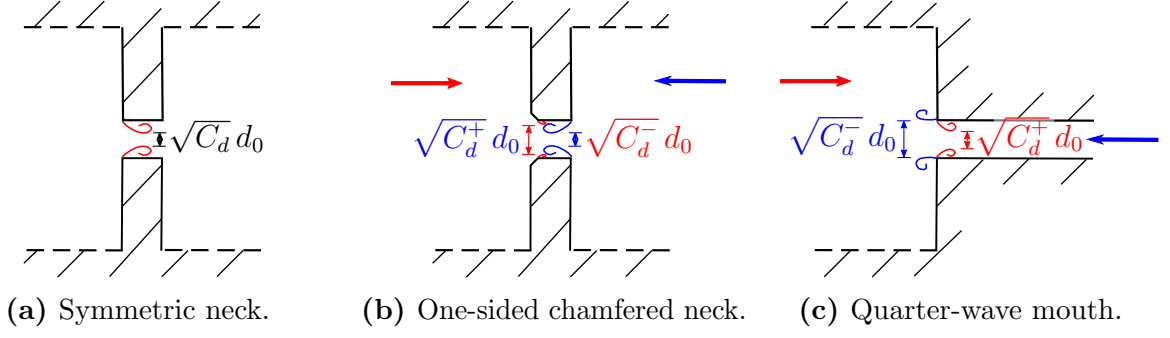


Figure 5.2: Considered resonator openings with particle flow direction depend separation behavior.

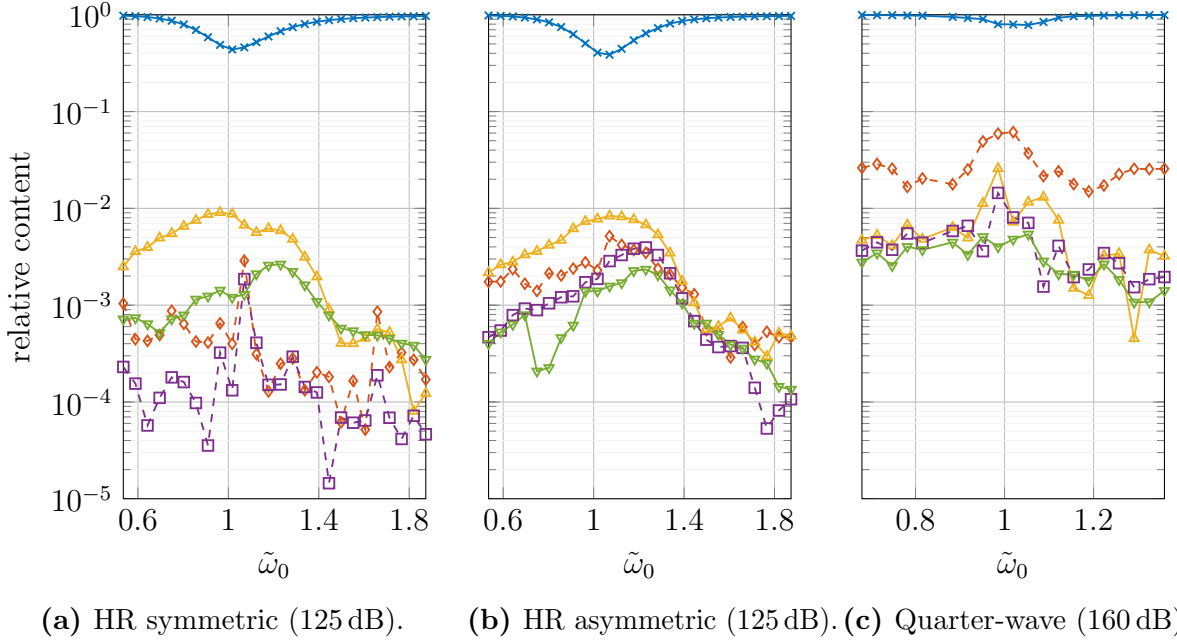


Figure 5.3: Scattering to harmonics plotted in logarithmic scale for the three considered test cases: 1st = fundamental $\text{---}\times\text{---}$; 2nd $\text{---}\diamond\text{---}$; 3rd $\text{---}\triangle\text{---}$; 4th $\text{---}\square\text{---}$; 5th $\text{---}\nabla\text{---}$. (Reproduced from [41].)

sumed during the inflow and a constant—but possibility different—factor C_d^- during the outflow phase. This is sketched schematically for the three cases considered in Fig. 5.2. The analysis of the Fourier transformed nonlinear pressure drop term predicts that the OHO pattern is pronounced if C_d^+ and C_d^- are similar. Conversely, if these factors differ from each other, the OHO pattern weakens. To study the scattering to higher harmonics for the quarter-wave resonator, an analogous analysis is performed for the area jump. Here, the analysis predicts that the second harmonic is the dominant higher harmonic. These analytical predictions are confirmed by CFD simulations. Exemplarily, CFD results are presented in Fig. 5.3 for three test cases: Two Helmholtz resonators—one with a symmetric as well as another one with an asymmetric neck—and a quarter-wave resonator.

The incident SPL is fixed for the frequency variation presented and $\tilde{\omega}_0$ denotes the excitation frequency normalized with the corresponding eigenfrequency. In this figure, the proportions scattered in the first five harmonics, defined as

$$\frac{|\hat{g}(n\omega_0)|}{|\hat{f}(\omega_0)|}, \quad (5.1)$$

are plotted. For the fundamental harmonic ($n = 1$) $\text{---}\ast\text{---}$, this is equivalent to the reflection coefficient. The major part of the incident harmonic wave is reflected into the fundamental harmonic. For the Helmholtz resonator with symmetric neck, the odd harmonics ($n = 3$ $\text{---}\triangle\text{---}$, $n = 5$ $\text{---}\nabla\text{---}$) clearly dominate over the even harmonics, see Fig. 5.3a. As predicted by the quasi-steady analysis, this OHO pattern gets weaker for the Helmholtz resonator with an asymmetric neck (see Fig. 5.3b) and totally vanishes for the quarter-wave resonator, where the 2nd harmonic $\text{---}\diamond\text{---}$ is the dominant higher harmonic (see Fig. 5.3c). However, the scattering to higher harmonics remains overall on a moderate level for the Helmholtz resonator. For the quarter-wave resonator, a higher proportion is scattered into the higher harmonics (up to 15% for high SPL).

6 Aeroacoustic Characterization by Data-Based Reduced-Order Modeling

This chapter summarizes the work on the field of data-based reduced-order modeling and positions it briefly in the literature context. The aim is to determine a reduced-order model (ROM) which can be evaluated efficiently while reproducing the essential system dynamics correctly. Models derived from first principles are referred to as *white-box models*, as for instance the models for the resonator dynamics presented in Sec. 2.5. In the following, a different methodology is applied: the models are developed based on data series using SI methods. Since usually a model structure is specified without considering explicitly the physics or the governing equations involved, such a model is called a *black-box model*. The data are acquired by CFD simulations excited with a broadband signal covering the entire frequency range of interest. Hence, the overall procedure is referred to as *CFD/SI method*. This method gives good results in various aero- and thermoacoustic setups, especially in the linear regime, see Polifke [53] for a review on the work done in his group or Innocenti *et al.* [99] applying this approach on a preferably premixed flame. With this approach, not only transfer functions but also aero- or thermoacoustic sources for the noise can be estimated in parallel. For instance, Sovardi *et al.* [100] characterized the scattering behavior and the noise source of an orifice in presence of low Mach number mean flow. Selimefendigil [101] determined nonlinear models for heat sources using different model structures such as artificial neuronal networks. However, Jaensch and Polifke [102] demonstrated the high uncertainty which can be involved in nonlinear identification processes if only relatively short time series data are available. Hence, attention regarding the robustness and the validation of the estimated models is required, especially for nonlinear models. As mentioned above, the approach is based on broadband excitation. Broadband characterization for orifices and resonators is also considered by other authors. In both experiments and DNS simulations, Tam *et al.* [75] excited a resonator by a long broadband signal and determined the linear frequency response by using the discrete Fourier transform. Bodén [24, 103] applied a high-amplitude signal triggering nonlinear effects at an orifice. By assuming a physically motivated model structure, the linear and the nonlinear contributions were separated.

6.1 Linear System Identification and Prediction Error Method

The idea of SI is to estimate a ROM based on broadband time series which comprises of input and output data. In this work, only single-input/single-output (SISO) systems are considered. The method is briefly introduced in the discrete time framework since measurements and simulations can only provide sampled, i.e., as discrete time series. The time series is assumed to be sampled equidistantly with a constant time step Δt . The discrete time index k denotes the sample for the instant in time $t_k = k\Delta t$. In the application at hand, the sampled f - and g -wave time series are the input and output data. Any discrete LTI system (with input $f[k]$ and output $g[k]$) can be written as

$$A(q^{-1}) g_{\text{model}}[k] = \frac{B(q^{-1})}{F(q^{-1})} f[k] + \frac{C(q^{-1})}{D(q^{-1})} e[k], \quad (6.1)$$

where A , B , C , F , and D are polynomials in the time shift operator¹ q . Such a polynomial acts as a digital filter, hence the effect of the polynomial B with the degree n_b applied on $f[k]$ can exemplarily be written as $B(q^{-1})f[k] = \sum_{i=0}^{n_b} b_i q^{-i} f[k] = \sum_{i=0}^{n_b} b_i f[k-i]$. A fraction of two polynomials, say $(B/F)f[k]$, can be evaluated by polynomial expansion leading possibly to a filter with an infinite number of filter coefficients being applied on $f[k]$ even for finite polynomial orders. The variable $e[k]$ stands for a *white* noise source, which is uncorrelated to the input. When the non-deterministic output of the model is *colored*, meaning that the corresponding signal has a non-constant spectral density, at least one of the polynomials A , C , or D differs from unity. Usually, some polynomials are set to unity when specific phenomena are considered. Moreover, the polynomial orders of the remaining polynomial have to be fixed before the SI process, which requires some phenomenological understanding of the problem and/or an iterative procedure. All polynomial coefficients are collected in the vector of unknowns θ .

The task in the SI process is to estimate the optimal values of parameter $\hat{\theta}$. For that purpose, the time series data of the CFD simulation are used as so-called *training data set*. The parameters $\hat{\theta}$ are usually determined by least square method such that the difference of the model output $g_{\text{model}}[k](\theta)$ defined in Eq. (6.1) and of the measured CFD output $g_{\text{CFD}}[k]$ is minimized:

$$\hat{\theta}_{\text{model}} = \underset{\theta}{\operatorname{argmin}} \sum_k (g_{\text{model}}[k](\theta) - g_{\text{CFD}}[k])^2. \quad (6.2)$$

This approach to predict the free model parameters is called the *prediction error method* (PEM), see Tangirala [104].

An estimated model in the discrete time domain can be converted into other domains. Therefore, the z -transform \mathcal{Z} is introduced, which can be considered as the “discrete Laplace transformation”. The variable z is defined as $z = \exp(s\Delta t)$, where s is the Laplace variable. The z -transformation of the discrete time input signal $f[k]$ reads as:

$$\mathcal{Z}\{f[k]\}(z) = F_z(z) = \sum_{k=0}^{\infty} f[k] e^{-k\Delta t s} = \sum_{k=0}^{\infty} f[k] z^{-k}. \quad (6.3)$$

¹Example for the time shift operation: $q^{-1}f[k] = f[k-1]$.

Applying the z -transform to $B(q^{-1})f[k]$, yields

$$\begin{aligned} \mathcal{Z}\{B(q^{-1})f[k]\}(z) &= \sum_{k=0}^{\infty} \left(\sum_{i=0}^{n_b} b_i f[k-i] \right) z^{-k} = \\ &= b_0 \sum_{k=0}^{\infty} f[k] z^{-k} + b_1 z^{-1} \sum_{k=0}^{\infty} f[k-1] z^{-(k-1)} + \dots = B(z^{-1}) F_z(z) . \end{aligned} \quad (6.4)$$

The polynomial $B(q^{-1})$ in the time shift operator q^{-1} just transforms into a polynomial $B(z^{-1})$ with the same coefficients in the z -domain. Using the bilinear (Tustin) approximation, transfer functions in z can be transformed into the Laplace domain and vice versa, see [104]. Overall, the model estimated is also valid for decaying or increasing amplitudes. Thus, a model of the type defined in Eq. (6.1) is well suited for performing stability analysis.

6.2 Linear Aeroacoustic Characterization of Resonators

The SI procedure briefly described in Sec. 6.1 is applied on the input/output data from CFD simulations of the acoustic resonators (see Sec. 4.1). In this section, only the linear response is considered, i. e., the resonators are excited with sufficiently low amplitudes. The entering f -wave serves as the input and the reflected g -wave as the output. Hence, models for the reflection coefficient R are estimated. In the aeroacoustic modeling of resonators, no colored noise is expected in absence of turbulent mean flow. Consequently, a model structure with $A = C = D = 1$ is selected, which is called an *output-error* (OE) model. This model is presented as a block diagram in Fig. 6.1. CFD/SI with a second-order OE model gives good results in the linear regime, see Förner and Polifke [105] (reproduced in the Appendix on p. 83ff.). Exemplarily, Fig. 6.2 presents the frequency responses of estimated OE models for four test cases. The models agree well with measurements from Hersh *et al.* [20] and Temiz [34], which are also included in this figure. The estimated models can be converted into impedance models. However, the resistance values can differ significantly from measurements due to the ill-conditioned conversion for frequencies apart from the eigenfrequency, see Sec. 2.3. In a successive study, Förner and Polifke [15] show

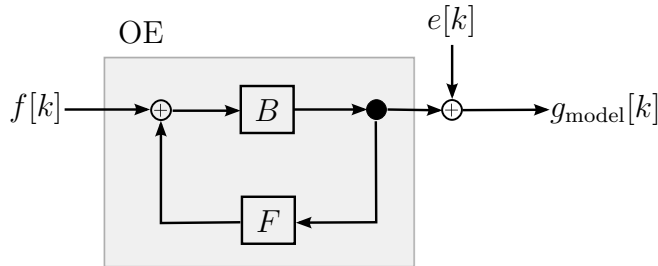


Figure 6.1: Block diagram of an output-error model reproduced from [15].

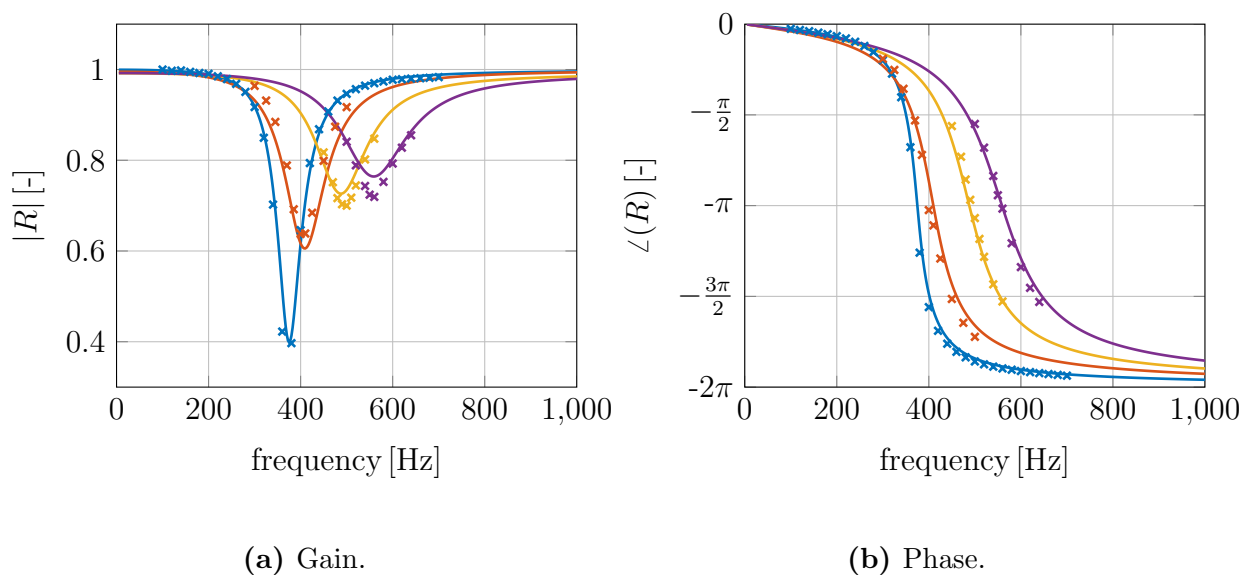


Figure 6.2: SI-estimated (—) and measured (\times) reflection coefficient R for four test cases indicated by the colors. (The presented figure is similar as in [15].)

that this approach can also provide local-linear models in the nonlinear regime. Such a local-linear model is a linear model suitable for a fixed amplitude range in the nonlinear regime.

6.3 Nonlinear Aeroacoustic Characterization of Resonators

The linear CFD/SI approach introduced in Sec. 6.2 is now extended into the nonlinear regime. Only a very limited number of linear black-box model structures are available and the output-error model structure is found to provide quantitatively accurate estimated models for the Helmholtz resonator dynamics in the linear regime. Contrary, there exists a large variety of nonlinear models which can be used for SI. Representatives of nonlinear black-box models are Volterra series as well as artificial neural networks [104]. These model types are in principle capable of modeling various nonlinear behavior. However, for the test cases considered, a huge number of model parameters is required such that identification results achieved with reasonably long time series are not robust.

Therefore, Förner and Polifke [15] (reproduced in the Appendix on p. 110ff.) introduce a *gray-box model* structure that exploits a priori knowledge of the system dynamics. Neuro-fuzzy networks offer the opportunity to incorporate such knowledge in the model structure, see, e. g., Nelles [106] or Babuška and Verbruggen [107]. Such a network is developed for modeling the specific case of the resonator. It is referred to as local-linear neuro-fuzzy network (LLNFN) and its block diagram is sketched in Fig. 6.3. Several output-error models OE_i ($i = 1, 2, \dots, N$) form the skeletal structure of the network. These submodels are wired via a so-called *fuzzy-neuron layer* to the input channel $f[k]$. The input signal

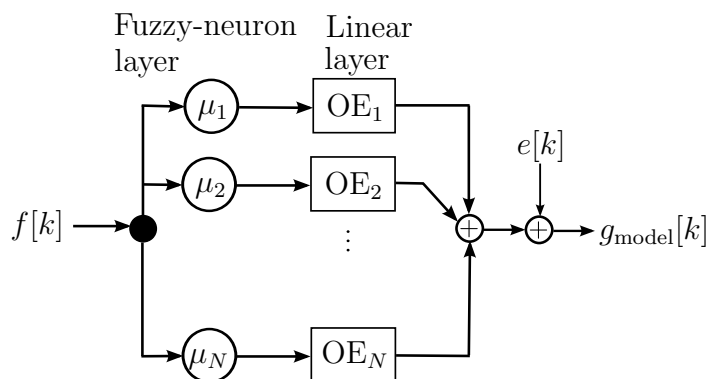


Figure 6.3: Block diagram of a local-linear neuro-fuzzy model with output-error blocks (see Fig. 6.1) as submodels; reproduced from [15].

is distributed within this layer over the submodels depending on the RMS of the velocity at the reference surface. The RMS of the velocity (for a fixed geometry) seems to be the parameter controlling the nonlinear behavior also in the case of non-harmonic excitation, as suggested by Bodén [24]. Each submodel has its *neuron* which applies a *membership function* μ_i to the input signal. This membership function takes a value within the interval $[0, 1]$ depending on the RMS of the particle velocity. If this RMS value agrees exactly with or differs significantly from the reference velocity $u_{\text{ref},i}$ of the membership function μ_i , it takes the values true and false corresponding to 1 and 0, respectively. However, the membership function cannot only yield the values “true” (1) and “false” (0), as in Boolean logic, but also every intermediate state in the interval $[0, 1]$, as in fuzzy logic. A common-sense interpretation of the role of the membership function is developed as follows (for $N = 3$): If the amplitudes are low, the first model OE_1 is taken to describe the resonator behavior. The second model OE_2 is considered in the medium amplitude regime and model OE_3 in the high-amplitude regime. This decision is made not in a strict but in a fuzzy way, which means that the response can be formed proportionally by more than one model OE_i . For instance, a linear combination of OE_1 and OE_2 is used in the low-medium amplitude regime.

An iterative procedure to train LLNFNs is developed and applied to several test cases. The input signal is designed in a way that it contains the entire frequency and amplitude range of interests. The quality of the estimated models is assessed in both the time and the frequency domain. The response of the estimated models is computed for a second independent input signal, which was not used to train the model. The validation against *test data* is an important step in SI to ensure that estimated models do not suffer from over-parameterization. A model is denoted as *over-parameterized* when it has so many free parameters that it can, on the one hand, achieve a good fit to the training data thanks to the large degrees of freedom, but gives, on the other hand, poor predictions for another set of input data, the test data [108, p. 133]. The estimated models perform competitively well on the test data set for all test cases studied. Hence, the LLNFN model is deemed robust against over-parameterization. Using the describing functions for the reflection coefficient and the impedance, the estimated models are compared against measurements from Hersh *et al.* [20] and Temiz [34]. Besides small deviations for very high amplitudes, good agreement is achieved for all test cases studied.

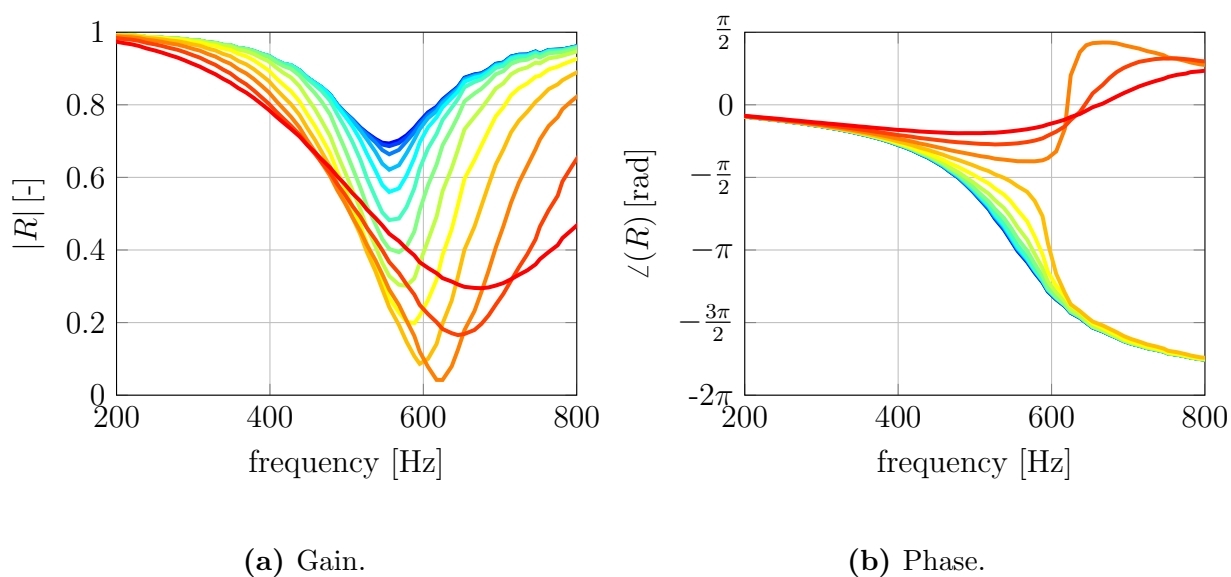


Figure 6.4: Estimated impedance describing function with total SPLs ranging from 80 dB (bluish) to 140 dB (reddish) in steps of 5 dB. (Reproduced from [15].)

The estimated LLNFN models can be evaluated efficiently in the entire frequency and amplitude range they have been trained for. Figure 6.4 presents, exemplarily for a test case, a describing function for the reflection coefficient R in a frequency range [200, 800] Hz and a SPL range [80, 140] dB in 5 dB steps. It can be observed that the impedance changes smoothly with SPL and frequency, which makes this model attractive to serve as a boundary condition in CFD or CAA simulations. Using a linear model instead would require that this model is adapted a priori to the conditions and a linear model can never reflect changing conditions by its design. Moreover, the LLNFN model structure makes a model—once estimated—readily available also for other time steps or in Laplace domain. Each submodel can be converted to a function in the Laplace variable s by the Tustin transformation $z \rightarrow s$ (see Sec. 6.1). By another reverse transformation $s \rightarrow z$, the estimated model can be applied for fixed time step of arbitrary size. Alternatively, the boundary condition can directly operate with the model representation in Laplace domain [109], which has the advantage that the time step can vary within the simulation. Such possibilities are in general not given by other nonlinear models applied in SI, e. g., by artificial neural networks.

Moreover, the provided procedure could support the design of future resonators. When the designer has access to a validated CFD setup for resonator simulations, he/she can rapidly estimate how geometrical, flow, or temperature conditions influence the linear and nonlinear resonator behavior, since only one CFD simulation is required. Thus, this procedure can also be used for the uncertainty quantification of the resonator response. It is known that, for instance, the manufacturing process of acoustic liners strongly impacts the actual damping behavior, see Murray *et al.* [94]. With the proposed method, one could quantify with low computational effort how the manufacturing tolerances influence the damping performance.

7 Summary and Conclusion

The present thesis addresses the nonlinear damping behavior of acoustic resonators such as quarter-wave and Helmholtz resonators. This nonlinear behavior originates from flow separation at the edges of the resonator openings in the presence of high acoustic amplitudes. In particular, this thesis focuses on the following aspects: high-fidelity fluid dynamic simulations of such devices, gathering in-depth knowledge about the nonlinear mechanisms, and the data-based, reduced-order modeling of this behavior.

First, a parametric study by Förner *et al.* [50] accomplished with a low-order network model in the frequency domain is presented. Special attention is paid to the impact of the resonators on the linear stability of the system. It is observed that well-tuned resonators significantly increase the stability margins. This tuning process is most efficient if the overall coupled system formed by the combustion chamber and the resonators is considered. The resonators are described by a local-linear impedance model, which can reflect the impact of high sound pressure level by an appropriate constant resistance term. The stability margins show a high sensitivity towards this term, emphasizing the need for accurate modeling of the nonlinear effects. This need becomes even more evident for simulations in the time domain, where the SPL can change rapidly such that local-linear models cannot be applied.

In major parts of the thesis, high-fidelity compressible fluid dynamic simulations are conducted, see [15, 34, 41, 105]. The results presented are independent of mesh and solver setting. In absence of a mean flow, sub-grid scale modeling in large eddy simulations has a minor impact on the acoustic damping in the simulations as long as the Stokes layer and the edge regions, where the flow separates, are highly resolved. As an alternative to the compressible approach, the nonlinear behavior can also be characterized by incompressible simulations [29]. This study was conducted in collaboration with J. Tournadre and P. Martínez-Lera from Siemens Industry Software in Leuven, Belgium. A Helmholtz resonator is segregated in its acoustically compact neck and its backing volume. While the backing volume can be modeled analytically in a linear fashion, the behavior of the neck is simulated including the nonlinear effects present. In the incompressible simulations, it is essential to set the input velocity such that the velocity in the segregated neck agrees with the velocity in the composed resonator. Obeying this scaling rule, the overall impedance is given by the assembly of the transfer impedance of the segregated neck and the surface impedance of the backing volume also in the nonlinear regime.

In collaboration with M. A. Temiz, I. Lopez Arteaga, and A. Hirschberg from TU Eindhoven, the impact of the edge shape on the induced flow and the damping performance is studied [34]. Two major effects are detected: Firstly, with increasing chamfer size at the edge, the eigenfrequency shifts to higher frequencies, corresponding to a reduction of the effective length used in most impedance models. Secondly and more significantly, it

is observed that already small chamfers at the edges influence the flow significantly. The presence of a chamfer reduces the size of the separation zone at the leading edge corresponding to a larger vena contracta factor. By this mechanisms, the nonlinear resistance is reduced noticeably.

The nonlinear aeroacoustic behavior of both quarter-wave and Helmholtz resonators is further investigated with respect to the scattering to higher harmonics [41] together with the cooperation partners in Leuven mentioned above. These resonators are acoustically excited with harmonic signals varying in frequency and amplitude and the spectrum of the reflected wave is evaluated. For the Helmholtz resonator, a pattern in the harmonics—named OHO pattern—is observed where only odd harmonics are present in the scattered harmonic. This pattern is weaker if the neck of the resonator is chamfered on one side. For the quarter-wave resonator, the OHO pattern totally vanishes. This observation in the simulations is substantiated by a quasi-steady analysis. In this analysis, it is shown that OHO pattern occurs due to the flow symmetry present for the Helmholtz resonator.

The main achievement of this thesis is the development of data-based reduced-order models (ROMs) for the reflection behavior of acoustic resonators. In the post-processing of fluid dynamic simulations, system identification techniques are used to estimate ROMs based on the simulation data acquired. For the identification of a linear model, the resonator is excited with a low-amplitude broadband signal covering the entire frequency range of interest. Based on the input data and the detected reflection, a linear model for the reflection coefficient is developed. Here, a second-order output-error model structure is adopted [105]. This auto-regressive structure can parametrize a digital filter with an infinite number of filter coefficients using five parameters. A good agreement of the frequency responses of the estimated models with measurements is achieved. Hence, such models can be employed for the stability analysis performed by other tools. Hereby, the models can be transformed to digital filters with differing sampling rates or in other domains as the Laplace domain to satisfy the requirements of the analysis tools.

The system identification approach is extended into the nonlinear regime [15]. For that purpose, a gray-box model structure, named local-linear neuro-fuzzy network (LLNFN), is developed, suited for the specific setup of the resonator reflection. The model consists of output-error submodels, which are wired via fuzzy neurons to the input channel. Based on the root mean square of the particle velocity in the resonator neck, the input signal is distributed into those submodels. In the simulation providing the data for the training of the model, the amplitude of the excitation signal is successively ramped up such that the entire amplitude range of interest is covered. A procedure training the model without bias is developed. The estimated nonlinear models are proven to be robust against over-parameterization. Evaluating describing functions for the reflection coefficient and the impedance, a good agreement with measurements has been achieved for all test cases considered. Moreover, the sampling rate of the estimated model can be adapted to another rate since all linear submodel can be transformed easily. Overall, such LLNFN models can support stability analysis in the nonlinear regime, since they offer a high accuracy along with low numerical costs. Hence, they can serve as an acoustic nonlinear boundary in fluid dynamic or aeroacoustic simulations. Furthermore, the efficient and robust nonlinear characterization makes this approach also feasible to support the resonator design in an early stage of development.

The results of the author's work have been published in several papers. The key papers with the original abstracts and the respective contributions of the author are listed in the following sections.

7.1 Mapping the Influence of Acoustic Resonators on Rocket Engine Combustion Stability

A thermoacoustic linear stability analysis of a generic rocket combustion chamber is conducted employing a low-order network model. Special attention is paid to the modeling of the resonator ring, as presented in Sec. 3.2.

Original Abstract: A mode-based, acoustic low-order network model for rocket chambers with resonator ring is introduced. This model involves effects of dissipation as well as scattering and mode coupling associated with a resonator ring. Discontinuities at the interface between acoustic elements are treated with integral mode matching conditions. Eigenfrequencies and accordingly the linear system stability can be determined with the generalized Nyquist plot method based on the network model. Due to low computational cost, parameter studies can be performed in a reasonable time. An additional chamber eigenmode is observed for well-tuned resonators. Both the original and the additional mode show favorable stability properties for a generic test chamber. The optimal length and number of cavities are identified for that chamber. The need of analyzing the coupled system of resonators and combustion chamber in the design process is made evident by the discrepancy between detected values and those of an a priori consideration. Derived stability maps demonstrate that the region of stable operation is increased considerably by inserting well-tuned resonators. The destabilizing influence of temperature deviations in the cavities is quantified. Such sensitivities to modifications of design conditions can be extenuated by a ring configuration with several non-identical resonator types. Moreover, the strong impact of the nonlinear correlation factor in the resonator modeling on the overall system stability is worked out.

Contribution: The low-order tool by Cárdenas Miranda and Polifke [65] was further developed by the author. The simulations were conducted and the manuscript was drawn up by the lead author.

Status: Published in the Journal of Propulsion and Power.

Reference: ForneCarde15, reproduced on p. 66ff.

7.2 Determination of Acoustic Impedance for Helmholtz Resonators Through Incompressible Unsteady Flow Simulations

A technique for the nonlinear aeroacoustic characterization of a Helmholtz resonator by incompressible simulations is developed, see Sec. 4.2. The proposed procedure is based on the segregation of the resonator into its components, as explained in Sec. 2.5.

Original Abstract: The present study investigates the physics of Helmholtz resonators under a large range of excitation amplitudes through an approach based on incompressible computational fluid dynamics simulations. By doing so, this work proposes and assesses an alternative approach to the more widespread one based on compressible flow simulations to analyze the non-linear regime of Helmholtz resonators. In the present methodology, the resonator is decomposed into its two main components: an assumed incompressible orifice neck and a compressible backing volume. The transfer impedance of the single orifice is obtained by means of an incompressible solver of the flow equations without turbulence modeling, whereas an analytical model accounts for the compliance of the gas in the backing cavity. The proposed methodology is compared for validation purposes to both numerical results of the full compressible equations and experimental data for the complete resonator at different SPLs. The agreement between the results of the two numerical approaches is found to be good. Numerical results match also fairly well with experimental data but a systematic over-prediction of the resistance by simulations is observed. Accounting for the presence of micro-rounded edges, presumably present due to manufacturing processes, allows a better agreement between numerical and experimental results.

Contribution: The paper is the outcome of an intensive collaboration with Jonathan Tournadre from Siemens Industry Software (Leuven, Belgium)/KU Leuven. The compressible CFD simulations were performed by the present author, while Tournadre conducted the incompressible ones. The modeling and the writing of the manuscript were done by both parties involved to an equal extent.

Status: Published in AIAA Journal.

Reference: TournForne17, reproduced on p. 74ff.

7.3 On the Non-Linear Influence of the Edge Geometry on Vortex Shedding in Helmholtz Resonators

Flow separation at the edges of the resonator opening increases the acoustic resistance in the nonlinear regime, as explained in Sec. 2.5. Blunt resonator edges reduce the separation zone in comparison to a sharp contour, leading to a significant reduction of the nonlinear resistance, see Sec. 5.1.

Original Abstract: This study investigates the effect of edge profile of a Helmholtz

resonator neck in non-linear regime by means of experiments and large eddy simulations. The dissipation mechanisms in a Helmholtz resonator differ significantly, depending on the sound pressure level. At low levels, i. e., in the linear regime, thermo-viscous effects are responsible for the dissipation of the acoustic energy since the oscillating flow follows the neck geometry. However, increasing the sound pressure level results in flow separation at the edges. At these points, vortices form which convert acoustic perturbation energy to the hydrodynamic mode. This is a strong non-linear effect increasing the dissipation considerably. To observe this effect, experiments and numerical simulations are carried out for combinations of various backing volumes, sound pressure levels, and neck profiles. The neck profiles are selected as 45°-chamfers due to manufacturing concerns. Hereby, a strong dependence on the edge shape is observed in both experiments and numerical simulations. The presence of the chamfer reduces the vortex shedding in comparison to the sharp edge significantly, which leads to a lower acoustic resistance.

Contribution: The CFD simulations were conducted by the author, while the measurements were carried out by M. A. Temiz at TU Eindhoven. The manuscript was written by both parties involved to an equal extent.

Status: This paper was submitted to and presented at the 22nd International Congress on Sound and Vibration (ICSV22) held in Florence, Italy, from 12 to 16 July 2015. It was published in the ICSV22 Conference Proceedings under the copyright of the International Institute of Acoustics and Vibration (IIAV).

Reference: ForneTemiz15, reproduced on p. 83ff.

7.4 Scattering to Higher Harmonics for Quarter-Wave and Helmholtz Resonators

The inflow and outflow through the neck of a Helmholtz resonator are almost perfectly symmetric, inducing a pattern in the higher harmonics in the spectrum of the scattered acoustic wave, see Sec. 5.2. This finding is confirmed by CFD simulation (cf. Sec. 4.1) and quasi-steady analysis (cf. Sec. 2.5).

Original Abstract: The nonlinear response of acoustic resonators is investigated over a broad range of frequencies and amplitudes. Helmholtz resonators with a symmetric and with an asymmetric neck, respectively, as well as quarter wave resonators are considered. Describing functions for impedance and reflection coefficient of a Helmholtz resonator at various sound pressure levels are determined from compressible flow simulation and validated against experimental data. The particular focus of the present study is the non-linear scattering to higher harmonics. For the Helmholtz resonator with a symmetric neck, a distinct pattern in the amplitudes of the higher harmonics is observed, where the odd harmonics dominate the response, while the even harmonics are almost negligible. Such an “Odd-Harmonics-Only” (OHO) pattern, which was observed previously in experiment at orifices, is explained by a quasi-steady analysis based on the Bernoulli equation, assuming a symmetric flow pattern at the neck. For the Helmholtz resonator with an asymmetric neck, it is observed in CFD simulations that even harmonics contribute noticeably to

the resonator response, such that the OHO pattern is less pronounced. For the markedly asymmetric geometry of the quarter wave resonator, the second harmonic is dominant and the OHO pattern vanishes completely. The quasi-steady analysis is extended successfully to describe also nonlinear scattering to higher harmonics for asymmetric configurations and flow patterns. Overall, the scattering to higher harmonics remains on a moderate level even at very high excitation levels for the Helmholtz resonator configurations. For the quarter wave resonator, the scattering is more pronounced and contributes perceptibly to the response at high excitation amplitudes.

Contribution: The paper is the outcome of an intensive collaboration of Jonathan Tournadre from Siemens Industry Software (Leuven, Belgium)/KU Leuven with the author. The compressible CFD simulations were performed by the author, while Tournadre conducted the incompressible ones. The modeling and the writing of the manuscript were done by both parties involved to an equal extent.

Status: The paper is published in AIAA Journal.

Reference: ForneTourn17, reproduced on p. 91ff.

7.5 Aeroacoustic Characterization of Helmholtz Resonators in the Linear Regime with System Identification

The linear acoustic behavior of Helmholtz resonators can accurately be characterized by the CFD/SI approach, see Sec. 6.2.

Original Abstract: The dissipation of acoustic energy in Helmholtz resonators is investigated by means of large eddy simulation (LES) and system identification. At low sound pressure level, thermo-viscous effects dominate this dissipation. This is linear, i. e., independent of perturbation amplitude. LES/system identification methods are applied in this study to the linear regime. For that purpose, the system is interpreted as a single-input / single-output system of two characteristic waves. An Output-Error model for the reflection coefficient valid for the whole frequency range of interest is estimated from a single LES time series. The resonator admittance and impedance are derived from that model. For a set of test cases, comparison against experimental results and established models shows good agreement for the gain and phase of the admittance as well as of the reactance. The acoustic resistance value is captured with good accuracy close the eigenfrequency of the resonator.

Contribution: The author performed the CFD simulations as well as the linear system identification and composed the manuscript.

Status: This paper was submitted to and presented at the 22nd International Congress on Sound and Vibration (ICSV22) held in Florence, Italy, from 12 to 16 July 2015. It was published in the ICSV22 Conference Proceedings under the copyright of the International Institute of Acoustics and Vibration (IIAV). The paper was peer-reviewed.

Reference: FornePolif15, reproduced on p. 102ff.

7.6 Nonlinear Aeroacoustic Characterization of Helmholtz Resonators with a Local-Linear Neuro-Fuzzy Model

A proposed nonlinear gray-box model enables an accurate characterization of the resonator behavior in the nonlinear regime, see Sec. 6.3.

Original Abstract: The nonlinear acoustic behavior of Helmholtz resonators is characterized by a data-based reduced-order model, which is obtained by a combination of high-resolution CFD simulation and system identification. It is shown that even in the nonlinear regime, a linear model is capable of describing the reflection behavior at a particular amplitude with quantitative accuracy. This observation motivates to choose a *local-linear* model structure for this study, which consists of a network of parallel linear submodels. A so-called fuzzy-neuron layer distributes the input signal over the linear submodels, depending on the rms of the particle velocity at the resonator surface. The resulting model structure is referred to as an *local-linear neuro-fuzzy network*. System identification techniques are used to estimate the free parameters of this model from training data. The training data are generated by CFD simulations of the resonator, with persistent acoustic excitation over a wide range of frequencies and sound pressure levels. The estimated nonlinear, reduced-order models show good agreement with CFD and experimental data over a wide range of amplitudes for several test cases.

Contribution: The author developed and implemented the Local-Linear Neuro-Fuzzy Model. He performed the CFD simulations and wrote the manuscript.

Status: The paper is published in the Journal of Sound and Vibration.

Reference: FornePolif17, reproduced on p. 110ff.

Bibliography

- [1] D. Zhao and X. Y. Li. A Review of Acoustic Dampers Applied to Combustion Chambers in Aerospace Industry. *Prog. Aerosp. Sci.*, 74:114–130, 2015. doi: 10.1016/j.paerosci.2014.12.003.
- [2] J. W. S. Rayleigh. The Explanation of Certain Acoustical Phenomena. 18:319–321, 1878. doi: 10.1038/018319a0.
- [3] D. T. Harrje. Liquid Propellant Rocket Combustion Instability. Technical Report NASA-SP-194, Scientific and Technical Information Office, National Aeronautics and Space Administration, Washington, DC, U.S.A., 1972. URL <https://ntrs.nasa.gov/search.jsp?R=19720026079>.
- [4] *The Jet Engine*. Rolls-Royce Ltd., Derby, U.K., 5th edition, 1996. ISBN 0902121235.
- [5] L. Zhou. *Acoustic Characterization of Orifices and Perforated Liners with Flow and High-Level Acoustic Excitation*. PhD Thesis, 2015. URL <http://www.dissertations.se/dissertation/6fa6d5eb4d/>.
- [6] H. L. F. von Helmholtz. *Die Lehre von den Tonempfindungen als Physiologische Grundlage für die Theorie der Musik*. Friedrich Vieweg & Sohn, Braunschweig, second edition, 1865. URL https://archive.org/stream/bub_gb_n0osAAAAYAAJ#page/n11/mode/2up.
- [7] L. Rayleigh. *The Theory of Sound*. Macmillan, London, 1896. ISBN 0-486-60292-3.
- [8] L. Davidson. Fluid Mechanics, Turbulent Flow and Turbulence Modeling. 2015. URL http://www.tfd.chalmers.se/~lada/postscript_files/solids-and-fluids_turbulent-flow_turbulence-modelling.pdf.
- [9] S. W. Rienstra and A. Hirschberg. An Introduction to Acoustics. Technical Report IWDE 92-06, Eindhoven University of Technology, 2015. URL <http://www.win.tue.nl/~sjoerdr/papers/boek.pdf>.
- [10] Q. Zhang. *Direct Numerical Investigation and Reduced-Order Modeling of 3-D Honeycomb Acoustic Liners*. PhD Thesis, University of Illinois at Urbana-Champaign, 2014. URL <https://www.ideals.illinois.edu/handle/2142/49603>.
- [11] S. W. Rienstra. 1-D Reflection at an Impedance Wall. *J. Sound Vib.*, 125(1):43–51, 1988. doi: 10.1016/0022-460X(88)90413-0.

- [12] R. L. Panton and J. M. Miller. Resonant Frequencies of Cylindrical Helmholtz Resonators. *J. Acoust. Soc. Am.*, 57(6):1533–1535, 1975. doi: 10.1121/1.380596.
- [13] M. Schmid, R. Blumenthal, M. Schulze, W. Polifke, and T. Sattelmayer. Quantitative Stability Analysis Using Real Frequency Response Data. *J. Eng. Gas Turbines Power*, 135(12):121601, 2013. doi: 10.1115/1.4025299.
- [14] M. A. Temiz, J. Tournadre, I. Lopez Arteaga, and A. Hirschberg. Non-Linear Acoustic Transfer Impedance of Micro-Perforated Plates with Circular Orifices. *J. Sound Vib.*, 366:418–428, 2016. doi: 10.1016/j.jsv.2015.12.022.
- [15] K. Förner and W. Polifke. Nonlinear Aeroacoustic Identification of Helmholtz Resonators Based on a Local-Linear Neuro-Fuzzy Network Model. *J. Sound Vib.*, 407:170–190, 2017. doi: 10.1016/j.jsv.2017.07.002.
- [16] P. Dean. An in Situ Method of Wall Acoustic Impedance Measurement in Flow Ducts. *J. Sound Vib.*, 34(1):97 – 130, 1974. doi: 10.1016/S0022-460X(74)80357-3.
- [17] M. Bambauer. *Numerical Investigation of the Impact of Grazing Flow on the Damping Performance of Acoustic Resonators*. Semester Thesis, TUM, München, Germany, 2017. URL <https://mediatum.ub.tum.de/doc/1345899/1345899.pdf>.
- [18] L. J. Sivian. Acoustic Impedance of Small Orifices. *J. Acoust. Soc. Am.*, 7(2):94–101, 1935. doi: 10.1121/1.1915795.
- [19] U. Ingård and S. Labate. Acoustic Circulation Effects and the Nonlinear Impedance of Orifices. *J. Acoust. Soc. Am.*, 22(2):211–218, 1950. doi: 10.1121/1.1906591.
- [20] A. S. Hersh, B. E. Walker, and J. W. Celano. Helmholtz Resonator Impedance Model, Part 1: Nonlinear Behavior. *AIAA J.*, 41(5):795–808, 2003. doi: 10.2514/2.2041.
- [21] U. Ingard. Nonlinear Distortion of Sound Transmitted through an Orifice. *J. Acoust. Soc. Am.*, 48(1A):32–33, 1970. doi: 10.1121/1.1912106.
- [22] A. Cummings. Transient and Multiple Frequency Sound Transmission Through Perforated Plates at High Amplitude. *J. Acoust. Soc. Am.*, 79(4):942–951, 1986. doi: 10.1121/1.393691.
- [23] K. Förner, J. Tournadre, P. Martínez-Lera, and W. Polifke. Scattering to Higher Harmonics for Quarter Wave and Helmholtz Resonators. In *22nd AIAA/CEAS Aeroacoustics Conference*, Lyon, France, 2016. doi: 10.2514/6.2016-2968.
- [24] H. Bodén. Acoustic Characterisation of Perforates Using Non-Linear System Identification Techniques. In *13th AIAA/CEAS Aeroacoustics Conference (28th AIAA Aeroacoustics Conference)*, Rome, Italy, 2007. doi: 10.2514/6.2007-3530.
- [25] H. Bodén. Acoustic Properties of Perforates Under High Level Multi-Tone Excitation. In *19th AIAA/CEAS Aeroacoustics Conference*, Berlin, Germany, 2013. doi: 10.2514/6.2013-2175.

-
- [26] H. Bodén. Determination of the Acoustic Properties of Liners Under High Level Multi-Tone Excitation. In *22nd AIAA/CEAS Aeroacoustics Conference*, Lyon, France, 2016. doi: 10.2514/6.2016-2977.
- [27] P. G. Serrano, G. Gabard, P. B. Murray, and R. J. Astley. Non-Linear Interaction of Multiple Tones on Perforated Liners. In *22nd AIAA/CEAS Aeroacoustics Conference*, Lyon, France, 2016. doi: 10.2514/6.2016-2790.
- [28] U. Ingard and H. Ising. Acoustic Nonlinearity of an Orifice. *J. Acoust. Soc. Am.*, 42(1):6–17, 1967. doi: 10.1121/1.1910576.
- [29] J. Tournadre, K. Förner, W. Polifke, P. Martínez-Lera, and W. Desmet. Determination of Acoustic Impedance for Helmholtz Resonators Through Incompressible Unsteady Flow Simulations. *AIAA J.*, 55(3):790–798, 2017. doi: 10.2514/1.J055337.
- [30] U. Ingard. On the Theory and Design of Acoustic Resonators. *J. Acoust. Soc. Am.*, 25(6), 1953. doi: 10.1121/1.1907235.
- [31] H. Bodén and L. Zhou. An Experimental Study of the Effect of Flow and High Level Acoustic Excitation on the Acoustic Properties of Perforates and Orifices. In *20th International Congress on Sound and Vibration (ICSV20)*, Bangkok, Thailand, 2013.
- [32] Q. Zhang and D. J. Bodony. Numerical Investigation and Modelling of Acoustically Excited Flow Through a Circular Orifice Backed by a Hexagonal Cavity. *J. Fluid Mech.*, 693:367–401, 2012. doi: 10.1017/jfm.2011.537.
- [33] E. Laudien, R. Pongratz, R. Piero, and D. Preclik. Fundamental Mechanisms of Combustion Instabilities: Experimental Procedures Aiding the Design of Acoustic Cavities. *Liq. Rocket Engine Combust. Instab.*, pages 377–399, 1995. doi: 10.2514/5.9781600866371.0377.0399.
- [34] K. Förner, M. A. Temiz, W. Polifke, I. Lopez Arteaga, and A. Hirschberg. On the Non-Linear Influence of the Edge Geometry on Vortex Shedding in Helmholtz Resonators. In *22nd International Congress on Sound and Vibration (ICSV22)*, Florence, Italy, 2015. URL http://iiav.org/archives_icsv_last/2015_icsv22/content/papers/papers/full_paper_1341_20150325133515128.pdf.
- [35] D. K. Singh and S. W. Rienstra. Nonlinear Asymptotic Impedance Model for a Helmholtz Resonator Liner. *J. Sound Vib.*, 333(15):3536–3549, 2014. doi: 10.1016/j.jsv.2014.03.013.
- [36] G. D. Garrison, A. C. Schnell, C. D. Baldwin, and P. R. Russel. Suppression of Combustion Oscillations with Mechanical Damping Devices, Interim Report. Technical Report NAS8-21310, Pratt and Whitney Aircraft, West Palm Beach, Fla. Florida Research and Development Center, 1969.
- [37] E. J. Rice. A Model for the Acoustic Impedance of a Perforated Plate Liner with Multiple Frequency Excitation. Technical Report NASA-TM-X-67950, E-6636, NASA, 1971. URL <https://ntrs.nasa.gov/archive/nasa/casi.ntrs.nasa.gov/19720004979.pdf>.

- [38] A. Cummings and W. Eversman. High Amplitude Acoustic Transmission Through Duct Terminations: Theory. *J. Sound Vib.*, 91(4):503 – 518, 1983. doi: [http://dx.doi.org/10.1016/0022-460X\(83\)90829-5](http://dx.doi.org/10.1016/0022-460X(83)90829-5).
- [39] T. Elnady and H. Bodén. On Semi-Empirical Liner Impedance Modeling with Grazing Flow. In *9th AIAA/CEAS Aeroacoustics Conference and Exhibit*, Aeroacoustics Conferences. American Institute of Aeronautics and Astronautics, 2003. doi: 10.2514/6.2003-3304.
- [40] A. Cárdenas Miranda. *Influence of Enhanced Heat Transfer in Pulsating Flow on the Damping Characteristics of Resonator Rings*. PhD Thesis, TU München, 2014. URL http://www.tfd.mw.tum.de/fileadmin/w00bsb/www/Forschung/Dissertationen/Cardenas_2014_Influence_of_Enhanced_Heat_Transfer_in_Pulsating_Flow_on_the_Damping_Characteristics_of_Resonator_Rings.pdf.
- [41] K. Förner, J. Tournadre, P. Martínez-Lera, and W. Polifke. Scattering to Higher Harmonics for Quarter Wave and Helmholtz Resonators. *AIAA J.*, 55(4):1194–1204, 2017. doi: 10.2514/1.J055295.
- [42] M. G. Jones, M. B. Tracy, W. R. Watson, and T. L. Parrott. Effects of Liner Geometry on Acoustic Impedance. In *8th AIAA/CEAS Aeroacoustics Conference & Exhibit*, Breckenridge, Colorado, U.S.A., 2002. doi: 10.2514/6.2002-2446.
- [43] Q. Zhang and D. J. Bodony. Numerical Investigation of a Honeycomb Liner Grazed by Laminar and Turbulent Boundary Layers. *J. Fluid Mech.*, 792:936–980, 2016. doi: 10.1017/jfm.2016.79.
- [44] J. D. Eldredge and A. P. Dowling. The Absorption of Axial Acoustic Waves by a Perforated Liner with Bias Flow. *J. Fluid Mech.*, 485:307–335, 2003. doi: 10.1017/S0022112003004518.
- [45] V. Bellucci, P. Flohr, and C. O. Paschereit. Numerical and Experimental Study of Acoustic Damping Generated by Perforated Screens. *AIAA J.*, 42(8):1543–1549, 2004. doi: 10.2514/1.9841.
- [46] A. Scarpato, S. Ducruix, and T. Schuller. Optimal and Off-Design Operations of Acoustic Dampers Using Perforated Plates Backed by a Cavity. *J. Sound Vib.*, 332(20):4856–4875, 2013. doi: 10.1016/j.jsv.2013.03.030.
- [47] B. Čosić, T. G. Reichel, and C. O. Paschereit. Acoustic Response of a Helmholtz Resonator Exposed to Hot-Gas Penetration and High Amplitude Oscillations. *J. Eng. Gas Turbines Power*, 134(10):101503–101503, 2012. doi: 10.1115/1.4007024.
- [48] J. Rupp, G. Peacock, G. Regunath, and J. Carrotte. Assessment and Prediction of Helmholtz Resonator Performance Within Gas Turbine Combustion Systems. In *ASME Turbo Expo 2014*, Düsseldorf, Germany, 2014. doi: 10.1115/GT2014-26907.
- [49] J. Mayr. *Numerische Untersuchung von Helmholtz-Resonatoren mit Spülströmung*. Semester Thesis, TU München, Garching, Germany, 2016.

-
- [50] K. Förner, A. Cárdenas Miranda, and W. Polifke. Mapping the Influence of Acoustic Resonators on Rocket Engine Combustion Stability. *J. Propuls. Power*, 31(4):1159–1166, 2015. doi: 10.2514/1.B35660.
- [51] M. Bauerheim, F. Nicoud, and T. Poinso. Progress in Analytical Methods to Predict and Control Azimuthal Combustion Instability Modes in Annular Chambers. *Phys. Fluids 1994-Present*, 28(2):021303, 2016. doi: 10.1063/1.4940039.
- [52] A. Urbano, L. Selle, G. Staffelbach, B. Cuenot, T. Schmitt, S. Ducruix, and S. Candel. Exploration of Combustion Instability Triggering Using Large Eddy Simulation of a Multiple Injector Liquid Rocket Engine. *Combust. Flame*, 169:129–140, 2016. doi: 10.1016/j.combustflame.2016.03.020.
- [53] W. Polifke. Black-Box System Identification for Reduced Order Model Construction. *Ann. Nucl. Energy*, 67C:109–128, 2014. doi: 10.1016/j.anucene.2013.10.037.
- [54] J. Li and A. S. Morgans. Time Domain Simulations of Nonlinear Thermoacoustic Behaviour in a Simple Combustor Using a Wave-Based Approach. *J. Sound Vib.*, 346:345–360, 2015. doi: 10.1016/j.jsv.2015.01.032.
- [55] A. Huber, P. Romann, and W. Polifke. Filter-Based Time-Domain Impedance Boundary Conditions for CFD Applications. In *ASME Turbo Expo 2008*, ASME GT2008-51195, pages 901–911, Berlin, Germany, 2008. doi: 10.1115/GT2008-51195.
- [56] V. Bellucci, B. Schuermans, D. Nowak, P. Flohr, and C. O. Paschereit. Thermoacoustic Modeling of a Gas Turbine Combustor Equipped With Acoustic Dampers. *J. Turbomach.*, 127(2):372–379, 2005. doi: 10.1115/1.1791284.
- [57] R. Kaess, A. Huber, and W. Polifke. A time-domain impedance boundary condition for compressible turbulent flows. In *14th AIAA/CEAS Aeroacoustics Conference (29th AIAA Aeroacoustics Conference)*, AIAA-2008-2921, Vancouver, Canada, 2008. AIAA/CEAS. doi: 10.2514/6.2008-2921.
- [58] M. Schulze and T. Sattelmayer. A Comparison of Time and Frequency Domain Descriptions of High Frequency Acoustics in Rocket Engines with Focus on Dome Coupling. *Aerosp. Sci. Technol.*, 45:165–173, 2015. URL <http://www.sciencedirect.com/science/article/pii/S1270963815001546>.
- [59] T. Emmert, M. Meindl, S. Jaensch, and W. Polifke. Linear State Space Interconnect Modeling of Acoustic Systems. *Acta Acust. United Acust.*, 102(5):824–833, 2016. doi: 10.3813/AAA.918997.
- [60] S. Jaensch, M. Merk, E. Gopalakrishnan, S. Bomberg, T. Emmert, R. Sujith, and W. Polifke. Hybrid CFD/Low-Order Modeling of Nonlinear Thermoacoustic Oscillations. *Proc. Combust. Inst.*, 36(3):3827–3834, 2017. doi: 10.1016/j.proci.2016.08.006.
- [61] C. Pankiewicz and T. Sattelmayer. Time Domain Simulation of Combustion Instabilities in Annular Combustors. *J. Eng. Gas Turbines Power*, (125):677–685, 2003. doi: 10.1115/1.1582496.

- [62] F. Nicoud, L. Benoit, C. Sensiau, and T. Poinsot. Acoustic Modes in Combustors with Complex Impedances and Multidimensional Active Flames. *AIAA J.*, 45(2): 426–441, 2007. doi: 10.2514/1.24933.
- [63] J. Gikadi. *Prediction of Acoustic Modes in Combustors Using Linearized Navier-Stokes Equations in Frequency Space*. PhD Thesis, Technische Universität München, Garching, Germany, 2013. URL <https://mediatum.ub.tum.de/doc/1297356/1297356.pdf>.
- [64] M. Schulze. *Linear Stability Assessment of Cryogenic Rocket Engines*. PhD Thesis, TU München, 2016. URL <https://mediatum.ub.tum.de/doc/1297356/1297356.pdf>.
- [65] A. Cárdenas Miranda and W. Polifke. Combustion Stability Analysis of Rocket Engines with Resonators Based on Nyquist Plots. *J. Propuls. Power*, 30(4):962–977, 2014. doi: 10.2514/1.B35149.
- [66] M. Oswald and Z. Farago. Acoustics of Rocket Combustors Equipped with Absorber Rings. In *44th AIAA/ASME/SAE/ASEE Joint Propulsion Conference & Exhibit*, Hartford, CT, U.S.A., 2008. doi: 10.2514/6.2008-5112.
- [67] G. Gabard and R. J. Astley. A Computational Mode-Matching Approach for Sound Propagation in Three-Dimensional Ducts with Flow. *J. Sound Vib.*, 315(4–5):1103–1124, 2008. doi: 10.1016/j.jsv.2008.02.015.
- [68] W. A. Bell and B. T. Zinn. The Prediction of Three-Dimensional Liquid-Propellant Rocket Nozzle Admittances. Technical report, Georgia Institute of Technology, NASA CR- 121129, 1973. URL <https://ntrs.nasa.gov/archive/nasa/casi.ntrs.nasa.gov/19730009080.pdf>.
- [69] L. Crocco. Aspects of Combustion Stability in Liquid Propellant Rocket Motors Part 2: Low Frequency Instability with Bipropellants. High Frequency Instability. *J. Am. Rocket Soc.*, 22(1):7–16, 1952. doi: 10.2514/8.4410.
- [70] W. Polifke, C. O. Paschereit, and K. Döbbling. Constructive and Destructive Interference of Acoustic and Entropy Waves in a Premixed Combustor with a Choked Exit. *Int. J. Acoust. Vib.*, 6(3):135–146, 2001. doi: 10.20855/ijav.2001.6.382.
- [71] T. Sattelmayer and W. Polifke. A Novel Method for the Computation of the Linear Stability of Combustors. *Combust. Sci. Technol.*, 175(3):477–497, 2003. doi: 10.1080/00102200302387.
- [72] M. Schulze, R. Kathan, and T. Sattelmayer. Impact of Absorber Ring Position and Cavity Length on Acoustic Damping. *J. Spacecr. Rockets*, 52(3):917–927, 2015. doi: 10.2514/1.A33215.
- [73] C. K. W. Tam and K. A. Kurbatskii. Microfluid Dynamics and Acoustics of Resonant Liners. *AIAA J.*, 38(8):1331–1339, 2000. doi: 10.2514/2.1132.

-
- [74] C. K. W. Tam, K. A. Kurbatskii, K. K. Ahuja, and R. J. Gaeta. A Numerical and Experimental Investigation of the Dissipation Mechanisms of Resonant Acoustic Liners. *J. Sound Vib.*, 245(3):545–557, 2001. doi: 10.1006/jsvi.2001.3571.
- [75] C. K. W. Tam, H. Ju, M. G. Jones, W. R. Watson, and T. L. Parrott. A Computational and Experimental Study of Resonators in Three Dimensions. *J. Sound Vib.*, 329(24):5164–5193, 2010. doi: 10.1016/j.jsv.2010.06.005.
- [76] S. Mendez and J. D. Eldredge. Acoustic Modeling of Perforated Plates with Bias Flow for Large-Eddy Simulations. *J. Comput. Phys.*, 228(13):4757–4772, 2009. doi: 10.1016/j.jcp.2009.03.026.
- [77] A. Scarpato, S. Ducruix, and T. Schuller. A LES Based Sound Absorption Analysis of High-Amplitude Waves Through an Orifice with Bias Flow. In *ASME 2011 Turbo Expo*, pages 613–622, Vancouver, British Columbia, Canada, 2011. doi: 10.1115/GT2011-45639.
- [78] J. Tournadre, W. Desmet, and P. Martínez-Lera. Evaluation of Temperature Effects on Passive Acoustic Dampers with a Frequency-Domain Linearized Navier-Stokes Equations Solver. Athens, Greece, 07/1/16. URL http://iiav.org/archives_icsv_last/2016_icsv23/content/papers/papers/full_paper_857_20160523171052430.pdf.
- [79] C. Ji and D. Zhao. Lattice Boltzmann Investigation of Acoustic Damping Mechanism and Performance of an in-Duct Circular Orifice. *J. Acoust. Soc. Am.*, 135(6):3243–3251, 2014. doi: 10.1121/1.4876376.
- [80] OpenFOAM Foundation. OpenFOAM (Version 2.3.0) [software]. 2014. URL <http://www.openfoam.com/>.
- [81] S. Patankar. *Numerical Heat Transfer and Fluid Flow*. Taylor & Francis, 1980. ISBN 978-0-89116-522-4.
- [82] R. I. Issa. Solution of the Implicitly Discretised Fluid Flow Equations by Operator-Splitting. *J. Comput. Phys.*, 62:40 – 65, 1986. doi: 10.1016/0021-9991(86)90099-9.
- [83] Y. Qin. *Impact of LES Subgrid-Scale Modeling on the Acoustic and Flow Properties for Helmholtz Resonators Without Mean Flow*. Master’s Thesis, TU München, Garching, Germany, 2016. URL <https://mediatum.ub.tum.de/1311461>.
- [84] F. Caeiro, C. Sovardi, K. Förner, and W. Polifke. Shape Optimization of a Helmholtz Resonator using an Adjoint Method. *Int. J. Spray Combust. Dyn.*, (online first), 2017. doi: 10.1177/1756827717703576.
- [85] T. Poinso and S. K. Lele. Boundary Conditions for Direct Simulation of Compressible Viscous Flows. *J. Comp. Phys.*, 101(1):104–129, 1992. doi: 10.1016/0021-9991(92)90046-2.
- [86] S. Föllner and W. Polifke. Advances in Identification Techniques for Aero-Acoustic Scattering Coefficients from Large Eddy Simulation. In *18th International Congress*

- on Sound and Vibration (ICSV18)*, volume 4, pages 3122–3129, Rio de Janeiro, Brazil, 2011.
- [87] J. Tournadre, K. Förner, W. Polifke, P. Martínez-Lera, and W. Desmet. Determination of Acoustic Impedance for Helmholtz Resonators Through Incompressible Unsteady Flow Simulations. In *22nd AIAA/CEAS Aeroacoustics Conference*, Lyon, France, 2016. doi: 10.2514/6.2016-2917.
- [88] S. Jaensch, M. Merk, E. Gopalakrishnan, S. Bomberg, T. Emmert, R. Sujith, and W. Polifke. Hybrid CFD/Low-Order Modeling of Nonlinear Thermoacoustic Oscillations. In *36th Int'l Symposium on Combustion*, Seoul, Korea, 2016. doi: 10.1016/j.proci.2016.08.006.
- [89] P. Martínez-Lera, C. Schram, S. Föllner, R. Kaess, and W. Polifke. Identification of the aeroacoustic response of a low Mach number flow through a T-joint. *J. Acoust. Soc. Am.*, 126(2):582–586, 2009. doi: 10.1121/1.3159604.
- [90] M. S. Howe. *Theory of Vortex Sound*. Cambridge Texts in Applied Mathematics, 2003. ISBN 0-521-01223-6.
- [91] G. Nakiboğlu, S. P. C. Belfroid, J. Golliard, and A. Hirschberg. On the Whistling of Corrugated Pipes: Effect of Pipe Length and Flow Profile. *J. Fluid Mech.*, 672: 78–108, 2011. doi: 10.1017/S0022112010005884.
- [92] R. Lacombe, P. Moussou, and Y. Aurégan. Identification of Whistling Ability of a Single Hole Orifice from an Incompressible Flow Simulation. In *ASME 2011 Pressure Vessels and Piping Conference*, pages 261–267, Baltimore, Maryland, U.S.A., 2011. ASME/PVP. doi: 10.1115/PVP2011-57355.
- [93] J. Golliard, N. González-Díez, S. Belfroid, G. Nakiboğlu, and A. Hirschberg. U-RANS Model for the Prediction of the Acoustic Sound Power Generated in a Whistling Corrugated Pipe. (55683):V004T04A040, 2013. doi: 10.1115/PVP2013-97385.
- [94] P. Murray, P. Ferrante, and A. Scofano. Manufacturing Process and Boundary Layer Influences on Perforate Liner Impedance. In *11th AIAA/CEAS Aeroacoustics Conference*, Monterey, California, U.S.A., 2005. doi: 10.2514/6.2005-2849.
- [95] J. H. M. Disselhorst and L. V. Wijngaarden. Flow in the Exit of Open Pipes During Acoustic Resonance. *J. Fluid Mech.*, 99(02):293–319, 1980. doi: 10.1017/S0022112080000626.
- [96] M. A. Temiz, J. Tournadre, I. Lopez Arteaga, P. Martinez-Lera, and A. Hirschberg. Effect of Orifice Geometry on the Non-Linear Acoustic Resistance of Perforated Plates in the Transition Regime. Florence, Italy, 2015. URL http://iiav.org/archives_icsv_last/2015_icsv22/content/papers/papers/full_paper_1014_20150315164202977.pdf.
- [97] R. D. Blevins. *Applied Fluid Dynamics Handbook*. Van Nostrand Reinhold, NY, U.S.A., 1984. ISBN 0-442-21296-8.

-
- [98] A. Mages. *Numerische Untersuchung des akustischen nichtlinearen Dämpfungsverhaltens von perforierten Platten und Helmholtzresonatoren*. Bachelor's Thesis, TU München, Garching, Germany, 2016. URL <https://mediatum.ub.tum.de/node?id=1291369>.
- [99] A. Innocenti, A. Andreini, and B. Facchini. Numerical Identification of a Premixed Flame Transfer Function and Stability Analysis of a Lean Burn Combustor. *Energy Procedia*, 82:358–365, 2015. doi: <https://doi.org/10.1016/j.egypro.2015.11.803>.
- [100] C. Sovardi, S. Jaensch, and W. Polifke. Concurrent Identification of Aero-acoustic Scattering and Noise Sources at a Flow Duct Singularity in low Mach Number Flow. *J. Sound Vib.*, 377:90–105, 2016. doi: [10.1016/j.jsv.2016.05.025](https://doi.org/10.1016/j.jsv.2016.05.025).
- [101] F. Selimefendigil. *Identification and Analysis of Nonlinear Heat Sources in Thermo-Acoustic Systems*. PhD Thesis, TU München, 2010. URL http://www.tfd.mw.tum.de/fileadmin/w00bsb/www/Forschung/Dissertationen/2010_Selimefendigil_Identification_and_Analysis_of_Nonlinear_Heat_Sources_in_Thermo-Acoustic_Systems.pdf.
- [102] S. Jaensch and W. Polifke. Uncertainty Encountered When Modelling Self-Excited Thermoacoustic Oscillations with Artificial Neural Networks. *Int J Spray Combust Dyn*, online first, 2017. doi: [10.1177/1756827716687583](https://doi.org/10.1177/1756827716687583).
- [103] H. Bodén. Non-linear System Identification Techniques for Determination of the Acoustic Properties of Perforates. In *21st AIAA/CEAS Aeroacoustics Conference, AIAA Aviation*, Dallas, TX, U.S.A., 2015. doi: [10.2514/6.2015-3266](https://doi.org/10.2514/6.2015-3266).
- [104] A. K. Tangirala. *Principles of System Identification: Theory and Practice*. CRC Press, 2014. ISBN 978-1-4398-9602-0.
- [105] K. Förner and W. Polifke. Aero-Acoustic Characterization of Helmholtz Resonators in the Linear Regime with System Identification. In *22nd International Congress on Sound and Vibration (ICSV22)*, Florence, Italy, 2015. URL http://iiav.org/archives_icsv_last/2015_icsv22/content/papers/papers/full_paper_596_20150401121136373.pdf.
- [106] O. Nelles. *Nonlinear System Identification*. Springer Berlin Heidelberg, Berlin, Heidelberg, 2001. ISBN 978-3-642-08674-8.
- [107] R. Babuška and H. Verbruggen. Neuro-Fuzzy Methods for Nonlinear System Identification. *Annu. Rev. Control*, 27(1):73–85, 2003. doi: [10.1016/S1367-5788\(03\)00009-9](https://doi.org/10.1016/S1367-5788(03)00009-9).
- [108] K. J. Keesman. *System Identification*. Advanced Textbooks in Control and Signal Processing. Springer London, London, 2011. ISBN 978-0-85729-521-7.
- [109] S. Jaensch, C. Sovardi, and W. Polifke. On the Robust, Flexible and Consistent Implementation of Time Domain Impedance Boundary Conditions for Compressible Flow Simulations. *J. Comput. Phys.*, 314:145–159, 2016. doi: [10.1016/j.jcp.2016.03.010](https://doi.org/10.1016/j.jcp.2016.03.010).

- [110] M. Oschwald, Z. Farago, G. Searby, and F. Cheuret. Resonance Frequencies and Damping of a Combustor Acoustically Coupled to an Absorber. *J. Propuls. Power*, 24(3):524–533, 2008. doi: 10.2514/1.32313.
- [111] C. Sovardi, S. Jaensch, K. Förner, F. Selimefendigil, and W. Polifke. Parametric vs. Nonparametric Identification of Nonlinear Acoustic Scattering at Duct Discontinuities Based on LES Data. In *Proceedings of the Summer School Program SFB TRR40*, Garching, Germany, 2013. URL http://www.sfbtr40.de/fileadmin/Summer_Programs/Summer_Program_2013/13-SP2013.pdf.
- [112] T. Emmert, S. Jaensch, C. Sovardi, and W. Polifke. taX - a Flexible Tool for Low-Order Duct Acoustic Simulation in Time and Frequency Domain. In *7th Forum Acusticum*, Krakow, 2014. DEGA. URL <http://www.fa2014.agh.edu.pl>.
- [113] K. Förner and W. Polifke. Aero-Acoustic Characterization of a Helmholtz Resonator in the Linear Regime with System Identification. In N. A. Adams, R. Radespiel, T. Sattelmayer, W. Schröder, and B. Weigand, editors, *Annual Report*, pages 33 – 45. Sonderforschungsbereich/Transregio 40, 2014. URL <http://www.sfbtr40.de/fileadmin/Annual-Reports/annualreport2014/a3-2014.pdf>.
- [114] K. Förner, A. Cárdenas Miranda, and W. Polifke. Mapping the Influence of Acoustic Resonators on Rocket Engine Combustion Stability. In N. A. Adams, R. Radespiel, T. Sattelmayer, W. Schröder, and B. Weigand, editors, *Annual Report*, pages 33 – 45. Sonderforschungsbereich/Transregio 40, 2013. URL <http://www.sfbtr40.de/fileadmin/Annual-Reports/annualreport2013/a3-2013.pdf>.
- [115] W. Polifke, J. van der Hoek, and B. Verhaar. Everything you always wanted to know about f and g. Technical report, Technical Report of ABB Corporate Research, Baden, Switzerland, 1997.
- [116] K. Förner, J. Tournadre, P. Martínez-Lera, and W. Polifke. Characterization of the Nonlinear Response of a Helmholtz Resonator. In N. A. Adams, R. Radespiel, T. Sattelmayer, W. Schröder, and B. Weigand, editors, *SFB/TRR40 Annual Report 2015*, pages 33 – 45. Sonderforschungsbereich/Transregio 40, 2015. URL <http://www.sfbtr40.de/fileadmin/Annual-Reports/annualreport2015/annualreport-2015-a3.pdf>.
- [117] M. L. Munjal. *Acoustics of Ducts and Mufflers*. Wiley, Chichester, West Sussex, United Kingdom, second edition edition, 2014. ISBN 978-1-118-44312-5.
- [118] J. Tournadre, K. Förner, W. Polifke, P. Martínez-Lera, and W. Desmet. Influence of Vortex Disruption on the Nonlinear Acoustic Response of Orifices. *Submitt. J. Sound Vib.*, 2016.
- [119] K. Förner and W. Polifke. Streuung in höhere Harmonische bei akustischen Resonatoren. In *DGLR/DEGA-Workshop Strömungsschall*, Braunschweig, Germany, 2015. URL http://www.dglr.de/fileadmin/inhalte/dglr/fb/q2/workshop-q23-braunschweig-2015/Session4/DGLRWorkshop_2015_Foerner_Stroemungsschall.pdf.

- [120] C. Gscheidle. *Untersuchungen Zur (Linearen) Modellierung Der Transienten Wärmefreisetzung Laminarer Flammen Bei Akustischer Anregung*. Bachelor's Thesis, Technische Universität München, Garching, 2015.
- [121] L. Maier. *Analytical and Numerical Evaluation of the Impedance's Impact on the Acoustic Mode Shapes*. Bachelor's Thesis, TUM, München, Germany, 2016. URL <https://mediatum.ub.tum.de/1319700>.
- [122] K. Förner and W. Polifke. Nonlinear Aeroacoustic Identification of the Helmholtz Resonator Response Based on a Local Linear Neuro-Fuzzy Model. In N. A. Adams, R. Radespiel, T. Sattelmayer, W. Schröder, and B. Weigand, editors, *Annual Report*, pages 35–50. Sonderforschungsbereich/Transregio 40, 2016. URL <http://www.sfbtr40.de/fileadmin/Annual-Reports/annualreport2016/Jahresbericht-2016-A3.pdf>.
- [123] F. Caeiro, C. Sovardi, K. Förner, and W. Polifke. Shape Optimization of a Helmholtz Resonator using the Adjoint Method. In *Int. Symp. on Thermoacoustic Instabilities in Gas Turbines and Rocket*, Garching, Germany, 2016.
- [124] C. F. Silva, K. Förner, and W. Polifke. Notes on Computational Thermo-Fluid Dynamics. 2016. URL <https://mediatum.ub.tum.de/doc/1328442/1328442.pdf>.
- [125] T. Steinbacher, K. Förner, and W. Polifke. Grundlagen der numerischen Thermofluidodynamik. 2016. URL <https://mediatum.ub.tum.de/doc/1345187/1345187.pdf>.
- [126] L. Hege. *Numerische Parameterstudie einer Konfiguration zur kombinierten Prall- und Effusionskühlung*. Semester Thesis, TU München, Garching, Germany, 2017. URL https://mediatum.ub.tum.de/603844?query=f%C3%B6rner&show_id=1346255.
- [127] L. Schuwerk. *Numerische Untersuchung der gekoppeltenn Wärmeübertragung bei kombinierter Prall- und Effusionskühlung*. Semester Thesis, TU München, Garching, Germany, 2017.

BIBLIOGRAPHY

List of Figures

- 1.1 Resonators in technical applications. 2
- 2.1 Sketches of basic resonator types with acoustic traveling f - and g -waves. . . 6
- 2.2 Snapshots of streamlines in the vicinity of a Helmholtz resonator neck generated with the CFD environment introduced in Chp. 4. 7
- 2.3 Segregation of the Helmholtz resonator into its components. 14
- 2.4 Vena contracta of the flow due to flow separation. 16
- 2.5 Analogy of a resonator to a mechanical mass-spring-damper system. 16
- 2.6 Impedance and reactance determined by the generic SDOF model in Eq. (2.38) for a normally damped $-\cdots-$, an optimally damped $—$, and over-damped system $---$ 17
- 2.7 CFD simulation (cf. Chp. 4) with grazing flow (from left to right) in the nonlinear regime; vortices are visualized with the Q-criterion. 19
- 3.1 Acoustic network of a generic test chamber with resonator ring. (Reproduced from [50].) 23
- 3.2 Stability map in dependency on the flame parameters n_f and τ for the undamped (blue solid) and well-tuned damped (red dashed) chamber. (Reproduced from [50].) 23
- 4.1 Computational domain for the Helmholtz resonator. 26
- 4.2 Reflection coefficient R and normalized impedance z for a configuration from [20]: Measurements (\star) from [20, Fig. 12a] and CFD simulations ($- \bullet -$) for 75 dB (\bullet), 120 dB ($\color{red}\bullet$), 130 dB ($\color{orange}\bullet$), and 140 dB ($\color{purple}\bullet$). (Figure is reproduced from [15]). 28
- 5.1 Helmholtz resonator with a chamfer of length l_c at the edges of the neck. . . 32
- 5.2 Considered resonator openings with particle flow direction depend separation behavior. 33

LIST OF FIGURES

5.3	Scattering to harmonics plotted in logarithmic scale for the three considered test cases: 1 st = fundamental $\color{blue}{\times}$; 2 nd $\color{red}{\diamond}$; 3 rd $\color{orange}{\triangle}$ 4 th $\color{purple}{\square}$; 5 th $\color{green}{\nabla}$. (Reproduced from [41].)	33
6.1	Block diagram of an output-error model reproduced from [15].	37
6.2	SI-estimated (—) and measured (\star) reflection coefficient R for four test cases indicated by the colors. (The presented figure is similar as in [15].) . .	38
6.3	Block diagram of a local-linear neuro-fuzzy model with output-error blocks (see Fig. 6.1) as submodels; reproduced from [15].	39
6.4	Estimated impedance describing function with total SPLs ranging from 80 dB (bluish) to 140 dB (reddish) in steps of 5 dB. (Reproduced from [15].)	40

Supervised Students

Associated with this Ph. D. thesis are a number of student theses (Semesterarbeit, Bachelor's and Master's thesis) as well as works performed by student researchers (HiWis, WiHis) that were supervised by the author of the present work. These theses were prepared at the Thermofluidynamics Group, Technische Universität München in the years 2013 through 2017 under the close supervision of the present author. Parts of these supervised theses have been incorporated into the present thesis. The author would like to express his sincere gratitude to all formerly supervised students for their commitment and support of this research project and of the Ph. D. thesis at hand.

Student	Thesis/Work packages
Maximilian Bambauer	Semesterarbeit Numerical Investigation of the Impact of Grazing Flow on the Damping Performance of Acoustic Resonators [17] (online available) January 23, 2017
Faisal Caeiro	HiWi Numerical Study on the Impact of Temperature Gradients on the Damping Performance of Quarter-Wave Resonators January – May 2016
Lukas Hege	Semesterarbeit, extern at Universität der Bundeswehr München (in German) Numerische Parameterstudie einer Konfiguration zur kombinierten Prall- und Effusionskühlung [126] (online available) filed in January 30, 2017
Daniel Kümmel	HiWi Stability Analysis with a Low-Order Network Tool March 2014 – July 2015

Supervised Students

Alexander Mages	Bachelor's thesis Numerische Untersuchung des akustischen nichtlinearen Dämpfungsverhaltens von perforierten Platten und Helmholtzresonatoren [98] (online available) January 24, 2016
Lukas Maier	Bachelor's thesis Analytical and Numerical Evaluation of the Impedance's Impact on the Acoustic Mode Shapes [121] (online available) filed in July 20, 2016
Johannes Mayr	Semesterarbeit (in German) Numerische Untersuchung von Helmholtz-Resonatoren mit Spülströmung [49] filed in April 10, 2016
Yupeng Qin	Master's thesis Impact of LES Subgrid-Scale Modeling on the Acoustic and Flow Properties for Helmholtz Resonators Without Mean Flow [83] (online available) filed in April 29, 2016
Leonhard Schuwerk	Semesterarbeit, extern at Universität der Bundeswehr München (in German) Numerische Untersuchung der gekoppelten Wärmeübertragung bei kombinierter Prall- und Effusionskühlung [127] filed in January 25, 2017
Daxin Wu	HiWi Numerical Study on the Impact of Temperature Gradients on the Damping Performance of Quarter-Wave Resonators September – December 2015

A Reproduction of Papers

The major publication related to the topic of the thesis are reproduced in the following. Additionally, preliminary results were presented in joint work with colleagues at the Summer School Program SFB TRR40 2013 [111], at the DGLR/DEGA-Workshop Strömungsschall 2015 [119], at the 22nd AIAA/CEAS Aeroacoustics Conference 2016 [23, 87] and at the International Symposium on Thermoacoustic Instabilities in Gas Turbines and Rocket 2016 [123]. Project reports were published in book-form [113, 114, 116, 122]. Moreover, the segregation approach—for the incompressible characterization of Helmholtz Resonators presented in Sec. 4.2—was applied in combination with an adjoint method for the shape optimization of the neck of a Helmholtz resonator. This paper is accepted for publication in the International Journal of Spray and Combustion Dynamics [84]. Furthermore, the author contributed to lecture notes [124, 125], which are freely available online.

Mapping the Influence of Acoustic Resonators on Rocket Engine Combustion Stability

K. Förner,* A. Cárdenas Miranda,† and W. Polifke‡
Technische Universität München, D-85748 Garching, Germany

DOI: 10.2514/1.B35660

A mode-based, acoustic low-order network model for rocket chambers with resonator ring is introduced. This model involves effects of dissipation as well as scattering and mode coupling associated with a resonator ring. Discontinuities at the interface between acoustic elements are treated with integral mode-matching conditions. Eigenfrequencies and accordingly the linear system stability can be determined with the generalized Nyquist plot method based on the network model. Because of low computational cost, parameter studies can be performed in a reasonable time. An additional chamber eigenmode is observed for well-tuned resonators. Both the original and the additional mode show favorable stability properties for a generic test chamber. The optimal length and number of cavities are identified for that chamber. The need for analyzing the coupled system of resonators and combustion chamber in the design process is made evident by the discrepancy between detected values and those of an a priori consideration. Derived stability maps demonstrate that the region of stable operation is increased considerably by inserting well-tuned resonators. The destabilizing influence of temperature deviations in the cavities is quantified. Such sensitivities to modifications of design conditions can be extenuated by a ring configuration with several nonidentical resonator types. Moreover, the strong impact of the nonlinear correlation factor in the resonator modeling on the overall system stability is worked out.

Nomenclature

A	= system matrix of network model
c	= speed of sound
d	= diameter of quarter-wave tube
F_{mn}, G_{mn}	= amplitudes of up- and downstream traveling waves
f_{mn}, g_{mn}	= up- and downstream traveling waves
i	= imaginary unit equal to $\sqrt{-1}$
J_m	= m th Bessel function of first kind
k_{mn}^{\pm}	= axial wave number
L	= length of the thrust chamber
l, l_e, l_r	= geometric, effective, and equivalent mass length of quarter-wave resonator
M	= Mach number
N	= number of modes considered in mode matching
n	= pressure interaction index, Eq. (16)
n_R	= number of cavities placed in resonator ring
p'	= acoustic fluctuating pressure
Q	= heat release
R	= radius of thrust chamber; reference length scale
r_{in}, r_{out}	= radius of curvature at nozzle entrance and throat, respectively
T	= transfer matrix
T	= cycle
t	= time
U	= mean flow velocity
x, r, θ	= axial, radial, and tangential coordinates
x_F, x_R	= axial position of flame front and resonator ring center, respectively
Z	= $\Theta + i\Psi$ acoustic impedance
α^{\pm}	= radial wave numbers
Γ	= growth rate, Eq. (19)

γ	= isentropic exponent
ΔT	= deviation from design temperature
ϵ_{nl}	= nonlinear resistance factor
θ_{nozzle}	= nozzle half-angle
κ	= acoustic balancing parameter defined by Eq. (14)
λ_{mn}	= n th roots of the derivative of the m th Bessel function of first kind
μ	= dynamic viscosity
Ξ	= excess temperature
ξ	= ratio of specific impedances
ρ	= density
τ	= combustion time lag, Eq. (16)
Ω	= $\omega + i\theta$ complex valued angular frequency
ω_{ref}	= angular frequency of the undamped $1T1L$ mode; used to normalize frequency and time scales

Subscripts

m, n, l	= azimuthal, radial, and axial mode order
R	= evaluation at the resonator
u, d	= property evaluated up- and downstream, respectively

Superscripts

u, d	= property evaluated up- and downstream, respectively
$'$	= first-order fluctuation

I. Introduction

FEEDBACK between unsteady heat release and acoustics can lead to self-excited thermoacoustic instabilities in rocket combustion chambers. The resulting high-frequency oscillations can lower the motor performance or, due to the high-energy density, even destroy the thrust chamber within a short time. Acoustic resonators, such as Helmholtz resonators or quarter-wave length cavities, are commonly used for the dissipation of acoustic energy and detuning the system such that these oscillations are damped [1,2]. Figure 1 shows a generic combustion chamber with resonators arranged in a ring.

The damping behavior of the cavities depends on several design parameters, such as their length, diameter, the number of cavities, etc. Moreover, transient operating conditions such as temperature or the

Received 10 November 2014; revision received 20 February 2015; accepted for publication 20 February 2015; published online 20 April 2015. Copyright © 2015 by Wolfgang Polifke. Published by the American Institute of Aeronautics and Astronautics, Inc., with permission. Copies of this paper may be made for personal or internal use, on condition that the copier pay the \$10.00 per-copy fee to the Copyright Clearance Center, Inc., 222 Rosewood Drive, Danvers, MA 01923; include the code 1533-3876/15 and \$10.00 in correspondence with the CCC.

*Ph.D. Student, Professur für Thermofluidynamik; foerner@tfd.mw.tum.de.

†Professur für Thermofluidynamik; cardenas@tfd.mw.tum.de.

‡Professor, Professur für Thermofluidynamik; polifke@tfd.mw.tum.de.

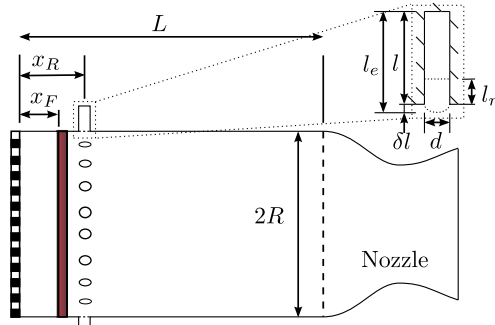


Fig. 1 Sketch of a generic thrust chamber.

sound pressure level (SPL) influence the resonator performance [3,4]. Identification of an optimal design is not a trivial task because the stabilizing impact can only be estimated in combination with the main driving and damping mechanisms in the chamber (cf. [2]).

An acoustic network model approach has been introduced by Cárdenas Miranda and Polifke [5] capable of analyzing the linear stability of a rocket engine combustion chamber equipped with a resonator ring in the frequency domain. The stability of each mode (composed of axial and tangential contributions) is determined with a generalized Nyquist criterion [6]. Following this approach, the chamber is divided in subsystems or “elements,” which form an interconnected network. Major attention in modeling is put on the resonator ring, which is represented as a duct segment with finite wall impedance. The acoustics within this segment are described analytically. With suitable matching conditions derived from mass and momentum conservation via the Galerkin approach, this model accounts for wave scattering as well as the mode coupling effects to higher radial modes. In this study, this network model is used to analyze the influence of resonator parameters on the overall stability in detail. Quantitative validation against experimental data was not object of the present paper. This would require more sophisticated submodels.

The paper is organized as follows: In Sec. II, the network modeling detailed in [5] is summarized and the main features of each element are discussed. The results of an extensive parameter study with focus on the $1T1L$ mode are presented in Sec. III. The generic test chamber used for the study is introduced first. An optimal tuned resonator ring is sought by variations of the cavity length and the number of resonators. Stability margins in terms of the flame parameters of the undamped chamber are compared with the well-tuned damping case. Moreover, the effect of temperature deviation in the cavities is examined for two configurations: one ring equipped with only one type of resonators and another with differing types but the same total number of resonators. Finally, the influence of nonlinear correlation terms associated with the SPL is investigated before concluding in Sec. IV.

II. Low-Order Network Model

In this section, the low-order network model of a rocket engine combustion chamber from [5] is presented briefly. This model captures the important thermoacoustic interactions with low computational costs. In the network, the different parts of the combustion chamber are modeled as separate (thermo)acoustic elements as illustrated in Fig. 2. For each such element, the main features are summarized and discussed. By connecting these elements, a linear system is formed, which can be used to find the eigenfrequencies and thus to determine the linear stability of the corresponding eigenmode.

A. Duct Segment

The three-dimensional, linear acoustic field in terms of the pressure fluctuation p' with uniform mean flow in the axial direction $\mathbf{v}_0 = [U, 0, 0]^T$ can be described by the convective wave equation

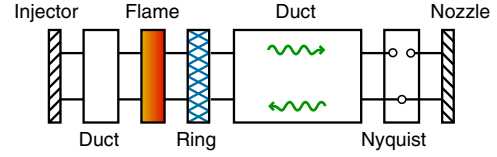


Fig. 2 Acoustic network of a generic test chamber with Nyquist element; reproduced from [5].

$$\frac{1}{c^2} \left(\frac{\partial}{\partial t} + U \frac{\partial}{\partial x} \right)^2 p' = \nabla^2 p' \quad (1)$$

Hereby, the viscous dissipation is neglected and a constant speed of sound c is assumed. In a cylindrical duct with radius R , the solution of this equation with harmonic time dependency reads in cylindrical coordinates (x, r, θ) as

$$\begin{aligned} \frac{p'}{c_0 \rho_0} &= \sum_{m,n} [J_m(\alpha_{mn}^+ r) F_{mn} e^{-ik_{mn}^+ x} + J_m(\alpha_{mn}^- r) G_{mn} e^{-ik_{mn}^- x}] e^{i\Omega t} e^{im\theta} \\ &= \sum_{m,n} (f_{mn} + g_{mn}) \end{aligned} \quad (2)$$

Here, J_m denotes the m th Bessel function of the first kind. The numbers m and n describe the tangential and radial mode order, respectively. The solution can be interpreted as a combination of left and right traveling waves f_{mn} and g_{mn} . Note that the preceding expression is complex valued with its real part corresponding to the physical pressure. The propagation in the x direction of the corresponding wave is determined by the axial wave number k_{mn}^\pm and the mode shape by the radial wave number α_{mn}^\pm . These numbers are linked by the dispersion relation

$$(\alpha_{mn}^\pm)^2 = (\Omega/c - M k_{mn}^\pm)^2 - (k_{mn}^\pm)^2 \quad (3)$$

where M is the Mach number U/c .

Moreover, the wave numbers α_{mn}^\pm have to be determined such that the boundary condition at the duct wall is satisfied. These conditions are usually given in terms of an acoustic impedance Z , which is the ratio of the fluctuating pressure \hat{p}' and velocity normal to the surface \hat{u}'_\perp in the frequency domain:

$$Z(\omega) = \frac{\hat{p}'}{\hat{u}'_\perp} = \Theta + i\Psi \quad (4)$$

The real part Θ (the so-called resistance) mainly describes the dissipative effects, whereas the imaginary part Ψ (the reactance) describes the phase shift or time delay.

In the presence of axial mean flow, the boundary conditions for $p'(x, r, \theta)$ are given by Myers [7] as

$$-\frac{i\Omega}{\rho} \frac{\partial p'}{\partial r} = \left(i\Omega + U \frac{\partial}{\partial x} \right)^2 \frac{p'}{Z(\Omega)} \quad (5)$$

For a hard-wall boundary condition with $Z|_{r=R} = \infty$, this simplifies to

$$\frac{d}{dr} \left[J_m(\alpha r) \right]_{r=R} = 0 \quad (6)$$

with the real-valued, frequency-constant solutions $\alpha_{mn}^\pm = \alpha_{mn}^- = \pm \lambda_{mn}/R$, where λ_{mn} denotes the n th root of $(d/dr)J_m$. For a duct with finite shell impedance, the situation changes: The solutions are complex valued as well as frequency dependent and $\alpha_{mn}^+ \neq \alpha_{mn}^-$ holds. In this case, the wave numbers have to be determined by solving the nonlinear equation numerically, which arises by inserting the analytical solution (2) and the dispersion relation (3) into the Myers boundary condition (5).

Having computed the axial wave numbers, the propagation of waves in a duct of length Λ with constant shell impedance can be described by the corresponding transfer matrix \mathbf{T}_{mn} :

$$\begin{bmatrix} f_{mn}^u \\ g_{mn}^u \end{bmatrix} = \mathbf{T}_{mn} \begin{bmatrix} f_{mn}^d \\ g_{mn}^d \end{bmatrix} \quad (7)$$

The expressions f_{mn}^u , g_{mn}^u , f_{mn}^d , and g_{mn}^d denote the left and right traveling wave of the mode (m, n) upstream and downstream of the duct, respectively. This transfer matrix is given as

$$\mathbf{T}_{mn} = \begin{bmatrix} e^{-ik_{mn}^+ \Lambda} & 0 \\ 0 & e^{-ik_{mn}^- \Lambda} \end{bmatrix} \quad (8)$$

It is obvious that, in such a duct, only transmission takes place, without any reflection or scattering, neither into the same mode nor into any other mode.

B. Resonator Ring

In the network model, the resonator ring is modeled as a duct segment with finite shell impedance. At connections of duct segments with differing shell impedances, appropriate matching conditions have to be set. Here, a Galerkin-based approach is used to satisfy mass and momentum conservation in a weak sense. In the present report, only the main ideas behind this resonator ring model are given (for details refer to [5]).

A common model for the impedance of the mouth of the quarter-wave length resonator with diameter d and length l , as shown in Fig. 1, is given by Laudien et al. [8] as

$$Z_R = 2 \left(1 + \epsilon_{nl} + \frac{l}{d} \right) \sqrt{2\mu_R \rho_R \Omega} - ic\rho \cot\left(\frac{\Omega l}{c}\right) \quad (9)$$

The reactance of this model is described in an analytical way, whereas the resistance is determined empirically. The so-called nonlinear factor ϵ_{nl} has to be determined experimentally in dependence on the SPL. The length l , describes the corresponding length to the effective mass (in analogy to the Helmholtz resonator). The effective length $l_e = l + \delta l$ ($\delta l \approx 0.42d$ [9]) is slightly larger than the geometric length, because it accounts for the fluid in front of the resonator mouth taking part in the resonator oscillation. The dynamic viscosity at the resonator opening is denoted with μ_R and the density with ρ_R . Because the duct model introduced earlier can only deal with duct segments with a homogeneous shell impedance, it is reasonable to define an equivalent impedance Z_{eq} [8]

$$\frac{Z_{eq}}{A_{ref}} = \left(\sum_j \frac{A_j}{Z_j} \right)^{-1} \quad (10)$$

Here, Z_j corresponds to the impedance at the area A_j and A_{ref} to the total area

$$\sum_j A_j$$

It should be pointed out that this approach can formally handle resonator rings with several resonator types. This is reasonable as long as the assumption of a homogeneous wall impedance is valid (i.e., there are not too many different resonator types and they are mounted well distributed around the circumference). Having set the homogeneous shell impedance, the transfer matrix can be computed as discussed in Sec. II.A.

At the interface between the hard-wall and finite shell impedance duct segment, transmission, reflection, and radial mode coupling occur. As shown in [5], these effects are considered in appropriate mode-matching conditions, which can be derived from mass and momentum conservation on a control volume enclosing the connection. For every tangential order m , these quantities can only be conserved in a weak integral sense with weighting functions

$\Psi_{m\nu}(r, \theta)$, $\nu = 1, \dots, N$. Decreasing the volume thickness to zero, only surface and line integrals remain. For the coefficients

$$\begin{aligned} \mathbf{q}^h &= [F_{m0}^h, G_{m0}^h, F_{m1}^h, G_{m1}^h, \dots, F_{mN}^h, G_{mN}^h]^T, \\ \mathbf{q}^s &= [F_{m0}^s, G_{m0}^s, F_{m1}^s, G_{m1}^s, \dots, F_{mN}^s, G_{mN}^s]^T \end{aligned} \quad (11)$$

on the hard- and soft-wall side, the linear system

$$\mathbf{Q}^s \mathbf{q}^s = \mathbf{Q}^h \mathbf{q}^h \quad (12)$$

follows, where \mathbf{Q}^s and \mathbf{Q}^h are square $2N \times 2N$ matrices (cf. [10,11]). With $\Psi_{m\nu} = J_m(\lambda_{m\nu} r/R)$, the matrix \mathbf{Q}^s is of block-diagonal structure due to the orthogonality of the Bessel functions. The transfer matrix connecting a hard-wall segment with a soft-wall segment is given as $\mathbf{T}^{sh} = (\mathbf{Q}^s)^{-1} \mathbf{Q}^h$ and, analogously, $\mathbf{T}^{hs} = (\mathbf{T}^{sh})^{-1}$ for a connection, vice versa. In total, the transfer matrix of the resonator ring is given as [5]

$$\mathbf{T}_{ring} = \mathbf{T}^{sh} \mathbf{T}^s \mathbf{T}^{hs} \quad (13)$$

where \mathbf{T}^s is the transfer matrix of the soft-wall segment of the resonator. In contrast to a simple duct segment, scattering (i.e., reflection and transmission of acoustic waves), as well as coupling of radial modes of different orders, take place here. Thus, these effects are considered in addition to the direct dissipation of acoustic energy in the following stability analysis.

C. Injector Plate, Flame, and Nozzle

Because this study focuses on accurate modeling of the resonator ring, relatively simple models for the injector plate and the combustion process are used. Nevertheless, it is possible to capture the main driving and damping effect with these models.

At the injector plate, the acoustic mass flow fluctuations are assumed to be zero $(\rho_1 u_1)' = 0$. Consequently, the acoustic behavior is given by [12]

$$(\kappa_{mn}^+ + M)f_{mn} + (\kappa_{mn}^- + M)g_{mn} = 0 \quad (14)$$

with

$$\kappa_{mn}^\pm = \frac{k_{mn}^\pm}{\omega/c + M k_{mn}^\pm} \quad (15)$$

The flame is modeled in an thermoacoustic element of zero thickness with the well-known sensitive time lag model proposed by Crocco [13]

$$\frac{\dot{Q}'}{Q} = n(1 - e^{i\Omega\tau}) \frac{p''}{p''} \quad (16)$$

This “ $n - \tau$ model” relates the relative pressure fluctuation p''/p'' on the cold, upstream side to the relative heat release \dot{Q}'/Q with a time lag τ and an interaction index n . Using the linearized Rankine–Hugoniot equations [14], this expression can be written in terms of characteristic wave amplitudes [6]:

$$\begin{aligned} f_{mn}^d + g_{mn}^d &= \xi[1 - M^u \Xi(\gamma n(1 - e^{i\Omega\tau}) + \kappa_{mn}^{+,u})] f_{mn}^u \\ &+ \xi[1 - M^u \Xi(\gamma n(1 - e^{i\Omega\tau}) + \kappa_{mn}^{-,u})] g_{mn}^u, \\ \kappa_{mn}^{+,d} f_{mn}^u + \kappa_{mn}^{-,d} g_{mn}^d &= [\kappa_{mn}^{+,u} + M^u \gamma \Xi n(1 - e^{i\Omega\tau})] f_{mn}^u \\ &+ [\kappa_{mn}^{-,u} + M^u \gamma \Xi n(1 - 4e^{i\Omega\tau})] g_{mn}^u \end{aligned} \quad (17)$$

with the isentropic exponent γ and the excess temperature $\Xi = (T^u/T^d) - 1$. The ratio of specific impedances $\xi = \rho_2 c_2 / (\rho_3 c_3)$ is determined by momentum conservation as [5]

$$\xi = \frac{1}{2} \left(\sqrt{(\Xi + 1)(1 + \gamma M^2)} + \sqrt{\Xi(1 + \gamma M^2)^2 + (1 - \gamma M^2)^2} \right) \quad (18)$$

For the nozzle, the model of Bell and Zinn [15] is used based on an implementation of Köglmeier et al. [16]. This admittance model incorporates the flow with Mach number M , isentropic exponent γ , and the mode shape (m, n) , as well as the nozzle geometry. The geometry is described by the radii of curvature at the nozzle entrance r_{in} and at the throat r_{out} , as well as by the nozzle half-angle θ_{nozzle} . For detailed discussion on the influence of the nozzle modeling refer, for example, to [17]. This model reflects the strong frequency-dependent damping of the nozzle accurately and is thus more sophisticated than the choked nozzle approach used in [5].

D. Determination of the Eigenfrequencies

Putting all acoustic elements together, the acoustic system can be described as a linear system with a system matrix $A(\Omega)$ for each frequency Ω . To get nontrivial solutions, it is necessary that $\ker(A(\Omega)) \neq \{0\}$. So, a resonant eigenfrequency Ω_{eig} has to satisfy $\det(A(\Omega_{eig})) = 0$. Having determined such a complex-valued eigenfrequency $\Omega = \omega + i\vartheta$, the linear stability of the corresponding eigenmode is designated by the sign of its complex part ϑ , since $p' \propto e^{-\vartheta t}$. The growth rate per cycle T is given as

$$\Gamma = e^{-\vartheta T} - 1 = \exp\left(-2\pi \frac{\vartheta}{\omega}\right) - 1 \quad (19)$$

This expression takes negative values for positive ϑ and vice versa. The eigenvalues determine the three-dimensional corresponding mode shapes. In this study, the focus is put on the stability analysis. For typical mode shape refer to [5].

The determination of the eigenvalues Ω_{eig} is a nonlinear problem. Thus, in general, it is very laborious to find these values directly by root-finding methods. Thus, the graphical Nyquist plot method based on the generalized Nyquist criterion [18] is used to approximate them. For this purpose, a Nyquist element is added to the network as illustrated in Fig. 2. Here, one channel (e.g., for the right traveling waves) is directly connected, whereas the other channel is cut. Now, the open-loop transfer function (OLTF) can be defined as

$$\text{OLTF}(\Omega) = -\frac{f_u}{f_d} \quad (20)$$

This function maps the complex plane uniformly on itself. In particular, all eigenfrequencies Ω_{eig} are mapped on the critical point $-1 + 0i$. By mapping the real-valued, positive frequencies ω on the open-loop transfer function curve $\text{OLTF}(\omega)$, the eigenfrequencies can be estimated by finding those frequencies ω_{min} where the OLTF curve has a local minimal distance to the critical point. This procedure is illustrated in Fig. 3. The value ω_{min} corresponds to the real part of an eigenvalue. The magnitude of its imaginary part can be estimated by the distance S_{min} to the critical point scaled with $1/\sigma$, where

$$\sigma = \lim_{\Delta\omega \rightarrow 0} \left| \frac{\text{OLTF}(\omega_{min} + \Delta\omega) - \text{OLTF}(\omega_{min} - \Delta\omega)}{\Delta\omega} \right| \quad (21)$$

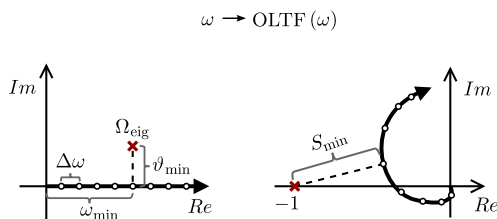


Fig. 3 Mapping of ω to the OLTF curve; reproduced from [5].

And so,

$$\Omega_{eig} \approx \omega_{min} + i \text{sign}(\text{RHS}) \frac{S_{min}}{\sigma}$$

where the sign $\text{sign}(\text{RHS})$ has to be determined using the right-hand side (RHS) rule. In [18], a polynomial fit to the discrete OLTF curve is proposed to determine the eigenvalues. For a linear fit, this reads as

$$\Omega_n \approx \omega_{min} + i \text{sign}(\text{RHS}) \frac{2|S_{min}|\Delta\omega}{|\text{OLTF}(\omega_{min} + \Delta\omega) - \text{OLTF}(\omega_{min} - \Delta\omega)|} \quad (22)$$

It should be mentioned that the preceding estimation is more accurate if the partial eigenvalue is located close to the real axis (i.e., at small growth or decay rates). Thus, the determination of the sign, which determines the stability of a mode, is very accurate. In the case of very high nominal growth or decay rates, quantitative accuracy decreases, whereas the trend is reproduced correctly.

In [5], a comparison of the Nyquist method using the linear fit with a direct root-finding method of $\det(A(\Omega))$ is given for a rocket combustion chamber, which shows that the Nyquist method provides reasonable results within this framework.

III. Parameter Study

As mentioned earlier, low-order models offer the advantage of low computational cost, such that extensive parameter studies can be performed. In this section, the influence of several parameters associated with the acoustic resonator ring is studied. In particular, the influence of the cavity length l , the number of cavities n_R , mean temperature deviation ΔT in the cavities, and the nonlinear factor ϵ_{nl} are examined by way of example. Stability maps are presented for both the undamped and damped case (i.e., combustion chamber without and with resonators). Such studies are important because the mounting of resonators can change the mode shapes and thus can also affect the damping and driving mechanisms significantly. In other words, the resonator design cannot be based solely on the eigenmodes and eigenfrequencies of the undamped chamber, but requires the study of the coupled system “chamber with resonator” to capture all interactions taking place (see, e.g., [2]).

A. Generic Combustion Chamber

A generic combustion chamber is defined, which is used for the semi-analytical studies on the stabilizing influence of the resonator ring. This chamber has radius R and length L . At distance x_F from the injector plate, the compact combustion front is located with excess temperature $\Xi = T_d/T_u - 1$. Further downstream, the resonator ring is placed with n_R cavities and center location x_R . If not mentioned explicitly, each of these cavities has the same length l and diameter d . All geometrical parameters are nondimensionalized with the chamber radius R . All following eigenfrequencies $\Omega = \omega + i\vartheta$ and time-dependent quantities are normalized with the real part of the $1T1L$ eigenfrequency ω_{ref} of the undamped chamber. Values for all parameters are listed as follows: $R = 1$, $L = 1.26$, $x_F = 0.11$, $x_R = 0.15$, $d = 0.078$, $l = 0.44$, $n_R = 22$, $\epsilon_{nl} = 65$, $r_{in} = 2.59$, $r_{out} = 0.97$, $\theta_{nozzle} = 25$, $\Xi = 12$, $\gamma = 1.13$, $n = 1.5$, $\tau = 3.10$. In this study, $N = 8$ radial modes were considered in the mode matching at the resonator interfaces (Sec. II.B).

The Nyquist plot for the tangential order $m = 1$ of the undamped chamber is shown in Fig. 4, where the curve describes clockwise circles by increasing the frequency. The three points on the OLTF curve with minimal distance to the critical point $-1 + 0i$ correspond to the $1T$, $1T1L$, and $1T2L$ eigenmodes. The $1T$ mode is located at the cut-on frequency of the first tangential order where the OLTF curve has its only discontinuity. The second detected mode $1T1L$ is unstable. Later, the curve approaches the origin, which is an outcome of the damping induced by the nozzle increasing with the frequency. Thus, the $1T2L$ is very clearly in the stable regime. This physical

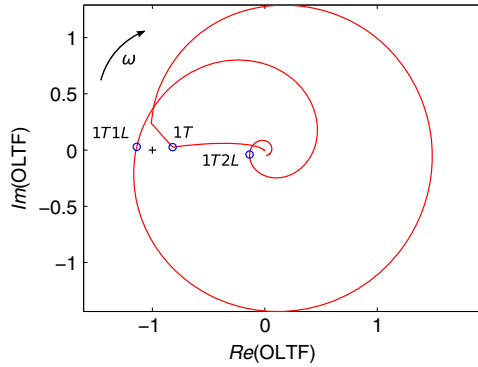


Fig. 4 Nyquist plot of the first tangential mode for the undamped chamber.

effect of high damping for high frequencies is not incorporated in the choked nozzle approach used in [5].

The eigenmodes of this chamber without resonator ring are presented in Table 1. The $1T1L$ mode is most unstable for this configuration with a growth rate of 4.92%, whereas the others are relatively stable. Thus, the following stability analysis is based on this mode. Studies for other modes can be performed in an analogous manner. Inserting the well-tuned reference resonator ring in the combustion chamber stabilizes the $1T1L$ mode; see the values for the undamped case in Table 1. Note that the formerly unstable $1T1L$ mode has been split into two modes $1T1L^\alpha$ and $1T1L^\beta$ of similar frequency when the resonator ring is inserted in the chamber. This behavior will be explained in Sec. III.B.

B. Cavity Length

The cavity length has a major influence on the damping behavior because the cavity eigenfrequency is given as $f_{R,k} = (2k + 1)c_R / (4l_c)$, $k = 0, 1, 2, \dots$. In Fig. 5, the real part ω and imaginary part ϑ of the $1T1L$ eigenfrequency are plotted, respectively. It can be observed that the $1T1L$ eigenmode splits into two modes when the resonator eigenfrequency is close to the eigenfrequency of the coupled system. This behavior has already been seen by other authors for experimental as well as numerical setups (cf. [19,20]). Both modes are always more stable than the undamped $1T1L$ mode, whose stability margin ϑ_{ref} is shown by a horizontal black dashed line in Fig. 5a. Not only the stability but also the physical frequencies change. For very short cavity lengths, the mode is hardly influenced: Eigenfrequency and corresponding stability are almost the same as for the undamped case. Increasing the cavity length toward the optimal length causes a decrease in eigenfrequency and increase in stability. Close to the optimal length, the second, so-called $1T1L^\beta$ mode appears. Both the original $1T1L^\alpha$ and the $1T1L^\beta$ modes are considerably more stable. One of them exhibits a lower and the other a higher frequency than the undamped $1T1L$ mode (see Fig. 5b). The optimal cavity length l_{opt} is reached where the two ϑ curves in Fig. 5a intersect. Further increase of the cavity length away from this optimal length leads on the one hand to a further stabilization of the original $1T1L^\alpha$ mode until it disappears completely. On the other hand, the second mode $1T1L^\beta$ tends to be more and more unstable and

asymptotically approaches both the stability margin and the frequency of the undamped $1T1L$ mode. The observed shift in the real part of the eigenfrequency ω is the reason why here and in the following figures ϑ is plotted instead of the growth rate Γ . The growth rate Γ is defined per cycle T which is changing with ω , whereas ϑ is independent of T and thus more reasonable for comparison in this context.

For the chosen parameters, the optimal damping is achieved with a cavity length of $l_{\text{opt}} \approx 0.438$, which was also chosen for the reference resonator configuration. For lengths in a range around l_{opt} , the $1T1L$ eigenmodes remain stable (i.e., $\vartheta > 0$). A priori, the optimal length can be estimated using the real part of eigenfrequency ω_{ref} from the undamped analysis. Accordingly, the estimated length would be $l_{\text{est}} = c_R / (4\omega_{\text{ref}}) - \delta l = 0.454$. This estimated length from the decoupled analysis is also shown in Fig. 5a with a black dashed line. It can clearly be seen that, for optimizing the resonator design, only the coupled system provides accurate results. In this case, the a priori optimal length is already slightly in the unstable region (see Fig. 5a).

The effect of splitting eigenmodes is also illustrated by the Nyquist plot in Fig. 6. For well-tuned resonators, a loop appears in the OLTF curve such that two points with minimal distance to the critical point occur instead of one for the undamped case. These two minima correspond to the two eigenmodes $1T1L^\alpha$ and $1T1L^\beta$. For a cavity length slightly smaller than l_{opt} , this loop is located at a higher frequency than the original eigenmode frequency. The longer the cavities are, the lower the corresponding frequency of the loop location is. In the complex plane, this cavity length increment corresponds to a counterclockwise movement of this loop. For cavity lengths far away from the optimal length, this loop disappears again.

C. Number of Cavities

Another major design parameter is the number of cavities n_R mounted in the resonator ring. The configuration remains unstable when only few resonators ($n_R < 8$) are inserted (see the solid curve in Fig. 7a). When n_R is increased, the original $1T1L$ mode is more and more stabilized. But for larger values of $n_R (> 15)$, the second $1T1L$ mode is detectable, which gets less stable by further increasing n_R and is very close to the unstable regime from $n_R = 36$ onward (see the dashed red curve in Fig. 7a). The generic test chamber is most stable for $n_R = 19$. For the reference resonator ring configuration, $n_R = 22$ cavities were selected because this number is located in the optimal region. The corresponding real parts of the eigenfrequencies are plotted in Fig. 7b.

D. Stability Map

The stability map of the $1T1L$ mode is shown in Fig. 8 in dependency on the flame parameters n and τ . The solid curve marks the transition from the stable (below) to the unstable regime (above) for the undamped chamber. The shape of the curve can be explained by the definition of the flame model used [Eq. (16)]. Understandably, the mode tends to be more unstable for higher interaction indices because this directly increases the driving influence. The time lag τ causes the largest amplification when it matches the eigenfrequency ω such that $\tau\omega \approx \pi$. The reason why the most unstable operating point is not directly located at $\tau\omega_{\text{ref}} = \pi$ is that the system eigenfrequency slightly changes with variation of the time lag τ . This is compared with the damped case with the well-tuned reference resonator ring. The resulting stability margins are marked by the dashed red line in

Table 1 Real part of eigenfrequencies and corresponding growth rates for undamped and well-tuned damped chamber

Chamber	Values								
Undamped	$1L$	$1T$	$1T1L$	$2L$	$2T$	$1T2L$	$2T1L$	$3L$	
ω	0.53	0.79	1	1.10	1.32	1.44	1.54	1.74	
Γ	-70.9%	-0.26%	4.92%	-98.1%	-0.15%	-83.7%	-2.69%	-99.9%	
Damped	$1L$	$1T$	$1T1L^\alpha$	$1T1L^\beta$	$2L$	$2T$	$1T2L$	$2T1L$	$3L$
ω	0.51	0.79	0.98	1.05	1.09	1.32	1.41	1.54	1.68
Γ	-69.1%	-0.26%	-13.7%	-8.59%	-96.5	-0.15%	-78.0%	-1.56%	-99.9%

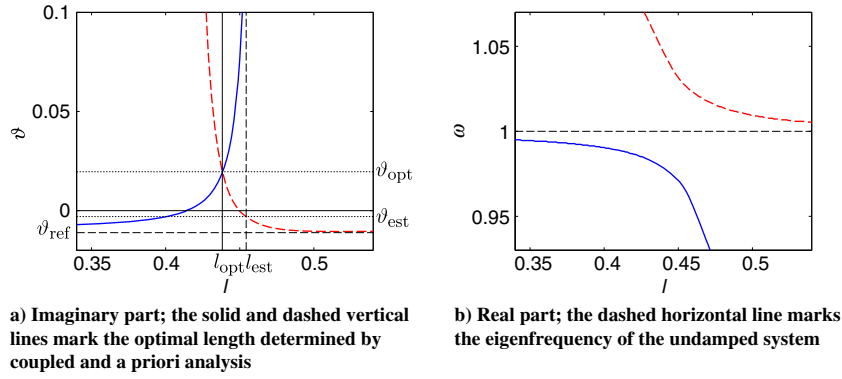


Fig. 5 Eigenfrequencies of the split 1T1L modes vs cavity length l .

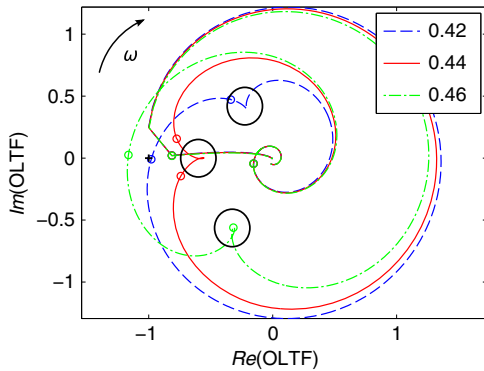


Fig. 6 Nyquist plot for three different cavity lengths: 0.42, 0.44, and 0.46.

the same figure. A significant increment of stable operation range can be observed clearly. As explained in Sec. III.B, the 1T1L mode splits into two modes. Here, only the dominant (i.e., more unstable) 1T1L mode is plotted. This explains the appearance of the sharp corner at around $n \approx 2.03$ and $\tau \approx 3.41$, where the stability margins of the 1T1L $^\alpha$ and 1T1L $^\beta$ modes meet and the dominance switches from one to the other mode.

E. Temperature

The cavity eigenfrequency depends linearly on the mean cavity speed of sound $f_R \propto c_R$. Changing the mean cavity temperature T_R detunes the cavity eigenfrequency, since $c_R \propto \sqrt{T_R}$. This effect is also reflected in the coupled analysis. In Fig. 9, the imaginary and real part of the dominant 1T1L eigenfrequency are plotted against the deviation of mean temperature in the cavities ΔT with the solid lines, where ΔT is normalized by the design temperature in the cavities. As

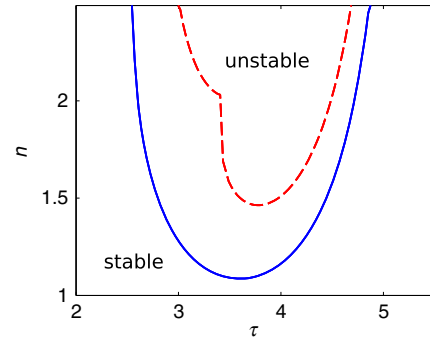


Fig. 8 Stability map in dependency on the flame parameter n and τ for undamped (solid) and well-tuned damped (dashed) chamber.

expected, the configuration tends to be less stable apart from the design temperature (see Fig. 9a).

An often used design criterion is the absorption coefficient

$$\alpha(\Omega) = 1 - \left| \frac{Z(\Omega) - \rho_R c_R}{Z(\Omega) + \rho_R c_R} \right|^2 \quad (23)$$

This coefficient can be seen as the ratio of the dissipated acoustic energy to the incident acoustic energy. By definition, the maximum absorption factor is unity. This coefficient is plotted over the frequency for the reference configuration with the solid line in Fig. 10. The absorption is highest close to the reference frequency and decays rapidly apart from it. A possibility to reduce the sensitivity to deviations of the design value is to modify the ring such that more than a single resonator type is used. In the modified ring, the same number of cavities is mounted but the length of six resonators is elongated and the length of another six is shrunk by 10%. The

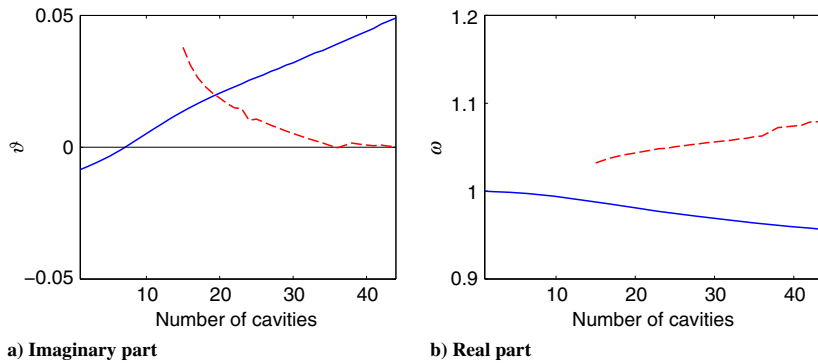


Fig. 7 Eigenfrequencies of the split 1T1L modes vs number of cavities n_R .

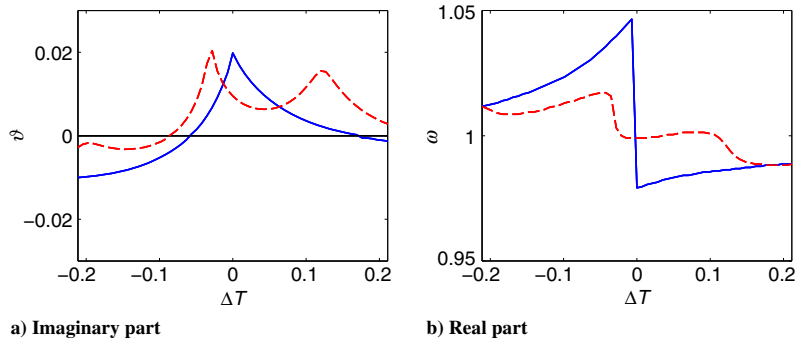


Fig. 9 Dominant 1T1L eigenfrequency vs temperature deviation ΔT for two resonator ring configuration: reference configuration (solid) and modified configuration (dashed).

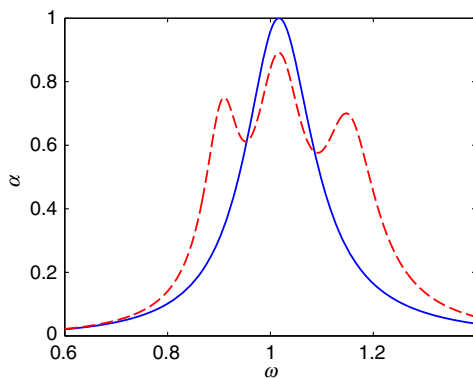


Fig. 10 Absorption coefficient α in dependency vs frequency for reference resonator ring (solid) and modified configuration from Sec. III.E (dashed).

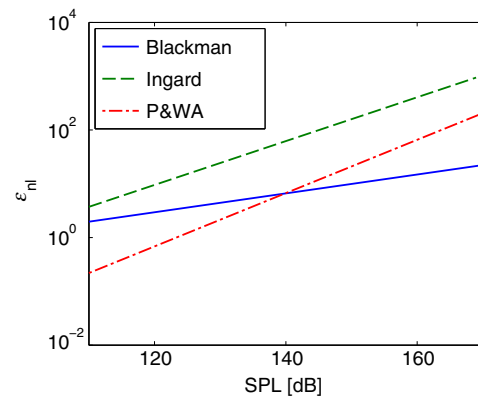


Fig. 12 Nonlinear factors assembled in [21] measured by Blackman, Ingard, and Pratt & Whitney Aircraft (P&WA).

modified cavity types have lower and higher eigenfrequencies, respectively. By changing the temperature, all eigenfrequencies shift. With different cavity lengths in the array of resonators, the likelihood grows that one type matches the coupled eigenfrequency and thus damps efficiently. The absorption for the modified resonator ring is also shown in Fig. 10 with a dashed curve. It is still maximum close to ω_{ref} but a good performance close to the eigenfrequencies of the additional resonator types is realized. Thus, with such a modification, the range of high absorption can be broadened efficiently but with a slightly lower maximal absorption.

The modified resonator ring achieves the requested stabilization also in the coupled analysis (see the red dashed curves in Fig. 9). It can be clearly observed that the stable range is increased by this a modification (see Fig. 9a).

F. Nonlinear Factor

In the impedance model of the quarter-wave resonator introduced in Eq. (9), the nonlinear factor ϵ_{nl} plays an important role. The empirical correlation term accounts for nonlinear damping mechanisms due to flow separation at the cavity mouth. At high SPLs, this mechanism dominates the linear, viscous damping and, consequently, the resistance is mainly determined by that factor in this regime.

Now, its influence on the coupled system stability is examined. The imaginary and real parts of the dominant 1T1L eigenfrequency are plotted with respect to ϵ_{nl} in Fig. 11. When increasing this term, the system stabilizes significantly until a saturation is reached at $\epsilon_{opt} \approx 100$. Subsequently, the system is overdamped and the stability drops down again and even becomes unstable for very high values of ϵ_{nl} (see Fig. 11a). The reason is that, for very large $\epsilon_{nl} \rightarrow \infty$, the soft-

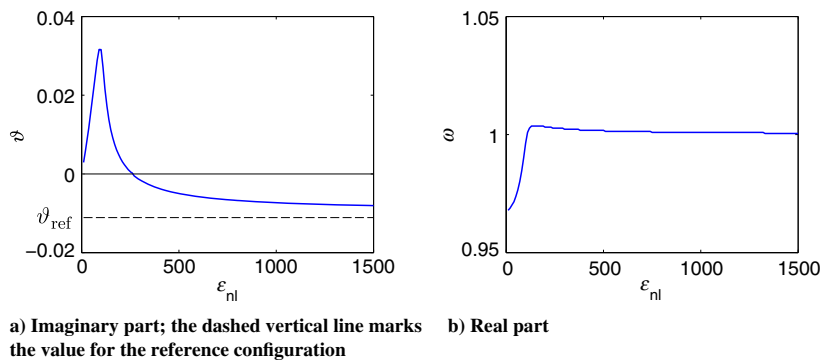


Fig. 11 Dominant 1T1L eigenfrequency vs nonlinear factor ϵ_{nl} .

wall duct behaves more and more like a hard wall, and accordingly, ϑ approaches the stability margin of the undamped chamber ϑ_{ref} .

Some measurements with Helmholtz resonators from [21] for the nonlinear factor ϵ_{nl} in dependency on the SPL are summarized in Fig. 12. A considerable scatter can be observed. This underlines that such a factor has to be determined for the specific geometric setting, because a transfer from another setup might be defective and the overall stability is influenced in a sensitive manner by such uncertainty. Valid impedance models require robust estimates for the occurring SPLs and a correlation that is valid for the geometry under consideration.

IV. Conclusions

A low-order network model of a complete rocket engine combustion chamber has been presented. Hereby, the chamber has been divided into several elements, in which the linear acoustics have been modeled separately. Matching conditions have been set up at the interfaces of duct segments with different shell impedances. Following the Galerkin approach, mass and momentum conservation across the interface has been guaranteed in a weak sense. These conditions also have included scattering and mode coupling effects at the resonator ring. Stability analysis has been performed using the generalized Nyquist criterion to determine the eigenfrequencies.

This procedure has been applied to perform an extensive parameter study and generate stability maps. First, the analysis has been carried out for the cavity lengths. When the resonator eigenfrequencies have been close to an eigenfrequency of the coupled system, the process has been stabilized and a splitting of this chamber eigenfrequency has occurred. The damping effect of cavities with matching lengths has become apparent. Moreover, it has been observed that, in general, the resonator design according to the undamped system is not sufficient. Instead, the coupled system of the chamber and the resonators has to be taken into account. To achieve optimal damping, only a moderate number of cavities has turned out to be needed. Deviations in mean temperature from the design condition have shown a clear destabilizing impact due to the modification of the speed of sound within the cavities. Inserting a set of nonidentical resonators has observably lowered this undesired effect. A strong impact of the nonlinear acoustic dissipation parameter on the overall stability has been observed, which occurs due to flow separation at the cavity mouth at high SPLs. This has emphasized the need for the knowledge of occurring SPLs and of accurate modeling of this nonlinear effect for the specific geometric setting.

Acknowledgments

Financial support has been provided by the German Research Foundation (DFG, Deutsche Forschungsgemeinschaft) in the framework of the Sonderforschungsbereich Transregio 40, project number A3. The authors want to acknowledge Stefan Köglmeier for providing his implementation of the nozzle admittance model, as well as Daniel Kümmel for his help with formatting and editing.

References

[1] Oberg, C., "Combustion Stabilization with Acoustic Cavities," *Journal of Spacecraft and Rockets*, Vol. 8, No. 12, 1971, pp. 1220–1225. doi:10.2514/3.30366

[2] Acker, T., and Mitchell, C., "Combustion Zone-Acoustic Cavity Interactions in Rocket Combustors," *Journal of Propulsion and Power*, Vol. 10, No. 2, 1994, pp. 235–243. doi:10.2514/3.23734

[3] Garrison, G., Schnell, A., Baldwin, C., and Russell, P., "Suppression of Combustion Oscillations with Mechanical Damping Devices, Interim Report," Pratt and Whitney Aircraft, Interim Rept. PWA FR-3299, West Palm Beach, FL, 1969.

[4] Hersh, A., Walker, B., and Celano, J., "Helmholtz Resonator Impedance Model, Part 1: Nonlinear Behavior," *AIAA Journal*, Vol. 41, No. 5, 2003,

pp. 795–808. doi:10.2514/2.2041

[5] Cárdenas Miranda, A., and Polifke, W., "Combustion Stability Analysis of Rocket Engines with Resonators Based on Nyquist Plots," *Journal of Propulsion and Power*, Vol. 30, No. 4, 2014, pp. 962–977. doi:10.2514/1.B35149

[6] Cárdenas Miranda, A., and Polifke, W., "Damping Characteristics of Resonator Rings with Application to Low Order Stability Prediction of Rocket Thrust Chambers," *Fourth European Conference for Aerospace Sciences*, St. Petersburg, Russia, July 2011.

[7] Myers, M., "On the Acoustic Boundary Condition in the Presence of Flow," *Journal of Sound and Vibration*, Vol. 71, No. 3, 1980, pp. 429–434. doi:10.1016/0022-460X(80)90424-1

[8] Laudien, E., Pongratz, R., Pierro, R., and Preclik, D., "Experimental Procedures Aiding the Design of Acoustic Cavities," *Progress in Astronautics and Aeronautics*, Vol. 96, 1995, pp. 377–399. doi:10.2514/5.9781600866371.0377.0399

[9] Ingard, U., "On the Theory and Design of Acoustic Resonators," *Journal of the Acoustical Society of America*, Vol. 25, No. 9, 1953, pp. 10–37. doi:10.1121/1.1907235

[10] Gabard, G., and Astley, R., "Computational Mode-Matching Approach for Sound Propagation in Three-Dimensional Ducts with Flow," *Journal of Sound and Vibration*, Vol. 315, No. 4, Feb. 2008, pp. 1103–1124. doi:10.1016/j.jsv.2008.02.015

[11] Gabard, G., "Mode-Matching Techniques for Sound Propagation in Lined Ducts with Flow," *Proceedings of the 16th AIAA/CEAS Aeroacoustic Conference*, AIAA, Reston, VA, 2010, pp. 1–12; also AIAA Paper 2010-3940, 2010.

[12] Kopitz, J., Huber, A., Sattelmayer, T., and Polifke, W., "Thermoacoustic Stability Analysis of an Annular Combustion Chamber with Acoustic Low Order Modeling and Validation Against Experiment," *Proceedings of ASME Turbo Expo 2005 Power for Land, Sea and Air*, American Soc. for Mechanical Engineers Paper GT2005-68797, June 2005.

[13] Crocco, L., "Aspects of Combustion Instability in Liquid Propellant Rocket Motors Part 2: High Frequency Instability," *Journal of the American Rocket Society*, Vol. 22, No. 1, 1952, pp. 7–16. doi:10.2514/8.4410

[14] Polifke, W., Paschereit, C., and Döbbling, K., "Constructive and Destructive Interference of Acoustic and Entropy Waves in a Premixed Combustor with a Chocked Exit," *International Journal of Acoustics and Vibration*, Vol. 6, No. 3, 2001, pp. 135–146.

[15] Bell, W., and Zinn, B., "Prediction of Three-Dimensional Liquid-Propellant Rocket Nozzle Admittances," Georgia Inst. of Technology, NASA CR-121129, Atlanta, 1973.

[16] Köglmeier, S., Kaess, R., Morgenweck, D., Vollmer, K., Kathan, R., and Sattelmayer, T., "Rapid Approach for the Prediction of Complex Acoustic Resonance Frequencies in Rocket Combustion Chambers; HF2 Testcase," *Second REST Modelling Workshop*, Ottobrunn, Germany, 2010.

[17] Kathan, R., Morgenweck, D., Kaess, R., and Sattelmayer, T., "Validation of the Computation of Rocket Nozzle Admittances with Linearized Euler Equations," *Progress in Propulsion Physics*, Vol. 4, March 2013, pp. 135–148. doi:10.1051/eucass/201304135

[18] Sattelmayer, T., and Polifke, W., "Novel Method for the Computation of the Linear Stability of Combustors," *Combustion Science and Technology*, Vol. 175, No. 3, 2003, pp. 477–497. doi:10.1080/00102200302387

[19] Oschwald, M., and Farago, Z., "Acoustics of Rocket Combustors Equipped with Absorber Rings," *44th Joint Propulsion Conference*, AIAA, Reston, VA, July 2008, p. 10; also AIAA Paper 2008-5112, 2008.

[20] Pieringer, J., "Simulation selbsterregter Verbrennungsschwingungen in Raketenschubkammern in Zeitbereich," Ph.D. Thesis, Technische Universität München, Munich, 2008.

[21] Marino, P., Bohn, N., Russell, P., Schnell, A., and Parsons, G., "Study of the Suppression of Combustion Oscillations with Mechanical Damping Devices," NASA CR-90094, 1967.

K. Frendi
Associated editor



Determination of Acoustic Impedance for Helmholtz Resonators Through Incompressible Unsteady Flow Simulations

J. Tournadre*

Siemens Industry Software, 3001 Leuven, Belgium

K. Förner[†] and W. Polifke[‡]

Technical University of Munich, 85748 Garching bei München, Germany

P. Martínez-Lera[§]

Siemens Industry Software, 3001 Leuven, Belgium

and

W. Desmet[¶]

KU Leuven, 3001 Leuven, Belgium

DOI: 10.2514/1.J055337

The present work proposes and assesses a methodology based on incompressible computational fluid dynamics simulations to study the acoustic behavior of Helmholtz resonators under a large range of excitation amplitudes. It constitutes an alternative approach to the more widespread one based on compressible flow simulations to analyze the nonlinear regime of Helmholtz resonators. In the present methodology, the resonator is decomposed into its two main components: an assumed incompressible orifice neck and a compressible backing volume. The transfer impedance of the single orifice is obtained by means of an incompressible solver of the flow equations without turbulence modeling, whereas an analytical model accounts for the compliance of the gas in the backing cavity. The proposed methodology is compared for validation purposes to both numerical results of the full compressible equations and experimental data for the complete resonator at different sound pressure levels. A good agreement between the results of the two numerical approaches could be achieved. Numerical results match also fairly well with experimental data, but a systematic overprediction of the resistance by simulations is observed. Accounting for the presence of microrounded edges, presumably present due to manufacturing processes, allows a better agreement between numerical and experimental results.

Nomenclature

$A_f, A_{f,o}$	=	input amplitudes for compressible simulations, m/s
A_u	=	input amplitudes for incompressible simulations, m/s
c	=	speed of sound, m/s
d_{cav}	=	back-cavity diameter, m
d_o	=	orifice diameter, m
F_r, G_r	=	Riemann invariants, m/s
$f_{H,lin}$	=	Helmholtz resonance frequency in linear regime, Hz
He	=	Helmholtz number
l_o	=	orifice thickness, m
l_{cav}	=	back-cavity length, m
P	=	total pressure, Pa
p	=	pressure, Pa
$R_{exp/num}$	=	reflection coefficient
S_o/bc	=	orifice/back-cavity cross-sectional area, m ²
Sh	=	Shear number
u'	=	fluctuating velocity in duct, m/s
u'_o	=	fluctuating velocity in orifice, m/s

Z	=	acoustic impedance, (Pa · s)/m
z	=	normalized acoustic impedance
Δp	=	pressure loss, Pa
λ_a	=	acoustic wavelength, m
ρ	=	density, kg/m ³
σ	=	open area ratio
ϕ	=	acoustic velocity potential, m ² /s
Ω	=	vorticity, m ⁻¹

Superscripts

$\hat{\bullet}$	=	Fourier transformed variable
\bullet'	=	time fluctuating quantity

I. Introduction

ACOUSTIC damping systems, such as Helmholtz resonators, perforated liners, and quarter-wavelength cavities, are commonly used in multiple industrial applications to reduce sound transmission and to control acoustic feedback that can lead to instabilities, for instance, in combustion systems like aeroengines or gas turbines. When designed properly, such devices dissipate the acoustic energy at a specific bandwidth. The behavior of such an acoustic damper is often characterized by its acoustic impedance, which is defined in the frequency domain as the ratio of the pressure to the normal acoustic velocity. The acoustic dissipation mechanisms, and therefore the impedance values, differ significantly depending on the amplitude of the acoustic excitation. For low excitation amplitudes, the viscous dissipation dominates. In this case, the impedance is independent of the sound amplitude, and the resonator or orifice behaves like a linear system. Numerical methods based on linearized equations, like the linearized Navier–Stokes equations, allow for an efficient treatment of this linear regime with limited computational costs [1]. By increasing the excitation amplitudes, nonlinear effects appear and become progressively dominant. Such nonlinear effects originate from flow separation at the neck of the resonator, which transfers acoustic energy to the hydrodynamic field. The creation of vortices at the orifice neck

Received 10 May 2016; revision received 4 August 2016; accepted for publication 4 August 2016; published online 19 October 2016. Copyright © 2016 by the authors. Published by the American Institute of Aeronautics and Astronautics, Inc., with permission. All requests for copying and permission to reprint should be submitted to CCC at www.copyright.com; employ the ISSN 0001-1452 (print) or 1533-385X (online) to initiate your request. See also AIAA Rights and Permissions www.aiaa.org/randp.

*Ph.D. Student, Department of Mechanical Engineering, Researchpark 1237, Interleuvenlaan 68; also KU Leuven, Department of Mechanical Engineering, Celestijnenlaan 300B; jonathan.tournadre@kuleuven.be.

[†]Ph.D. Student, TUM, Professur für Thermofluidynamik, Boltzmannstr. 15.

[‡]Full Professor, TUM, Professur für Thermofluidynamik, Boltzmannstr. 15.

[§]Senior RTD Engineer, Researchpark 1237, Interleuvenlaan 68.

[¶]Ph.D. Student, Department of Mechanical Engineering, Celestijnenlaan 300B.

increases considerably the dissipation of the acoustic energy. This feature is of importance for the design of acoustic dampers, as it impacts substantially the sound wave attenuation. The nonlinear regime is, however, more complex to predict accurately due to the intricate nature of the physical phenomena taking place. Linear numerical methods are therefore not suitable at medium and high excitation amplitudes, and nonlinear time domain solvers are needed.

The present work investigates the capability of an incompressible unsteady computational fluid dynamic approach to study numerically the aeroacoustic response of a Helmholtz resonator to an external acoustic excitation. Different sound pressure levels (SPLs) are included in this study to cover the different regimes of an investigated Helmholtz resonator. Incompressible flow computations have already successfully been used in the past to characterize the acoustic behavior of confined flow systems. In the work of Martínez-Lera et al. [2], an approach combining incompressible computational fluid dynamics (CFD) and vortex sound theory [3] was applied successfully to a two-dimensional laminar flow through a T joint. This methodology was further improved and applied to corrugated pipes by Nakiboğlu [4] and to a large orifice configuration with through flow by Lacombe et al. [5] for whistling prediction. In contrast to those previous works, the present study focuses on both linear and nonlinear regimes of Helmholtz resonators in the absence of mean flow. The extension to the case with flow can be done easily due to the present general formulation and arguments presented by Nakiboğlu [4] and Golliard et al. [6].

Section II explains in detail the methodology applied here for the numerical acoustic characterization of a Helmholtz resonator. The numerical setup and the postprocessing steps used to determine the surface impedance of the resonator are described. In Secs. III and IV, the results for the impedance describing functions estimated by the proposed approach are shown for the linear and nonlinear regimes, respectively. In both cases, the results are compared to impedance values obtained using compressible flow computation of the complete resonator and validated against measurements data. Section V concludes this paper with an overview of the main observations of this study.

II. Description of Methodology and Case Study

A. Decomposed Helmholtz Resonator

The basic idea of using an incompressible solver to study the acoustic behavior of a Helmholtz resonator, placed at the termination of a duct as depicted in Fig. 1a, appears as a contradiction at first thought. The incompressible nature of the fluid violates indeed the principle of mass conservation if a nonzero inlet velocity is prescribed at the open side of the duct closed by the resonator, which makes impossible the direct study of this configuration by incompressible CFD simulation. The methodology proposed here to face this issue is to decompose the complete Helmholtz resonator into its two main components: the orifice neck and the backing cavity (see Fig. 1b). Such a decomposition has already been proposed by Ingard and Ising [7]. For most of the configurations of interest, the orifice can be considered acoustically compact; i.e., the Helmholtz number He ,

which describes the ratio of the neck length or diameter to the acoustic wavelength λ_a , is small ($He \ll 1$). Thus, the flow through the orifice can be treated as incompressible. The compressible effects occur solely in the backing volume. The orifice transfer impedance Z_o is often used to quantify the acoustic behavior of an orifice. It is defined as the ratio of the Fourier component (superscript $\hat{\cdot}$) of the fluctuating pressure drop $\Delta \hat{p}' = \hat{p}'_1 - \hat{p}'_2$ and velocity normal to the reference surface in the duct front of the resonator u' , i.e.,

$$Z_o = \frac{\Delta \hat{p}'}{\hat{u}'} \quad (1)$$

Note that in the previous definition the velocity \hat{u}' is the cross-sectional surface averaged velocity in the resonance tube. There are other authors using the cross-sectional surface averaged velocity in the orifice u'_o instead. These two velocities are related via the porosity of the resonator plate σ , such that $u' = \sigma u'_o$. The porosity is defined as $\sigma = S_o/S_{bc}$, with S_o and S_{bc} denoting the cross-sectional areas of the orifice and backing cavity, respectively.

The contribution of the backing volume can be described in terms of a surface impedance, $Z_{bc} = \hat{p}'_2/\hat{u}'_2$, which is done here analytically, as described in Sec. II.A.2. The orifice transfer impedance can therefore be expressed as

$$Z_o = \frac{\hat{p}'_1 - Z_{bc}\hat{u}'_2}{\hat{u}'_1} \quad (2)$$

Because of the acoustically compact neck and the same areas on both sides of the orifice, it is reasonable to assume $\hat{u}'_1 = \hat{u}'_2$. Thus, the surface impedance of the resonator Z_r is given in this lumped model as (cf. Ingard and Ising [7])

$$Z_r = Z_o + Z_{bc} \quad (3)$$

The present study builds on this Helmholtz resonator decomposition and aims to investigate the validity of this decomposition at different levels of sound excitation. In doing so, the advantages of an incompressible solver are exploited for the simulation of the flow through the orifice, including the vortex generation responsible for the nonlinear acoustic losses. Details on the estimation of the orifice transfer impedance and backing volume surface impedance are given in the following sections.

1. Orifice Impedance Z_o

The methodology to get the orifice transfer impedance from the incompressible simulations is explained in this section. In the plane wave regime, a one-dimensional approximation along the duct is possible, and the area-averaged absolute pressure at several sections of the duct is stored at each time step of the flow simulation. This allows computing the pressure differences between two arbitrarily chosen sections separated by the orifice: $\Delta p_{AB} = p_A - p_B$ is the pressure jump (or loss) between the sections A on the inlet side and B on the outlet side (see Fig. 2).

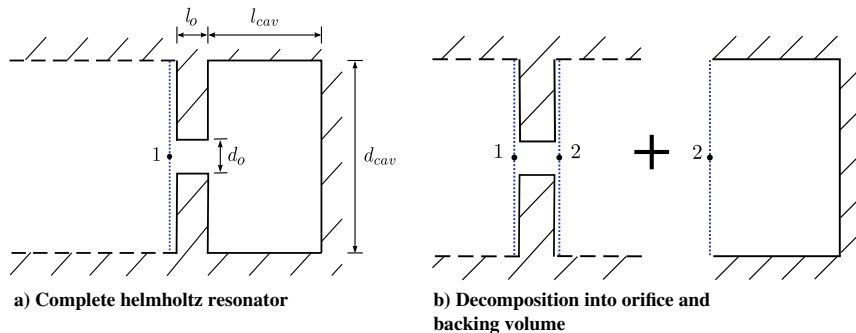


Fig. 1 Sketch of the considered geometry and reference cut planes 1 and 2 for the decomposed resonator model.

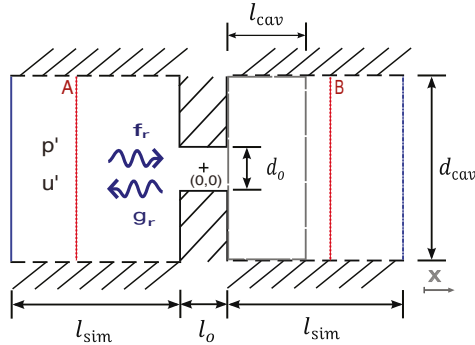


Fig. 2 Geometrical configuration for the Helmholtz resonator study and boundary conditions: (---) slip wall, (—) no-slip wall, (→) prescribed fluctuating velocity, and (---) fixed pressure boundary conditions.

In a general manner, for an incompressible fluid, the momentum equation yields

$$\nabla P = -\rho \frac{\partial \mathbf{u}}{\partial t} - \rho(\mathbf{\Omega} \times \mathbf{u}) + \rho \nu \nabla^2 \mathbf{u} \quad (4)$$

where P is the total pressure $P = p + \rho \|\mathbf{u}\|^2/2$, where \mathbf{u} stands for the velocity, $\mathbf{\Omega} = \nabla \times \mathbf{u}$ denotes the vorticity, and ρ and ν are the medium density and kinematic viscosity, respectively. The second term on the right-hand side of Eq. (4) is related to the acoustic power in an inviscid and homentropic flow according to Howe's energy corollary [3]. The third term describes the viscous dissipation effects. The total pressure difference ΔP between two sections can be expressed as the sum of two distinct contributions: $\Delta P = \Delta P_{\text{pot}} + \Delta P_s$. The pressure difference ΔP_{pot} is related to a potential flow solution [first term on the right-hand side of Eq. (4)], which would be the solution in the absence of vorticity and viscous effects, whereas ΔP_s is linked to sink/source terms for the sound with both vorticity and viscous effects taken into account [last two terms on the right-hand side of Eq. (4)]. In the numerical models, the viscous dissipation at the walls of the main duct is neglected, and slip boundary conditions are applied. As a consequence, the vorticity and viscous effects can be neglected for the wave propagation in the ducts so that $\Delta P_{\text{duct},s} = 0$ inside the duct segments. In the one-dimensional approximation, ΔP_{pot} can be expressed as

$$\Delta P_{\text{pot}} = -\rho \int_L \frac{\partial u_x}{\partial t} dx \quad (5)$$

with L the total length between the two sections, x the coordinate along the duct axis, and u_x the axial component of the velocity at the x location (see Fig. 2). Inside the duct segments, $\Delta P_{\text{duct},\text{pot}}$ can be interpreted as a result of the propagation along the duct of the fluctuation in velocity u_x . The pressure losses can be divided spatially between ducts and orifice parts, leading to

$$\begin{aligned} \Delta P_{AB} &= \Delta P_o + \Delta P_{\text{duct}} \\ &= \Delta P_o + \Delta P_{\text{duct},\text{pot}} + \Delta P_{\text{duct},s} \end{aligned} \quad (6)$$

with ΔP_{AB} the total pressure losses between the measurement sections A and B and ΔP_{duct} the total pressure losses in the two duct segments. From this, the expression to compute the orifice pressure drop ΔP_o is

$$\Delta P_o = \Delta P_{AB} - \Delta P_{\text{duct},\text{pot}} \quad (7)$$

There are two different ways to determine the orifice transfer impedance values from the measured pressure time series, depending on whether the potential flow pressure loss correction inside the duct is done directly on the pressure time data, or in the frequency domain

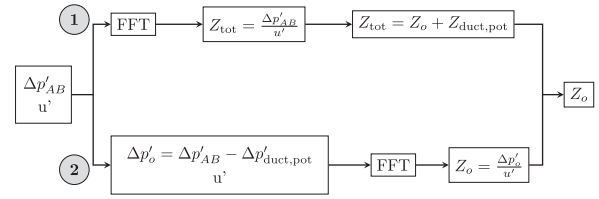


Fig. 3 Diagram of the two approaches to get the transfer impedance of the orifice from $\Delta p'$: approach 1 (top) and approach 2 (bottom).

on the impedance itself. Those two approaches to estimate the orifice impedance from the pressure and velocity time series are schematized in Fig. 3.

In approach 1, the impedance due to the duct potential pressure loss $Z_{\text{duct},\text{pot}}$ is subtracted from the total measured impedance Z_{tot} to estimate the transfer impedance from the orifice Z_o as

$$Z_o = Z_{\text{tot}} - Z_{\text{duct},\text{pot}} \quad (8)$$

For an orifice of thickness l_o placed between the measurement sections A and B, as illustrated in Fig. 2, $Z_{\text{duct},\text{pot}}$ is computed as

$$Z_{\text{duct},\text{pot}} = j\rho\omega(L_{AB} - l_o)u' \quad (9)$$

where L_{AB} is the distance between the measurement sections A and B, u' is the velocity perturbation inside the duct parts, ω is the angular frequency, and j is the imaginary number $\sqrt{-1}$.

In approach 2, the duct pressure loss is directly subtracted from the time pressure data. As u' does not depend on the position x in the duct segments, one gets

$$\Delta P_{\text{duct}} = \rho(L_{AB} - l_o) \frac{\partial u'}{\partial t} \quad (10)$$

where $\partial u'/\partial t$ can be computed analytically for harmonic excitation inlet velocity or has to be computed numerically from the velocity time series in case of broadband excitation.

2. Backing Volume Impedance Z_{bc}

The contribution of the backing volume can also be described in terms of a surface impedance $Z_{bc} = \hat{p}'_1/\hat{u}'_2$, which can be determined through an analytical model. Two analytical expressions for the backing volume are shown here. Using the one-dimensional acoustic equations, the impedance is given as

$$Z_{bc} = -j \cot(kl_{\text{cav}})\rho c \quad (11)$$

where k denotes the wave number $k = \omega/c$, c is the speed of sound in the medium, and l_{cav} is the length of the backing cavity. When the whole volume is compressed and expanded simultaneously, the following expression for the impedance can be derived using the isentropic compressibility $\beta \equiv 1/(\rho c^2)$:

$$Z_{bc} = -j \frac{\rho c^2 S_{bc}}{V\omega} \quad (12)$$

This is the same formulation as in, e.g., Keller and Zauner [8]. Both Eqs. (11) and (12) describe the same behavior for $l_{\text{cav}} \ll \lambda_a$. This can be observed by means of the Laurent series of Eq. (11): $Z_{bc}/(\rho c) = -i[1/(kl_{\text{cav}}) - kl_{\text{cav}}/3 - k^3 l_{\text{cav}}^3/45 + \mathcal{O}(k^5 l_{\text{cav}}^5)]$. The first term of the expansion is identical to the expression in Eq. (12). Note that both expressions deliver a purely reactive contribution from the backing cavity. Equation (12) is used in the present study.

B. Case Configuration and Numerical Setup

The geometric configuration for the incompressible simulations as well as the definition of the boundary conditions for the unsteady CFD are illustrated in Fig. 2. The numerical domain consists of an orifice of

diameter $d_o = 4.2$ mm and thickness $l_o = 4.0$ mm, placed in a duct of diameter $d_{\text{cav}} = 50$ mm. This gives a porosity σ of the resonator front plate of 0.71%. Those dimensions have been chosen according to the Ref. [9], corresponding to the case with sharp edges, used for comparison (see Sec. II.C). The original resonator design has a cavity length of $l_{\text{sim}}/d_{\text{cav}} = 0.4$. The extension of the computational domain in the axial direction l_{sim} should be long enough to allow measurement sections to be put out of the area that is influenced by hydrodynamic fluctuations. For the investigated case described through this work, $l_{\text{sim}}/d_{\text{cav}}$ equals 10 and has been taken long to allow different measurement sections at $x/d_{\text{cav}} = [\pm 8, \pm 6, \pm 4, \pm 2]$ along the duct for assessment of the methodology. Numerically determined impedance results have been shown independent of the location of the chosen measurement sections after post-processing. This ensures that the impedance results are not polluted due to vortices crossing the measurement sections. The length $l_{\text{sim}}/d_{\text{cav}} = 2$ has been found to be sufficient for the investigated geometry at the investigated SPLs, and it reduces considerably the computational cost and time.

Figure 2 presents also the boundary conditions used for the unsteady incompressible CFD computations. The wall of the duct is defined as the slip-wall boundary condition. This assumption implies that no boundary layer develops along the duct and that the velocity profile is constant through the section. Such a hypothesis is fair, as it has been observed in various compressible studies, e.g., the large-eddy simulation (LES) computations performed by Alenius [10], that changing this boundary condition does not affect the local orifice behavior. This assumption is of importance for the present study, as it allows one to easily discard pressure losses occurring in the duct upstream and downstream of the orifice. The wall of the orifice plate is, however, prescribed as no-slip boundary condition as the resolution of the boundary layers in the vicinity of the orifice is of major importance for a correct orifice impedance estimation. The velocity is prescribed at the duct inlet boundary as a time-dependent harmonic fluctuation with zero mean. Finally, a fixed pressure boundary condition is applied to the outlet side of the duct to close the problem definition.

The present approach is limited to cases in which the hydrodynamic vortex structures are contained inside the numerical domain. As the boundary conditions for the incompressible simulations are defined through prescribed velocity and pressure values, vortices crossing the domain limits are not accounted for by boundary treatment. Violation of this rule has shown to deliver inaccurate results as the numerical problem formulation is inconsistent in that case. If vortices approach the in-/outflow boundaries, the computational domain has to be extended. This can be required for configurations with orifices of small diameter at high excitation amplitudes, as for those cases the vortices can travel far away from the production zone.

In this work, the incompressible finite-volume solver of a commercial code (ANSYS Fluent v14/v15) is used to characterize the flow. The chosen solver is pressure based, time-dependent, implicit, and second order in time and space. The pressure correction scheme applied is Semi-Implicit Method for Pressure-Linked Equations. No turbulence modeling is applied for the presented simulation results as the Reynolds number based on the orifice size and velocity fluctuation amplitude at the orifice is rather low (maximum $Re \approx 3000$ at high excitation levels). Turbulence modeling has shown very limited impact on the estimated orifice transfer impedance under the present operating conditions. Comprehensive parameter studies regarding grid, time step, and solver parameters have been performed to ensure that the presented results are independent of those numerical settings. Standard parameters for the results presented here are the minimal size of mesh cell $h_{\text{min}} = 10^{-5}$ m, time step $dt = 10^{-6}$ s, number of iterations per time step $N_{\text{iter}} = 20$. Both two-dimensional axisymmetric and three-dimensional simulations have been carried out in this work to investigate three-dimensional effects.

C. References for Validation of Method

As mentioned in Sec. I, the results computed from incompressible unsteady CFD simulations are compared to two different data sets: compressible CFD results and experimental data performed on a

particular Helmholtz resonator geometry. This paragraph describes briefly those references and the geometric definition of this particular case. More detailed on the reference works can be found in the papers [9,11].

1. Numerical Compressible Computational Fluid Dynamics Reference Data

Compressible simulations of the Navier–Stokes equations with both laminar and turbulent models (LES with the k -equation eddy-viscosity model) performed with the Pimple algorithm of OpenFOAM [12] are used for comparison [9,11]. To distinguish, for the estimated resonator acoustic impedance, between the possible differences originating from the numerical solvers and from the modeling part, both open-end tube (without accounting for the cavity backing wall) and closed-end tube (Helmholtz resonator) configurations are simulated with the compressible solver. It was also verified that the turbulence modeling leads only to very minor differences. With the turbulence model activated, the acoustic resistance increased slightly. This shows that turbulent structures as represented by the subgrid scale model do not have a significant impact on the separation mechanism itself in the chosen SPL range.

In the compressible flow simulations, the computational domain is excited from the boundary opposite to the resonator at a distance $l_{\text{sim}}/d_{\text{cav}} = 2$ by imposing a propagating characteristic wave F_r of amplitude A_f . For this purpose, the Navier–Stokes characteristics boundary condition, cf. Poinot and Lele [13], is applied. Particular care has been taken to match A_f with the value of the amplitude A_i in the incompressible flow simulations to ensure the same excitation state of the orifice in both closed and open tubes. The method to define correctly the excitation amplitude is discussed in detail in Sec. II.D. The F_r wave can be imagined as a wave traveling in the right direction toward the orifice location, whereas G_r is the reflected one traveling back to the inlet. Shortly after the inlet, area-averaged pressure and velocity fluctuations were evaluated across a reference plane to determine F_r and G_r time series to evaluate the reflection coefficient R_{num} . For those harmonically excited simulations, the reflection coefficient is determined through $R_{\text{num}}(\omega) = \hat{g}_r(\omega)/\hat{f}_r(\omega)$, with angular frequency ω . The reflection coefficient is transformed to the resonator normalized surface impedance z_r , using the relation $z_r = (1 + R_{\text{num/exp}})/(1 - R_{\text{num/exp}})$.

2. Experimental Reference Data

In addition to the numerical results, a measurement campaign has been performed by Förner et al. [9] at the Eindhoven University of Technology on a Helmholtz resonator configuration. The experiments were carried out with an impedance tube in a semi-anechoic chamber. The resonator sample was placed at one extremity of the impedance tube. The measurement data give the surface impedance of the complete Helmholtz resonator. The tube has six BSWA MPA416 microphones with the average sensitivity of 50.45 mV/Pa, equally distributed along the 1-m-long tube. The microphones have been calibrated to measure the reflection coefficient R_{exp} in the frequency range [100–700 Hz]. The numerical work will limit itself to this frequency range. The reflection behavior of the test object has been studied for various SPLs. Data for the cases 89.3 and 119.7 dB are presented here for assessment of the investigated methodology. Those SPL values are controlled over the entire frequency range at a reference position, here the closest microphone from the resonator front plate placed 49.7 mm away. The 89.3 dB case is in the linear regime, while in the 119.7 dB case, nonlinearities are present.

D. Setting Excitation Amplitudes

For the purpose of comparing results of the incompressible simulations with existing experimental data, it is necessary to ensure that the velocities in the orifice agree with each other for the different setups. This fact is also relevant for comparison with the compressible solver, as the definition of the excitation between compressible and incompressible solvers is fundamentally different. The excitation is given by a time-varying axial velocity fluctuation at the inlet boundary for the incompressible simulations, whereas it is

defined through injection of an F_r wave for the compressible ones. The reflection coefficient is therefore a key parameter to match results in the nonlinear regime. This has been found to be a challenge from a practical point of view. Drawing impedance curves from a particular resonator at a certain SPL given at a reference position can also be achieved by the present incompressible approach without any knowledge of intermediate variables such as the reflection coefficient. This requires, nevertheless, in general, several simulation trials for one case, in which the input velocity is progressively modified until the SPL matches the target one.

To compare the results from the investigated methodology to existing data sets, the following procedure has been applied, based on the relations between propagating waves F_r and G_r and primitive variables p' and u' . Below the cut-off frequency of the duct, and in the case of no mean flow, the acoustics can be described as the superposition of the Riemann invariants defined by $F_r = 1/2(p'/(\rho c) + u')$ and $G_r = 1/2(p'/(\rho c) - u')$. In the resonance tube, a standing wave is developed with a fluctuating pressure at the position x ,

$$p'(x) = \rho c[F_r(x) + G_r(x)] \quad (13)$$

In the experimental setup, the reference microphone was mounted at a distance of $l_{\text{ref}} = 0.0497$ m away from the resonator front face. This is selected as the reference position x_{ref} for the SPL. Moreover, the reflection coefficient $R = G_r/F_r$, depends on both frequency and amplitude. The reflected wave at the reference position is thus $G_r(x_{\text{ref}}) = R(\omega, \text{SPL}) \exp(-j\omega 2l_{\text{ref}}/c) F_r(x_{\text{ref}})$. Accordingly, the fluctuating pressure at position x_{ref} is given as $p'(\rho c) = [1 + R(\omega, \text{SPL}) \exp(-j\omega 2l_{\text{ref}}/c)] F_r(x_{\text{ref}})$. Considering the ratio of rms values to harmonic amplitude being $1/\sqrt{2}$, the amplitude A_f of the incoming wave $F_r = A_f \exp(j\omega t)$ is given as

$$A_f = 10^{\text{SPL}/20} \frac{\sqrt{2} p_a}{|1 + R(\omega, \text{SPL}) \exp(-j\omega 2l_{\text{ref}}/c)| \rho c} \quad (14)$$

where $p_a = 20 \mu\text{Pa}$ is the commonly used reference sound pressure in air.

The fluctuating velocity u' is given as the difference of the Riemann invariants, i.e., $u' = F_r - G_r$. Thus, the amplitude of the velocity A_u at the resonator mouth position (at $x_o = -l_o/2$ in this work) can be calculated as

$$A_{u(x_o)}(\omega, \text{SPL}) = A_f(\omega, \text{SPL}) |1 - R(\omega, \text{SPL})| \quad (15)$$

For the incompressible simulations, the inlet amplitude prescribed at the inlet boundary is directly given by Eq. (15). For the compressible simulations, in the case of the full resonator configuration, the inlet boundary condition is A_f given by Eq. (14). Finally, exchanging the backing cavity with a nonreflecting outlet ($Z = \rho c$), the amplitude of the F_r wave has to be corrected. The reflection coefficient of the corresponding orifice R_o (i.e., open tube) can be estimated as

$$R_o = \frac{z_r - z_{bc}}{z_r - z_{bc} + 2} \quad (16)$$

Thus, the amplitude of the i wave in the open-end tube configuration $A_{f,o}$ should be set as

$$A_{f,o} = A_f \frac{|1 - R|}{|1 - R_o|} \quad (17)$$

Table 1 lists the values of the different excitation amplitudes needed to ensure the same state at the orifice neck for five frequencies close to the resonator eigenfrequency and for the two investigated SPLs. As the primitive variables and Riemann variables are linked through the reflection coefficient, values of velocity at the orifice coming from the compressible simulations are still slightly different, but these deviations have been judged to have only a small impact on

Table 1 Example of inlet excitation amplitudes for F_r and u' at two different SPLs

Frequency, Hz	340	360	380	400	420
SPL = 89.3 dB					
A_f , m/s	0.0020	0.0033	0.0019	0.0013	0.0011
A_u , m/s	0.0021	0.0043	0.0024	0.0014	0.0009
$A_{f,o}$, m/s	0.0076	0.0165	0.0097	0.0057	0.0041
SPL = 119.7 dB					
A_f , m/s	0.0552	0.0601	0.0574	0.0490	0.0401
A_u , m/s	0.0411	0.0474	0.0471	0.0407	0.0295
$A_{f,o}$, m/s	0.1500	0.1823	0.1891	0.1693	0.130

the estimated impedance values. Note that in the linear regime (here at 89.3 dB), even if specific values are given in Table 1, computations give the same impedance values taking different inlet velocity amplitudes, as long as these prescribed excitation amplitudes are small enough to remain in the linear regime of the resonator.

III. Results Obtained for Small Excitation Amplitudes: Linear Regime

For harmonic pulsating flows at the orifice, the impedance value for each excitation frequency is computed by dividing the Fourier coefficients of the fluctuating pressure loss through the orifice $\Delta \hat{p}'$ with the velocity perturbation \hat{u}' . Each frequency requires therefore one CFD simulation. The harmonic fluctuating inlet velocity is given for a given angular frequency ω by

$$u'(t) = A_u \sin(\omega t) \quad (18)$$

where the amplitude of inlet velocity A_u is defined as described in Sec. II.D.

A. Resonator Impedance in Linear Regime

Figure 4 shows the obtained normalized surface impedance curves for the case SPL = 89.3 dB over the frequency range [100–700 Hz] compared to the experimental data and the values obtained from the system identification of the complete three-dimensional resonator model with the compressible solver. Impedance values are normalized by the characteristic isentropic impedance $Z_0 = \rho c$. For each simulation set, it is verified that the impedance values are independent of the measurement sections selected for determining the pressure loss.

All results show a fair agreement around the Helmholtz resonance frequency $f_{H,\text{lin}} = 372$ Hz in the linear regime. The reactance $Im(z_r)$ matches well with the experimental data over the entire frequency range. However, one can see that the discrepancies increase slightly with increasing frequency. The incompressible harmonic results lead to a better reactance prediction than the compressible solver far from the resonator eigenfrequency. The same observation can be made on the resistance $Re(z_r)$. Notice also that both experimental and compressible values present a large error far from the resonance frequency as the impedance values are obtained using the reflection coefficient R_{exp} or R_{num} , so that even a small error on the reflection coefficient gives a larger uncertainty on the impedance in such a condition. This comes from the fact that the transformation from $R_{\text{exp/num}}$ to $Re(z_r)$ is ill conditioned away from the eigenfrequency in the case of the complete Helmholtz resonator, as the magnitude of the reflection coefficient is close to unity at these frequencies. The resistance obtained by incompressible simulations seems a bit lower than experimental data, but the trend in frequency (given by the slope) is well predicted.

B. Comparison of Two Approaches in Harmonic Case

The two approaches to extract Z_o from the incompressible results, as discussed in Sec. II.A, are investigated here in the case of the linear regime with harmonically excited resonator. The difference in concept between those approaches lies in the correction of the

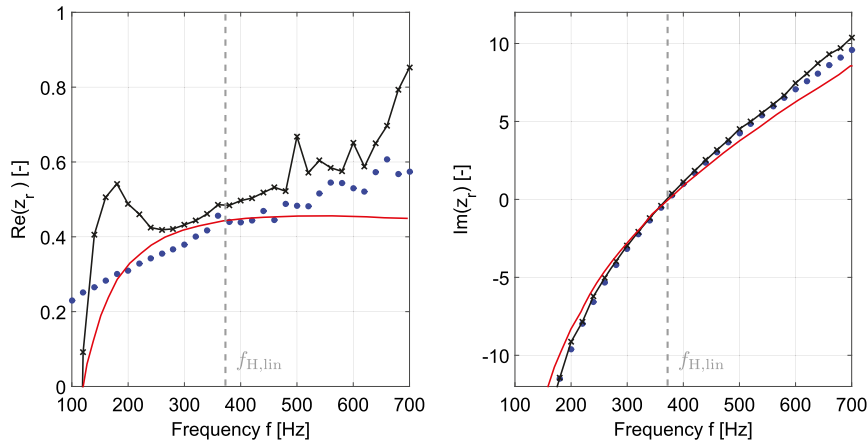


Fig. 4 Normalized resistance $Re(z_r)$ (left) and reactance $Im(z_r)$ (right) of the Helmholtz resonator, obtained with the methodology based on incompressible simulations, compared to experimental data and broadband compressible numerical results (case SPL = 89.7 dB): (•) two-dimensional incompressible, (—) three-dimensional compressible with broadband excitation, and (•×) experimental data.

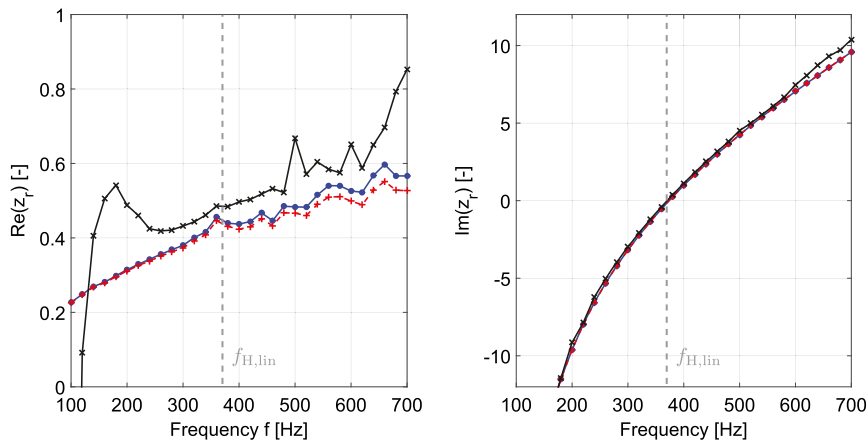


Fig. 5 Normalized resistance $Re(z_r)$ (left) and reactance $Im(z_r)$ (right) of the Helmholtz resonator evaluated from incompressible simulations with the approaches 1 and 2: (••) approach 1, (•+•) approach 2, and (•×) experimental results.

pressure losses in the duct segments: in the frequency domain (approach 1) or in the time domain (approach 2). Figure 5 shows that there is a good agreement between impedance values resulting from both approaches. The reactance values in particular are very similar. More discrepancies can be noticed on the resistive part of the impedance with the difference between the approaches growing when the frequency is increasing. It was observed that approach 2 is more sensitive to the simulation parameters (time step, mesh refinement, and dependency of the measurement section) than approach 1, but both approaches converge to the same impedance values. Approach 1 can therefore be favored for its robustness. Those conclusions drawn for the linear regime with harmonic signal excitation have been verified to be valid for the nonlinear regime and for the linear regime with broadband excitation as well.

IV. Results Obtained for Higher Excitation Amplitudes

This section presents the results obtained for higher excitation amplitudes, where flow separates at the edges of the orifice, i.e., in the nonlinear resonator regime.

A. Resonator Impedance in Nonlinear Regime

Figure 6 presents the normalized impedance obtained at a SPL of 119.7 dB from the different numerical methods performed on the investigated resonator geometry compared to the experimental data. Three-dimensional simulations have been performed with a much

shorter computational domain with $l_{sim}/d_{cav} = 2$. The three-dimensional mesh consists of nearly 1.5 million cells. Impedance results from different measurement sections have been shown to be identical.

The main conclusion from this work is that the tested numerical models, in spite of their differences in terms of physics and methodology, are in very good agreement. Nevertheless, a systematic overprediction of the resistance compared to experimental results can be seen. The discrepancy is expected to be of physical nature, as mesh/time-step influences have been discarded. The reason for this discrepancy is still under investigation. The comparison of the results for the whole resonator and the results obtained by simulating separately the orifice and the back cavity shows overall that the combined model gives very satisfying results and that this model is still valid for this range of moderately high sound amplitudes. Some small differences between the two- and three-dimensional models can be observed, but the overall impact of three-dimensional effects is rather small, although it clearly increases with increasing velocity at the orifice. The flow visualization (not shown here) suggests that the eddies dissipate in an asymmetrical manner but that this asymmetry does not influence the separation process itself. Thus, the three-dimensional effects are not important from an acoustical point of view for the considered SPLs. For the reactance, numerical and experimental data are very similar, with a very good match of all numerical results. In detail, it seems, however, that the numerical approaches underpredict to some very small extent the reactance,

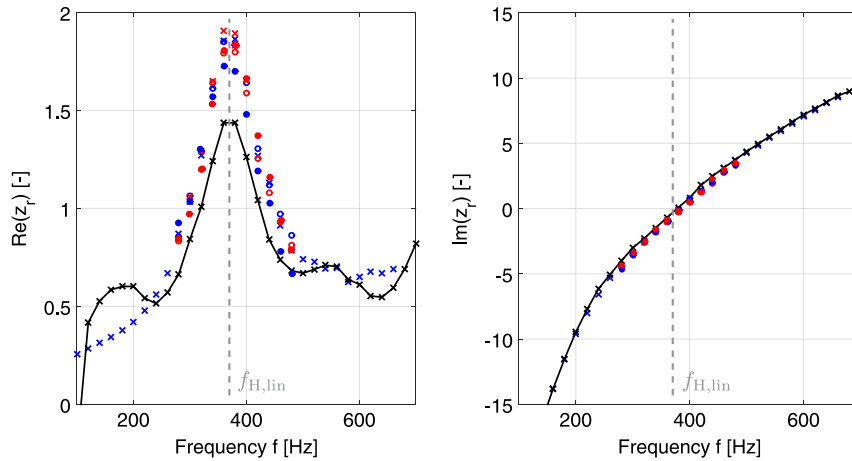


Fig. 6 Comparison of numerical results from the different solvers with experimental data for the case at 119.7 dB: (-x-) experimental results [9], (x) two-dimensional incompressible decomposed model, (o) two-dimensional compressible decomposed model, (•) two-dimensional full resonator, (x) three-dimensional incompressible decomposed model, (o) three-dimensional compressible decomposed model, and (•) three-dimensional full resonator.

giving a slightly higher resonance frequency. When compared to the previous linear regime case, one can note that the reactance is only in a minor way affected by variation of the excitation amplitude.

Complementary computations have been run for a different Helmholtz resonator geometry, based on the case studied by Hersh et al. [14] (see Fig. 12a in the referred work), to see if the overprediction in resistance is also present. For this second resonator geometry, the dimensions of the acoustic resonator are $l_o = 1.59$ mm, $d_o = 6.35$ mm, $l_{cav} = 25.4$ mm, and $d_{cav} = 50.8$ mm. Figure 7 shows the comparison of the numerical results from both incompressible and compressible numerical approaches to the experimental data of the literature. The general trends for both resistive and reactive parts with respect to increasing excitation amplitudes are correctly captured by the numerical methods. A good quantitative agreement is also obtained. A shift in the resonance frequency can be clearly observed in Fig. 7, with a growing deviation from its value in the linear regime $f_{H,lin}$ toward higher frequencies for increasing SPLs. This shift occurs due to a decrease of the reactance for increasing excitation amplitudes, which is related to a reduction of the effective length by vortex shedding [15]. Since the neck geometric length is smaller in this case than for the first resonator configuration investigated, this effect is much more visible here. The present cases correspond to high Strouhal numbers $Sh \gg 1$, with $Sh \in [25-60]$, where $Sh = d_o \sqrt{\omega \rho} / (4\mu)$ is the ratio of the Stokes layer thickness to the orifice diameter. The physical interpretation of the nonlinear impedance at such high Shear number values was shown [15] to be

more complicated than at smaller Sh , due to complex vortex shedding effects, and requires further investigation. The resistance overprediction from the numerical methods seems to be still present in this case, even if significantly less pronounced.

B. Effects of Rounded Edges

One possible reason for the systematic difference between experimental and numerical impedance results has been thought to originate from the existence of some rounding of the edges for the experimental Helmholtz resonator test sample. It was already shown in previous works [9,16] that the presence of chamfers strongly changes the structures of the produced vortices and the resistance at moderate and high excitation amplitudes. In the present study, the size of the considered chamfers is much smaller so that one can speak about microchamfers or microrounded edges. These microrounded edges are investigated as representing more realistic edges, similarly to the ones expected from manufacturing processes.

Figure 8 shows the impact of microrounded edges on the impedance for both linear and nonlinear regimes. In the linear regime, the microrounded edges affect neither the determined resistance nor reactance. This is expected as the volume of the orifice is not considerably modified by the microchamfering and therefore the reactance, related to the inertial effects, is not altered. The geometrical modification at the orifice edges does not influence the flowpath, producing no change for the pressure drop and therefore no change in the resistance, either. In the nonlinear regime, one can

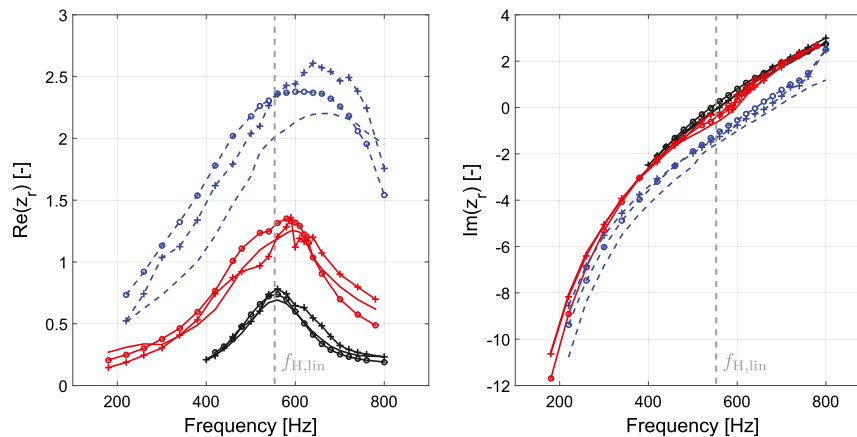


Fig. 7 Normalized resistance $Re(z_r)$ (left) and reactance $Im(z_r)$ (right) for the Hersh Helmholtz resonator configuration at three SPLs (—) 120 dB, (—) 130 dB, and (---) 140 dB, obtained from the (-+-) incompressible method, (-o-) compressible method, and (—) experimental data from Hersh [14].

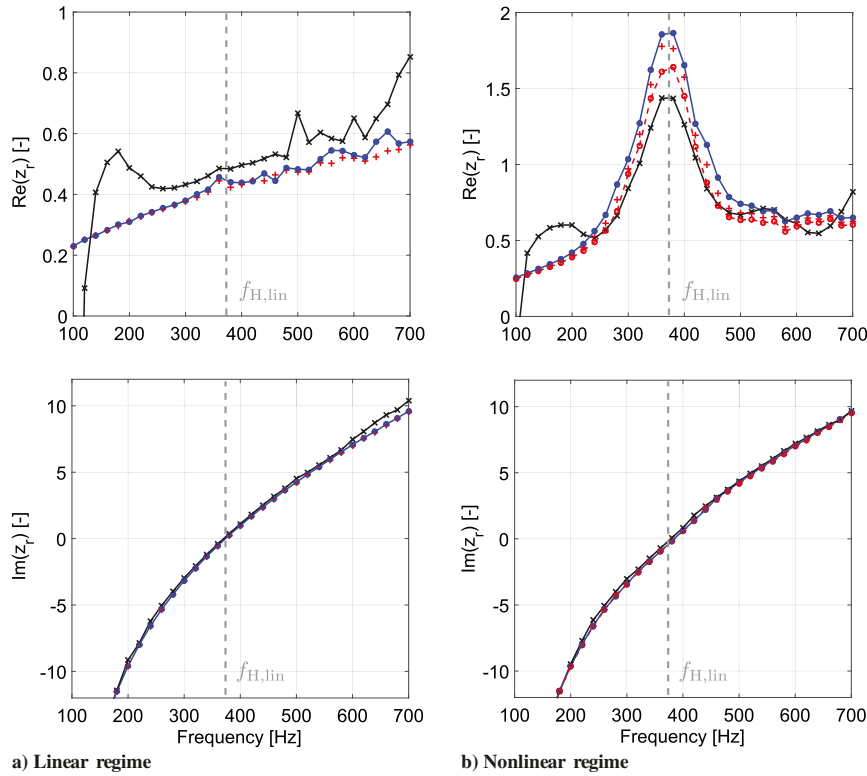


Fig. 8 Impact of edge rounding on the computed Helmholtz resonator impedance for the configuration described in Sec. II.B, in the a) linear and b) nonlinear regimes: (—●—) sharp edges incompressible, (—×—) experimental data, (+) $R_f = 40 \mu\text{m}$ rounded edges incompressible, and (—○—) $R_f = 80 \mu\text{m}$ rounded edges incompressible.

observe from Fig. 8 that even small microrounded edges can affect significantly the predicted resistance values. Results for two different rounded edge radii are shown, $R_f = 40 \mu\text{m}$ and $R_f = 80 \mu\text{m}$, respectively. These radii represent 1 and 2% of the orifice thickness. From those observations, accounting for rounded edges tends to decrease the resistance, delivering a better agreement with the experimental results. After consideration of the rounded edge radius for the actual test sample, which is found to be close to $80 \mu\text{m}$, the extent of this change for the present case seems, however, to not fully explain the observed discrepancies in resistance between the numerical and experimental approaches. A rounded edge radius larger than $120 \mu\text{m}$ would indeed be required in the simulations to equal the experimental resonance peak in resistance. No impact on the reactance can be noticed. Additional flow computations have shown that the impact of rounded edges on the impedance is captured in a similar manner for both compressible and incompressible cases, for both rounded edges and straight chamfer situations. The actual microscale geometry does not change the results significantly.

V. Conclusions

A method to numerically characterize the aeroacoustic behavior of Helmholtz resonators without mean flow has been investigated. Both linear and nonlinear regimes have been studied. A procedure to assess the present methodology, by ensuring the same velocities in the orifice as in compressible flow simulations and experiments, is described in this paper. The impedance values obtained with the incompressible computational fluid dynamics (CFD) simulation of the orifice combined with an analytical backing volume model are in good agreement with results from a compressible simulation of a complete resonator. The numerical results for the resistance in the nonlinear regime show a systematic overprediction with respect to experimental data. The impact of microrounded edges on the estimated impedance has been investigated. Even if the presence of microrounded edges was deemed insufficient to explain alone the

discrepancies, such geometrical details were found to affect significantly the computed resonator resistance and should therefore be included for accurate predictions of the acoustic behavior of Helmholtz resonators in their nonlinear regime.

The presented approach has shown, nevertheless, to give satisfying results for the acoustic impedance of Helmholtz resonators. It is an alternative for the study of the nonlinear regime of such acoustic damping systems. The proposed methodology can be applied for the study of both linear and nonlinear regimes of the Helmholtz resonator with commercial CFD software with moderate computational costs. One of the most significant advantages of this methodology is that it does not rely on the reflection coefficient to estimate the impedance (as in experiments or compressible simulations) and instead the impedance is directly computed from the pressure and velocity. Impedance curves are therefore valid on a broader frequency range than just around the resonator resonance frequency. This approach can be extended to the study of an orifice with bias or grazing flow in a straightforward manner following previous works [2,4,6]. In the no-mean-flow case, two possible approaches in the postprocessing of the orifice transfer impedance have been studied. The difference in concept between those approaches lies in the correction of the pressure losses in the duct segments: in the frequency domain (approach 1) or in the time domain (approach 2). A general conclusion is that both approaches investigated in this work lead to similar impedance prediction, but approach 1 has been shown to be more robust. Finally, the possible impact of three-dimensional effects on the impedance results presented in this work has been investigated and judged minor for the applied conditions.

Acknowledgments

The authors gratefully acknowledge the financial support from the Research Fund KU Leuven, from the European Commission provided in the framework of the EU Seventh Framework Programme (FP7) Marie Curie Initial Training Network Thermo-

acoustic and Aero-acoustic Nonlinearities in Green combustors with Orifice structures (Grant Agreement 316654) and of the FP7 Collaborative Project Integrated Design of Optimal Ventilation Systems for Low Cabin and Ramp Noise (Grant Agreement 314066) as well as from the German Research Foundation within Project A3 of the Sonderforschungsbereich Transregio 40. Furthermore, the authors thank the Leibniz Supercomputing Centre for the access to its cluster system.

References

- [1] Denayer, H., Tournadre, J., De Roeck, W., Desmet, W., and Martínez-Lera, P., "Combined Numerical and Experimental Study of a Slit Resonator Under Grazing Flow," *Proceedings of the 20th AIAA/CEAS Aeroacoustics Conference*, AIAA Paper 2014-2959, 2014.
- [2] Martínez-Lera, P., Schram, C., Föller, S., Kaess, R., and Polifke, W., "Identification of the Aeroacoustic Response of a Low Mach Number Flow Through a T-Joint," *Journal of the Acoustical Society of America*, Vol. 126, No. 2, 2009, pp. 582–586.
doi:10.1121/1.3159604
- [3] Howe, M. S., "Theory of Vortex Sound," *Cambridge Texts in Applied Mathematics*, Cambridge Univ. Press, Cambridge, England, U.K., 2003, pp. 114–132.
- [4] Nakiboğlu, G., Belfroid, S. P. C., Golliard, J., and Hirschberg, A., "On the Whistling of Corrugated Pipes: Effect of Pipe Length and Flow Profile," *Journal of Fluid Mechanics*, Vol. 672, No. 1, 2011, pp. 78–108.
doi:10.1017/S0022112010005884
- [5] Lacombe, R., Moussou, P., and Aurégan, Y., "Identification of Whistling Ability of a Single Hole Orifice from an Incompressible Flow Simulation," *Proceedings of the ASME, Pressure Vessels and Piping Conference, Fluid-Structure Interaction*, Vol. 4, ASME Paper PVP2011-57355, 2011, pp. 261–267.
doi:10.1115/PVP2011-57355
- [6] Golliard, J., González-Díez, N., Belfroid, S., Nakiboğlu, G., and Hirschberg, A., "U-RANS Model for the Prediction of the Acoustic Sound Power Generated in a Whistling Corrugated Pipe," *Proceedings of the ASME, Pressure Vessels and Piping Conference, Fluid-Structure Interaction*, Vol. 4, ASME Paper PVP2013-97385, Paris, France, July 2013, Paper V004T04A040.
doi:10.1115/PVP2013-97385
- [7] Ingard, U., and Ising, H., "Acoustic Nonlinearity of an Orifice," *Journal of the Acoustical Society of America*, Vol. 42, No. 1, 1967, pp. 6–17.
doi:10.1121/1.1910576
- [8] Keller, J., and Zauner, E., "On the Use of Helmholtz Resonators as Sound Attenuators," *Journal of Applied Mathematics and Physics*, Vol. 46, No. 3, 1995, pp. 297–327.
doi:10.1007/BF01003552
- [9] Förner, K., Temiz, M. A., Polifke, W., Arteaga, I. L., and Hirschberg, A., "On the Non-Linear Influence of the Edge Geometry on Vortex Shedding in Helmholtz Resonators," *Proceedings of the 22nd International Conference on Sound and Vibration*, The International Inst. of Acoustics and Vibration (IIAV) and the Acoustical Soc. of Italy (AIA) Paper 2015-1341, 2015.
- [10] Alenius, E., "Flow Duct Acoustics: An LES Approach," Ph.D. Thesis, Royal Inst. of Technology, Stockholm, Sweden, 2012.
- [11] Förner, K., and Polifke, W., "Aero-Acoustic Characterization of a Helmholtz Resonator in the Linear Regime with System Identification," *Proceedings of the 22nd International Conference on Sound and Vibration*, The International Inst. of Acoustics and Vibration (IIAV) and the Acoustical Soc. of Italy (AIA) Paper 2015-596, 2015.
- [12] "OpenFOAM (Open Field Operation and Manipulation)," Software Package Ver. 2.3.0, OpenFOAM Foundation, London, U.K., Feb. 2014.
- [13] Poinso, T. J., and Lele, S. K., "Boundary Conditions for Direct Simulations of Compressible Viscous Flows," *Journal of Computational Physics*, Vol. 101, No. 1, 1992, pp. 104–129.
doi:10.1016/0021-9991(92)90046-2
- [14] Hersh, A. S., Walker, B. E., and Celano, J. W., "Helmholtz Resonator Impedance Model, Part 1: Nonlinear Behavior," *AIAA Journal*, Vol. 41, No. 5, 2003, pp. 795–808.
doi:10.2514/2.2041
- [15] Temiz, A. M., Tournadre, J., Lopez-Artega, I., and Hirschberg, A., "Non-Linear Acoustic Transfer Impedance of Micro-Perforated Plates with Circular Orifices," *Journal of Sound and Vibration*, Vol. 366, No. 1, 2016, pp. 418–428.
doi:10.1016/j.jsv.2015.12.022
- [16] Laudien, E., Pongratz, R., Pierro, R., and Preklik, D., "Fundamental Mechanisms of Combustion Instabilities: Experimental Procedures Aiding the Design of Acoustic Cavities," *Liquid Rocket Engine Combustion Instability*, AIAA, Washington, D.C., 1995, pp. 377–399.

P. G. Tucker
Associate Editor



ON THE NON-LINEAR INFLUENCE OF THE EDGE GEOMETRY ON VORTEX SHEDDING IN HELMHOLTZ RESONATORS

Kilian Förner¹†, Muttalip Aşkın Temiz², Wolfgang Polifke¹, Ines Lopez Arteaga², and Avraham Hirschberg³

¹*Professur für Thermofluidodynamik, Technische Universität München, Germany*

† *e-mail: foerner@tfd.mw.tum.de*

²*Eindhoven University of Technology, Dept. of Mechanical Engineering, Eindhoven, The Netherlands.*

³*Eindhoven University of Technology, Dept. of Applied Physics, Eindhoven, The Netherlands.*

This study investigates the effect of edge profile of a Helmholtz resonator neck in non-linear regime by means of experiments and large eddy simulations. The dissipation mechanisms in a Helmholtz resonator differ significantly, depending on the sound pressure level. At low levels, i. e., in the linear regime, thermo-viscous effects are responsible for the dissipation of the acoustic energy since the oscillating flow follows the neck geometry. However, increasing the sound pressure level results in flow separation at the edges. At these points, vortices form which convert acoustic perturbation energy to the hydrodynamic mode. This is a strong non-linear effect increasing the dissipation considerably. To observe this effect, experiments and numerical simulations are carried out for combinations of various backing volumes, sound pressure levels, and neck profiles. The neck profiles are selected as 45°-chamfers due to manufacturing concerns. Hereby, a strong dependence on the edge shape is observed in both experiments and numerical simulations. The presence of the chamfer reduces the vortex shedding in comparison to the sharp edge significantly, which leads to a lower acoustic resistance.

1. Introduction

Helmholtz resonators are passive sound absorbers having a wide range of application areas from ancient Greek theaters [1] to aerospace industry [2]. These resonators are named after the first scientist to analyze them theoretically: Hermann von Helmholtz [3].

A Helmholtz resonator is a combination of an air *backing volume* and an opening, which is referred to as the *neck* of the resonator. When excited by a pressure perturbation, the air volume acts as a spring due to its compressibility and causes oscillation of the air in the neck. This spring-mass model is introduced by Rayleigh [4] simplifying Helmholtz's pioneer work. Later, Ingard and Labate [5] observed that there are two main dissipation mechanisms in the Helmholtz resonators. The first is due to thermo-viscous boundary layers, which is linear; and the other one is due to vortex shedding, which is non-linear. This non-linear dissipation effect is addressed by Ingard and Ising [6]. They considered the neck separately, performed pressure as well as particle velocity measurements, and observed that this non-linear mechanism causes a decrease in the reactance of the oscillating air within the neck.

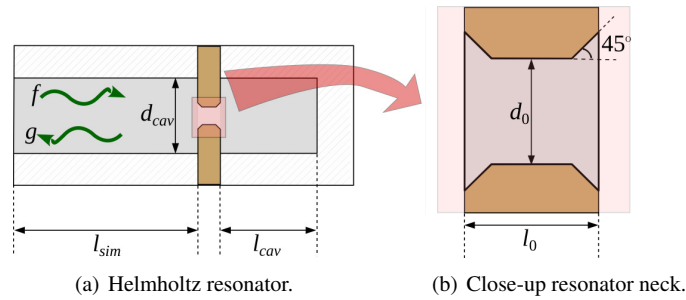


Figure 1: Sketch of the Helmholtz resonator geometry.

In 1979, Hersh *et al.* [1] derived non-linear differential equations to model the non-linear response of the Helmholtz resonators. Yet none of the studies mentioned so far focuses on the effect of the edge profile of the neck on the non-linearity of the resonator. In similar configurations, a huge impact of the edge geometry was observed, see, e. g., the study for a resonance tube by Disselhorst and van Wijngaarden [7].

In this study, three different neck samples are used. One of these samples has the sharp and other two have the 45°-chamfered edge profile in combination with different chamfer lengths. The purpose of the study is to understand the effect of edge profile of the neck on the non-linear response of the Helmholtz resonator. To achieve this purpose, large eddy simulations (LES) and impedance tube measurements are carried out. The geometry of the Helmholtz resonator domain is sketched in Fig. 1.

2. Modeling of Helmholtz Resonators

The dynamic behavior of the Helmholtz resonator is commonly described in frequency domain with its *surface impedance* Z_s . The impedance is defined as the ratio of the Fourier transforms of the fluctuating pressure \hat{p}' to the fluctuating velocity \hat{u}' , i. e., $Z_s(\omega) = \hat{p}'(\omega)/\hat{u}'(\omega)$. Thus, the impedance Z_s can be seen as transfer function from u' to p' . The real part of the impedance is referred to as the so-called *resistance* and the imaginary as *reactance*. Such a description in frequency domain is actually only valid for linear transfer functions. The non-linear dynamic response of resonators is commonly given by describing functions. That means that the impedance is defined depending on the amplitude. This approach neglects higher harmonics. Nevertheless, it reflects the major dynamics well. As mentioned above, the behavior of the resonator is often described as mass-spring-damper system and reads as

$$(1) \quad Z_s(\omega) = R_l + R_{nl} + i(m\omega - K/\omega).$$

Here, the term m accounts for the mass in the neck taking part in the oscillation and K for the compressibility of the backing volume. The variable R_l denotes the linear resistance reflecting for the thermo-viscous losses due to friction at the walls of the neck. If the amplitudes are large enough, the flow separates at the edges transforming additional energy to the hydrodynamic mode from the acoustic mode, which is irrotational by definition. This is a non-linear mechanism depending on the current amplitude and is captured by the term R_{nl} . All terms in Eq. (1) are determined by analytical models but they also contain some empirical correlation values. According to Keller and Zauner [8] and Garrison *et al.* [9], they are approximately given as

$$(2) \quad m = (1 + s) l_e \bar{\rho}, \quad K = \frac{A \bar{\rho} c^2}{V}, \quad R_l = s \bar{\rho} (l_0 + l_s) \omega, \quad \text{and} \quad R_{nl} = \epsilon_{nl} s \bar{\rho} d_0 \omega,$$

where the mean pressure, density, and speed of sound are denoted by \bar{p} , $\bar{\rho}$, and c , respectively. The geometry is described by the backing volume V as well as by the neck area A , and length l_0 . The

boundary layer effects are included in the parameter s^1 . The effective mass oscillating around the neck is determined by adding a correction to the neck length. Similarly for the viscous losses, l_0 is extended by l_s . The non-linear losses are captured by the non-linear correlation factor ϵ_{nl} . The angular eigenfrequency of the resonator is given as the ratio of m to K , thus $\omega_{eig} = c \sqrt{A/(V(1+s)l_e)}$. In the following, the impedance Z_s is normalized by the free impedance $\bar{\rho}c$, i. e., $Z = Z_s/(\bar{\rho}c)$.

In the resonance tube located in front of the resonator, the acoustic field can be described by the Riemann invariants defined as $f = 1/2(p'/(\bar{\rho}c) + u')$ and $g = 1/2(p'/(\bar{\rho}c) - u')$ and depicted in Fig 1. In terms of these quantities, the impact of the Helmholtz resonator is determined by the reflection coefficient $R = g/f$. The relation between this coefficient R and the normalized impedance Z is given by $Z = (1 + R)/(1 - R)$.

3. Setup

Several test cases are investigated both numerically and experimentally. These cases consist of combinations of three different neck profiles and two different backing volume lengths l_{cav} in a resonance tube with diameter d_{cav} . The considered necks have the same length l_0 and diameter d_0 but differ in their edge profiles. One of the necks has a sharp edge ($l_c = 0$) where the other two have 45°-chamfers with different sizes l_c . The geometrical specifications are given in Tab. 1. The reflection behavior of these test cases is studied for various SPLs, in particular for 89.3, 115.6, and 119.7 dB.

Table 1: Geometric properties (in mm).

Considered chamfer lengths			Volume lengths		Common parts		
l_c	l_c	l_c	l_{cav}	l_{cav}	l_0	d_0	d_{cav}
0	0.35	1.0	10	20	4.0	4.2	50

3.1 Experimental Setup

The experiments have been carried out with an impedance tube in an semi-anechoic chamber. The tube has six BSWA MPA416 microphones with the average sensitivity of 50.45 mV/Pa. They are equally distributed along the 1-m long tube and the distances between two successive microphones are 175 mm. The microphones are relatively calibrated to carry out reflection coefficient measurements from 100 Hz to 700 Hz. The inner diameter of the tube, d_{cav} , is 50 mm.

The data acquisition and signal processing is done by a combination of NI PCIe-6361 X-Series DAQ card and LabView[®]. One analogue output channel for the loudspeaker and six analogue input channels for microphones are used. The sampling rate for generated signal is 20 kHz while it is 10 kHz for recording. The closest microphone to the tube termination is selected as the reference input. The LabView[®] script regulates the excitation amplitude of the loudspeaker for each frequency step. Doing so, it is possible to have the same – or very close – SPLs throughout the entire frequency span. It is important to note here that this reference microphone is placed 49.7 mm away from the tube termination. Accordingly, the SPLs are calculated at this position. The reference position would ideally be located at the resonator mouth, but due to physical constraints, placing a microphone at that position was not possible in this setup.

Some precautions are taken to minimize the measurements errors. First, the recorded data from the microphones are processed using a lock-in method instead of using FFT. Secondly, the visco-thermal effects in the tube are included [10] and implemented in the wave decomposition [11]. Finally, instead

¹ $s = (1 + (\kappa - 1)/\sqrt{Pr})\sqrt{2\nu/\omega}/d_0$, where the variables Pr , κ , and ν denote the Prandtl number, the heat capacity ratio, and the kinematic viscosity, respectively.

of assuming a value for the speed of sound, it is treated as an extra unknown in the over-determined set of equations [12]. With all these specifications and precautions, the deviation from the theoretical closed-end reflection coefficient value is less than 0.5 % in the frequency of interest.

3.2 Numerical Setup

The compressible Navier-Stokes equations with k-equation eddy-viscosity subgrid-scale model are solved in 3D using the Pimple algorithm of OpenFOAM [13]. The tolerance for stop criterion for outer iteration loops accounting for compressible pressure-velocity coupling are set low – i. e., accurate – enough to resolve the acoustic field in details. Here, a threshold for the pressure residual of 10^{-5} was applied. The time step size Δt is adjusted such that the acoustic CFL number $c \Delta t / \Delta x$ is clearly below unity in the main parts. Only close to the walls, this number can be slightly larger, but the acoustic behavior is still resolved accurately in those regions due to implicit time integration.

The geometrical dimensions of the neck configurations and of the backing volumes are set in analogy to the experimental setup properties summarized in Tab. 1. At the corresponding boundaries, the no-slip condition is utilized. The slip condition is used at the cylindrical wall of the impedance tube which does not belong to the resonator itself. For each geometry investigated, a structured o-grid mesh with at least 0.8 million cells is set up. Hereby especially, the boundary layer, whose thickness can a priori be estimated by the Stokes length $\delta_s = 2\pi \sqrt{2\nu/\omega}$, must be resolved well for the frequencies of interest. In the linear regime, grid independence studies and validation have proved the appropriateness of such a setting, see [14].

At the distance $l_{sim} = 10$ cm, the inlet patch is located, where the Navier-Stokes characteristics boundary condition (NSCBC), c. f. [15], is applied. This boundary condition ensures a low acoustic reflection of the outgoing g wave. Simultaneously, an input signal can be imposed for the incoming f wave. At this inlet plane, the fluctuating pressure p' and velocity u' are measured. From these quantities, the time series of the Riemann invariants f and g can be computed directly. For that purpose, the distance l_{sim} is chosen large enough such that non-acoustic disturbances as the vortices present in the vicinity of the neck do not influence the measurement.

The reflection coefficient is estimated from the measured input f and output g time series. First, these time series are shifted with respect to each other to account for the time it takes to travel from the reference plane to the resonator and back. Then for the identification, two approaches are applied depending of the present regime. In the linear regime corresponding to a low SPL as 89.3 dB, linear system identification techniques are used. Here, the domain is excited with a well-designed broadband signal. From the response, a second order Output-Error model is estimated, valid for the whole frequency range of interest [14]. In the non-linear regime with higher amplitudes, harmonic simulations are performed with several angular frequencies ω_m . For the determination of the numerical $R_{num}(\omega_m) = \text{fft}(g)(\omega_m) / \text{fft}(f)(\omega_m)$, the signals are additionally truncated to get rid of the transient starting behavior and to have a signal length of a multiple of the period $1/(2\pi \omega_m)$. The amplitude of the input signal f is calculated according to the the experimental data.

4. Results

Gain and phase of the reflection coefficient are presented for the SPLs investigated for all cases with $l_{cav} = 20$ mm in Fig. 2. The reflection coefficient is transformed to the normalized surface impedance Z , using the relation $Z = (1 + R)/(1 - R)$ and plotted in Fig. 3. Due to lack of space, only the results for the backing volume with 20 mm length are shown in the present paper. The following discussions and findings are equally supported by the other cases with 10 mm backing volume length.

For all geometries, experiment and simulation agree very well in the linear regime. The evaluation of the 89.3 dB simulations confirms that the flow does not separate at the edges. That means that the Stokes boundary layer is resolved sufficiently in the simulations to capture the thermo-viscous dissipation taking place in that region. In the non-linear regime, the agreement is only of qualitative, but

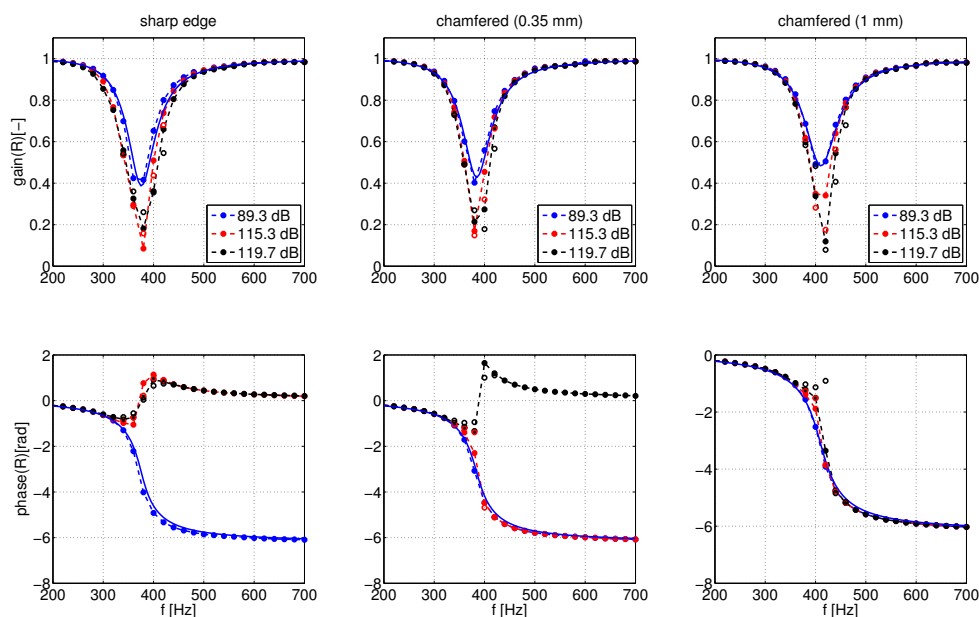


Figure 2: Reflection coefficient in gain and phase representation for all configurations with $l_{cav} = 20$ mm. "—●—": measurement results; "—": linear SI results; and "○": harmonic simulation results. The colors correspond to different SPLs as indicated by the legends in the subfigures.

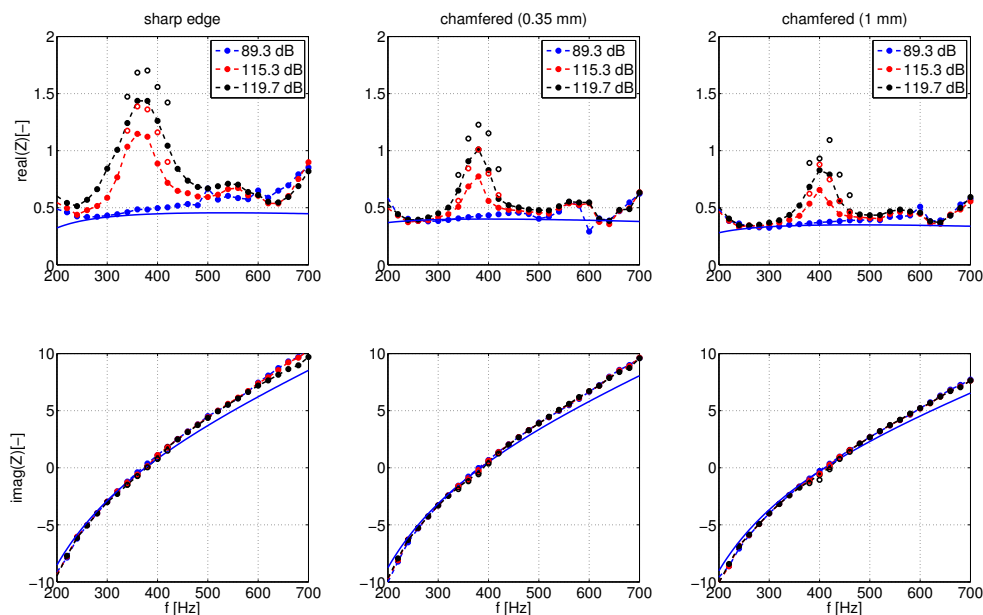


Figure 3: Normalized impedance determined in resistance and reactance representation for all configurations with $l_{cav} = 20$ mm. "—●—": measurement results; "—": linear SI results; and "○": harmonic simulation results. The colors correspond to different SPLs as indicated by the legends in the subfigures.

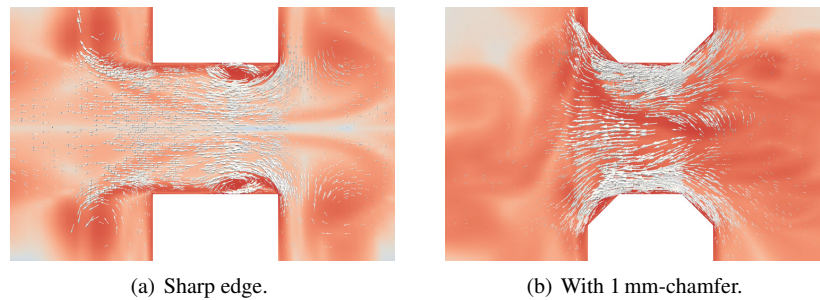


Figure 4: Snapshots of the velocity field (white arrows) in the neck during the outflow with 119.7 dB.

not of quantitative nature. The reactance $\Im(Z)$ curves still match for all cases and amplitudes in that regime. But, the non-linear resistance is systematically over-predicted by the numerical simulations for all cases. The reason for this over-prediction is topic of ongoing research. The grid dependency as well as the influence of the sub-grid scale modeling have to be studied in more detail. Another reason might be that the edges are perfectly sharp in the simulation, whereas they are not in reality. Nevertheless, the simulations provide a detailed view on the flow present in the resonator. The following statements are confirmed by both experiment and simulation in the same manner.

First, the influence of the edge geometry on the eigenfrequency is discussed. This is a linear effect and, thus, independent on the current SPL. Only for very high amplitudes beyond the SPL considered in this study, the eigenfrequency is nominally influenced by the amplitude, see for instance [1]. The eigenfrequency can be detected by the minimal gain of the reflection coefficient. The corresponding phase is either $-\pi$ in the non-over-damped case or 0 in the over-damped case. Moreover, the reactance $\Im(Z)$ vanishes at the eigenfrequency. With these criteria, a shift of the eigenfrequency towards higher frequencies with increasing the chamfer size can be observed. In the specific case of 20 mm cavity length, the eigenfrequency rises from around 375 Hz without a chamfer, to approximately 385 Hz and 410 Hz with the 0.35 mm and 1 mm-chamfer, respectively. This shift can be explained by a reduction of the effective length with increasing the chamfer length. For the three cases, the resulting effective length are 7.19 mm, 6.82 mm, and 6.02 mm, respectively. The detected effective length of the unchamfered case go in line with the correlation by Ingard [16]. He suggested for large aspect ratios ($d_0/\sqrt[3]{V} \ll 1$) an end correction of $8/(3\pi)d_0$, which would lead to an effective length of 7.56 mm. The observed reduction of the effective length with non-sharp edges has already been seen by other authors, see, e. g. [8]. In the analogy of the mass-spring-damper system discussed in Sec. 2, this means that less mass in the neck is taking in the oscillation with increasing the chamfer size.

Moreover, a reduction of the non-linear resistance can be observed in the presence of a chamfer. As discussed in Sec. 2, the non-linear resistance results from the flow separation the resonator edges. Two velocity field snapshots during the outflow for a sharp and a 1-mm-chamfered edge case with 119.7 dB excitation are presented in Fig. 4. In the sharp edge case visualized in Fig. 4(a), it can be observed that the flow separates at both the inner and the outer edge. Two large recirculation zones are temporally formed downstream of the respective edge. One of these zones is located in front of the resonator mouth and the other in the neck. Chamfering the sharp edges produces four obtuse edges that cause the flow to separate with smaller recirculation zones; see Fig. 4(b). The observed contraction of the stream motivates a comparison with the quasi-static theory including the vena contracta effect. The vena contracta for large amplitudes for sharp edges is about 0.70 while it is 0.95 for chamfered edges [17]. Since the non-linear losses scale approximately linear with the square of the jet velocity, the non-linear residence is inversely proportional to the square of the vena contracta factor. This explains the observed difference in the non-linear residence for high amplitudes by a factor of around two, see Fig. 3 and discussion below.

In the non-linear regime, increasing the amplitude always promotes the separation and, thus, leads to higher non-linear losses. This results in larger resistance values for higher excitation amplitudes in all cases, see Fig. 3. If the resonator is normally damped, the normalized acoustic resistance $\Re(Z)$ is below unity – the optimal resistance value for normal incident acoustic waves, i. e., $\Re(Z) < 1$. In that case, the increase of the acoustic resistance leads to a lower gain of the reflection coefficient, as it can be seen in the right columns of Figs. 2 and 3. This lower gain means that a higher proportion of the acoustic energy is dissipated. The situation changes in the over-damped case where $\Re(Z) > 1$ (c. f. left column in Figs. 2 and 3): Here, the additional non-linear resistance leads to a decrease in absorption. The normal and over-damped cases can also be distinguished by the examination the phase curve of the reflection coefficient $\angle R$. These phase angles differ from each other close to the eigenfrequency. In the over-damped case, it is 0 whereas it is $-\pi$ in the normal damped case. In both cases, the waves f and g are in phase – i. e., $\angle R = 0 \pmod{2\pi}$ – away from the eigenfrequency.

With the 1 mm-chamfer, none of the investigated SPLs lead to an over-damped behavior, whereas both non-linear cases are in the over-damped region for the sharp edge geometry. Notice that not only the non-linear but also the linear resistance varies with the edge profile. For instance, linear resistance decreases by 11% and 22% for the cases of 0.35 mm and 1.0 mm-chamfers, respectively. This shows that increasing the chamfer size reduces the thermo-viscous effect around the neck. Yet the impact on the resistance becomes more striking in the non-linear regime caused by a reduction of shedding. With the 0.35 mm-chamfer, the non-linear resistance is reduced by approximately 47% and 55% for the 115.3 dB and 119.7 dB case, respectively. A reduction of 57% and 70% is measured with the 1 mm-chamfer. The stated values correspond to experimental data. The magnitudes are similar for the simulation. Mainly, the presence of a chamfer reduces the non-linear losses significantly. The actual length of the chamfer also influences this reduction but in a minor manner. Moreover, it can be observed that the relative reduction is larger for higher SPL. This fits well to the above discussed flow properties: the strong separation with its large recirculation zones causes the high non-linear acoustic absorption in the sharp edge case. Much less energy is taken from the acoustics by the four separation areas with little recirculation in the chamfered case. The separation process itself is mainly determined by the sharpness of the edge.

5. Conclusion and Outlook

The influence of the edge shape of a Helmholtz resonator has been investigated by means of both experiments and LES simulations. To study this influence, various combinations of necks with different chamfer sizes and backing volumes have been considered. By variation of the SPL, the linear regime, where thermo-viscous losses are dominant, as well as the non-linear regime, where vortex shedding leads to additional losses, have been included.

In the linear regime, the results obtained from both methods match very well. The results agree qualitatively in the non-linear regime as well, even though the absolute values slightly disagree. The simulations overpredict the non-linear resistance. The reason for this disagreement is topic of ongoing research. Nevertheless, the following statements are supported equally by both the experimental and numerical investigations.

By increasing the chamfer size, a shift towards higher eigenfrequency frequencies has been observed. This shift occurs due to the fact that the oscillating mass in the neck is reduced, i. e., the effective length is shortened. This reduction is in good agreement with other correlation available in the literature.

Another important observation is that a chamfered edge profile reduces the vortex shedding in the resonator neck significantly. Depending on the SPL, the chamfered edge profile reduces the non-linear resistance about the half of its value compared to the sharp edge case. This reduction is mainly due to presence of the chamfer, but depends only weakly on its length. To the authors' knowledge, this is the first time that this effect has been quantified for the Helmholtz resonator.

Acknowledgments

Financial support has been provided by the German Research Foundation (Deutsche Forschungsgemeinschaft – DFG) in the framework of the Sonderforschungsbereich Transregio 40, Project A3. The presented work is part of the Marie Curie Initial Training Network Thermo-acoustic and aero-acoustic non-linearities in green combustors with orifice structures (TANGO). We gratefully acknowledge the financial support from the European Commission under call FP7-PEOPLE-ITN-2012. Furthermore, the authors would like to thank the Leibniz Supercomputing Centre (LRZ) for the access to its cluster system.

REFERENCES

1. Hersh, A. S., Walker, B. E. and Celano, J. W. Helmholtz Resonator Impedance Model, Part 1: non-linear Behavior. *AIAA Journal*, **41**(5), 795–808, (2003).
2. Tang, P. K. and Sirignano, W. A. Theory of a Generalized Helmholtz Resonator. *Journal of Sound and Vibration*, **26**(2), 247–262, (1972).
3. Helmholtz, H. L. F. *On the Sensations of the Tone As a Psychological Basis for the Theory of Music (Third Edition)*, Longmans, Green and Co., Chp. 3, (1895).
4. Rayleigh, J. W. S. *The Theory of Sound (Second Edition)*, Macmillan and Co., Chp. XVI, (1896).
5. Ingard, U. and Labate, S. Acoustic Circulation Effects and the non-linear Impedance of Orifices, *Journal of Acoustical Society of America*, **22**(2), 211–218, (1950).
6. Ingard, U. and Ising, H. Acoustic Nonlinearity of an Orifice, *Journal of Acoustical Society of America*, **42**(1), 6–17, (1967).
7. Disselhorst, J. H. M. and van Wijngaarden, L. Flow in the exit of open pipes during acoustic resonance, *Journal of Fluid Mechanics*, **99**, 293–319, (1980).
8. Keller, J. J. and Zauner, E. On the Use of Helmholtz Resonators as Sound Attenuators, *Zeitschrift für angewandte Mathematik und Physik ZAMP*, **46**(3), 297–327, (1995).
9. Garrison, G. D., Schnell, A. C., Baldwin, C. D. and Russell, P. R. Suppression of Combustion Oscillations with Mechanical Damping Devices, *Interim Report PWA FR-3299, Pratt & Whitney Aircraft*, (1969).
10. Peters, M. C. A. M., Hirschberg, A., Reijnen, A. J. and Wijnands, A. P. J. Damping and reflection coefficient measurements for an open pipe at low Mach and low Helmholtz numbers, *Journal of Fluid Mechanics*, **256**, 499–534, (1993).
11. Jang, S.-H. and Ih, J.-G. On the multiple microphone method for measuring in-duct acoustic properties in the presence of mean flow, *Journal of Acoustical Society of America*, **103**(3), 1520–1526, (1998).
12. Aurégan, Y. and Leroux, M. Failures in the discrete models for flow duct with perforations: An experimental investigation, *Journal of Sound and Vibration*, **265**, 109–121, (2003).
13. OpenFOAM (Open Field Operation and Manipulation), see <http://www.openfoam.org>.
14. Förner, K. and Polifke, W. Aero-Acoustic Characterization of Helmholtz Resonators in the Linear Regime with System Identification *Proceedings of the 22th International Congress on Sound and Vibration*, (2015).
15. Polifke, W., Wall, C. and Moin, P. Partially Reflecting and Non-Reflecting Boundary Conditions for Simulation of Compressible Viscous Flow, *Journal of Computational Physics*, **213**, 437–449, (2006).
16. Ingard, U. On the Theory and Design of Acoustic Resonators, *Journal of Acoustical Society of America*, **25**(6), 1037–1061, (1953).
17. Blevins, R. D. *Applied Fluid Dynamics Handbook*, Van Nostrand Reinhold, NY, (1984).

Scattering to Higher Harmonics for Quarter-Wave and Helmholtz Resonators

K. Förner*

Technische Universität München, 85748 Garching, Germany

J. Tournadre[†] and P. Martínez-Lera[‡]

Siemens, 3001 Leuven, Belgium

and

W. Polifke[§]

Technische Universität München, 85748 Garching, Germany

DOI: 10.2514/1.J055295

The nonlinear response of acoustic resonators is investigated over a broad range of frequencies and amplitudes. Helmholtz resonators with a symmetric neck and an asymmetric neck, respectively, as well as quarter-wave resonators are considered. Describing functions for impedance and the reflection coefficient of a Helmholtz resonator at various sound pressure levels are determined from compressible flow simulation and validated against experimental data. The particular focus of the present study is the nonlinear scattering to higher harmonics. For the Helmholtz resonator with a symmetric neck, a distinct pattern in the amplitudes of the higher harmonics is observed, where the odd harmonics dominate the response, whereas the even harmonics are almost negligible. Such an “odd-harmonics-only” pattern, which was observed previously in an experiment at the orifices, is explained by a quasi-steady analysis based on the Bernoulli equation, assuming a symmetric flow pattern at the neck. For the Helmholtz resonator with an asymmetric neck, it is observed in computational fluid dynamics simulations that even harmonics contribute noticeably to the resonator response, such that the odd-harmonics-only pattern is less pronounced. For the markedly asymmetric geometry of the quarter-wave resonator, the second harmonic is dominant and the odd-harmonics-only pattern vanishes completely. The quasi-steady analysis is extended successfully to also describe nonlinear scattering to higher harmonics for asymmetric configurations and flow patterns. Overall, the scattering to higher harmonics remains on a moderate level, even at very high excitation levels for the Helmholtz resonator configurations. For the quarter-wave resonator, the scattering is more pronounced and contributes perceptibly to the response at high excitation amplitudes.

Nomenclature

A_f, A_u	=	input amplitudes, m/s
A_0	=	cross-section area of the orifice, m ²
C_d	=	contraction factor
c_0	=	speed of sound, m/s
d_{cav}	=	backcavity diameter, m
d_0	=	neck diameter and quarter-wave resonator diameter, m
f, g	=	Riemann invariants, m/s
l_c	=	reference length defined in Eq. (4), m
l_{cav}	=	backcavity length, m
l_{ch}	=	chamfer length, m
l_e	=	effective length, m
l_0	=	neck thickness and quarter-wave resonator length, m
i	=	imaginary unit $\sqrt{-1}$
p	=	pressure, Pa
p_c	=	reference pressure defined in Eq. (3), Pa
p_{ref}	=	reference pressure for the calculation of the sound pressure level; 20 μ Pa

p_{rms}	=	root mean square of the overall pressure, Pa
R	=	reflection coefficient
t	=	time, s
t_c	=	reference time defined in Eq. (3), s
u'_0	=	fluctuating velocity in the neck, m/s
u'	=	fluctuating velocity in the resonator tube, m/s
Z, z	=	acoustic impedance (nonnormalized and normalized), Nsm ⁻³
Δp	=	pressure loss, Pa
ρ_0	=	density, kg/m ³
σ	=	open area ratio
ϕ	=	acoustic velocity potential, m ² /s
ω_{eig}	=	resonator angular eigenfrequency, rad/s
ω_0	=	fundamental angular frequency, rad/s

Superscripts

AJ	=	quantity corresponding to the area jump
HR	=	quantity corresponding to the Helmholtz resonator
QW	=	quantity corresponding to the quarter-wave resonator
$\hat{}$	=	Fourier transformed variable
\sim	=	nondimensional quantity
$\tilde{}$	=	acoustic fluctuating part of the variable

Presented as Paper 2016-2968 at the 22nd AIAA/CEAS Aeroacoustics Conference, Lyon, France, 30 May–1 June 2016; received 18 April 2016; revision received 29 August 2016; accepted for publication 7 September 2016; published online 8 December 2016. Copyright © 2016 by Wolfgang Polifke. Published by the American Institute of Aeronautics and Astronautics, Inc., with permission. All requests for copying and permission to reprint should be submitted to CCC at www.copyright.com; employ the ISSN 0001-1452 (print) or 1533-385X (online) to initiate your request. See also AIAA Rights and Permissions www.aiaa.org/randp.

*Ph.D. Student, TUM, Professur für Thermofluidynamik, Boltzmannstraße 15.

[†]Ph.D. Student, Researchpark 1237, Interleuvenlaan 68; also KU Leuven, Department of Mechanical Engineering, Celestijnenlaan 300B.

[‡]Senior RTD Engineer, Researchpark 1237, Interleuvenlaan 68.

[§]Full Professor, TUM, Professur für Thermofluidynamik, Boltzmannstraße 15.

I. Introduction

ACOUSTIC resonators are used in various industrial applications to reduce sound emission [1] or to avoid thermoacoustic instabilities [2,3]. Two basic types of such resonators are the Helmholtz and the quarter-wave resonators [4], which are sketched in Fig. 1.

The scattering behavior of such resonators is investigated in this study under ambient conditions without mean flow. During operation in industrial applications, the scattering behavior of resonators can be strongly influenced by the working conditions. Some of these

influencing effects are listed here. In most applications, a grazing flow over the resonators is present. This can cause a shift in the resonator eigenfrequency and has an impact on the resistance. This has been studied, e.g., experimentally by Jones et al. [5] and numerically by Zhang and Bodony [6]. Especially in gas turbines, resonators are often purged to guard them from the hot gas in the combustion chamber and to guarantee constant working conditions. Moreover, this increases the acoustic losses significantly; see, for instance, the work of Eldredge and Dowling [7], Bellucci et al. [8], or Scarpato et al. [9]. When the amplitude of the acoustic excitation rises and the purging flow rate is too low, hot gas can penetrate the resonator opening. This can detune the resonator and should thus be avoided; see, e.g., the studies by Čosić et al. [10] and Rupp et al. [11].

The present study will be based on two approaches: computational fluid dynamics (CFD) and one-dimensional (1-D) quasi-steady analysis. CFD simulations were performed by Tam et al. [12–14]. In a series of papers [12–14], they studied slit and Helmholtz resonators using direct numerical simulation (DNS) techniques: first, in a two-dimensional (2-D) setup; and later, in a 3-D configuration. The DNS approach was also pursued by Zhang and Bodony, who studied the influence of laminar and turbulent grazing flows [6,15] and the interaction between neighboring cavity openings [16]. Mendez and Eldredge [17] determined the influence of purging flow via large-eddy simulations (LESs). The LES approach is also followed in the present study. Moreover, the linearized Navier–Stokes equations can be used to investigate the linear response of a resonator, as was done by Tournadre et al. [18] for the investigation of temperature effects. An alternative approach to those explicitly solving the Navier–Stokes equations is the Lattice Boltzmann method, which is based on particle collision models and promises a low numerical cost; see, for instance, the work of Ji and Zhao [19]. Another alternative is to characterize an orifice (corresponding to the resonator neck) by incompressible simulations and add the contribution of the compressible backing volume analytically [20].

On the side of the analytical modeling of Helmholtz resonators, a 1-D semiempirical quasi-steady approach is followed in the present study, as is often done in the literature. The idea of this ansatz is to analyze the Helmholtz resonator decomposed in an acoustically compact orifice and a compressible backing volume. The motion of the fluid in the neck can then be described by a 1-D quasi-steady equation containing semiempirical correlations; see the studies by Ingard [21], Ingard and Ising [22], Melling [23], Cummings [24], Hersh et al. [25], as well as Singh and Rienstra [26].

Physically, resonators dissipate acoustic energy due to the thermoviscous losses at the walls. It is well known that, for sufficiently high excitation amplitudes, additional acoustic energy is absorbed due to flow separation at the resonator edges. Flow separation processes are very sensitive to the edge shape. The edge shape impact was investigated for open-end pipes by Disselhorst and Wijngaarden [27], as well as Atig et al. [28]. Temiz et al. [29] investigated this effect for orifice configurations. Its influence on the resonator impedance was evaluated by Laudien et al. [30] and Förner et al. [31].

The acoustic dissipation by flow separation is a nonlinear phenomena. Its nonlinear behavior can be detected by two aspects for

a harmonic excitation: On the one hand, the amplitude and phase of the reflected wave at the frequency of excitation may depend on the amplitude of the excitation. This behavior can be described in terms of describing functions for the resonator impedance or its reflection coefficient; see, for instance, the work of Hersh et al. [25] and Singh and Rienstra [26], or the Appendix of the present paper. On the other hand, scattering of acoustic energy to other frequencies may occur. To the authors' knowledge, this has not yet been studied in detail for resonators. The scattering to higher harmonics at an orifice, which is closely related to the Helmholtz resonator, was studied experimentally and analytically by Ingard and Ising [22,32] as well as Cummings [24]. An odd-harmonics-only (OHO) pattern in the higher harmonics was observed, where only the odd harmonics are present in the response. This observation could be explained by a quasi-steady analysis based on the Bernoulli equation.

The present study investigates the nonlinear acoustic scattering of both Helmholtz and quarter-wave resonator designs by means of CFD simulations. The appearance of the OHO pattern is found to depend on the symmetry of the configuration under study. The quasi-steady theory for scattering to higher harmonics at symmetric orifices [24,32] is extended to also describe asymmetric configurations and flow conditions, such that it can be applied to Helmholtz resonators with an asymmetric neck or quarter-wave resonators.

The paper is organized as follows: The approaches to describe the resonator response restricted to the fundamental frequency are presented in Sec. II. The quasi-steady theory from the literature is also introduced in this section. In Sec. III, this theory is applied and extended for the considered cases and the scattering behavior is evaluated. Section IV presents the scattering behavior observed in the CFD simulations for both the Helmholtz and quarter-wave resonators. The behavior is also compared to analytical prediction. Finally, the findings are summarized in Sec. V.

II. Physical Background

In this section, the basic terminology to characterize acoustic resonators is introduced. Moreover, a quasi-steady analysis based on the incompressible Bernoulli equation is presented, which accounts for nonlinearities of the pressure drop across the neck of a resonator. Throughout the whole study, the geometrical quantities, shown in Fig. 1, are denoted as follows: For the Helmholtz resonators, the lengths and diameters of the neck and of the backing volume are referred to as l_0 , d_0 , l_{cav} , and d_{cav} , respectively. The length and diameter of the quarter-wave resonator are named as l_0 and d_0 . The open area ratio is denoted by σ .

A. Impedance and Reflection Coefficient Describing Functions

The behavior of an acoustic resonator is often described in the frequency domain by its impedance Z . It is defined as the ratio of the Fourier transforms ($\hat{\cdot}$) of the fluctuating acoustic pressure p' and velocity u' normal to the reference surface:

$$Z(\omega_0) = z(\omega) c_0 \rho_0 = \frac{\hat{p}(\omega_0)}{\hat{u}(\omega_0)} \quad (1)$$

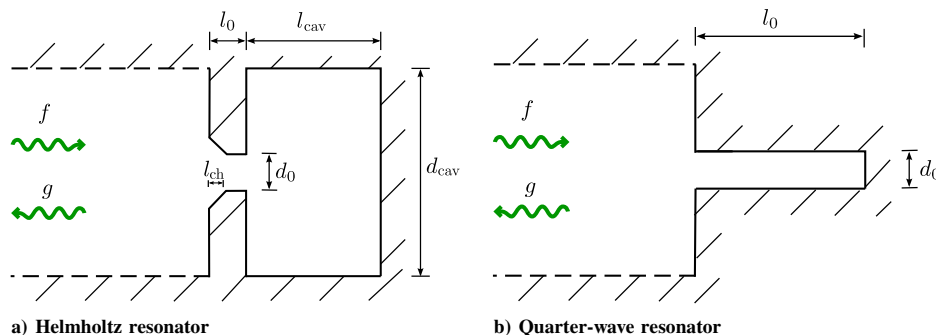


Fig. 1 Sketch of both resonator types considered. Slip walls in the simulations are marked by dashed lines.

Here, ω_0 denotes the angular excitation frequency. The real part of the impedance is referred to as resistance and its imaginary part as reactance. In the following, impedance values normalized with the air specific impedance $\rho_0 c_0$ are denoted by lowercase z . Here, ρ_0 and c_0 stand for the mean density and the speed of sound, respectively.

The resonator can also be characterized in terms of characteristic wave amplitudes f and g , assuming 1-D acoustics in front of the resonator. These f and g quantities can be considered as right- and left-traveling waves, respectively. In the absence of mean flow, they are defined as $f = (p' / (\rho_0 c_0) + u') / 2$ and $g = (p' / (\rho_0 c_0) - u') / 2$. The ratio of the reflected $\hat{g}(\omega_0)$ wave to the normally incident $\hat{f}(\omega_0)$ wave in the frequency domain is defined as the reflection coefficient $R(\omega_0) = \hat{g}(\omega_0) / \hat{f}(\omega_0)$. Its relation to the impedance is given by the following:

$$R(\omega_0) = \frac{\hat{g}(\omega_0)}{\hat{f}(\omega_0)} = \frac{Z(\omega_0) - \rho_0 c_0}{Z(\omega_0) + \rho_0 c_0} = \frac{z(\omega_0) - 1}{z(\omega_0) + 1} \quad (2)$$

At the resonator angular eigenfrequency ω_{eig} , the reactance vanishes $\Im(Z(\omega_{\text{eig}})) = 0$ and, accordingly, the optimal resistance equals the specific impedance $\rho_0 c_0$ of the medium, where no reflection takes place at all (i.e., $|R(\omega_{\text{eig}})| = 0$). Thus, the gain of the reflection coefficient decreases with the increasing sound pressure level (SPL) until it reaches the optimal resistance $\Re(z(\omega_{\text{eig}})) = 1$. For a resistance larger than this optimal value $\Re(z(\omega_{\text{eig}})) > 1$, the resonator is called overdamped. In that case, the reflection coefficient grows with a further increase of the resistance, as can be also observed in Sec. IV.

The concepts introduced previously are not adequate to characterize nonlinear phenomena because Z and R do not depend on the excitation amplitude. To extend the impedance to the nonlinear regime, the describing function approach is commonly used; see, for instance, the work of Hersh et al. [25], which is referred to as the impedance describing function in the following. Here, the impedance is specified, not only in dependency on the frequency but also on the excitation amplitude. This is commonly done in terms of the sound pressure level present at a certain reference position. The value of this SPL is defined as $20 \log_{10}(p_{\text{rms}} / p_{\text{ref}})$, where p_{rms} and p_{ref} denote the root mean square of the fluctuating pressure and the reference pressure in air of $20 \mu\text{Pa}$, respectively. Note that this approach cannot represent the nonlinear behavior in a comprehensive manner but only the behavior for the fundamental frequency of excitation. In particular, the scattering to higher harmonics is not included in this describing approach, which is investigated in the current paper.

B. Flow Separation as the Cause of Nonlinear Behavior

The Helmholtz resonator can be analyzed as a combination of an acoustically compact orifice and a backing volume in the linear and nonlinear regimes [20]. Thus, the loss mechanisms for a Helmholtz resonator are the same as those at an orifice. To understand those mechanisms, the 1-D unsteady Bernoulli equation with suitable

extensions for the loss terms can be studied for an orifice, as sketched in Fig. 2a; see, e.g., [24,32,33]. In the quarter-wave resonator case, the situation is different due to the asymmetry of the area jump, as sketched in Fig. 2b, but it can be analyzed in a similar framework. The following discussion helps to understand how the nonlinear losses are caused in both configurations.

The analysis is presented in nondimensional form. Nondimensional quantities are indicated by the superscript \sim . The reference time t_c and pressure p_c used for the nondimensionalization are defined as follows:

$$t_c = \frac{l_c}{c_0} \quad \text{and} \quad p_c = \rho_0 c_0^2 \quad (3)$$

The reference length scale l_c , which was already introduced to define the timescale t_c , is set differently for the orifice and the area jump to account for the different typical scales present. It is set such that the corresponding nondimensional angular eigenfrequencies $\tilde{\omega}_{\text{eig}} = \omega_{\text{eig}} t_c$ for the Helmholtz and quarter-wave resonators are unity, i.e., $\tilde{\omega}_{\text{eig}} = \omega_{\text{eig}} t_c = 1$. These eigenfrequencies of $\omega_{\text{eig}}^{\text{HR}}$ and $\omega_{\text{eig}}^{\text{QW}}$ can be approximated as Helmholtz and quarter-wave resonators

$$\omega_{\text{eig}}^{\text{HR}} = c_0 \sqrt{\frac{\sigma}{l_{\text{cav}}(l_0 + 2\Delta l)}} \quad \text{and} \quad \omega_{\text{eig}}^{\text{QW}} = \frac{\pi c_0}{2(l_0 + \Delta l)} \quad (4)$$

respectively. The length correction Δl accounts for fluid in front of the resonator opening taking part in the oscillation and can be set according to Ingard [21] as $4 / (3\pi) d_0$, where d_0 is the diameter of the opening. This geometrical length l_0 and the length corrections ($2\Delta l$ and Δl , respectively) are usually combined to the so-called effective lengths l_e , as described in more detail in Eq. (7). The corresponding length scales are set as follows:

$$l_c^{\text{HR}} = \sqrt{\frac{l_{\text{cav}}(l_0 + 2\Delta l)}{\sigma}} \quad \text{and} \quad l_c^{\text{QW}} = \frac{2(l_0 + \Delta l)}{\pi} \quad (5)$$

At first, the Helmholtz resonator is considered. It is assumed here that the resonator neck is acoustically compact such that it can be treated as an incompressible orifice. Viscous losses are neglected at the beginning of this consideration, and the Bernoulli equation is studied. This equation reads in terms of fluctuating quantities in nondimensional form as follows:

$$\frac{\partial \tilde{\phi}'}{\partial \tilde{t}} + \frac{1}{2} \tilde{u}'^2 + \tilde{p}' = \text{const.} \quad (6)$$

where $\tilde{\phi}$ is the nondimensionalized potential $\tilde{u} = \tilde{\nabla} \tilde{\phi}$. The preceding equation is integrated from positions 1 to 2, sketched in Fig. 2a. The nondimensionalized effective length \tilde{l}_e is introduced to express the result in a compact form:

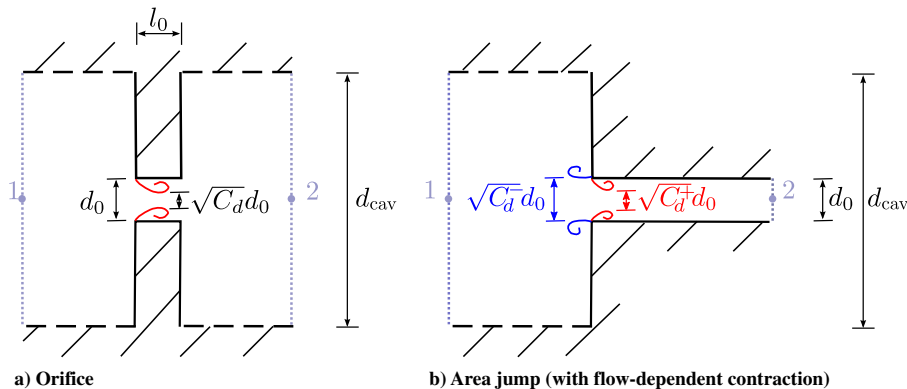


Fig. 2 Sketch of the corresponding geometries for the incompressible quasi-steady analysis.

$$\tilde{\phi}'_2 - \tilde{\phi}'_1 = \int_1^2 \tilde{u}'(\tilde{x}) d\tilde{x} = \int_1^2 \frac{\tilde{A}_0 \tilde{u}'_0}{\tilde{A}(\tilde{x})} d\tilde{x} = \tilde{u}'_0 \tilde{l}_e = \frac{\tilde{u}'_0}{\sigma} \tilde{l}_e \quad (7)$$

Here, \tilde{A}_0 and \tilde{u}'_0 denote the nondimensionalized cross-section area and the velocity in the orifice, respectively. The \tilde{x} -dependent area formed by the flowpath is $\tilde{A}(\tilde{x})$. Note that the effective length equals the nondimensionalized geometrical length of the orifice \tilde{l}_0 with an additional, nondimensionalized end correction $2\Delta\tilde{l}$ added; see, e.g., Ingard [21]. The pressure drop $\Delta\tilde{p}' = \tilde{p}'_1 - \tilde{p}'_2$ over the orifice without losses can be expressed as follows:

$$\Delta\tilde{p}' \approx \frac{1}{\sigma} \tilde{l}_e \frac{\partial \tilde{u}'}{\partial \tilde{t}} \quad (8)$$

The losses caused by friction at the orifice walls, which are not considered in the preceding equation, can be included by an appropriate real-valued constant \tilde{R}_l (see, e.g., the work of Boden and Zhou [34]). When the acoustical partial displacement in the orifice reaches the same order as the orifice diameter \tilde{d}_0 or is larger (i.e., when the Strouhal number $Sr = \tilde{\omega} \tilde{d}_0 \sigma / |\tilde{u}'|$ is small), the flow cannot follow the edge contour anymore and separates. Thus, the flow takes less area to jet through the orifice, as sketched in Fig. 2a. The ratio of the flow core area to the geometrical cross-sectional area is described by the contraction factor C_d , which is also often referred to as the discharge coefficient [15,25]. In the linear regime where $Sr \gg 1$, it can be assumed the $C_d \approx 1$, whereas $C_d < 1$ in the nonlinear regime. Besides the Strouhal number, the edge shape also has a strong impact on the separation process. The sharper the edge, the more pronounced the separation [30,31]. Using the contraction factor, the velocity in the orifice can be expressed as $\tilde{u}'_0 = 1/(C_d \sigma) \tilde{u}'$. When such a jet forms, it takes energy from the acoustics, which is dissipated in the vortex structures generated due to the separation. If it is assumed that the kinetic energy of the flow in the orifice $1/2(1/(C_d \sigma) \tilde{u}')^2$ is fully dissipated and does not recuperate downstream of the orifice (see, for instance, the work of Ingard [32]), it follows that

$$\Delta\tilde{p}' \approx \underbrace{\frac{1}{\sigma} \tilde{l}_e \frac{\partial \tilde{u}'}{\partial \tilde{t}}}_{\text{inertia}} + \underbrace{\tilde{R}_l \tilde{u}'}_{\text{viscosity}} + \underbrace{\frac{1}{2} \frac{|\tilde{u}'|^2}{(C_d \sigma)^2}}_{\text{flow separation}} \quad (9)$$

It can be seen in the preceding expression that the loss terms due to friction and flow separation contribute to the resistive part. When the losses and the pressure drop are not in equilibrium, the fluid in the orifice is accelerated, which solely impacts the reactance of the transfer impedance ($\partial \tilde{u}' / \partial \tilde{t} = i\tilde{\omega} \tilde{u}$). Moreover, it can be seen that only the flow separation behaves in a nonlinear fashion in this model.

In analogy, an acoustically compact area jump, as sketched in Fig. 2b, can be considered for the investigation of a quarter-wave resonator. In comparison to the formulations for the orifice found in the literature, an additional term is introduced that also behaves nonlinearly. By integration of the Bernoulli equation [Eq. (6)], the additional term $1/2\tilde{u}'^2(1/\sigma^2 - 1)$ appears due the nonequal cross-section area on both sides. In this case, the pressure drop can be expressed as follows:

$$\Delta\tilde{p}' \approx \frac{1}{\sigma} \tilde{l}_e^{AJ} \frac{\partial \tilde{u}'}{\partial \tilde{t}} + \frac{1}{2} \tilde{u}'^2 \left(\frac{1}{\sigma^2} - 1 \right) + \tilde{R}_l^{AJ} \tilde{u}' + \frac{1}{2} \frac{|\tilde{u}'|^2}{(C_d \sigma)^2} \quad (10)$$

In the preceding, \tilde{l}_e^{AJ} and \tilde{R}_l^{AJ} denote a suitable nondimensionalized effective length and linear loss term for the area jump, respectively.

III. Scattering to Higher Harmonics Described by Quasi-Steady 1-D Analysis

In contrast to linear systems, nonlinear systems can respond not only at the fundamental angular frequency ω_0 of the excitation but also at its multiples: the so-called higher harmonics. The fundamental frequency ω_0 is referred to as the first harmonic, and any multiples $n\omega_0$ are referred to as the n th harmonic ($n \in \mathbb{N}$). In the following, the

spectrum of the response is studied numerically in dependency on the excitation frequency and amplitude. To the authors' knowledge, this is studied for the first time in detail for resonator configurations. The orifice, which is from a geometrical point of view close to the Helmholtz resonator, is investigated experimentally and analytically with respect to its scattering behavior; see, e.g., the work of Ingard and Ising [22,32] and Cummings [24]. A pattern in the harmonics is observed in those studies, where the odd harmonics (third, fifth, ...) dominate clearly over the even ones (second, fourth, ...). This pattern is referred to as odd-harmonics only in the following. Ingard [32] and Cummings [24] explained the appearance of the OHO pattern by studying quasi-steady 1-D equations.

In the following, these considerations are extended step by step to also account for an asymmetric orifice and for an area jump, as they are present for a Helmholtz resonator with an asymmetric neck and a quarter-wave resonator. This analysis is applied to predict the relative contributions of the first five harmonics for Helmholtz resonators with symmetric and asymmetric necks, as well as quarter-wave resonators.

The appearance or absence of the OHO pattern can be explained by studying quasi-steady 1-D equations, such as Eqs. (9) and (10). Similar considerations were made by Ingard [32] and Cummings [24]. The theory presented in the literature is restricted to orifices assuming a time-invariant contraction factor C_d for the whole cycle.

In the current study, the contraction coefficient C_d is assumed to be constant during the inflow and outflow half-cycles:

$$C_d = \begin{cases} C_d^+, & \text{for } \tilde{u}' \geq 0 \\ C_d^-, & \text{for } \tilde{u}' < 0 \end{cases} \quad (11)$$

First, the orifice is considered where the pressure drop is described by Eq. (9). The only nonlinear term is given as $1/[2(C_d \sigma)^2] |\tilde{u}'|^2$. Accordingly, this is the only term that can contribute to the scattering to higher harmonics. Thus, the other terms are disregarded in the analysis because the focus of the study is the scattering behavior to higher harmonics, i.e.,

$$\Delta\tilde{p}'(\tilde{t}) 2\sigma^2 = \frac{1}{C_d^2} \tilde{u}' |\tilde{u}'| \quad (12)$$

If a sinusoidal velocity $\tilde{u}'(\tilde{t}) = \tilde{A}_u \sin(\tilde{\omega}_0 \tilde{t})$ is assumed, the Fourier series of this pressure drop reads as

$$\Delta\tilde{p}'(\tilde{t}) \frac{2\sigma^2}{\tilde{A}_u^2} = \frac{a_0}{2} + \sum_{n=1}^{\infty} a_n \cos(n\tilde{\omega}_0 \tilde{t}) + b_n \sin(n\tilde{\omega}_0 \tilde{t}) \quad (13)$$

with the constants

$$a_n = \begin{cases} \frac{1}{2} (C_d^+ - C_d^-), & \text{for } n = 0 \\ \frac{1}{4} (C_d^- - C_d^+), & \text{for } n = 2 \\ 0, & \text{else} \end{cases} \quad (14)$$

and

$$b_n = \begin{cases} \frac{-4(C_d^- + C_d^+)}{\pi(n^2 - 4n)}, & \text{for odd } n \\ 0, & \text{else} \end{cases} \quad (15)$$

It can be seen that, for symmetric flow conditions with $C_d^+ = C_d^-$, the coefficients $a_n = 0$ for all n . Thus, only contributions with $b_n \neq 0$ remain for odd n . It can be concluded that the appearance of the OHO pattern is due to the symmetry of the flow.

This flow symmetry is broken for an asymmetric geometry. Note also that the mean flow may lead to different flow contraction conditions during the inflow and outflow phases, as shown by Zhang and Bodony [35] for a Helmholtz resonator with grazing flow. The flow asymmetry due to flow separation at sufficiently high amplitudes can be described like this for a one-sided chamfered orifice: At the sharp orifice edge, the flow contracts (i.e., $C_d^+ < 1$), whereas it does not at the chamfered edge (i.e., $C_d^- \approx 1$).

Table 1 Geometric properties of the considered Helmholtz and quarter-wave resonators in dimensional and nondimensional forms

	l_0 , mm	d_0 , mm	l_{cav} , mm	d_{cav} , mm	l_{ch} , mm	σ , %	$\omega_{\text{eig}}/(2\pi)$, Hz	\tilde{l}_0	\tilde{d}_0	\tilde{l}_{cav}	\tilde{d}_{cav}	\tilde{l}_{ch}	$\tilde{\omega}_{\text{eig}}$
HRS	4.0	4.2	20	50	0	0.71	373	0.0274	0.0288	0.1369	0.3423	0	1
HRA	4.0	4.2	20	50	0.35	0.71	373	0.0274	0.0288	0.1369	0.3423	0.0024	1
QW	143	6.35	—	—	—	1.56	589	1.5561	0.0691	—	—	—	1

The asymmetry increases when the area jump is studied instead of the orifice. The separation term [Eq. (12)] analyzed by Fourier transform in Eqs. (13–15) is also part of the nonlinear response. Due to the change in cross section at the area jump, an additional term appears in Eq. (10). This term can be expressed as follows:

$$\frac{1}{2} \tilde{A}_u^2 \sin^2(\tilde{\omega}_0 \tilde{t}) \left(\frac{1}{\sigma^2} - 1 \right) = \frac{1}{4} \tilde{A}_u^2 \left(\frac{1}{\sigma^2} - 1 \right) (1 - \sin(2\tilde{\omega}_0 \tilde{t})) \quad (16)$$

The preceding expression contributes significantly to the second harmonic, and thus amplifies the disappearance of the OHO pattern.

The following conclusions can be made from the preceding considerations: The Helmholtz resonator with a symmetric neck shows the OHO pattern, where the harmonics decrease with increasing order. If its neck is asymmetric (e.g., with $C_d^+ \approx 0.7$ for a sharp edge and $C_d^- \approx 0.95$ for a 45 deg chamfered edge; see [36]), the OHO pattern gets weaker. The third harmonic is still dominant. But now, the second harmonic is predicted to be more pronounced than the fifth one. When a quarter-wave resonator is considered, strong scattering in the second harmonic is expected. Overall, the scattering to higher harmonics is much larger here than in the case of a Helmholtz resonator (for $\sigma \ll 1$).

In the preceding discussion, only the nonlinear terms are considered. It can be seen in Eqs. (13) and (16) that their contribution scales with the square of the amplitude of the velocity \tilde{A}_u^2 , whereas all the other linear terms scale with the amplitude of the velocity \tilde{A}_u . Thus, it can be concluded that the impact of the nonlinear term responsible for the scattering to higher harmonics rises with increasing velocity.

IV. Scattering to Higher Harmonics Observed in CFD Simulations

In this section, the predicted patterns in the amplitudes of the higher harmonics are verified and quantified with compressible CFD simulations for three resonator configurations. These considered configurations as well as the computational setup are introduced in Sec. IV.A. A qualitative comparison of compressible Helmholtz resonator simulations and incompressible orifice simulations is performed in Sec. IV.B. By doing so, a link from the incompressible theory to compressible resonator simulations is provided. Moreover, the flow separation for the three test cases is investigated during the inflow and outflow phases in this section. Finally, the results of the compressible simulations of three resonators are presented and discussed in Sec. IV.C.

A. Simulation Setup and Definition of the Test Cases

1. Definition of Test Cases

In the present numerical study, a quarter-wave (QW) resonator as well as Helmholtz resonators with symmetric (HRS) and asymmetric (HRA) necks are considered. The generic geometries are sketched in Fig. 1. The neck of configuration HRA is chamfered by 45 deg on the outside, with a length in the axial direction of $l_{\text{ch}} = 0.35$ mm. The values of all geometric quantities are listed in Table 1 in dimensional and nondimensional forms. The HRS configuration is set as in [31] to have access to validation data. The chamfer length is set small enough that it influences the linear response of the resonator only marginally.

2. CFD Solver Setup

Compressible CFD simulations are performed with the PIMPLE algorithm of OpenFOAM [37]. The slip condition is applied at the cylindrical wall of the impedance tube and the no-slip condition is

used at the resonator itself; see Fig. 1. At the inlet, the Navier–Stokes characteristics boundary condition (cf. Poinso and Lele [38]) is used. This boundary condition ensures a low acoustic reflection of the outgoing g wave. Simultaneously, an excitation signal can be imposed for the incoming f wave, which is set sinusoidally [$f = A_f \sin(\omega_0 t)$] with different fundamental frequencies: $\omega_0/(2\pi)$. At this inlet plane, the fluctuating pressure p' and velocity u' are monitored. From these dimensional quantities, the time series of the nondimensional \tilde{f} and \tilde{g} waves can be computed directly. As explained previously, the incoming wave scatters in the harmonics of the reflected wave $\tilde{g}(n\tilde{\omega}_0)$. In the following figures, the amplitudes of the higher harmonics $\tilde{g}(n\tilde{\omega}_0)$ are normalized by the amplitude of the fundamental harmonic of the incoming wave $\tilde{f}(\tilde{\omega}_0)$, which can be written as follows:

$$\frac{|\hat{\tilde{g}}(n\tilde{\omega}_0)|}{|\hat{\tilde{f}}(\tilde{\omega}_0)|} \quad (17)$$

In the postprocessing, the transient parts of the data series have been removed and then truncated to a multiple of the period T to avoid leakage in the spectra. For further details on the solver, refer to [31]. The simulations use three-dimensional (3-D) meshes of at least 1.5 million cells. Note that this is, overall, a rather coarse mesh in comparison to DNSs available in the literature [15]. However, the mesh is refined carefully in the Helmholtz resonator neck (and the quarter-wave resonator mouth, respectively), and especially at the edges because, here, the mechanisms responsible for the acoustic dissipation take place. The mesh independence with respect to the acoustic impedance is checked for HRS up to an overall SPL of 125 dB. Overall, reasonable results with relatively low computation cost can be achieved, enabling for extensive parameter studies.

The compressible CFD simulations are performed as LESs with the k -equation eddy-viscosity model as a subgrid-scale (SGS) model. Several SGS models have been tested. However, the acoustic response of the resonator depends only very weakly on the SGS modeling. Vortex structures are formed in the vicinity of the resonator neck due to the pulsation forcing of the flow. The dissipation to thermal energy of these vortices follows mainly the turbulent cascade. However, the separation process itself, responsible for the nonlinear acoustic dissipation, is almost not influenced by the vortices. This can also be seen with the Reynolds number based on the orifice size and velocity amplitude at the orifice, which remains rather low (maximum $\text{Re} \approx 3000$ at 119.7 dB for HRS). Accordingly, the impact of the SGS model on acoustic properties remains very small as the separation process at the edges is resolved sufficiently. Moreover, comprehensive parameter studies regarding mesh, time-step, and solver parameters are performed to ensure that the presented results are independent of the numerical settings. The solver is validated in detail in the linear regime for various configurations in [31]. In the nonlinear regime, the solver is validated against the measurements of M. A. Temiz[†] based on describing functions for the HRS configuration; see the Appendix.

To compare the simulation with the measurement, the input amplitude A_f of the f waves must be set such that the superposition of the waves f and the reflected $g = Rf$ matches the desired SPL; see [20] for more details. This requires an a priori knowledge of the reflection coefficient or an iterative process. In the following, this approach of setting the input amplitude is solely used for validation

[†]Private communication by M. A. Temiz, Technische Universiteit Eindhoven, Department of Mechanical Engineering, Eindhoven, The Netherlands.

purposes. Besides that, the SPL is set only with respect to the input signal f ignoring the reflected acoustic g wave. This is referred to as input SPL in the following. Note that the input SPL and the actual SPL differ from each other.

For the orifice configuration, incompressible simulations are also performed with the SIMPLE algorithm of the commercial software ANSYS Fluent v15. A detailed description of the corresponding solver setting can be found in [20]. For a given geometry and excitation frequency, the nonlinear behavior is linked to the magnitude of the velocity in the orifice and resonator neck, respectively. For a valid comparison, the input amplitude in the incompressible simulation has to be set such that velocities in the orifice agree with the velocities in the Helmholtz resonator neck.

B. Validation of Modeling Assumptions via CFD

1. Linking the Incompressible and Compressible Approaches

The orifice is treated as incompressible in the analysis of Sec. III, whereas the CFD simulations of the Helmholtz resonator are set up compressibly. Accordingly, a quantitative comparison between those two is not directly possible. Therefore, incompressible orifice CFD simulations are also considered in this section, which allow a link from the CFD simulations to the 1-D quasi-steady theory. The compressible resonator simulations and the incompressible orifice simulations can be compared qualitatively.

A sinusoidal velocity $\tilde{u}'(\tilde{t}) = A_u \sin(\tilde{\omega}_0 \tilde{t})$ is assumed in the analysis of Sec. III. The higher harmonics occur there solely in the pressure drop $\Delta \hat{p}(n\tilde{\omega}_0)$ over the orifice. This pressure drop including the higher harmonics is also determined via incompressible CFD simulations with sinusoidal velocity excitation. For these incompressible simulations, the orifice corresponding to the resonator neck of HRS is considered as geometry. The amplitudes A_u of the velocities in the incompressible simulations are adjusted such that they coincide with the velocity amplitudes in the resonator neck present for a SPL of 119.7 dB at the reference distance of $l_{\text{ref}} = 49.7$ mm. The higher harmonics in the pressure drop are presented in Fig. 3a. In this figure, the amplitude of the n th harmonic is normalized by the fundamental harmonic $\Delta \hat{p}(\tilde{\omega}_0)$, such that this harmonic is represented as

$$\frac{|\Delta \hat{p}(n\tilde{\omega}_0)|}{|\Delta \hat{p}(\tilde{\omega}_0)|} \quad (18)$$

Moreover, the results of 1-D simulations [39] of the quasi-steady equation [Eq. (9)] are included in this figure. It can be observed that both the 1-D quasi-steady equation [Eq. (9)] and the incompressible CFD simulation exhibit the OHO predicted by the quasi-steady analysis. The third harmonic is dominant, followed by the fifth harmonics, as predicted by the analysis. The magnitude of the odd harmonics obtained by the 1-D simulations of the quasi-steady

equation [Eq. (9)] agrees well with the one of the CFD simulations. The scattering to higher harmonics takes place mainly close to the angular eigenfrequency $\tilde{\omega}_{\text{eig}} \approx 1$, where the velocities in the orifice are largest.

In Fig. 3b, the higher harmonics in the scattered g wave [as defined in Eq. (17)] are plotted for the compressible LESs of the symmetric Helmholtz resonator. Again, the input amplitudes A_f are set in a way that a SPL of 119.7 dB at the reference distance $l_{\text{ref}} = 49.7$ mm is achieved. The 1-D quasi-steady equation [Eq. (9)] can be rewritten in terms of Riemann invariants f and g to a 1-D ordinary differential equation (ODE), which can be solved numerically [39]. The scattered higher harmonics described by this 1-D quasi-steady ODE are also included in this figure. Both compressible approaches, the LES and the 1-D ODE, have the OHO pattern as predicted by the 1-D quasi-steady analysis in Sec. III. There are almost no contributions to the even harmonics for both compressible approaches. Also here, the scattering to higher harmonics occurs mainly close to the angular eigenfrequency $\tilde{\omega}_0 \approx 1$. This also agrees with the incompressible analysis because the velocities in the resonator neck are largest close to the eigenfrequency. It can be observed that the third harmonics of this quasi-steady 1-D approach agree very well these of the 3-D LESs. The fifth harmonic is underpredicted by the 1-D approach. Overall, the nonlinear term in the quasi-steady equation [Eq. (9)], once written in terms of Riemann invariants, describes the mechanisms responsible for the scattering to higher harmonics accurately.

It can be summarized that the OHO pattern is present for both symmetric orifices and Helmholtz resonators. For both configurations, the mechanism responsible for the scattering to higher harmonics can be explained well by studying the 1-D quasi-steady equation [Eq. (9)] as it is done in Sec. III.

2. Contraction Behavior for the Three Considered Configurations

Before the scattering to higher harmonics in the compressible CFD simulations for each resonator is discussed, the flow contraction is investigated for these configurations. In Fig. 4, a snapshot of the flowfield during the inflow and outflow phases with maximal contraction is presented for all configurations. These snapshots are cropped to the vicinity of the resonator neck and mouth, respectively. Note that the separation process is a transient process such that, for a precise prediction, phase averaging over several periods and (subsequently) averaging over time would be required, as was done by Zhang and Bodony [15]. Here, only the order of magnitude and the influence of the edge on separation behavior are evaluated optically with the presented snapshots. The separation zones are marked with thick lines at the upper edges in each figure. The resonators are excited at a frequency close to their eigenfrequencies $\tilde{\omega}_0 \approx 1$ (corresponding to 380 Hz) with an input SPL of 125 dB (for HRS and HRA) and at $\tilde{\omega}_0 \approx 1$ (corresponding to 580 Hz) with 160 dB (for QW). Configuration QW is excited with a higher SPL in comparison to the Helmholtz resonator configurations because it requires a higher SPL to trigger nonlinear

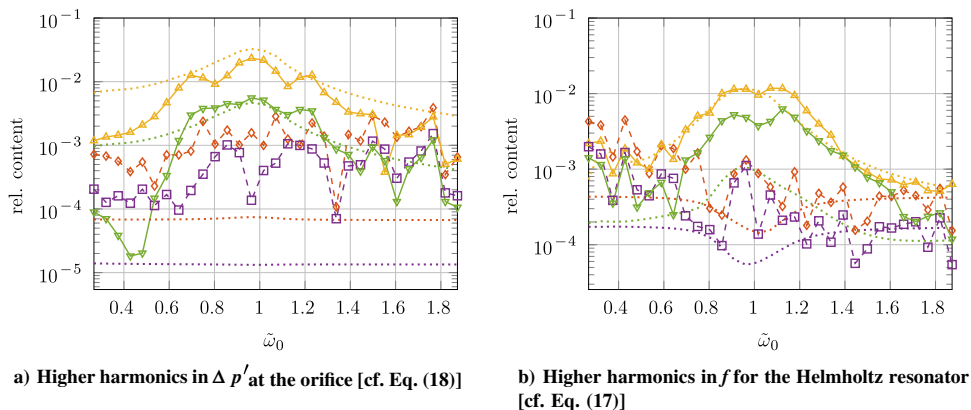


Fig. 3 Higher harmonics for the Helmholtz resonator HRS and the corresponding orifice at 119.7 dB: second harmonic in CFD simulations $-\diamond-$, third $-\triangle-$, fourth $-\square-$, fifth $-\nabla-$; harmonics with quasi-steady 1-D analysis are plotted with dotted lines (rel., relative).

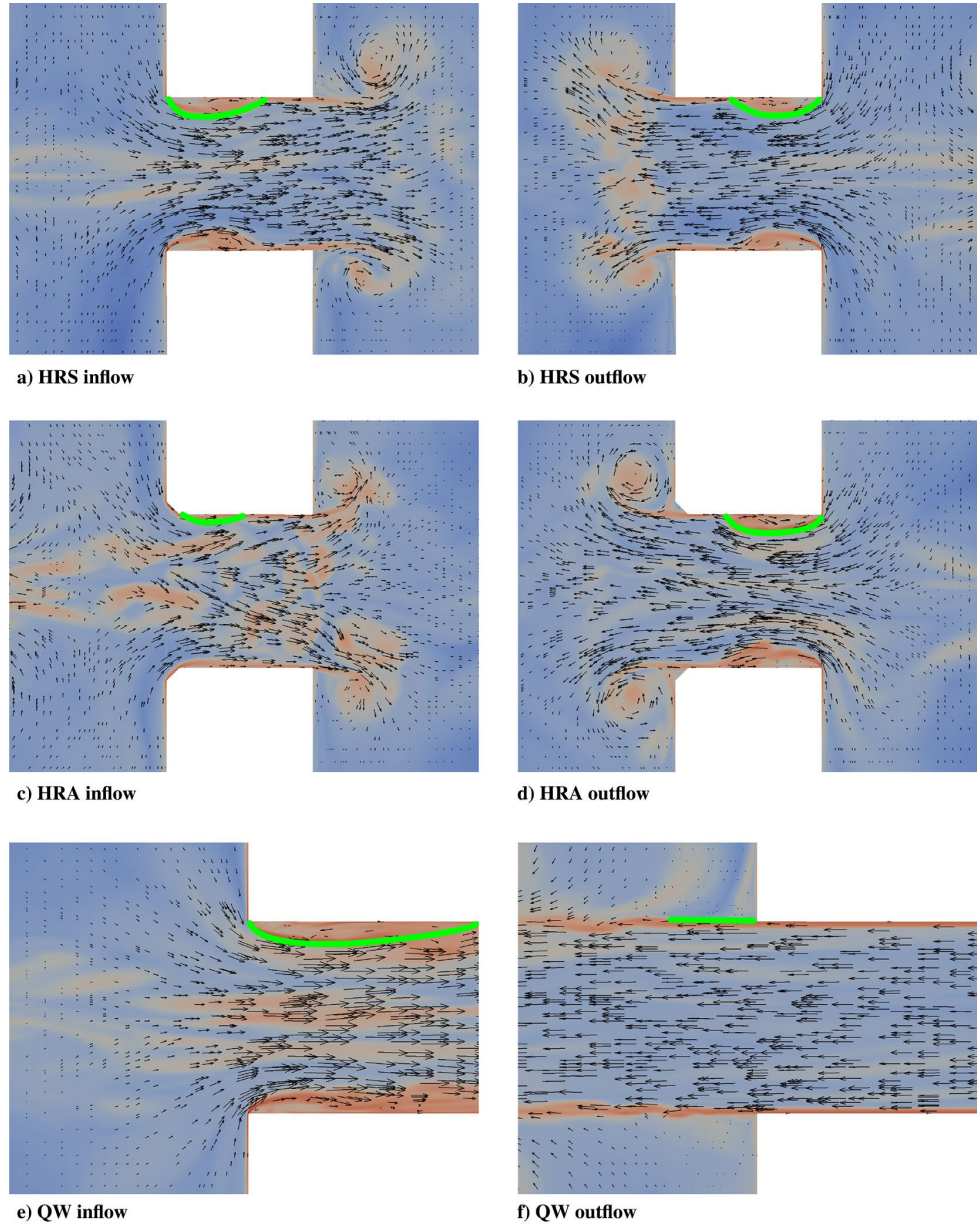


Fig. 4 Flow visualization in a 2-D cutting plane in the vicinity of the resonator neck/mouth during the inflow and outflow phases for the three configurations considered at excitation frequency close to the eigenfrequency $\tilde{\omega}_0 = 1$ with input SPL 125 dB for HRS and HRA, and with input SPL 160 dB for QW. On the upper half, the contraction is marked in green for each case.

behavior, as will be shown in Sec. IV.C.3. As explained previously, these SPL values are set here and in the following as input SPLs, which means that the SPL values refer solely to the input f waves while ignoring the reflected g waves. The separation behavior is similar for the inflow and outflow for HRS; see Figs. 4a and 4b. A contraction ratio of ≈ 0.7 , as can be found in the literature [15,36], is confirmed by the simulation. The asymmetric neck induces an asymmetric separation behavior. During the outflow, the contraction remains the same as for HRS; see Fig. 4d. However, the flow contracts less with a factor of $C_d^+ \approx 0.9$ for the inflow (Fig. 4c), which is close to the literature values (0.95 in Blevins's textbook [36]). The separation is also asymmetric for the quarter-wave resonator with $C_d^+ \approx 0.7$ and $C_d^- \approx 1$, as can be seen in Figs. 4e and 4f. Overall, it can be concluded that the assumption of Sec. III that the contraction depends on the flow direction is reasonable.

C. Scattering to Higher Harmonics Determined by CFD Simulations

1. Scattering to Higher Harmonics at the Helmholtz Resonator with Symmetric Neck

The amplitudes of the higher harmonics $n\tilde{\omega}_0$ up to order $n = 5$ of the resonator response for an input SPL of 125 dB are plotted in Fig. 5a for the fundamental excitation frequency $\omega_0/(2\pi)$ in the range of 200–700 Hz, corresponding to $\tilde{\omega}_0 \in [0.54, 1.87]$. All harmonics with larger order ($n > 5$) are negligible with a relative content of less than 2%. It can be observed that the damping of the fundamental harmonic (line marked with \rightarrow) is best close to the resonator eigenfrequency, i.e., where $\tilde{\omega}_0$ is close to unity. On the other hand, scattering to higher harmonics mainly occurs close to that frequency. This is in line with expectations because the velocity in the neck is largest in this frequency range and is causing strong nonlinear effects here. Away from the eigenfrequency, velocities are smaller and the

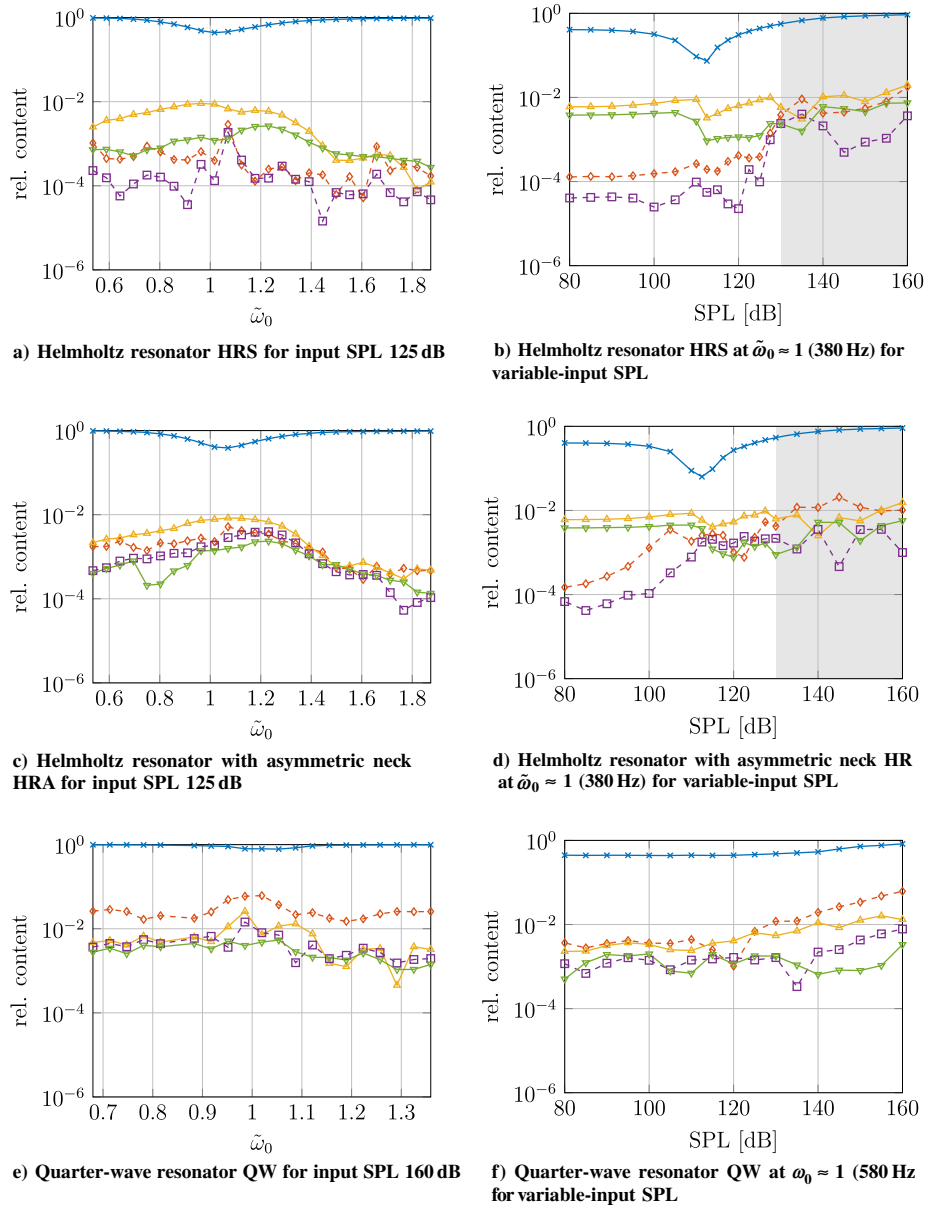


Fig. 5 Scattering to harmonics plotted in logarithmic scale: fundamental \times , second \diamond , third \triangle , fourth \square , fifth ∇ .

system behaves almost linearly. As expected, the OHO pattern occurs (i.e., the odd harmonics contribute predominantly to the response), whereas the even harmonics are almost absent. The third harmonic (line marked with \triangle) clearly dominates over the even ones (second is shown as \diamond , fourth is shown as \square). The contribution of the harmonics becomes less and less considerable with increasing order n . The impact of the fifth harmonic (line marked with ∇) is noticeably smaller than the third but is still more prominent than even harmonics.

In Fig. 5b, the scattering to the harmonics is depicted under variation of the input SPL for an excitation frequency close to eigenfrequency $\tilde{\omega}_0 \approx 1$ [corresponding to $\omega_0/(2\pi) = 380$ Hz]. The reflection coefficient and the resistance are presented in Fig. 6 (\triangle). Note that the reflection coefficient equals the scattering into the fundamental harmonic, which is also shown in Figs. 5a and 5b. With increasing input SPL, the fundamental harmonic first decays (up to 110 dB) because the resistance increases; see Fig. 6b. The optimal damping for orthogonal incident acoustic waves is achieved with a

normalized impedance of $z = 1$. Increasing the excitation further leads to higher resistance, but the reflection also increases. This occurs due to the overdamping of the system. The trend of increasing resistance with increasing SPL can also be explained by studying the 1-D equation for the pressure drop; see Eq. (9). The only nonlinear term in this equation corresponds to the flow separation. The corresponding nonlinear resistance scales with the amplitude of the velocity in the neck, which itself increases with rising SPL. This can also be seen in experimental [40] and numerical [15] studies.

The scattering to higher harmonics increases with increasing amplitude in the normal-damped range ($z < 1$). Close to the region of optimal damping ($z = 1$), the scattering to higher harmonics abruptly attains a local minimum. This minimum cannot be explained with the analysis of Sec. III because the velocity in the neck is actually further increasing. Furthermore, the scattering to higher harmonics does not totally vanish for low amplitudes. The considerations made previously would actually suggest a monotonic increase of the scattering with the amplitude, starting with no scattering and reaching

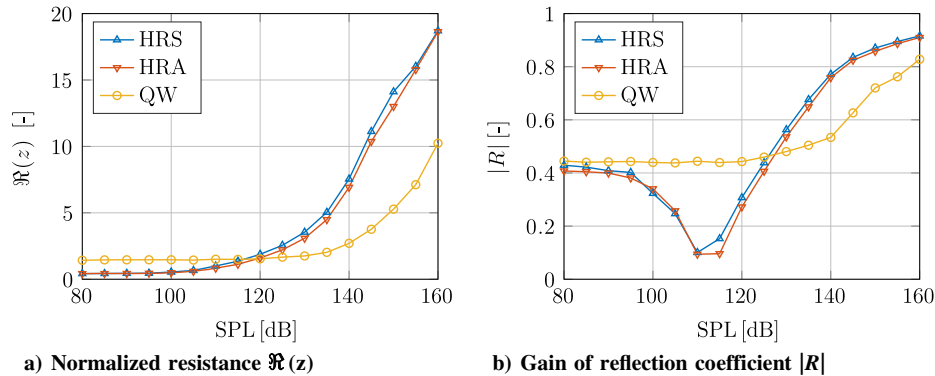


Fig. 6 Gain of reflection coefficient $|R|$ and normalized resistance $\Re(z)$ under variation of the input SPL at the corresponding eigenfrequency $\tilde{\omega}_0 \approx 1$.

asymptotically a limit. The reasons for the discrepancy to the presented simulation results are still unknown. In the overdamped range, the scattering increases again by increasing the input SPL. The overall scattering remains small for this resonator setup, even for very high excitation levels. Thus, modeling the nonlinear behavior only for the fundamental frequency $\tilde{\omega}_0$ with the describing function approach (see Sec. II.A) reflects the main mechanisms accurately in that case.

It can be observed that the OHO pattern vanishes in a range of very high SPL (≥ 130 dB), which is shaded in Figs. 5b and 5d (for HRA). The interaction of the vortices formed at leading and trailing edges is identified as the cause of this behavior. The exact mechanism and the circumstances when the OHO pattern is absent will be discussed in detail in a separate paper.

2. Scattering to Higher Harmonics at the Helmholtz Resonator with Asymmetric Neck

The gain of the reflection coefficient and resistance for various SPLs are included in Fig. 6 for the configuration with the asymmetric neck HRA. The chamfer size is set such that the linear impedance is almost not influenced by the chamfer. Thus, the eigenfrequency remains the same as for HRS and the excitation for that case is set to 380 Hz. The nonlinear resistance can be observed to decrease slightly in comparison to the unchamfered case HRS; see Fig. 6a. This decrease arises from the lower flow contraction during the outflow phase; see [31]. The scattering to the harmonics $n\tilde{\omega}_0$ ($n \in \{1, 2, \dots, 5\}$) is shown for an input SPL of 125 dB in Fig. 5c for a range of 200–700 Hz for the fundamental excitation frequency $\omega_0/(2\pi)$, corresponding to $\tilde{\omega}_0 \in [0.68, 1.36]$. Moreover, the scattered higher harmonics are presented for an excitation close to eigenfrequency $\tilde{\omega}_0 \approx 1$ (corresponding to 380 Hz) with varying input SPLs in Fig. 5d. As predicted, the second harmonic increases in comparison to HRS with symmetric neck. According to the analysis of Sec. III, the second harmonic should be weaker than the third but stronger than the fifth one. However, the increase of the second harmonic is moderate such that the second and fifth harmonics have about an equal strength in the CFD simulations.

3. Scattering to Higher Harmonics at the Quarter-Wave Resonator

For the quarter-wave resonator, the behavior changes significantly with respect to the Helmholtz resonators. For QW, the scattering to higher harmonics is mostly into the second harmonic, which again fits well to the analysis of Sec. III. This can be seen in Fig. 5e for a constant SPL of 160 dB and in Fig. 5f for the excitation eigenfrequency close to eigenfrequency $\tilde{\omega}_0 \approx 1$ (corresponding to 580 Hz) in a range of 80–160 dB. The frequency sweep is performed for QW at 160 dB instead of 125 dB for Helmholtz resonator configurations due to the higher SPL required to trigger nonlinear behavior. This can be seen in Fig. 6a (—○—). For HRS, the resistance starts to increase at a SPL of about 105 dB due to nonlinear effects. For QW, this occurs at about 125 dB. This difference can be explained only partially due to the different open

area ratios σ . Thus, the different threshold to trigger nonlinearities originates mainly due to the different resonator concepts. Moreover, the overall scattering increases as well. The maximal scattering is in the order of 2% for the Helmholtz resonators. Here, for QW, the relative scattering to the second harmonic can reach values up to the order of 10%. This difference in magnitude of the Helmholtz and the quarter-wave resonator is backed by the quasi-steady analysis.

V. Conclusions

The nonlinear acoustic response of quarter-wave and Helmholtz resonators has been studied by means of compressible computational fluid dynamics (CFD) simulations. Particular attention was paid to the scattering to higher harmonics. For the Helmholtz resonators, the higher harmonics exhibited an odd-harmonics-only pattern, where only the odd harmonics were present, whereas the even ones were negligible. Such patterns were observed previously at symmetric orifices, and they were explained by a 1-D quasi-steady analysis based on the Bernoulli equation with suitable extra terms for the losses [22,24,32]. The current study extended the analysis, such that it was also applicable to configurations that exhibited asymmetric flow patterns, e.g., Helmholtz resonators with asymmetric necks or quarter-wave resonators.

The following observations are observed in CFD simulations and confirmed by the quasi-steady analysis: For the Helmholtz resonator with a symmetric neck, the scattering to higher harmonics exhibits the odd-harmonics-only (OHO) pattern. The OHO pattern is weaker if a Helmholtz resonator with an asymmetric neck is considered. It is concluded that the pure OHO pattern occurs due to the flow symmetry during the inflow and outflow phases through the symmetric resonator neck. For the quarter-wave resonator, corresponding to a simple discontinuity in the cross-sectional area in the 1-D compact analysis, a larger threshold for the excitation is required to trigger noticeable nonlinear effects. If scattering takes place in this configuration, the second harmonic is the dominant higher harmonic, and the OHO pattern vanishes completely.

Overall, the scattering to higher harmonics is more pronounced for the quarter-wave resonator, for which values up to the order of 10% of the incident wave are observed. In contrast, Helmholtz resonators exhibit quite moderate nonlinear scattering (up to 2%), even for very high excitation levels. One may conclude that, in many cases, describing functions for impedance or reflection coefficients characterize the nonlinear response of resonators with acceptable accuracy.

Appendix: Solver Validation in the Nonlinear Regime

The solver validation in the nonlinear regime is presented using impedance describing function measurements performed by M. A. Temiz (see footnote ⁶) from the Eindhoven University of Technology on configuration HRS in a frequency range of [100,700] Hz corresponding to $\tilde{\omega}_0 \in [0.27, 1.87]$. Figure A1 shows the normalized impedance and the reflection coefficient for overall SPLs of 120 and

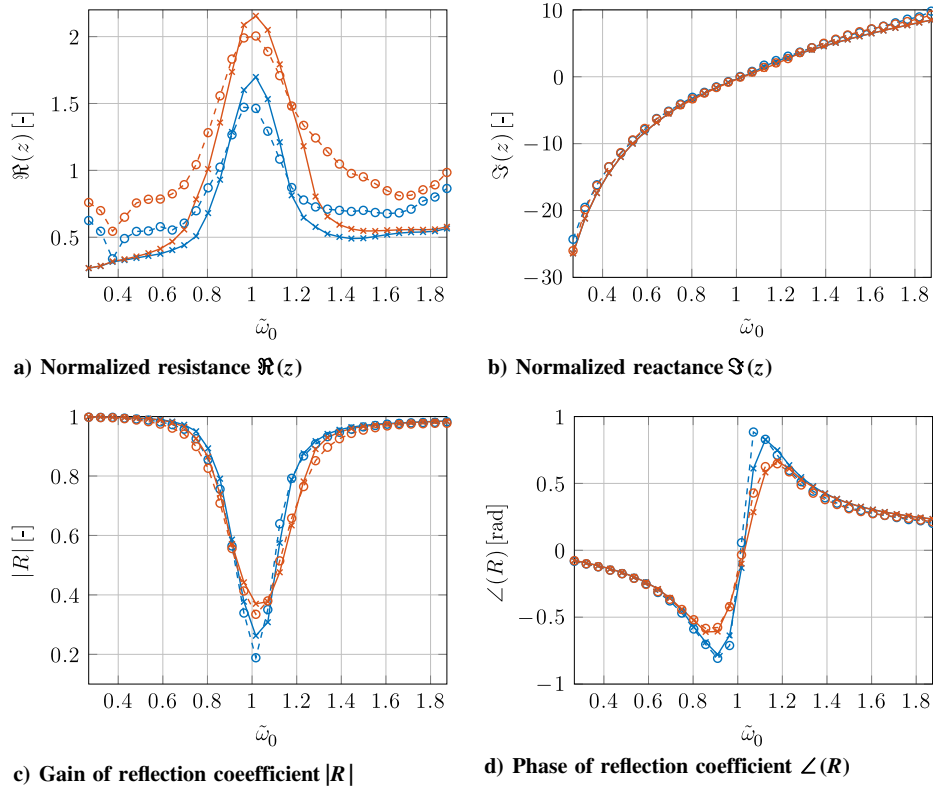


Fig. A1 Comparison of LES (circles) and measurement (x) for HRS at SPLs of 120 dB and 125 dB.

125 dB obtained by the measurements and the CFD simulations. In those simulations, the input amplitudes of the f wave are set in a way that the acoustic SPL directly in front of neck matches the target value. Because the nonlinear effects mainly affect the resistance $\Re(z)$, it is more challenging to capture this quantity correctly in the CFD simulation (see Fig. A1a) than the reactance $\Im(z)$, which always fits very accurately (see Fig. A1b). The curves agree quite reasonably, but the numerics slightly overpredict the nonlinear resistance. A reason for this is (at least partially) that the edges in the CFD mesh are perfectly sharp, whereas the real sample is not due to manufacturing reasons [20]. The measurements are also a bit shaky away from the eigenfrequency. This shaky behavior does not originate from physics but from the ill-conditioned transformation from the reflection coefficient to resistance. The reflection coefficient is in both the experiment and CFD the quantity that is directly and subsequently transformed to the impedance. Thus, a comparison in the reflection coefficient is more suitable. This is depicted in Figs. A1c and A1d. Here, the curve match is almost perfect and shows the quality of the computational setup.

Acknowledgments

Financial support for K. Förner was provided by the German Research Foundation (Deutsche Forschungsgemeinschaft) in the framework of the Sonderforschungsbereich Transregio 40, Project A3. J. Tournadre is member of the Marie Curie Initial Training Network Thermo-Acoustic and Aero-Acoustic Nonlinearities in Green Combustors with Orifice Structures, financed by the European Commission under FP7-PEOPLE-ITN-2012. A preliminary version of this work was presented at the 22nd AIAA/CEAS Aeroacoustics Conference 2016. Furthermore, the authors thank the Leibniz Supercomputing Centre for the access to its cluster system, A. Mages for his help, and M. A. Temiz from Eindhoven University of Technology for providing measurement data.

References

- [1] *The Jet Engine*, 5th ed., Rolls-Royce Ltd., Derby, U.K., 1996.
- [2] Bellucci, V., Flohr, P., Paschereit, C. O., and Magni, F., "On the Use of Helmholtz Resonators for Damping Acoustic Pulsations in Industrial Gas Turbines," *Journal of Engineering for Gas Turbines and Power*, Vol. 126, No. 2, 2004, pp. 271–275. doi:10.1115/1.1473152
- [3] Förner, K., Cárdenas Miranda, A., and Polifke, W., "Mapping the Influence of Acoustic Resonators on Rocket Engine Combustion Stability," *Journal of Propulsion and Power*, Vol. 31, No. 4, 2015, pp. 1159–1166. doi:10.2514/1.B35660
- [4] Sohn, C. H., and Park, J. H., "A Comparative Study on Acoustic Damping Induced by Half-Wave, Quarter-Wave, and Helmholtz Resonators," *Aerospace Science and Technology*, Vol. 15, No. 8, 2011, pp. 606–614. doi:10.1016/j.ast.2010.12.004
- [5] Jones, M. G., Tracy, M. B., Watson, W. R., and Parrott, T. L., "Effects of Liner Geometry on Acoustic Impedance," *8th AIAA/CEAS Aeroacoustics Conference and Exhibit*, AIAA Paper 2002-2446, 2002. doi:10.2514/6.2002-2446
- [6] Zhang, Q., and Bodony, D. J., "Numerical Investigation of a Honeycomb Liner Grazed by Laminar and Turbulent Boundary Layers," *Journal of Fluid Mechanics*, Vol. 792, April 2016, pp. 936–980. doi:10.1017/jfm.2016.79
- [7] Eldredge, J. D., and Dowling, A. P., "The Absorption of Axial Acoustic Waves by a Perforated Liner with Bias Flow," *Journal of Fluid Mechanics*, Vol. 485, May 2003, pp. 307–335. doi:10.1017/S0022112003004518
- [8] Bellucci, V., Flohr, P., and Paschereit, C. O., "Numerical and Experimental Study of Acoustic Damping Generated by Perforated Screens," *AIAA Journal*, Vol. 42, No. 8, 2004, pp. 1543–1549. doi:10.2514/1.9841
- [9] Scarpato, A., Ducruix, S., and Schuller, T., "Optimal and Off-Design Operations of Acoustic Dampers Using Perforated Plates Backed by a Cavity," *Journal of Sound and Vibration*, Vol. 332, No. 20, 2013, pp. 4856–4875. doi:10.1016/j.jsv.2013.03.030

- [10] Čosić, B., Reichel, T. G., and Paschereit, C. O., "Acoustic Response of a Helmholtz Resonator Exposed to Hot-Gas Penetration and High Amplitude Oscillations," *Journal of Engineering for Gas Turbines and Power*, Vol. 134, No. 10, 2012, Paper 101503.
doi:10.1115/1.4007024
- [11] Rupp, J., Peacock, G., Regunath, G., and Carrotte, J., "Assessment and Prediction of Helmholtz Resonator Performance Within Gas Turbine Combustion Systems," *ASME Turbo Expo 2014*, American Society of Mechanical Engineers Paper GT2014-26907, New York, 2014.
doi:10.1115/GT2014-26907
- [12] Tam, C. K. W., and Kurbatskii, K. A., "Microfluid Dynamics and Acoustics of Resonant Liners," *AIAA Journal*, Vol. 38, No. 8, 2000, pp. 1331–1339.
doi:10.2514/2.1132
- [13] Tam, C. K. W., Ju, H., and Walker, B. E., "Numerical Simulation of a Slit Resonator in a Grazing Flow Under Acoustic Excitation," *Journal of Sound and Vibration*, Vol. 313, Nos. 3–5, 2008, pp. 449–471.
doi:10.1016/j.jsv.2007.12.018
- [14] Tam, C. K. W., Ju, H., Jones, M. G., Watson, W. R., and Parrott, T. L., "A Computational and Experimental Study of Resonators in Three Dimensions," *Journal of Sound and Vibration*, Vol. 329, No. 24, 2010, pp. 5164–5193.
doi:10.1016/j.jsv.2010.06.005
- [15] Zhang, Q., and Bodony, D. J., "Numerical Investigation and Modelling of Acoustically Excited Flow Through a Circular Orifice Backed by a Hexagonal Cavity," *Journal of Fluid Mechanics*, Vol. 693, Feb. 2012, pp. 367–401.
doi:10.1017/jfm.2011.537
- [16] Zhang, Q., and Bodony, D. J., "Direct Numerical Investigation of Acoustic Liners with Single and Multiple Orifices Grazed by a Mach 0.5 Boundary Layer," AIAA Paper 2016-3626, 2016.
doi:10.2514/6.2016-3626
- [17] Mendez, S., and Eldredge, J. D., "Acoustic Modeling of Perforated Plates with Bias Flow for Large-Eddy Simulations," *Journal of Computational Physics*, Vol. 228, No. 13, 2009, pp. 4757–4772.
doi:10.1016/j.jcp.2009.03.026
- [18] Tournadre, J., Desmet, W., and Martínez-Lera, P., "Evaluation of Temperature Effects on Passive Acoustic Dampers with a Frequency-Domain Linearized Navier–Stokes Equations Solver," *23rd International Conference on Sound and Vibration*, The International Institute of Acoustics and Vibration (IIAV) and Laboratory of Transportation Environmental Acoustics (LTEA) of the Univ. of Thessaly Paper 2016-857, Athens, Greece, July 2016, http://iiav.org/archives_icsv_last/2016_icsv23/content/papers/papers/full_paper_857_20160523171052430.pdf [retrieved 2016].
- [19] Ji, C., and Zhao, D., "Lattice Boltzmann Investigation of Acoustic Damping Mechanism and Performance of an In-Duct Circular Orifice," *Journal of the Acoustical Society of America*, Vol. 135, No. 6, 2014, pp. 3243–3251.
doi:10.1121/1.4876376
- [20] Tournadre, J., Förner, K., Polifke, W., Martínez-Lera, P., and Desmet, W., "Determination of Acoustic Impedance for Helmholtz Resonators Through Incompressible Unsteady Flow Simulations," *AIAA Journal*, 2016 (available online).
doi:10.2514/1.J055337
- [21] Ingard, U., "On the Theory and Design of Acoustic Resonators," *Journal of Acoustical Society of America*, Vol. 25, No. 6, 1953, p. 1037.
doi:10.1121/1.1907235
- [22] Ingard, U., and Ising, H., "Acoustic Nonlinearity of an Orifice," *Journal of Acoustical Society of America*, Vol. 42, No. 1, 1967, pp. 6–17.
doi:10.1121/1.1910576
- [23] Melling, T. H., "The Acoustic Impedance of Perforates at Medium and High Sound Pressure Levels," *Journal of Sound and Vibration*, Vol. 29, No. 1, 1973, pp. 1–65.
doi:10.1016/S0022-460X(73)80125-7
- [24] Cummings, A., "Transient and Multiple Frequency Sound Transmission Through Perforated Plates at High Amplitude," *Journal of the Acoustical Society of America*, Vol. 79, No. 4, 1986, pp. 942–951.
doi:10.1121/1.393691
- [25] Hersh, A. S., Walker, B. E., and Celano, J. W., "Helmholtz Resonator Impedance Model, Part I: Nonlinear Behavior," *AIAA Journal*, Vol. 41, No. 5, 2003, pp. 795–808.
doi:10.2514/2.2041
- [26] Singh, D. K., and Rienstra, S. W., "Nonlinear Asymptotic Impedance Model for a Helmholtz Resonator Liner," *Journal of Sound and Vibration*, Vol. 333, No. 15, 2014, pp. 3536–3549.
doi:10.1016/j.jsv.2014.03.013
- [27] Disselhorst, J. H. M., and Wijngaarden, L. V., "Flow in the Exit of Open Pipes During Acoustic Resonance," *Journal of Fluid Mechanics*, Vol. 99, No. 2, 1980, pp. 293–319.
doi:10.1017/S0022112080000626
- [28] Atig, M., Dalmont, J.-P., and Gilbert, J., "Termination Impedance of Open-Ended Cylindrical Tubes at High Sound Pressure Level," *Comptes Rendus de l'Académie des Sciences. Série IIb, Mécanique*, Vol. 332, No. 4, 2004, pp. 299–304.
doi:10.1016/j.crme.2004.02.008
- [29] Temiz, M. A., Tournadre, J., Lopez Arteaga, I., Martínez-Lera, P., and Hirschberg, A., "Effect of Orifice Geometry on the Non-Linear Acoustic Resistance of Perforated Plates in the Transition Regime," *22nd International Conference on Sound and Vibration*, The International Institute of Acoustics and Vibration (IIAV) and the Acoustical Soc. of Italy (AIA) Paper 2015-1014, Florence, Italy, 2015, http://iiav.org/archives_icsv_last/2015_icsv22/content/papers/papers/full_paper_1014_20150315164202977.pdf [retrieved 2016].
- [30] Laudien, E., Pongratz, R., Piero, R., and Preclik, D., "Fundamental Mechanisms of Combustion Instabilities: Experimental Procedures Aiding the Design of Acoustic Cavities," *Liquid Rocket Engine Combustion Instability*, Progress in Astronautics and Aeronautics, AIAA, Washington, D.C., 1995, pp. 377–399.
doi:10.2514/5.9781600866371.0377.0399
- [31] Förner, K., Temiz, M. A., Polifke, W., Lopez Arteaga, I., and Hirschberg, A., "On the Non-Linear Influence of the Edge Geometry on Vortex Shedding in Helmholtz Resonators," *22nd International Congress on Sound and Vibration (ICSV22)*, The International Institute of Acoustics and Vibration (IIAV) and the Acoustical Soc. of Italy (AIA) Paper 2015-1341, Florence, Italy, 2015, http://iiav.org/archives_icsv_last/2015_icsv22/content/papers/papers/full_paper_1341_20150325133515128.pdf.
- [32] Ingard, U., "Nonlinear Distortion of Sound Transmitted Through an Orifice," *Journal of the Acoustical Society of America*, Vol. 48, No. 1A, 1970, pp. 32–33.
doi:10.1121/1.1912106
- [33] Rienstra, S. W., and Hirschberg, A., "An Introduction to Acoustics," Eindhoven Univ. of Technology TR IWDE 92-06, Eindhoven, The Netherlands, 2015, <http://www.win.tue.nl/~sjoerdr/papers/boek.pdf>.
- [34] Boden, H., and Zhou, L., "An Experimental Study of the Effect of Flow and High Level Acoustic Excitation on the Acoustic Properties of Perforates and Orifices," *20th International Congress on Sound and Vibration (ICSV20)*, The International Institute of Acoustics and Vibration (IIAV) and Faculty of Science, Chulalongkorn Univ. Paper 2013-468, Bangkok, Thailand, 2013.
- [35] Zhang, Q., and Bodony, D. J., "Effects of the Turbulent Grazing Flow Over the Impedance Prediction of a Single-Orifice Helmholtz Resonator," *22nd AIAA/CEAS Aeroacoustics Conference*, AIAA, Reston, VA, 2016.
doi:10.2514/6.2016-2729
- [36] Blevins, R. D., *Applied Fluid Dynamics Handbook*, Van Nostrand Reinhold, New York, 1984, p. 71f.
- [37] OpenFOAM, Software Package, Ver. 2.3.0, OpenFOAM Foundation, London, U.K., 2014.
- [38] Poinso, T., and Lele, S. K., "Boundary Conditions for Direct Simulation of Compressible Viscous Flows," *Journal of Computational Physics*, Vol. 101, No. 1, 1992, pp. 104–129.
doi:10.1016/0021-9991(92)90046-2
- [39] Mages, A., "Numerische Untersuchung des Akustischen Nichtlinearen Dämpfungsverhaltens von Perforierten Platten und Helmholtzresonatoren," B.Sc. Thesis, Technische Univ. München, Garching, Germany, 2016, <https://mediatum.ub.tum.de/node?id=1291369> [retrieved 2016].
- [40] Bodén, H., "Acoustic Properties of Perforates Under High Level Multi-Tone Excitation," *19th AIAA/CEAS Aeroacoustics Conference*, AIAA Paper 2013-2175, 2013.
doi:10.2514/6.2013-2175

D. Papamoschou
Associate Editor



AERO-ACOUSTIC CHARACTERIZATION OF HELMHOLTZ RESONATORS IN THE LINEAR REGIME WITH SYSTEM IDENTIFICATION

Kilian Förner and Wolfgang Polifke

Professur für Thermofluidynamik, Technische Universität München, Germany
e-mail: foerner@tfd.mw.tum.de

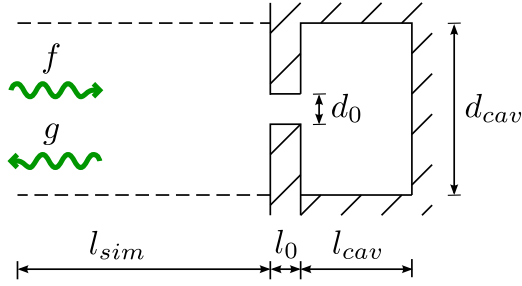
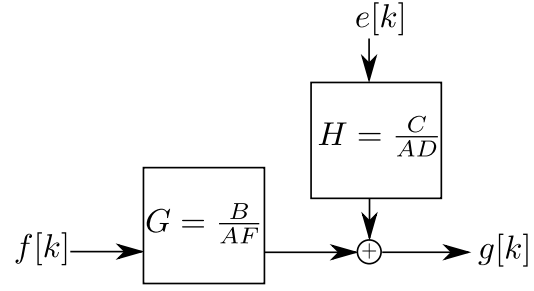
The dissipation of acoustic energy in Helmholtz resonators is investigated by means of large eddy simulation (LES) and system identification. At low sound pressure level, thermo-viscous effects dominate this dissipation. This is linear, i. e., independent of perturbation amplitude. LES/system identification methods are applied in this study to the linear regime. For that purpose, the system is interpreted as a single-input / single-output system of two characteristic waves. An Output-Error model for the reflection coefficient valid for the whole frequency range of interest is estimated from a single LES time series. The resonator admittance and impedance are derived from that model. For a set of test cases, comparison against experimental results and established models shows good agreement for the gain and phase of the admittance as well as of the reactance. The acoustic resistance value is captured with good accuracy close the eigenfrequency of the resonator.

1. Introduction

Acoustic resonators, such as Helmholtz resonators, perforated liners, or quarter wave length cavities, are commonly used to induce dissipation of acoustic energy in combustion systems like rocket combustion chambers, aero-engines, or gas turbines [1]. Thus, they can stabilize the combustion process or reduce the emitted sound to the environment.

The acoustic behavior of such resonators is often characterized by their acoustic impedance. The impedance describes the ratio of pressure and acoustic velocity and, thus, also how much energy is dissipated in the device. In the literature, there are several studies available that determine resonator impedance by empirical, analytical, or numerical means in dependency of frequency and sound pressure level (SPL). For example, Hersh *et al.* [2] and Melling [3] carried out experiments. For analytical derivations, refer for instance to [4, 5]. These analytical models introduce empirical correlation factors. Numerical studies approximating the impedance can be found, e. g., in [6, 7]. But none of these studies applies system identification (SI) methods as it is done here. SI methods promise accurate estimations over the whole frequency range of interest using a single time series data set.

In this study, the damping behavior of the Helmholtz resonator is examined numerically using the LES/SI approach and is organized as follows: First in Sec. 2, fundamentals of the Helmholtz resonator are reviewed and discussed. In Sec. 3, the answer of the resonator to well-designed broadband excitation is tracked. The gained CFD input-output data is used to perform a SI in the linear regime. The estimated reflection coefficient model and the derived the admittance as well as the impedance are validated against experiments and analysis before a conclusion and outlook are given in Sec. 4.


Figure 1: Sketch of the Helmholtz resonator domain with acoustic waves f and g .

Figure 2: Block diagram of a generic discrete linear model with input $f[k]$ and output $g[k]$.

2. Analysis of the Helmholtz Resonator

A Helmholtz resonator as sketched in Fig. 1 consists of a compact volume connected to the chamber by its neck. Qualitatively, the behavior of this resonator can be described as a mass-spring-damper system. The mass of the gas inside the neck is accelerated by the fluctuating chamber pressure. On the other side, the compressible gas in the backing volume acts as a spring. The motion in the neck causes viscous losses close to the walls. Increasing the excitation amplitudes leads to flow separation at the neck of the resonator, which converts acoustic perturbation energy to the hydrodynamic mode. The vortices formed remain laminar for moderate excitation levels and turn turbulent for yet larger levels. This effect is strongly nonlinear and increases the dissipation considerably. Close to the eigenfrequency of this systems, the motion in the neck is strongest and thus most acoustical losses occur in that frequency range.

Starting from mass and momentum equations, Keller and Zauner [4] developed the following expression for the fluctuating velocity u' in the neck:

$$(1) \quad \underbrace{(1+s)l_e\bar{\rho}}_{\text{I}}\ddot{u}' + \left(\underbrace{s\bar{\rho}(l_0+l_s)\omega}_{\text{IIa}} + \underbrace{\zeta\bar{\rho}|u'|}_{\text{IIb}} \right) \dot{u}' + \underbrace{\frac{A\bar{\rho}c^2}{V}}_{\text{III}} u = \underbrace{-p'}_{\text{IV}}.$$

Hereby, the parameters A and l_0 refer to the neck area and length, respectively. The corrected length l_e corresponds to the neck length plus a correction taking the additional mass next to the neck ends into account which participates in the oscillation. Similarly, l_s denotes a friction correction length and $\zeta \approx 1 - (d_0/d_{cav})^4$. The density is denoted by $\bar{\rho}$ and the fluctuating pressure by p' . The so-called boundary layer parameter s reflects the thermo-viscous dissipation.

This semi-analytical equation clearly shows the character of a mass-spring-damper system as described above, which is excited by the external fluctuating pressure p' (term IV). Term I accounts for the inertia of the mass within the neck. The compressibility of the backing volume is reflected in term III. The losses are included in terms II, where the first one (a) reflects the linear, thermo-viscous dissipation due to friction of the oscillating fluid at the neck walls. The second term (b) accounts for the nonlinear losses due to vortex shedding. This is illustrated in Fig. 3: For a small excitation amplitude, the flow does not separate as illustrated in Fig. 3(a). Increasing the amplitude leads vortex shedding at the edges and the flow loses its largely irrotational nature as show in Fig. 3(b). By this process, energy is extracted from the acoustic mode – which is irrotational – and fed into a hydrodynamic mode in form of vortices. These vortices are finally dissipated by the turbulent cascade process.

For small Stokes numbers $d_0 \ll \delta_s$, the boundary layer parameter can be estimated as $s = 1/d_0(1 + (\kappa - 1)/\sqrt{Pr})\sqrt{2\nu/\omega}$. The variables Pr , κ , and ν denote the Prandl number, the heat capacity ratio, and the kinematic viscosity, respectively. According to Ingard [9], the correction lengths can be estimated as $l_s \approx d_0$ and, for large aspect ratios ($d_0/\sqrt[3]{V} \ll 1$), $l_e \approx l_0 + 8/(3\pi)d_0$.

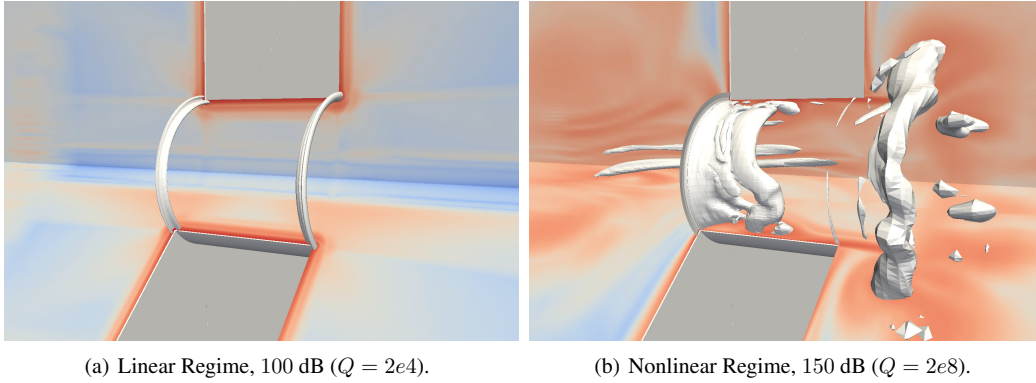


Figure 3: Vortices visualized by isosurfaces of the Q-criterion [8] for different SPLs¹ during the inflow excited close to eigenfrequency; background colored by vorticity in logarithmic scale.

The behavior of an acoustic resonator is often described in the frequency domain. Assuming harmonic periodicity – i. e., $u' = \hat{u} e^{i\omega t}$ and $p' = \hat{p} e^{i\omega t}$ – Eq. (1) can be rewritten as

$$(2) \quad (1 + s) l_e \bar{\rho} \omega i \hat{u} + (s \bar{\rho} (l_0 + l_s) \omega + \zeta \bar{\rho} \hat{u}) \hat{u} - \frac{A \bar{\rho} c^2}{V \omega} i \hat{u} = -\hat{p}.$$

The angular eigenfrequency of this system is given as:

$$(3) \quad \omega_{eig} = c \sqrt{\frac{A}{V(1+s)l_e}}.$$

Introducing the crude linearization $\zeta \bar{\rho} \hat{u}^2 \approx \epsilon_{nl} s \bar{\rho} d_0 \omega \hat{u}$ with a loss factor ϵ_{nl} , Eq. (2) can be rewritten in terms of the impedance [10]:

$$(4) \quad Z_m(\omega) = \frac{\hat{p}}{\hat{u}} = \bar{\rho} \left(1 + \frac{\kappa - 1}{\sqrt{Pr}} \right) \left(1 + \epsilon_{nl} + \frac{l_0}{d_0} \right) \sqrt{2\nu\omega} + i \left(l_e \bar{\rho} \omega (1 + s) - \frac{A \bar{\rho} c^2}{V \omega} \right).$$

Note that such a nonlinear factor ϵ_{nl} depends on both the geometry and strongly on the SPL [11]. For the following comparison, the impedance expression of the cavity mouth Z_m is scaled by the area ratio of the tube to mouth, i. e., $Z = d_{cav}^2 / d_0^2 Z_m$. The real part of the impedance Z is referred to as *resistance* and its imaginary part as *reactance*.

3. System Identification in the Linear Regime

In this section, the geometric and numerical setup used in this study are presented. Linear SI methods are introduced before the results of the identification are compared against analytical and empirical descriptions.

3.1 Geometric and Numerical Setup

The response of a Helmholtz resonator as sketched in Fig. 1 with a cylindrical neck and the backing volume is investigated numerically for three cases listed in Tab. 1 under ambient conditions. For validation purposes, the setups are chosen corresponding to the study of Hersh *et al.* [2].

¹ $20 \log_{10}(p_{rms}/20 \mu\text{Pa})$

Case I	Case II	Case III	Cases I – III		
l_0	l_0	l_0	d_0	l_{cav}	d_{cav}
5.08 cm	0.635 cm	0.159 cm	0.635 cm	2.54 cm	5.08 cm

Table 1: Geometry dimensions for the three cases investigated this study.

Acoustic excitation is imposed at the boundary opposite to the resonator situated at a distance $l_{sim} = 10$ cm. Shortly after this inlet, area averaged measurements are evaluated across a reference plane. The computational domain is set long enough such that non-acoustic disturbances occurring closer to the resonator do not influence the measurements. The acoustics is modeled using two Riemann invariants f and g which can be imaged as waves traveling with the speed of sound c in right and left direction, respectively. In absence of mean flow as in this study, they are defined as $f = 1/2(p' / (\bar{\rho}c) + u')$ and $g = 1/2(p' / (\bar{\rho}c) - u')$. At the inlet, a f wave signal can be imposed and low acoustic reflection of the outgoing g wave is realized by using Navier-Stokes characteristics boundary conditions (NSCBC), c. f. [12]. For the hard walls, no-slip boundary conditions are set, whereas, for the artificial boundaries marked by dashed lines in Fig. 1, slip conditions are utilized.

The compressible Navier-Stokes equations with k -equation eddy-viscosity model are solved using the Pimple algorithm of OpenFOAM [13] on block structured o-grids with at least 0.85 million cells. Each mesh resolution close to the neck walls is set fine enough to resolve the boundary layer for the frequency range of interest well. The boundary thickness can be estimated with the Stokes length $\delta_s = 2\pi\sqrt{2\nu/\omega}$, c. f. [6]. A comparison of radial profile of the root mean square of the axial velocity in the middle of the neck against the analytical solution in a infinitely long pipe [14] shows a good agreement, indicating that the boundary layer is resolved well. In the main parts, the acoustic CFL number $c\Delta t/\Delta x$ is clearly below unity. Close to the walls, this number is larger, but, by using implicit time integration, the acoustics are still resolved accurately in those regions. It should be emphasized that the tolerance for stop criterion for outer iteration loops accounting for compressible pressure-velocity coupling must be set low. Otherwise, the simulation could easily fail to express the speed of sound correctly and, accordingly, the a wrong resonator eigenfrequency would be predicted.

For the identification, a broadband input signal with a SPL of 75 dB is generated. A priori monofrequent simulations close to the eigenfrequency showed (see, e. g., in Fig. 3) that for such a moderate excitation level the flow remains in the linear regime for the frequency range of interest, i. e., the flow does not separate at the edges. In other words, the dominant nonlinearity in Eq. (1) - term IIb - stays small. The signal is designed in a way that it excites the whole frequency spectrum of interest and steep changes in the input signal are avoided, which could otherwise cause numerical difficulties. The requirements above are satisfied by a signal construction according to [15]. Doubling the number of cells provides a very similar response to such a signal. Thus, the solution can be expected to be independent of the mesh in the linear regime.

3.2 Methodology

In this section, linear SI methods are applied to identify a model of the resonator dynamics. Such methods have already been successfully applied to other thermo- or aero-acoustic systems, see, e. g., a review by Polifke [16] or Jaensch *et al.* [17] for recent developments. Linear SI methods are only applicable to dynamical systems behaving predominately in a linear manner. By construction of the input signal, this condition is satisfied, see Sec. 3.1. Thus, the following analysis is clearly restricted to the linear regime without flow separation. Using this methodology, the reflection coefficient over the whole frequency range of interest is estimated from time series data of a single, broadband excited CFD simulation.

The resonator can be considered as a single-input / single-output (SISO) system with input and output data $f[k]$ and $g[k]$, respectively. Hereby, k denotes the discrete time $k = t/\Delta t$ where Δt is the

sampling interval. The general form of a linear, parametric model is given as

$$(5) \quad A(q^{-1})g[k] = \frac{B(q^{-1})}{F(q^{-1})}f[k] + \frac{C(q^{-1})}{D(q^{-1})}e[k],$$

where q stands for the time shift operator and $e[k]$ is Gaussian white noise. The variables A , B , C , D , and F are polynomials in q^{-1} , so for instance $A(q^{-1}) = \sum_{i=0}^{n_a} a_i q^{-i}$. The polynomials A , C , D , and F are defined such their 0th coefficients are unity, thus $a_0 = c_0 = d_0 = f_0 = 1$. Figure 2 illustrates this process as a block diagram. The possible infinite answer of a system can be parametrized by the finite set of polynomial coefficients collected in the vector $\theta = (a_1, \dots, a_{n_a}, b_0, \dots, b_{n_b-1}, c_1, \dots, c_{n_c}, d_1, \dots, d_{n_d}, f_1, \dots, f_{n_f})^T$. Setting restrictions on these polynomials corresponds to choosing a specific model for the identification.

The system is described by two transfer functions, one for the input data R and one for the noise H . They are given as

$$(6) \quad R(q^{-1}) = \frac{B(q^{-1})}{A(q^{-1})F(q^{-1})} \quad \text{and} \quad H(q^{-1}) = \frac{C(q^{-1})}{A(q^{-1})D(q^{-1})}.$$

Knowing the parameters θ and all previous time steps up to $k-1$, the one step ahead prediction $\tilde{g}[k|k-1](\theta)$ for the next observed value $g[k]$ is calculated as

$$(7) \quad \tilde{g}[k|k-1](\theta) = H^{-1}(q^{-1})R(q^{-1})f[k] + (1 - H(q^{-1}))g[k].$$

Now, the parameters θ are determined in such a way that the squares of the discrepancies are minimized, i. e., the following optimization problem has to be solved:

$$(8) \quad \hat{\theta} = \underset{\theta}{\operatorname{argmin}} \sum_k (y[k] - \tilde{g}[k|k-1](\theta))^2.$$

The estimated model is assign with these optimal parameters $\hat{\theta}$. This procedure is called *prediction-error minimization* (PEM).

In this study, the Output-Error model is applied. This corresponds to a case where A as well as the noise model H are set to unity in Eq. (6) and the other polynomials can be chosen independently. This model was chosen since it turned out that modeling the error does not bring benefits for the resonator setup in the linear regime. Before identification, the CFD time series are shifted with respect to each other to account for the time it takes to travel from the reference plane to the resonator and back. Moreover, the CFD raw data, which is highly resolved in time, is downsampled in order to stabilize the identification process.

3.3 Results

In the following, the properties of estimated 2nd order Output-Error models ($n_f = 2$, $n_b = 3$) for the three test cases (see Tab. 1) are discussed and compared to experimental results [2] as well as to the analytic behavior described by Eq. (4). The nonlinear factor ϵ_{nl} is estimated according to Garrison *et al.* [11] as $\epsilon_{nl} \approx 1.62 (p_0/47.88 \text{ Pa})^{0.93}$, where p_0 is the amplitude of the incoming wave. In the linear regime, the value of the expression above is – as expected – quite small (0.0043). In all the following plots it is evident that the analytical model predicts a too low eigenfrequency for short neck lengths. This fact is not mentioned explicitly anymore.

From the estimated reflection coefficient R , the normalized impedance Z and admittance $Y = 1/Z$ can be derived from the relation

$$(9) \quad R(\omega) = \frac{\hat{g}}{\hat{f}} = \frac{Z-1}{Z+1} = \frac{1-Y}{1+Y},$$

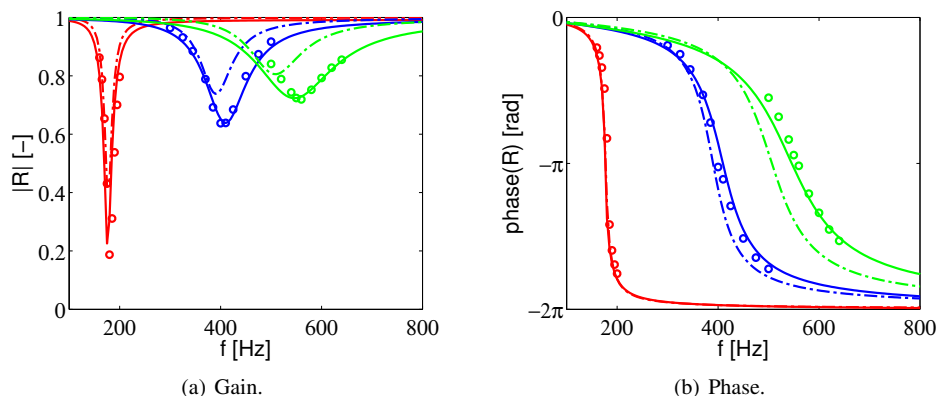


Figure 4: Reflection coefficient R of the estimated model (solid line), analytical solution Eq. (4) (dashed line), experiments [2] (circles) for Case I in red, Case II in blue, and Case III green.

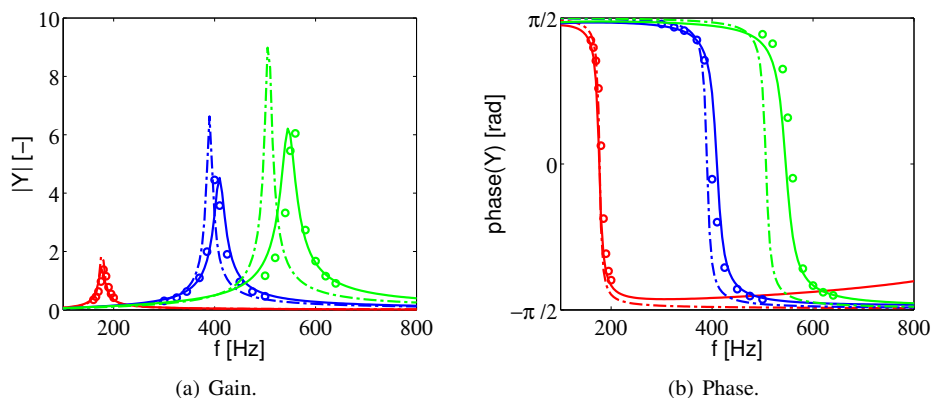


Figure 5: Normalized admittance Y of the estimated model (solid line), analytical solution Eq. (4) (dashed line), experiments [2] (circles) for Case I in red, Case II in blue, and Case III green.

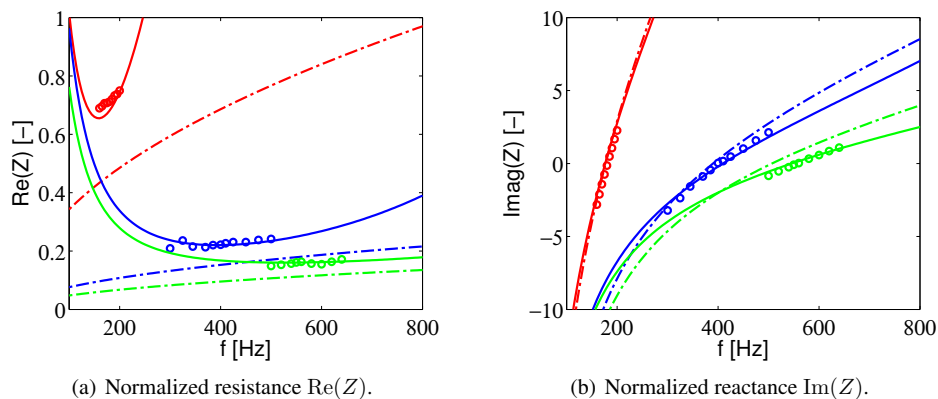


Figure 6: Normalized impedance Z of the estimated model (solid line), analytical solution Eq. (4) (dashed line), experiments [2] (circles) for Case I in red, Case II in blue, and Case III green.

where the $\hat{\cdot}$ indicates the Fourier transform of the associated quantity. Both the impedance Y and admittance Z are both normalized using the free impedance $\bar{\rho}c$ in the following.

The frequency response of R for these approaches and for all test cases is plotted in Fig. 4. The band stop character of R can clearly be observed considering the gain curves in Fig. 4(a). In the vicinity of the corresponding eigenfrequency, the gain is small, whereas it is close to unity away from this range. The three gain curves qualitatively match for all test cases. The estimated models capture the gain at eigenfrequency correctly, whereas the analytical model underestimates this quantity slightly. The phase of the response shown in Fig. 4(b) behaves similarly for all approaches. For low and high frequencies, the input and output signals are in phase and close to the eigenfrequency in antiphase.

The frequency response of the normalized admittance Y is displayed in Fig. 5. The admittance can be interpreted as the transfer function of the SISO system with fluctuating pressure \hat{p}' as input and velocity \hat{u}' as output. The gain shows a high resonant response close to the eigenfrequency, see Fig. 5(a). Figure 5(b) presents the corresponding phase curve for the admittance. For low and high frequencies the phase difference of \hat{p}' and \hat{u}' is $\pi/2$ and $-\pi/2$, respectively. At the eigenfrequency, the signals \hat{p}' and \hat{u}' are in phase. This behavior is described in the same way for the three cases.

Figure 6 shows the normalized impedance Z in its resistance/reactance representation. The reactance curves of the different approaches shown in Fig. 6(b) agree very well with each other for all cases. The magnitudes of the resistance are estimated correctly close to the corresponding eigenfrequency by the Output-Error models even though the trends are expressed incorrectly, see Fig. 6(a). This discrepancy in the trend can be explained with the ill-conditioned transformation from R to the resistance $\text{Re}(Z)$. Away from the eigenfrequency, the reactance dominates the impedance due to its larger numerical value and, thus, a wrong trend in the resistance is not manifested in the reflection coefficient as long as its value is good close to the eigenfrequency. The analytic model reflects the trend well, but the absolute values of the resistance are underestimated for the three test cases.

4. Conclusion and Outlook

The dynamic behavior of a Helmholtz Resonator has been analyzed. First, an analytical approach has been reviewed, where the movement of the gaseous mass within the neck is described in analogy to a mass-spring-damper system. By linearization of the nonlinear ODE derived from that model, an impedance model can be derived.

The flow in the vicinity of the neck has been examined by means of CFD simulations. For low SPLs, the flow does not separate at the edges and, thus, the resonator dynamics can be expected to behave linear in that regime. At higher excitation amplitudes, vortex shedding occurs, which leads to additional, nonlinear damping.

In the linear regime, a system identification has been performed on broadband CFD time series data using a 2nd order Output-Error model. This process provides a model that is valid over the whole frequency range of interest using the data of a single simulation. From the estimated reflection coefficient, the admittance as well as the impedance have been derived. The estimated quantities of each test case have been compared to analytical and empirical descriptions. The reflection coefficient and the admittance have always matched the reference values very well. Choosing the resistance/reactance representation for the impedance, the values of the reactance curves have agreed with each other for all three approaches. The resistance values close to the corresponding eigenfrequency have been caught well by the estimated models, but have shown wrong trends due to the ill-conditioned relation of resistance to reflection coefficient.

The present results demonstrate the feasibility of the CFD/SI method for this type of problem. The CFD/SI approach will be extended to the nonlinear regime in order to describe the resonator behavior at higher SPLs. Nonlinear SI methods, as for instance neural networks, can in principle account for such effects.

Acknowledgments

Financial support has been provided by the German Research Foundation (Deutsche Forschungsgemeinschaft – DFG) in the framework of the Sonderforschungsbereich Transregio 40, Project A3. Furthermore, the authors would like to thank the Leibniz Supercomputing Centre (LRZ) for the access to its cluster system.

REFERENCES

1. Zhao, D. and Li, X. Y. A Review of Acoustic Dampers Applied to Combustion Chambers in Aerospace Industry, *Progress in Aerospace Sciences*, [Online.] available: <http://dx.doi.org/10.1016/j.paerosci.2014.12.003>, (2014).
2. Hersh, A. S., Walker, B. E. and Celano, J. W. Helmholtz Resonator Impedance Model, Part 1: Nonlinear Behavior. *AIAA Journal*, **41**(5), 795–808, (2003).
3. Melling, T. H. The Acoustic Impedance of Perforates at Medium and High Sound Pressure Levels, *Journal of Sound and Vibration*, **29**(1), 1 – 65, (1973).
4. Keller, J. J. and Zauner, E. On the Use of Helmholtz Resonators as Sound Attenuators, *Zeitschrift für angewandte Mathematik und Physik ZAMP*, **46**(3), 297-327, (1995).
5. Singh, D. K. and Rienstra, S. W. Nonlinear Asymptotic Impedance Model for a Helmholtz Resonator, *Journal of Sound and Vibration*, **333**(15), 3536-3549, (2014).
6. Tam, C. K. W., Ju, H., Jones, M. G., Watson, W. R. and Parrott T. L. A Computational and Experimental Study of Resonators in Three Dimensions, *Journal of Sound and Vibration*, **329**(24), 5164–5193, (2010).
7. Zhang, Q. and Bodony, D. J. Impedance Prediction of Three-Dimensional Honeycomb Liners with Laminar/Turbulent Boundary Layers using DNS, *AIAA Paper 2011-2727* Presented at: 17th AIAA/CEAS Aeroacoustics Conference, (2013).
8. Hunt, J. C. R., Wray, A. A. and Moin, P. Eddies, Stream, and Convergence Zones in Turbulent Flows, *Center for Turbulence Research Report CTR-S88*, 193-208, (1988).
9. Ingard., U. On the Theory and Design of Acoustic Resonators, *Journal of Acoustical Society of America*, **25**(6), 1037–1061, (1953).
10. Cárdenas Miranda, A. *Enhanced Heat Transfer in Pulsating Flows*, Ph. D. thesis, Lehrstuhl für Thermodynamik, TU München, (2014).
11. Garrison, G. D., Schnell, A. C., Baldwin, C. D. and Russell, P. R. Suppression of Combustion Oscillations with Mechanical Damping Devices, *Interim Report PWA FR-3299, Pratt & Whitney Aircraft*, (1969).
12. Polifke, W., Wall, C. and Moin, P. Partially Reflecting and Non-Reflecting Boundary Conditions for Simulation of Compressible Viscous Flow, *Journal of Computational Physics*, **213**, 437–449, (2006).
13. OpenFOAM (Open Field Operation and Manipulation), see <http://www.openfoam.org>.
14. White, F. M. *Viscous Fluid Flow (Third Edition)*, McGraw-Hill Mechanical Engineering, Chp. 3, (2006).
15. Föller, S. and Polifke, W. Advances in Identification Techniques for Aero-Acoustic Scattering Coefficients from Large Eddy Simulation, *Proceedings of the 18th International Congress on Sound and Vibration*, Rio de Janeiro, Brazil, (2011).
16. Polifke, W. Black-Box System Identification for Reduced Order Model Construction, *Annals of Nuclear Energy*, **67c**, 109–128, (2014).
17. Jaensch, S., Emmert, T. and Polifke, W. A Grey-Box Identification Approach for Thermoacoustic Network Models, *Proceedings of ASME Turbo Expo 2014*, (2014).



Contents lists available at ScienceDirect

Journal of Sound and Vibration

journal homepage: www.elsevier.com/locate/jsvi

Nonlinear aeroacoustic characterization of Helmholtz resonators with a local-linear neuro-fuzzy network model



K. Förner*, W. Polifke

Technische Universität München, Fakultät für Maschinenwesen, Boltzmannstr. 15, 85748 Garching b. München, Germany

ARTICLE INFO

Article history:

Received 3 February 2017

Received in revised form

27 June 2017

Accepted 1 July 2017

Handling Editor: I. Lopez Arteaga

Keywords:

Helmholtz resonator

Acoustic liner

Nonlinear acoustics

Nonlinear system identification

CFD/SI

Impedance

ABSTRACT

The nonlinear acoustic behavior of Helmholtz resonators is characterized by a data-based reduced-order model, which is obtained by a combination of high-resolution CFD simulation and system identification. It is shown that even in the nonlinear regime, a linear model is capable of describing the reflection behavior at a particular amplitude with quantitative accuracy. This observation motivates to choose a *local-linear* model structure for this study, which consists of a network of parallel linear submodels. A so-called fuzzy-neuron layer distributes the input signal over the linear submodels, depending on the root mean square of the particle velocity at the resonator surface. The resulting model structure is referred to as an *local-linear neuro-fuzzy network*. System identification techniques are used to estimate the free parameters of this model from training data. The training data are generated by CFD simulations of the resonator, with persistent acoustic excitation over a wide range of frequencies and sound pressure levels. The estimated nonlinear, reduced-order models show good agreement with CFD and experimental data over a wide range of amplitudes for several test cases.

© 2017 Elsevier Ltd All rights reserved.

1. Introduction

Helmholtz resonators, as schematically sketched in Fig. 1, are used in various industrial applications to absorb sound. Arrays of such resonators are applied as liners in jet engines to reduce the emission of sound to the environment [1, p. 214ff]. Combustion systems as for instance gas turbines can become thermoacoustically unstable due to the feedback between the unsteady heat release and the acoustics within the chamber. Helmholtz resonators are often inserted to stabilize the combustion process [2].

The present paper introduces a data-based reduced-order model (ROM), a so-called local-linear neuro-fuzzy network. This model is defined in the time domain, is capable of considering a change in amplitude, and can capture nonlinear effects. The data for the identification of the model parameters is generated by broadband CFD simulation. Once such a ROM is identified, it can be evaluated efficiently and may serve, e.g., as a nonlinear boundary condition in simulations of compressible flow that require acoustic boundary conditions (BC), such as computational aeroacoustics (CAA). Moreover, the methodology proposed characterizes the nonlinear resonator behavior in an efficient and robust manner, and can thus support the proper tuning of a resonator.

As mentioned above, the resonator can respond in a linear and nonlinear fashion. Linear behavior of a system means that the relation between the system input and its output can be described by a linear transfer function. A linear transfer

* Corresponding author.

E-mail address: foerner@tfd.mw.tum.de (K. Förner).

<http://dx.doi.org/10.1016/j.jsv.2017.07.002>

0022-460X/© 2017 Elsevier Ltd All rights reserved.

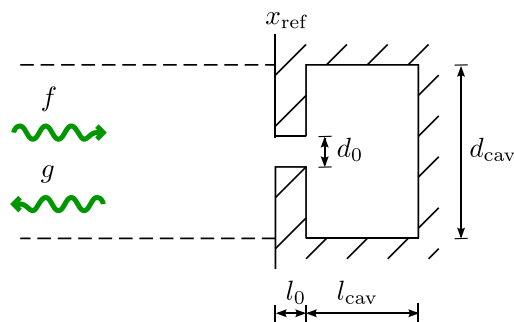


Fig. 1. Sketch with dimensioning of a Helmholtz resonator with acoustic waves f and g .

function can easily be transformed from the frequency/Laplace space to the time domain and vice versa by using the direct and inverse Fourier/Laplace transformation, respectively. If the resonator operates in the linear regime, its response is fully characterized by its impedance or equivalently by its reflection coefficient. Such a linear relation is valid for low acoustic amplitudes. However, when the particle velocity in the resonator neck increases beyond a certain level, the flow separates at the edges of the resonator leading to nonlinear effects as already early described by Sivian [3] as well as by Ingård and Labate [4]. The nonlinear behavior of an acoustic resonator manifests itself in several aspects: The most prominent nonlinear effect is that the harmonic behavior changes with the excitation amplitude. This effect can be modeled with an *impedance describing function*, which gives the impedance in dependency on the applied sound pressure level (SPL), see, e.g., Hersh et al. [5]. For many technical applications, the impedance describing function captures much of the dynamics for constant acoustic amplitudes. Scattering to higher harmonics [3,6,7] cannot be described by the impedance describing function, but this scattering remains on a very moderate level for Helmholtz resonators, see Förner et al. [8]. Moreover, the acoustic behavior at a certain frequency can noticeably be influenced by multi-tonal excitation, which means that in the excitation signal not only the that single frequency is present but also multiples of this frequencies, see Bodén Boden13, Boden16 and Serrano et al. [9].

Most available models are based on the first principle 1-D analysis of the fluctuating mass in the resonator neck, see, e.g., Rice [10], Cummings [7], Maa [11] as well as Hersh et al. [5]. An impedance describing function can be derived in a semi-analytical manner. Good agreement with experiments is achieved once the values of a set of correction parameters are correctly assigned. Such correction parameters are usually provided via correlation analysis and are valid for fixed amplitudes. That is why the transformation of this kind of model into time domain, where amplitudes vary dynamically, is not a trivial task.

The present methodology requires CFD simulations and broadband data analysis. Bodén [12,13] performed experimentally broadband forcing of an orifice and applied correlation analysis to separate the linear and the nonlinear contribution. Tam et al. [14] compared their direct numerical simulations (DNS) excited by a broadband signal against experiments. Tam et al. already showed in preceding studies [15,16] the potential of simulation to capture the resonator dynamics. The impact of purging flow is investigated via large eddy simulation by Mendez and Eldredge [17]. In a series of papers, Zhang and Bodony studied the effect of high amplitude excitation as well as the influence of laminar and turbulent grazing flow using the DNS approach, see e.g. [18,19].

The methodology proposed in this study applies the computational fluid dynamics/system identification (CFD/SI) approach to estimate a ROM, see Polifke [20]. Since usually a model structure is specified without considering explicitly the physics involved, such a model is called a “black-box model” in contrast to a “white-box model” derived from first principles. The model parameters are deduced from CFD time series, the so-called training data. In principle, the training data set can also be provided by experiment. This time series must cover the entire frequency range of interest for linear SI and also the entire amplitude range for nonlinear SI. Once the model structure is fixed, the model parameters are determined such that the difference between the model output and the training data is minimized in terms of a suitable norm. In order to ascertain good model performance, the estimated model is subsequently validated against an independent test data set. This methodology is applied in this study to several test cases without mean flow under ambient conditions. Since no restricting assumptions are made on the model structure, the proposed model should also be capable of characterizing more complex resonator configurations, as, e.g., in presence of purging or grazing flows, as well as other aeroacoustic devices, as for instance orifices.

Förner and Polifke [21] showed that the CFD/SI approach can provide quantitatively accurate black-box models for the Helmholtz resonator dynamics in the linear regime, i.e. for low excitation amplitudes. Only a very limited number of linear black-box models are available; the so-called output-error (OE) model has shown good performance. However, there exists a large variety of nonlinear models which can be used for SI. Representatives of nonlinear black-box models are Volterra series as well as artificial neural networks. These models are in principle capable of modeling any nonlinear behavior. However, for the test cases considered, a huge number of model parameters was required such that identification results that were achieved with reasonably long time series were not robust.

Therefore, this study introduces a “gray-box model” structure that exploits a priori knowledge of the system dynamics. Neuro-fuzzy networks offer the opportunity to incorporate such knowledge in the model structure, see, e.g., Nelles [22] or

Babuška and Verbruggen [23]. Building a network containing so-called fuzzy neurons offers additional freedom in the modeling. A fuzzy neuron applies a so-called membership function and becomes active only under certain conditions. The membership function takes a value within the interval $[0, 1]$. If these conditions are fully or not at all satisfied, true (1) or false (0) is assigned to this function, respectively. However, the membership function cannot only take on the values “true” and “false”, as in Boolean logic, but it can take on also every intermediate state in the interval $[0, 1]$, as in fuzzy logic.

The paper is organized as follows: Section 2 introduces acoustical quantities and the underlying physical mechanisms as well as the geometrical and computational setups of the present study. The linear system identification process using an output-error model is shown in Section 3. Moreover, the ability of that model type to characterize the resonator behavior in the linear regime as well as in the nonlinear regime in a local-linear fashion are discussed here. In Section 4, a local-linear neuro-fuzzy model to identify the nonlinear resonator response is proposed and an algorithm for the estimation of the free model parameter is derived. This procedure is applied to several test cases and validated against experimental data from the literature in Section 5. Conclusion and outlook are offered in Section 6.

2. Acoustical background and CFD setup

A Helmholtz resonator consists of a backing volume connected via a small neck to a larger volume as sketched in Fig. 1. This study considers resonators that are cylindrical, with lengths l_0, l_{cav} as well as diameters d_0, d_{cav} of the neck and the backing volume, respectively. The open area ratio d_0^2/d_{cav}^2 is denoted by σ . In the next section (Section 2.1), physical quantities to describe the resonator absorption behavior are introduced, and the pertinent mechanisms are outlined. The numerical setup used in the current study and a validation of the CFD solver is presented in Section 2.2. The design of the input signals is discussed here. Finally, the test cases considered are introduced in Section 2.3.

2.1. Acoustical quantities and physical mechanisms

The behavior of an acoustic resonator is often described in the frequency domain by its *impedance* Z . It is defined as the ratio of the Fourier transforms ($\hat{\cdot}$) of the fluctuating acoustic pressure p' and velocity u' normal to the reference surface at x_{ref} :

$$Z(\omega) = z(\omega) \rho_0 c_0 = \frac{\hat{p}'}{\hat{u}'} \quad (1)$$

The real part of the impedance is referred to as *resistance* and its imaginary part as *reactance*. Usually, the impedance is normalized with the specific impedance $\rho_0 c_0$, where ρ_0 and c_0 denote the mean density and the speed of sound, respectively.

The resonator can also be characterized in terms of characteristic wave amplitudes f and g , assuming 1-D acoustics in front of the resonator. These f and g can be considered as right and left traveling waves, respectively. In absence of mean flow, as in this study, they are defined as

$$f = \frac{1}{2} \left(\frac{p'}{\rho_0 c_0} + u' \right) \quad \text{and} \quad g = \frac{1}{2} \left(\frac{p'}{\rho_0 c_0} - u' \right) \quad (2)$$

The ratio of a normally incident wave \hat{f} to the reflected \hat{g} wave in frequency domain is called *reflection coefficient* R :

$$R(\omega) = \frac{\hat{g}}{\hat{f}} = \frac{z - 1}{z + 1} \quad (3)$$

The resonator behavior is often approximated with a simplified 1-D ordinary differential equation, see for instance Keller and Zauner [24] or Bodén and Zhou [25], which helps to understand the fundamental behavior of the resonator:

$$\underbrace{(l_0 + \Delta l) \rho_0}_{\text{I}} \frac{\ddot{u}'}{\sigma} + \underbrace{R_l}_{\text{IIa}} u' + \underbrace{\frac{1}{2} \rho_0 \frac{|\dot{u}'| u'}{\sigma^2 C_d^2}}_{\text{IIb}} + \underbrace{\frac{\rho_0 c_0^2}{l_{\text{cav}}}}_{\text{III}} u' = \underbrace{-\dot{p}'}_{\text{IV}} \quad (4)$$

The equation above has the structure of a mass-spring-damper system. The acoustic pressure (term IV) is driving the mass in the neck of the resonator. This oscillating mass is proportional to the geometrical length of the neck l_0 , elongated by a length correction Δl , cf. Ingard [26]. This correction accounts for the fluid in the vicinity of the neck taking part in the oscillation (term I). The resonator backing volume is filled with a compressible fluid, which acts like a spring (III). Losses are induced due to thermo-viscous losses described by the constant R_l (IIa) and due to flow separation (IIb). In the IIb-term, also the effect of flow contraction is captured in the so-called discharge coefficient C_d . For a harmonic signal $u'(t) = A_u \sin(\omega t)$, the term $|\dot{u}'| u'$ can be approximated by $A_u u'$ and, accordingly, the impedance can be described as:

A.6 Nonlinear Aeroacoustic Characterization of Helmholtz Resonators with a Local-Linear Neuro-Fuzzy Model

$$Z(\omega) = R_l + \frac{A_u}{2 C_d^2 \sigma^2} + i \left((l_0 + \Delta l) \rho_0 \frac{\omega}{\sigma} - \frac{\rho_0 c_0^2}{l_{\text{cav}}} \right). \quad (5)$$

In the formula above, it can be seen that an amplitude variation has a huge impact on the impedance. The nonlinear resistance ll_b is influenced, since A_u explicitly appears there. Also, the discharge coefficient C_d varies since the flow contraction mechanisms also depend on the amplitude. Moreover, the length correction Δl for the effective length in the reactance is also known to vary with the excitation amplitude, see for instance Ingard [26] or Temiz et al. [27]. In the range of small amplitudes, these effects are negligible, and the resonator is said to operate in the *linear regime*. With rising amplitudes, the nonlinear effects described above have a huge impact on the resonator response in the *nonlinear regime*. In the expressions above, a harmonic forcing with amplitude A_u is assumed. In the case of non-harmonic excitation, the root mean square (rms) of the velocity (for a fixed geometry) seems to be the parameter controlling the nonlinear behavior, see Bodén [12]. The strength of an acoustic signal is usually measured as SPL, which is defined via the rms of the acoustic pressure p_{rms} and the reference pressure $p_{\text{ref}} = 20 \mu\text{Pa}$ as

$$\text{SPL} = 20 \log_{10} \left(\frac{p_{\text{rms}}}{p_{\text{ref}}} \right) \text{dB}. \quad (6)$$

The expected behavior from the 1-D consideration above fits to experiments as for instance shown in Fig. 2 with measurements reproduced from Hersh et al. [5] for the test case HR1 (defined in Section 2.3). The resistance gets larger with increasing SPL, see, e.g., Fig. 2 on the left-hand side. The eigenfrequency can be detected by the zero-crossing of the reactance. In Fig. 2 on the right, it can be observed that the eigenfrequency shifts slightly to higher frequencies. The zero-crossing of the 140 dB reactance curve is at a higher frequency in comparison to the other curves. This nonlinear behavior manifests itself in the corresponding reflection coefficient as follows (see Fig. 3): First, the maximal absorption increases

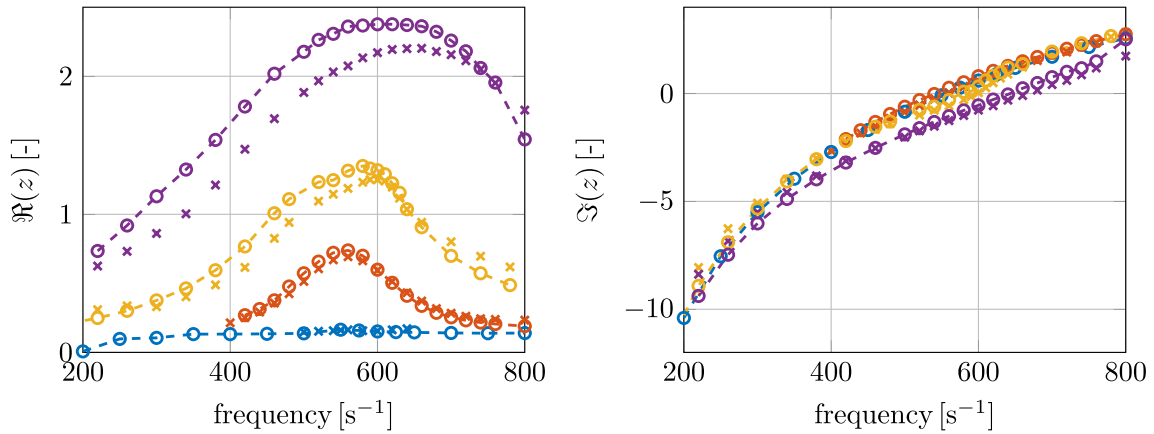


Fig. 2. Normalized impedance z for test case HR1: Measurements (\times) by Hersh et al. [5] and CFD simulations ($- \ominus -$) for 75 dB (\bullet), 120 dB (\bullet), 130 dB (\bullet), and 140 dB (\bullet).

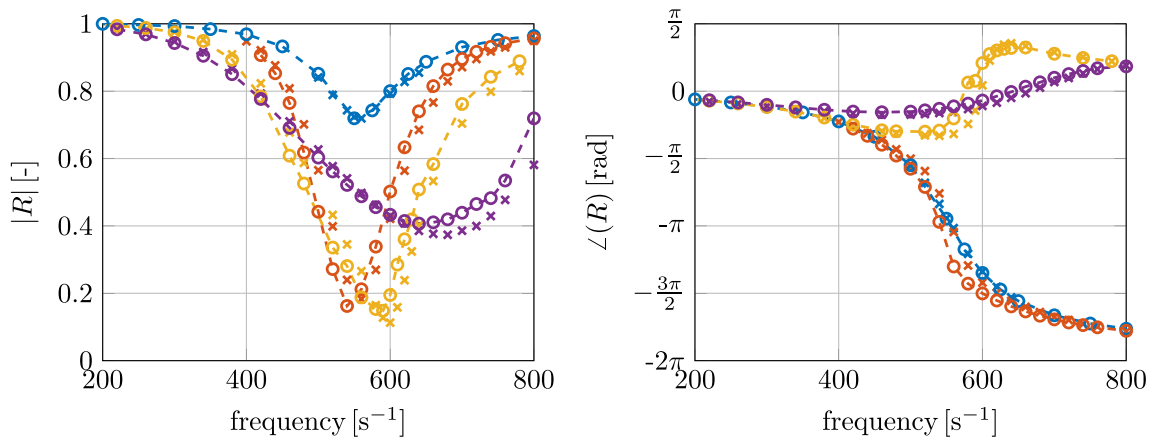


Fig. 3. Reflection coefficient R for test case HR1: Measurements (\times) by Hersh et al. [5] and CFD simulations ($- \ominus -$) for 75 dB (\bullet), 120 dB (\bullet), 130 dB (\bullet), and 140 dB (\bullet).

with SPL in the lower SPL range. When the normalized resistance exceeds unity, the maximal absorption decreases due to the so-called *over-damping* of the system, but the frequency bandwidth of high absorption becomes wider. For such an over-damped system, the phase curve differs from a normally damped system, see Fig. 3 on the right-hand side. All R -curves are in phase at frequencies far away from the eigenfrequency. Close to the eigenfrequency, normally damped systems are in antiphase, while over-damped systems are in phase.

2.2. CFD setup and solver validation

With the CFD/SI approach, training data for black-box ROMs are acquired from CFD simulations as time series of fluctuating flow variables. The CFD simulations are performed with OpenFOAM [28] solving the compressible, transient Navier-Stokes equations using the PIMPLE algorithm. The acoustic inlet boundary is realized with the Navier-Stokes characteristic boundary conditions (NSCBC) suggested by Poinso and Lele [29], where an arbitrary signal for the f wave traveling into the domain can be imposed, while maintaining a low reflection coefficient for the outgoing g wave. More details on the numerical solver are given by [21].

Results from a solver validation study for test case HR1 (defined in Section 2.3) are presented in Figs. 2 and 3. These figures show the normalized impedance and the reflection coefficient for experiments and CFD simulations considering three SPLs namely for 120, 130, and 140 dB. The numerics over-predict the resistance moderately for the 140 dB case and very slightly for the 130 dB case. Besides that small deviation in the resistance for high SPLs, all curves agree reasonably well. It can be concluded that the CFD simulation performed on a 3-D grid with 1.8 million cells is capable of capturing the acoustics in the nonlinear regime.

In order to compare simulations with measurements, the input amplitude of the f waves must be set such that the superposition of f and reflected wave $g = Rf$ matches the desired total SPL, cf. Eq. (2). Unless the reflection coefficient R is known a priori, an iterative process setting the input amplitude is required. Note that such an iterative approach of is used solely for validation purposes in this study. Besides that, the SPL in the CFD simulations is set only with respect to the input signal f , ignoring the reflected acoustic g wave, as it is also done by other authors, for instance by Zhang and Bodony [18]. This will be referred to as *incident SPL* in the following. Note that in general the incident SPLs and the actual total SPL differ from each other.

For the SI, broadband input-output data are required, which are generated by the CFD simulation. The time series of the acoustic forcing f wave and of the reflected g wave serve as input and output data set, respectively. Since the influence of 3-D effects is minor for the test cases considered [30], the broadband data for the SI was generated on a 2-D axisymmetric mesh. The acoustic input signals for the f wave are generated according to Föllner and Polifke [31]. This signal is designed such that it excites the entire frequency spectrum of interest while avoiding rapid changes in the input signal, which could cause numerical difficulties. Moreover, it shows a low autocorrelation. Otherwise, the SI might fail if an input signal with high autocorrelation would be considered [31]. The amplitude of this signal is successively ramped up in time to cover a wide range of amplitudes for the nonlinear SI. The signal with a length of 0.5 s is divided into equally sized parts on which the amplitude either is set constant or increases linearly in time to the next amplitude plateau. The nonlinear signal assesses the amplitude plateaus with incident SPLs of 75 dB, 110 dB, 120 dB, 130 dB, 140 dB, and 150 dB, respectively. This signal is plotted below in Fig. 9 of Section 4.2. For validation purposes, a second uncorrelated signal is generated [31] and ramped up in the same manner.

2.3. Test cases

Four test cases are considered in the present study. Their geometrical values are given in Table 1. To have access to experimental validation data, the test cases HR1, HR2, and HR3 are set as in Hersh et al. [5]. Test case HR4 corresponds to the test rig of Temiz [32].

3. Linear system identification on specified amplitude regimes

The idea of the CFD/SI approach is to estimate a ROM from time series generated by CFD simulation. The model structure is defined a priori, and the free model parameters are set such that a suitable objective function describing the difference

Table 1

Geometry dimensions and properties for the test cases investigated in this study. The first three configuration are set according to Hersh et al. [5] and the HR4 according to Temiz [32].

Case	l_0 [cm]	d_0 [cm]	l_{cav} [cm]	d_{cav} [cm]	f_{eig} [s ⁻¹]	σ [%]
HR1	0.159	0.635	2.54	5.08	≈560	1.56
HR2	0.318	0.635	2.54	5.08	≈490	1.56
HR3	0.635	0.635	2.54	5.08	≈400	1.56
HR4	0.4	0.42	2	5	≈380	0.71

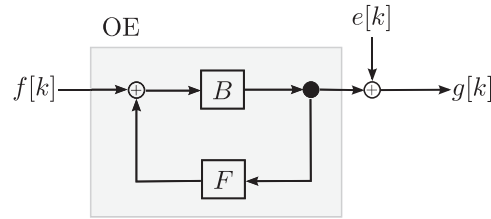


Fig. 4. Block diagram of the output-error model with input $f[k]$ and output $g[k]$.

between the model prediction and the CFD data is minimized. To achieve a good result, the chosen model structure has to be suitable to describe the phenomena.

Förner and Polifke [21] have shown that a second-order output-error model captures the linear dynamics of a Helmholtz resonator with good accuracy. Such a model is by design linear and thus cannot exhibit any amplitude-dependent behavior. However, it will be shown in Section 3.4 that such a model can describe the linearized behavior for a fixed SPL regime. But first the model structure and the estimation procedure are introduced in the next sub-section (Section 3.1). Linear models are estimated for the considered test cases in Section 3.2 and the uncertainty associated with the identification process is discussed in Section 3.3.

3.1. Methodology of an output-error model estimation

Since the CFD time series is a discrete time series, also the models have to be defined in a discrete framework. The time series is sampled equidistantly with a constant time step Δt . The discrete time index k denotes the sample for the instant in time $t_k = (k - 1)\Delta t$.

The response of an output-error model – see the block diagram in Fig. 4 – depends on present and previous input as well as on previous output. The time-discrete output-error model for the input $f[k]$ and the output $g[k]$ is given as a filter, which may formally be written as a fraction of two polynomials in the time shift operator¹ q :

$$g[k] = \frac{B(q)}{F(q)}f[k] + e[k] = \frac{b_0 + b_1q^{-1} + \dots + b_{n_b}q^{-n_b+1}}{1 + f_1q^{-1} + \dots + f_{n_f}q^{-n_f}}f[k] + e[k]. \quad (7)$$

The equation above models the transfer behavior $R = B/F$. Since no perfect match between the CFD data and the estimated model can be achieved, “noise” $e[k]$ is considered in the estimation process. The noise is the difference between the CFD output and the output of the estimated model, which is assumed to be white colored. In other words, it is assumed that there remains no further information in noise, i.e. the difference of CFD and model output. The order of the transfer function R is determined by the number of free parameters n_b and n_f in numerator and denominator, respectively. In the present study, $n_b = 3$ and $n_f = 2$ for all cases considered. All free parameters are assembled in the vector $\theta_{OE} = (b_0, b_1, \dots, b_{n_b}, f_1, f_2, \dots, f_{n_f})^T$.

The task in the system identification process is to estimate the optimal values of parameters $\hat{\theta}_{OE}$. For that purpose, the time series data of the CFD simulation is used as training data set. The parameters $\hat{\theta}_{OE}$ are determined such that the difference of the model output $g[k](\theta)$ defined in Eq. (7) and of the measured CFD output $g_{CFD}[k]$ is minimized in the following sense:

$$\hat{\theta}_{OE} = \underset{\theta}{\operatorname{argmin}} \sum_k w[k](g[k](\theta) - g_{CFD}[k])^2. \quad (8)$$

This least square optimization is weighted by a weighting function $w[k]$. As long as the SPL does not vary in the training data set – which is the case in this section – the weights are set to $w[k] \equiv 1$. This ansatz to predict the free model parameters is called the prediction error method (PEM), see Tangirala [33].

The above optimization problem (8) is nonlinear and, thus, cannot be solved directly. There are several algorithms available to solve this problem, see e.g. the textbook by Keesman [34]. Here, an iterative approach is presented, where the input and output data is pre-filtered such that white noise is realized in the end. This procedure, although well-known [34], is presented here since it is helpful to construct the optimization procedure for the nonlinear model proposed in Section 4.4.

The nonlinear optimization problem can be written in a pseudo linear way:

$$\hat{\mathbf{g}} = W^{1/2} \Phi_{OE} \hat{\theta}_{OE}, \quad (9)$$

¹ Example: $q^{-1}f[k] = f[k - 1]$.

where W denotes a diagonal matrix with $w[k]$ on its diagonal. The left-hand side represents the non-disturbed model output $\hat{g}[k] = B(q)/F(q)f[k]$ for $k = n_b + 1, n_b + 2, \dots, K$ and the so-called observation matrix Φ_{OE} is defined as (for $n_b > n_f$):

$$\Phi_{\text{OE}}(f, \hat{g}) = \begin{pmatrix} f[n_b] & f[n_b - 1] & \dots & f[1] & -\hat{g}[n_b - 1] & -\hat{g}[n_b - 2] & \dots & -\hat{g}[n_b - n_f] \\ f[n_b + 1] & f[n_b] & \dots & f[2] & -\hat{g}[n_b] & -\hat{g}[n_b - 1] & \dots & -\hat{g}[n_b + 1 - n_f] \\ \vdots & & & & & & & \vdots \\ f[K] & f[K - 1] & \dots & f[K - n_b] & -\hat{g}[K - 1] & -\hat{g}[K - 2] & \dots & -\hat{g}[K - 1 - n_f] \end{pmatrix} \quad (10)$$

It can be seen that the pseudo linear system in Eq. (9) cannot be solved directly for the unknowns θ_{OE} , since θ_{OE} is also needed to define the observation matrix Φ_{OE} and the left-hand side \hat{g} of this equation. But instead of \hat{g} , the measured CFD output g_{CFD} can be used to approximate the unknowns θ_{OE} . The solution for this weighted linear least square problem (8) is given as

$$\theta_{\text{OE}} \approx \underbrace{\left(\Phi_{\text{OE}}(f, g_{\text{CFD}})^T W \Phi_{\text{OE}}(f, g_{\text{CFD}}) \right)^{-1} \Phi_{\text{OE}}(f, g_{\text{CFD}})^T W g_{\text{CFD}}}_{=: \Phi_{\text{OE}}(f, g_{\text{CFD}})_W^\dagger} \quad (11)$$

The solve operator for the weighted least square problem is denoted as $(\cdot)_W^\dagger$ in the following. With this ansatz of using g_{CFD} instead of \hat{g} , a model is estimated which has a colored noise $1/F(q) e[k]$ instead of white noise. The model with colored noise is, in fact, autoregressive with exogenous terms (ARX). It has been observed that this ARX model shows inferior quality as the output-error model for the considered problem, especially for low frequencies. This colored noise can be overcome to obtain the output-error model when input and output are pre-filtered with $1/F(q)$ as shown below.

The considerations above lead to the following iterative procedure to determine $\hat{\theta}_{\text{OE}}$ correctly, cf. [34, Chp. 6.1.4]: The vector of unknowns is initialized with zeros, i.e. $\theta_{\text{OE}}^0 = 0$. Then, the iteration $l = 1, 2, \dots$ can be started:

First, the input and output are pre-filtered using the estimated model parameters of the previous iteration step $l - 1$:

$$f^l[k] = \frac{1}{F(\theta_{\text{OE}}^{l-1})(q)} f[k] \quad \text{and} \quad g^l[k] = \frac{1}{F(\theta_{\text{OE}}^{l-1})(q)} g_{\text{CFD}}[k]. \quad (12)$$

Note that the filter is just the identity in the first iteration step $l = 1$. The observation matrix is created with these filtered quantities:

$$\Phi_{\text{OE}}^l = \Phi_{\text{OE}}(f^l, g^l). \quad (13)$$

Now, the parameter vector can be calculated as the solution of the weighted least square problem for the current iteration step l :

$$\theta_{\text{OE}}^l = \left(\Phi_{\text{OE}}^l \right)_W^\dagger g^l. \quad (14)$$

This procedure is repeated until θ_{OE}^l converges to the solution $\hat{\theta}_{\text{OE}}$, which is usually the case after a few iterations.

3.2. Linear system identification

It has been remarked above that Helmholtz resonators can be linearly characterized with a second-order output-error model [21]. Here, a time series with length 0.1 s and an incident SPL of 75 dB are used for the CFD simulations for all four test cases. The estimated reflection coefficients are presented in Fig. 5. In Fig. 6, the corresponding normalized impedance is shown for HR1. In those figures, also the empirical data from Hersh et al. [5] and Temiz [32] are included. Good agreement can be seen for all test cases.

3.3. Uncertainty and Ill-conditioned transformation to resistance

The SI process is always linked to some uncertainty in the estimated model parameters. This uncertainty can be determined using statistic techniques under the assumption the original system has the same structure as the model system. With this assumption and $W = \mathbf{1}_{K-n_b}$, the covariance matrix in the estimated parameters $\text{Cov}\hat{\theta}_{\text{OE}}$ is given as [34]:

$$\text{Cov}\hat{\theta}_{\text{OE}} = \sigma_e^2 \left(\Phi_{\text{OE}}^T \Phi_{\text{OE}} \right)^{-1}, \quad (15)$$

where σ_e denotes the empirical standard deviation of the noise $e[k]$.

This uncertainty in the model parameter manifests itself in confidence intervals of the reflection behavior. In Fig. 5, the one (68.27%) and two standard deviation (95.45%) confidence intervals are shown for gain and phase of the reflection coefficient R estimated by an output-error model trained on a 0.1 s time series in the linear regime. This 0.1 s time series is

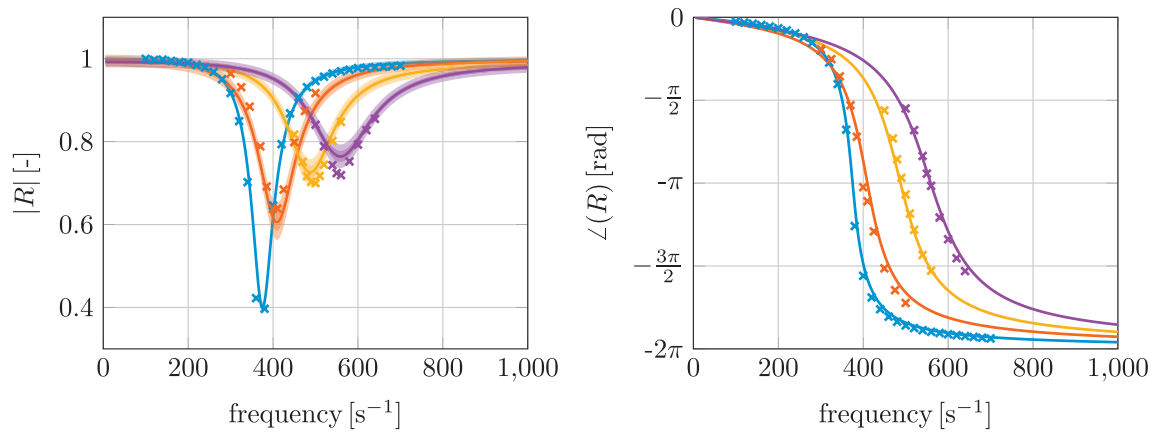


Fig. 5. SI-estimated (—) and measured (x) reflection coefficient R with 1 and 2 standard deviation confidence intervals for test cases HR1 (●), HR2 (●), HR3 (●), and HR4 (●).

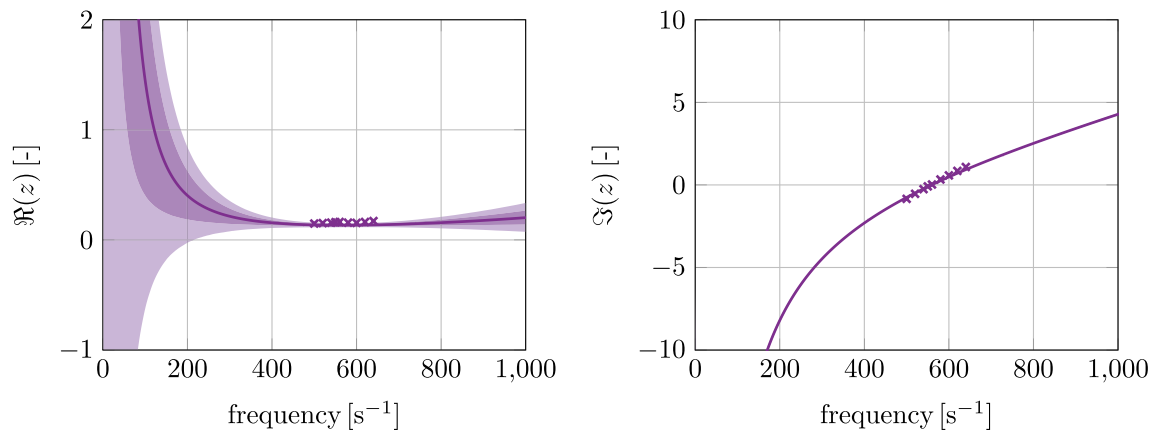


Fig. 6. SI-estimated (—) and measured (x) z with 1 and 2 standard deviation confidence intervals for test cases HR4.

sufficient to estimate the model parameters with high accuracy. For the gain $|R|$, the confidence interval can be visually detected even though they are quite small. The intervals in the phase curve can hardly be seen.

The estimated reflection behavior and its uncertainties can be propagated in an impedance representation and are shown in Fig. 6. For clarity, this is only presented for HR1. The uncertainties are propagated by Monte Carlo simulations with 1000 random experiments. Here, many models are considered with random model parameters set according to the distribution given by the covariance in Eq. (15). These models are transformed to the impedance and, then, the confidence intervals are defined by the corresponding quantiles. In the impedance representation, the impact of the uncertainty rises. The resistance $\Re(z)$ is determined with narrow uncertainty bounds only in the vicinity of the resonator eigenfrequency. Apart from that frequency, the resistance is associated with high uncertainty. This behavior arises from the ill-conditioned transformation $\Re(z) = \Re[(R + 1)/(R - 1)]$ whenever $\Re(z) \ll |\Im(z)|$. This ill-conditioned transformation does not only influence the numerical setup, but also experiments with resonance tubes, where also the reflection coefficient R is determined and the impedance z is deduced from it. Due to this ill-conditioned transformation, the following discussions concentrate on the reflection coefficient R .

3.4. Local-linear identification on specified amplitude levels

In the identification process, a linear model is estimated that provides the best fit for the training data. This model can be considered as a linearization of the actual nonlinear behavior around the current working condition. If the operating conditions in the training data sets differ, so do the estimated linear models. Different amplitude levels can be considered as different working condition, as seen in Eq. (5), where the amplitude shows up explicitly. Based on that idea, a series of linear models is estimated using data sets generated with an incident SPL of 75, 120, 130, and 140 dB, respectively. The corresponding reflection coefficients are plotted in Fig. 7. It can be seen that those models depict the trends expected for a correct representation of the nonlinear behavior: With rising SPL, the resistance also increases and, consequently, the minimal gain

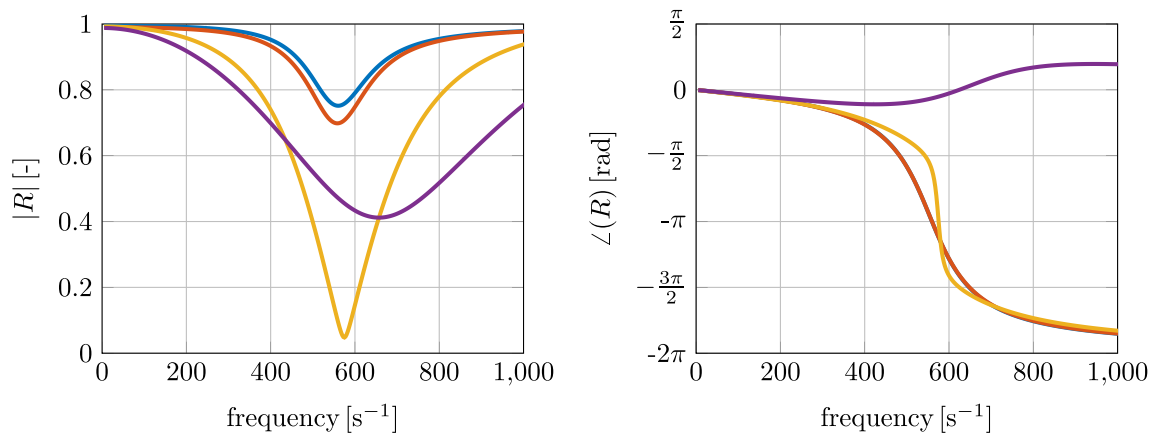


Fig. 7. CFD/SI estimated reflection coefficient R for local-linear output-error model with broadband incident SPL of 75 dB (—), 120 dB (—), 130 dB (—), and 140 dB (—).

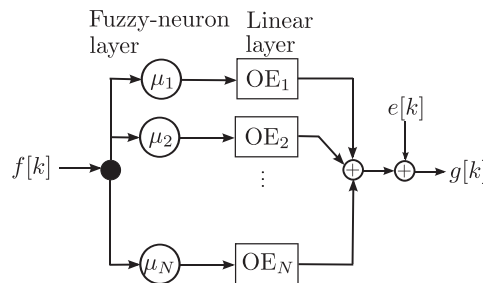


Fig. 8. Block diagram of the local-linear neuro-fuzzy model.

of the reflection coefficient drops. When the over-damped regime is reached, the maximal absorption decreases again, while the frequency bandwidth of high absorption gets wider. All estimated models are in phase (0 or multiples of 2π) for frequencies far away from the eigenfrequency. Close to the eigenfrequency, the normally damped systems are in antiphase, while the over-damped system is in phase.

Nevertheless, these local-linear models cannot predict the response to a dynamic time signal, since they are only valid close to the working conditions used within their estimation process. On the one hand, it is hard to judge whether the operating conditions for two differed signals agree. On the other hand, the condition can change during operation which can impossibly be reflected with a linear model. These drawbacks are remedied in the local-linear neuro-fuzzy model proposed in the following section.

4. Nonlinear system identification using a local-linear neuro-fuzzy model

As seen in the previous section, linear models can describe the resonator behavior also at large oscillation amplitudes in a local-linear manner. The proposed model exploits this idea and combines such local-linear submodels to a nonlinear model in the time domain. This is done with a so-called neuro-fuzzy network model structure [22,23]. The proposed model consists of a neuron layer and a second layer containing the linear submodels. The neuron layer distributes the input signal with respect to so-called membership functions over the second layer. Since every submodel behaves local-linearly, the model is denoted as local-linear neuro-fuzzy networks (LLNFN) in the following. Before results and validations for several test cases are presented in Section 5, the model is discussed in depth: First, the model is defined in Section 4.1 and the fuzzy membership functions being applied in the neuron layer are introduced in Section 4.2. An optimization problem for the parameter estimation is formulated in Section 4.3 and an iterative procedure to solve this problem is derived in Section 4.4.

4.1. Model structure

The proposed model combines N output-error submodels $OE_i(\theta_i)$ in a network as sketched in Fig. 8. Each linear submodel is able to describe the resonator behavior in certain amplitude ranges adequately (see Section 3.4). The free model parameters of the i^{th} submodel are denoted by θ_i and the overall free parameters are collected in the vector $\theta = (\theta_1, \theta_2, \dots, \theta_N)^T$. The linear submodels are wired via a neuron layer. Each subsystem i has its own neuron applying a so-called membership

function $\mu_i[k]$, $i = 1, 2, \dots, N$. The overall model response $g[k]$ is given as a linear combination of responses of the individual linear submodels:

$$g[k](\theta) = \sum_{i=1}^N \mu_i[k] \frac{B(\theta_i)(q)}{F(\theta_i)(q)} f[k] + e[k]. \quad (16)$$

For every instant in time k , each membership function μ_i maps to a value in the interval $[0, 1]$, where 0 means that the i^{th} submodel is not member of the current state (false) while 1 means the opposite (true). However, in fuzzy logic, there exists not solely the true (1) and false (0) state as in the Boolean logic but also every intermediate state. Overall, the membership functions are set in such a way that the total operating conditions are gradually distributed among the different subconditions, i.e., $\sum_{i=1}^N \mu_i[k] = 1$ for all k . The actual design of the membership functions is presented in the following section, a common-sense interpretation of the role of the membership function is developed as follows (for $N = 3$): If the amplitudes are low, the first model OE_1 is taken to describe the resonator behavior. The second model OE_2 is considered in the medium amplitude regime and model OE_3 in the high-amplitude regime. This decision is made not in a strict but in a fuzzy way, which means that the response can be formed proportionally by more than one model OE_i . For instance, a linear combination of OE_1 and OE_2 is used in the low-medium amplitude regime.

4.2. Fuzzy membership functions

A key point of the proposed model is the design of membership functions for the fuzzy neuron layer. This design is made a priori and is not included in the training process itself, as it is often done for other systems [22,23]. By doing so, the resulting optimization problem can be solved efficiently in an iteration of linear least square problems as shown below. Nevertheless, the N estimated linear subsystems $OE_i(\theta_i)$ depend on the actual choice of the membership functions. In the optimization process, these subsystems are determined such that the interconnected network minimizes the objective function for the current set of membership functions.

Since the rms of the velocity at the resonator surface x_{ref} is a reasonable measurement for the nonlinearity as discussed in Section 2.1, the membership functions are based on this value. By doing so, the membership functions are in principle capable of reflecting nonlinear effects due to a rising amplitude at a certain frequency as well as due to some non-harmonic effects. For that purpose, a sliding windowed rms of the (estimated) velocity is calculated

$$u_{\text{rms}}[k] = \text{rms}(u[k - k_T], u[k - k_T + 1], \dots, u[k - 1]). \quad (17)$$

The window length k_T is set such that it covers at least one eigenfrequency period $1/f_{\text{eig}}$. Note that the velocity $u[k]$ is not directly available. During the identification process, it is just given by the difference of the input f_{CFD} and output data g_{CFD} as $u[k] = f_{\text{CFD}}[k] - g_{\text{CFD}}[k]$. When an estimated model is simulated with an input f_{input} , the velocity is estimated using the predicted response g_{model} : $u[k] = f_{\text{input}}[k] - g_{\text{model}}[k]$. For HR1 excited with the input signal presented in Fig. 9, the sliding windowed rms value of the velocity is exemplarily plotted in Fig. 10. The input signal in Fig. 9 is set as described in Section 2.2.

The membership functions are realized as hat functions, which are called Takagi-Sugeno membership functions in this context [23,22]. Having set N reference velocities $u_{\text{ref},i}$, the membership functions $\mu_i[k]$ are defined (for $u_{\text{rms}}[k] \in [u_{\text{ref},1}, u_{\text{ref},N}]$) as:

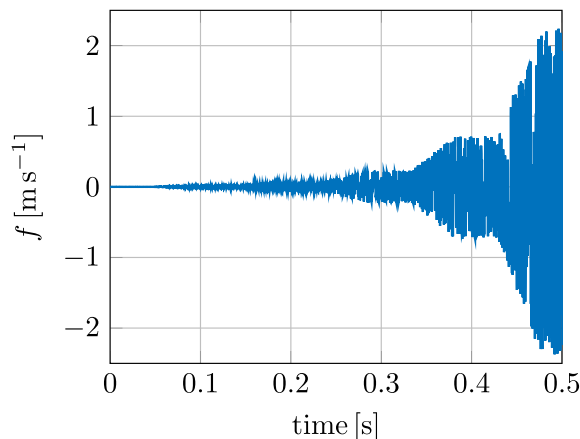


Fig. 9. Broadband excitation signals ramped up from incident SPL of 75–150 dB.

$$\mu_i[k] = \begin{cases} \frac{u_{\text{ref},i} - u_{\text{rms}}[k]}{u_{\text{ref},i} - u_{\text{ref},(i-1)}} & \text{if } u_{\text{rms}}[k] \in [u_{\text{ref},(i-1)}, u_{\text{ref},i}] \\ \frac{u_{\text{ref},i} - u_{\text{rms}}[k]}{u_{\text{ref},(i+1)} - u_{\text{ref},i}} & \text{if } u_{\text{rms}}[k] \in [u_{\text{ref},i}, u_{\text{ref},(i+1)}] \\ 0 & \text{else} \end{cases} \quad (18)$$

In words, this means that i^{th} membership function $\mu_i[k]$ is true (1) if the current rms velocity equals the i^{th} reference velocity $u_{\text{ref},i}$ and is false (0) if it differs significantly from this value. The intermediate states are defined by the relative distance of the current rms velocity $u_{\text{rms}}[k]$ to the neighboring reference velocities. The bounding membership functions $\mu_1[k]$ and $\mu_N[k]$ take the value true (1) if the amplitude $u_{\text{rms}}[k]$ is below or above their reference values, respectively. A possible set of five membership functions μ_i is plotted against u_{rms} in Fig. 11.

The following points should be considered for setting the reference velocities $u_{\text{ref},i}$: The lowest reference velocity $u_{\text{ref},1}$ has to be located clearly in the linear regime, while the highest velocity $u_{\text{ref},N}$ marks the maximal rms velocity for which the estimated model will saturate by design. The remaining reference velocities $u_{\text{ref},i}$ ($i = 2, 3, \dots, N - 1$) are located in between. They are not arranged in an equidistant manner, since the system dynamics changes most prominently in the transition from the linear to the nonlinear regime, such that more reference velocities should be located in this region. A grading has been applied to set the intermediate references for that purpose, i.e., $(u_{\text{ref},i+2} - u_{\text{ref},i+1}) / (u_{\text{ref},i+1} - u_{\text{ref},i}) = \Delta$. For the results presented in Section 5, the grading factor Δ has been set to 4, the first reference velocity has been selected as zero $u_{\text{ref},1} = 0$ [m/s] and the highest as 80% of the maximal velocity rms value in the training data set $u_{\text{ref},N} = 0.8 \max(u_{\text{rms}}[k])$. According to these rules, the five reference velocities for the membership functions shown in Fig. 11 have been set. Applying these

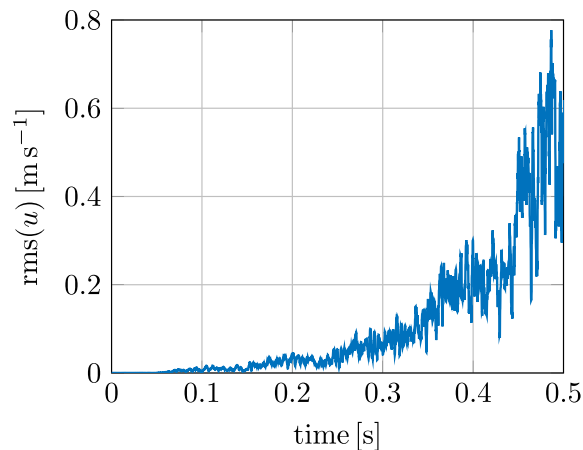


Fig. 10. Root mean square of u' for HR1.

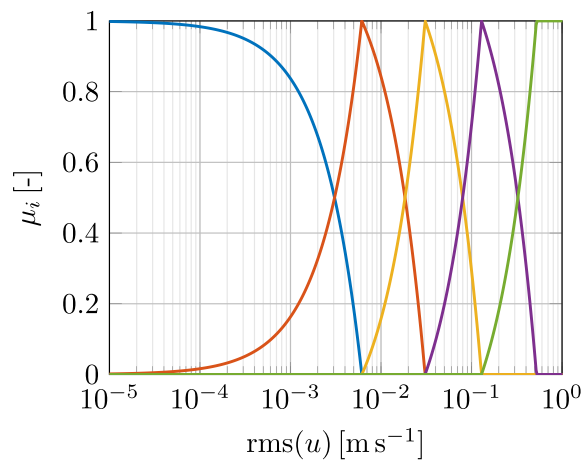


Fig. 11. Graphs of the membership functions.

membership functions on the velocity u_{rms} shown in Fig. 10 yields the distribution of μ_i over time presented in Fig. 12. It can be seen that the membership functions detect well the different levels of fluctuating velocities caused by the variation in the input f signal.

4.3. Global and multi-objective optimization problem

After the model structure is fixed, the set of unknown optimal parameters $\hat{\theta} = (\hat{\theta}_1, \hat{\theta}_2, \dots, \hat{\theta}_N)^T$ has to be determined. For that purpose, an optimization in the unknowns is formulated. A procedure to solve this nonlinear optimization is shown in the next section (Section 4.4). Following the PEM ansatz, the global difference between the model response $g[k](\theta)$ of Eq. (16) and the CFD measured response $g_{\text{CFD}}[k]$ shall be minimized. The corresponding global objective function reads as:

$$\hat{\theta} = \underset{\theta}{\operatorname{argmin}} \sum_k w[k] (g[k](\theta) - g_{\text{CFD}}[k])^2. \quad (19)$$

Since the amplitudes in the nonlinear regime can differ by several orders of magnitudes, an adaptive weighting $w[k] \neq \text{const.}$ is applied. This weighting emphasizes the time instances with low amplitudes in comparison to those with high amplitudes. Without such a weighting, the time instances with high amplitudes would dominate in the optimization, while the instances with low amplitudes would have almost no influence on the optimization result and, accordingly, the estimated model would perform poorly at low amplitudes. Here, the inverse of a squared sliding windowed rms of the input signal is used, i.e. $w[k] = 1/\text{rms}(f[k - k_T], f[k - k_T + 1], \dots, f[k])^2$. The window length k_T is set such that the rms window covers at least one eigenfrequency period $1/f_{\text{eig}}$.

Formulating the optimization problem only in the global manner shown above may lead to a nonlinear model with poor local behavior. For instance, the descending function of the estimated reflection coefficient R can show unphysical characteristics for some amplitudes. This effect is well known in the modeling with neuro-fuzzy networks, see, e.g., Babuška and Verbruggen [23]. A way to overcome this is to formulate local optimization problems for each submodel i :

$$\hat{\theta}_i = \underset{\theta_i}{\operatorname{argmin}} \sum_k H(\mu_i[k] - \zeta) w[k] (g_i[k](\theta_i) - \mu_i[k] g_{\text{CFD}}[k])^2. \quad (20)$$

Above, the model output of the i^{th} submodel is denoted by g_i . The function H and the parameter ζ denote the Heaviside function and a threshold when the subproblem is active, respectively. So, $H(\mu_i[k] - \zeta)$ equals zero whenever $\mu_i[k] < \zeta$ and it equals unity otherwise. A threshold $\zeta = 0.5$ has been used for the results presented below. Considering only the local optimization problems (20) would lead to a nonlinear model behaving well locally which, however, might perform sub-optimally on a global scale.

By formulating a multi-objective optimization problem, the advantages of both the global and the local ansatz can be combined, see Babuška and Verbruggen [23]. The multi-object function is received by a combination of the global and the local objective functions. For the problem considered here, it reads

$$\hat{\theta} = \underset{\theta}{\operatorname{argmin}} \sum_k w[k] \left((g[k](\theta) - g_{\text{CFD}}[k])^2 + \sum_{i=1}^N \delta_i H(\mu_i[k] - \zeta) (g_i[k](\theta_i) - \mu_i[k] g_{\text{CFD}}[k])^2 \right). \quad (21)$$

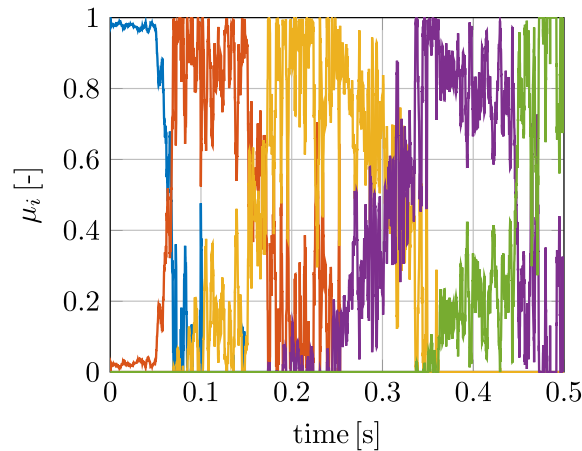


Fig. 12. Time series of membership functions for HR1.

A weighting parameter δ_i can be set for each subsystem i . For the results shown below, these weighting parameters have been chosen adaptively in such a manner that the global and the sum of all linear optimization problem are equally pronounced:

$$\delta_i = \frac{\|a_{\text{global}}\|_2}{N \|a_i\|_2}, \quad (22)$$

where $a_{\text{global}}[k] = \sqrt{w[k]} g_{\text{CFD}}[k]$ and $a_i[k] = H(\mu_i[k] - \zeta) \sqrt{w[k]} \mu_i[k] g_{\text{CFD}}[k]$.

4.4. Parameter estimation procedure

The nonlinear optimization problem (21) can be solved iteratively in a fashion similar to the one of the output-error model presented in Section 3.1. Note that this kind of problem is often solved via so-called instrumental variables methods, see, e.g., the textbook by Nelles [22]. However, an implementation based on such a method did not show good convergence for CFD data of the Helmholtz resonator. That is why an implementation based on pre-filtering is introduced here. For clarity, this is presented only for the global optimization. When the local problems are included, the dimension on the optimization has to be extended accordingly.

The vector of unknowns is initialized with zeros $\theta^0 = 0$ for $l = 0$ and, then, the iteration $l = 1, 2, \dots$ is started: First, the input f and measured output g_{CFD} are filtered to gain a white noise error:

$$f^l[k] = \sum_{i=1}^N \mu_i[k] \frac{1}{F(\theta_i^{l-1})(q)} f[k] \quad \text{and} \quad g^l[k] = \sum_{i=1}^N \mu_i[k] \frac{1}{F(\theta_i^{l-1})(q)} g_{\text{CFD}}[k]. \quad (23)$$

With these filtered quantities, the overall observation matrix $\Phi^l = \Phi(f^l, g^l)$ for the iteration step l is created. This overall observation matrix is constructed as a concatenation of the fuzzy-weighted output-error observation matrices $\mu_i \Phi_{\text{OE}}$:

$$\Phi^l = (\mu_1 \Phi_{\text{OE}}(f^l, g^l), \mu_2 \Phi_{\text{OE}}(f^l, g^l), \dots, \mu_N \Phi_{\text{OE}}(f^l, g^l)). \quad (24)$$

Now, the unknowns can be updated:

$$\theta^l = (\Phi^l)_{\text{W}}^\dagger g^l. \quad (25)$$

This procedure is repeated until convergence in θ^l is reached, which is usually after a few iterations.

Several setting of the model, as for instance the number of chosen submodels N , are determined before the identification process and, of course, influence the identification results. Potentially, the identified results differ from each other strongly such that a judgment on the model goodness is difficult, see Jaensch and Polifke [35] who applied SI based on artificial neural networks to characterized the acoustic flame response. The proposed model behave relatively robust regarding this issue, as shown in Appendix A.

5. Results and validation

In this section, LLNFN models proposed in Section 4 are estimated for the four test cases considered. For each test case, the same model structure is used, and the same input signal is applied in the CFD simulations. The input signal plotted in Fig. 9 is a ramped broadband signal up to a certain cut-off frequency and is constructed as explained in Section 2.2. These estimated models are validated and evaluated in both time (Section 5.1) and frequency domain (Section 5.2). Finally in Section 5.3, the flexibility of the LLNFN model is discussed briefly.

5.1. Validation and evaluation in time domain

The response of the estimated models is computed for a second independent input signal, which was not used to train the model. The validation against “test data”, is an important step in the SI, which ensure that estimated models do not suffer from over-parameterization. A model is denoted as over-parameterized when it has so many free parameters that it can, on the one hand, achieve a good fit to the training data due to the large degrees of freedom, but gives, on the other hand, poor predictions for another set of input data [34, p. 133].

For that purpose, a second random input signal is generated (see [31]) which has the same power spectrum but is statistically independent of the training signal, i.e., the cross-correlation between those signals is low. Both the training and the independent input signal are ramped up in the same manner. A common criterion to evaluate the similarity of two time signals g_{CFD} and g_{model} is the normalized root mean square error (NRMSE). Since the mean value of g_{CFD} equals zeros, it reads as:

$$\text{NRMSE} = 1 - \frac{\|g_{\text{CFD}} - g_{\text{model}}\|_2}{\|g_{\text{CFD}}\|_2}. \quad (26)$$

NRMSE takes the value of unity for a perfect fit. It gives the value zero when a time series is compared against the zero sequence and can be $-\infty$ in the worst case. However, this measure is not suitable in the considered cases since the time series contain sections where the fluctuation amplitudes differ by several orders of magnitudes from each other. Consequently, the NRMSE detects mainly the differences for high amplitudes and almost ignores those in the low amplitude range. To get an equal weighting for all amplitude ranges, both time series are scaled with the inverse of an moving rms of g_{CFD} :

$$\tilde{g}_{\text{CFD}}[k] = \frac{1}{\text{rms}(g_{\text{CFD}}[k - k_t], \dots, g_{\text{CFD}}[k])} g_{\text{CFD}}[k] \quad \text{and} \quad (27)$$

$$\tilde{g}_{\text{model}}[k] = \frac{1}{\text{rms}(g_{\text{CFD}}[k - k_t], \dots, g_{\text{CFD}}[k])} g_{\text{model}}[k]. \quad (28)$$

The NRMSE based on those scaled quantities is a suitable measure for the considered time series. This is denoted as relative NRMSE in the following.

The relative NRMSE is listed in Table 2 for all test cases considering different models. It is computed for both the training data and a second independent data set. The estimated local-linear neuro-fuzzy networks are referred to as LLNFNs. Moreover, the relative NRMSE values are given for a linear output-error model OE_{whole} estimated based on the whole training data. A second output-error model OE_{lin} estimated based on the linear regime of the training data is also included. Finally, an acoustically hard wall ($R = 1$) is considered in this table to allow for a more intuitive interpretation of the fit values. It can be seen that none of the listed models is over-parameterized, since the relative NRMSE values are equally good for the training and the independent data set. As expected, the hard wall performs worst. However, it exhibits still reasonable fit values, since the resonator behaves like a hard wall for frequencies away from its eigenfrequency. Especially for HR4 having a relatively narrow bandwidth, the NRMSE values are not bad for the hard wall case. Due to that narrow bandwidth of HR4, all models perform best for this test case. The two output-error models OE_{lin} and OE_{whole} behave much better than the hard wall, since they consider damping at the eigenfrequency. However, they cannot account for the amplitude-dependent damping behavior, since they are linear models. In acoustical CFD simulations, linear models tuned to a certain SPL are commonly used as boundary conditions. These two linear models illustrate the error that can occur if the tuning is either inadequate for current constant operating conditions, or cannot be good due to changing operating conditions. The LLNFN model has been constructed such that it can adapt to changing amplitudes and, accordingly, it also shows the best fit to the CFD data. This freedom is gained by an increase of the number of free parameters to $5N$ ($N = 5$ here) in comparison to 5 for the output-error models. Compared to other nonlinear models, like artificial neural networks, this number is still moderate. As mentioned above, it can clearly be observed that this model is not over-parameterized. For HR3 and HR4, the LLNFN model shows even a slightly better fit on the independent data than on the training data set.

5.2. Validation and evaluation in frequency domain

The validation of the estimated LLNFN models against measurements is performed in frequency domain, since measurements are only given this way. Moreover, this allows for a physical interpretation of the behavior of the estimated nonlinear models. Since the LLNFN models are defined in the time domain, their frequency response is evaluated by harmonic excitation of the model. Before the discrete Fourier transformation is performed on the input and the output data of the model, the time series are truncated to get rid of the transient behavior and to get a signal length which is a multiple of the excitation period. By doing so, leakage in the discrete Fourier transformation is avoided. This procedure requires low computational effort because both the evaluation of the model and the output post-processing can be performed very efficiently.

The model response is validated against impedance describing functions from experiment. Note that these functions are usually given in the literature with respect to the total SPL. For the comparison the incident SPL to the model is varied

Table 2
Relative NRMSE values for the four test cases.

Test case	Signal	LLNFN	OE_{whole}	OE_{lin}	Wall
HR1	Training data	0.80889	0.51775	0.59175	0.25876
	Independent data	0.79898	0.51271	0.57328	0.24044
HR2	Training data	0.83657	0.59619	0.68404	0.31907
	Independent data	0.83623	0.61231	0.68001	0.33761
HR3	Training data	0.8272	0.65564	0.74224	0.42223
	Independent data	0.82945	0.68531	0.72206	0.45654
HR4	Training data	0.9109	0.74692	0.78745	0.6427
	Independent data	0.91625	0.76707	0.77851	0.66115

iteratively to match the total SPL of the experiments. Test cases HR1 to HR3 are compared against measurements from Hersh et al. [5] and HR4 against measurements from Temiz [32]. In this section, only the plots of HR1 are presented to keep the paper compact. The figures for the three other test cases are shown in Appendix B.

Fig. 13 shows the impedance describing function of the estimated LLNFN model for the linear regime (75 dB) and three SPLs (120 dB, 130 dB, and 140 dB) located in the nonlinear regime. The same information in the impedance perspective is depicted in Fig. 14. For the interpretation of the resistance plot on the left-hand side of Fig. 14, it should be kept in mind that the transformation from reflection coefficient to resistance is ill-conditioned apart from the eigenfrequency as shown in Section 3.3. Thus, the resistance plot is most meaningful close to the resonator eigenfrequency and loses significance apart from it. It can be seen that the LLNFN model reflects well the general nonlinear change of the reflection coefficient. With rising amplitude, the gain of the reflection coefficient drops down until the resonator is over-damped. In the over-damped regime, the maximal absorption rises again with increasing amplitude, and simultaneously the bandwidth gets wider. Moreover, the eigenfrequency shifts to higher frequencies. In the linear regime, the model and the measurements agree well. A closer look at the nonlinear regime exposes some discrepancies between the estimated LLNFN model and the measurements. The LLNFN model predicts the eigenfrequency shift already for lower amplitudes than it occurs in experiments. Moreover, the nonlinear resistance is under-predicted by the LLNFN model. These systematic discrepancies are present for all four test cases, but they are strongest for HR1. Only for HR4, the LLNFN model does not over-predict the nonlinear resistance. For this test case, the simulation over-predicts the resistance, see Förner et al. [32], and the maximal SPL is lower than in the other test cases. The largest discrepancies occur for the test case HR1 presented in this section. They are smaller for the other cases as seen in Figs. B.1–B.3. Overall, the agreement is reasonably good for all test cases. It can be concluded that the LLNFN model provides a reasonable and robust methodology to describe the nonlinear behavior of Helmholtz resonators.

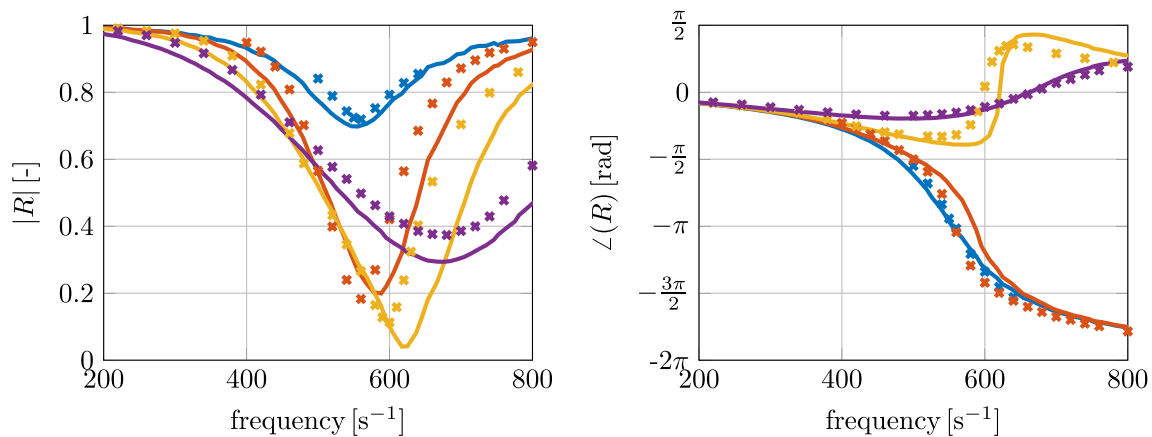


Fig. 13. Estimated (—) and measured [5] (×) reflection coefficients for HR1 for a SPL of 75 dB (●), 120 dB (●), 130 dB (●), and 140 dB (●).

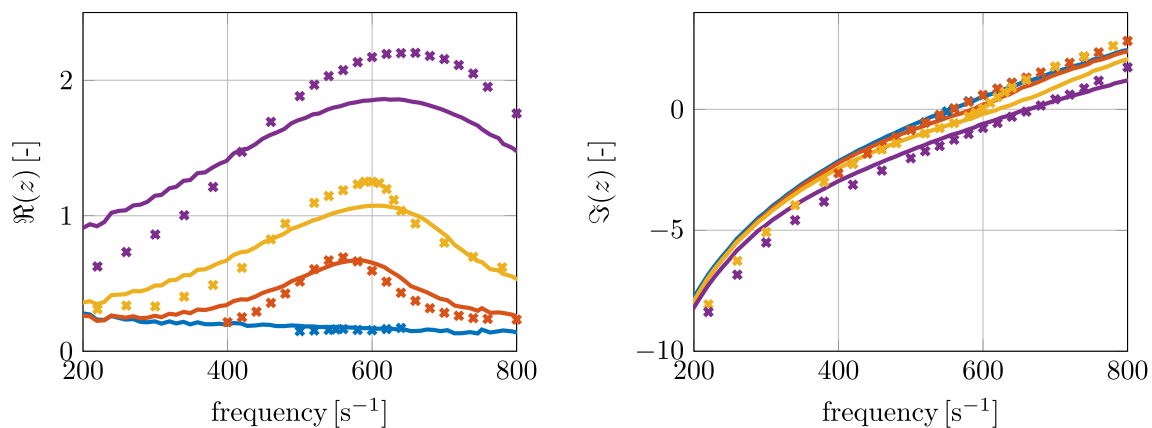


Fig. 14. Estimated (—) and measured [5] (×) reflection impedance describing function for HR1 for a SPL of 75 dB (●), 120 dB (●), 130 dB (●), and 140 dB (●).

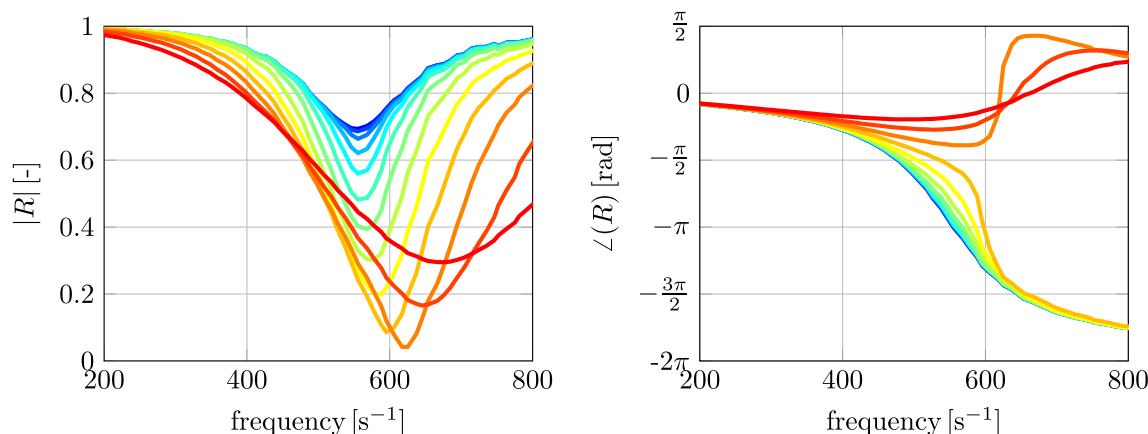


Fig. 15. Estimated impedance describing function for HR1 with total SPLs ranging from 80 dB (bluish) to 140 dB (reddish) in steps of 5 dB. (For interpretation of the references to color in this figure legend, the reader is referred to the web version of this article).

5.3. Flexibility and practicability of the LLNFM model

The LLNFM model cannot only reproduce measurements, but it can simulate reasonably well the response to any input signal up to the maximal amplitude that it has been trained for. Fig. 15 depicts the impedance describing function for total SPL ranging from 80 dB to 140 dB in steps of 5 dB. It can be seen that the impedance changes smoothly with SPL and frequency, which makes this model attractive to serve as boundary condition in CFD or CAA simulations, where acoustic boundaries are involved. Using a linear model instead would require that this model be adapted a priori to the conditions and a linear model can never reflect changing conditions by definition. Moreover, the LLNFM model structure, which consists of several parallel linear submodels, makes a model once estimated readily available also for other time steps or in Laplace space. Each submodel can be converted to a function in the Laplace variable s by the Tustin transformation $z \rightarrow s$. By another reverse transformation $s \rightarrow z$, the estimated model can be applied for any fixed time step. Alternatively, the boundary condition can directly operate with the model representation in Laplace space [36], which has the advantage that the time step can vary within the simulation. Such possibilities are in general not given by other nonlinear models applied in SI, e.g., by artificial neural networks.

Moreover, the provided procedure can be used for the design of future resonators. When the designer has access to a validated CFD setup for resonator simulations, he/she can rapidly get a reasonable idea how geometrical, flow, or temperature conditions influence the linear and nonlinear resonator behavior, since only one CFD simulation is required. Thus, this procedure can also be used for the uncertainty quantification of the resonator response. It is known that, for instance, the manufacturing process of acoustic liners strongly impacts the actual damping behavior, see Murray et al. [37]. With the proposed method, one could quantify with low computational effort how the manufacturing tolerances influence the achieved damping performance.

6. Conclusions

The paper proposes a local-linear neuro-fuzzy network to model the nonlinear resonator response in time domain. The free model parameters are determined via the CFD/SI approach, generated from time series data of a single CFD simulation. The nonlinear model consists of several linear submodels wired via fuzzy neurons in a network. It is shown that such linear models can describe the resonator behavior also in the nonlinear regime in a local-linear manner. This means that such a local-linear model is only valid in the amplitude regime it is has been trained. The fuzzy-neuron layer distributes an input signal over several linear submodels based on the rms of the particle surface velocity. By doing so, the interconnected nonlinear model is capable of describing the nonlinear behavior over a wide amplitude range. A multi-objective optimization problem is formulated and an iterative procedure for its solution is derived. Within this iterative procedure, the input and output time series are pre-filtered to achieve an unbiased model. The model structure is robust against over-parameterization, since the estimated models behave comparably well on training data and on independent test data. The estimated models are validated via describing functions for the reflection coefficient and the impedance against measurements from the literature for several test cases. Apart from slight deviations in the very high amplitude range, the estimated models perform very well for all test cases considered. It can be concluded that the proposed procedure offers a possibility to characterize the nonlinear resonator response over a wide range of frequencies and amplitudes with low computational effort.

Such estimated data-based ROMs can serve as boundary conditions in compressible flow or acoustic simulations to correctly capture the nonlinear effects of a resonator or liner with marginal extra numerical costs. The efficient and robust nonlinear characterization makes this approach also feasible to support the resonator design in an early stage of development.

Acknowledgments

Financial support has been provided by the German Research Foundation (Deutsche Forschungsgemeinschaft – DFG) in the framework of the Sonderforschungsbereich Transregio 40 (DFG-TRR40), Project A3. The Leibniz Supercomputing Centre (LRZ) is gratefully acknowledged for providing access to its cluster system. The authors thank their colleagues Armin Witte and Stefan Jaensch for the fruitful discussion and M.A. Temiz from TU Eindhoven for providing measurement data for test case HR4.

Appendix A. Robustness of the LLNFN model

The model structure has to be defined a priori. If the model structure does not correspond well to the system behavior, no good estimated models can be achieved in the end. In this section, the sensitivity of the estimated model behavior on the model structure is evaluated with respect to the number of submodels N considered. In Fig. A.1, reflection coefficients are plotted for incident SPLs of 75, 110, 120, 130, and 140 dB for estimated LLNFN models with N varying from 3 to 7. It can be observed that the curves of the different models coincide relatively well with the exception $N = 3$. The curves of this outlier model ($N = 3$) are plotted with dashed lines. Moreover, it can be seen that the coincidence is better in the high than in the lower amplitude regime. Overall, it can be concluded that the LLNFN model structure is relatively robust against changes in N except when very few subsystems are incorporated. This robustness is also found (not shown here) with respect to other parameters as the grading to locate the reference velocities Δ and the weights of the local optimization problems δ_i . The identification only fails if the reference velocities $u_{\text{ref},i}$ are arranged such that one or more submodels are “blocked”. Blocked means that almost no training data reaches this submodel which leads to an ill-conditioned optimization process. However, this can be detected easily by the user and another distribution of the reference velocities $u_{\text{ref},i}$ can be chosen.

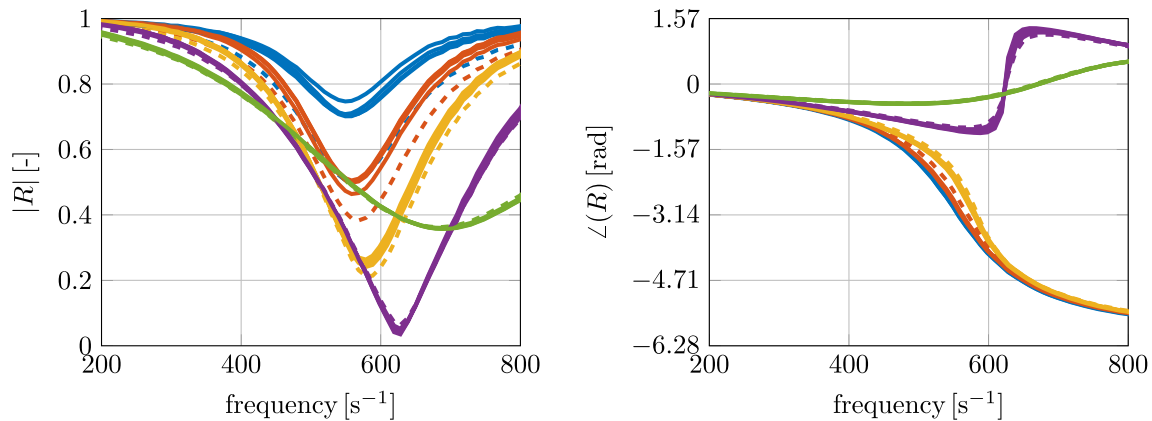
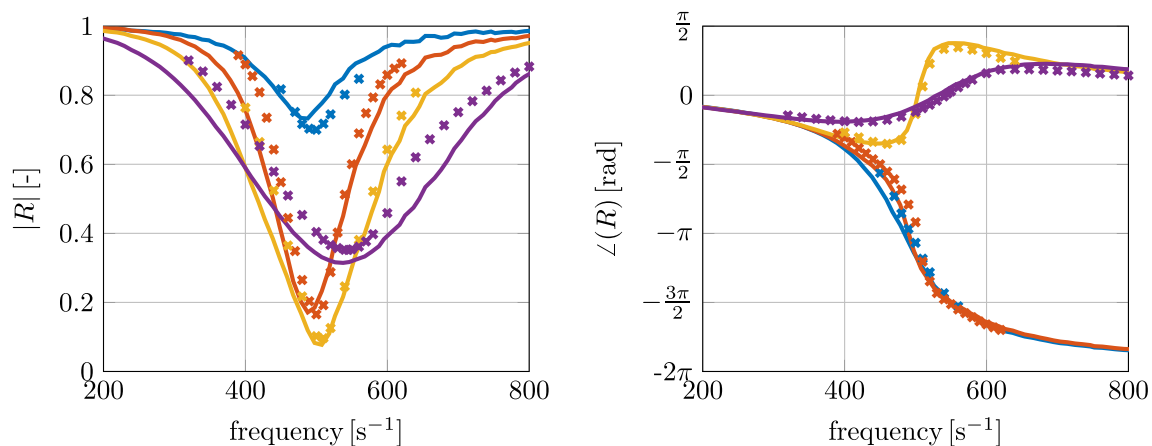


Fig. A.1. Estimated Reflection coefficients for LLNFN models with N varying from 3 to 7 for incident SPLs of 75, 110, 120, 130, and 140 dB. The graphs for $N = 3$ are dashed.

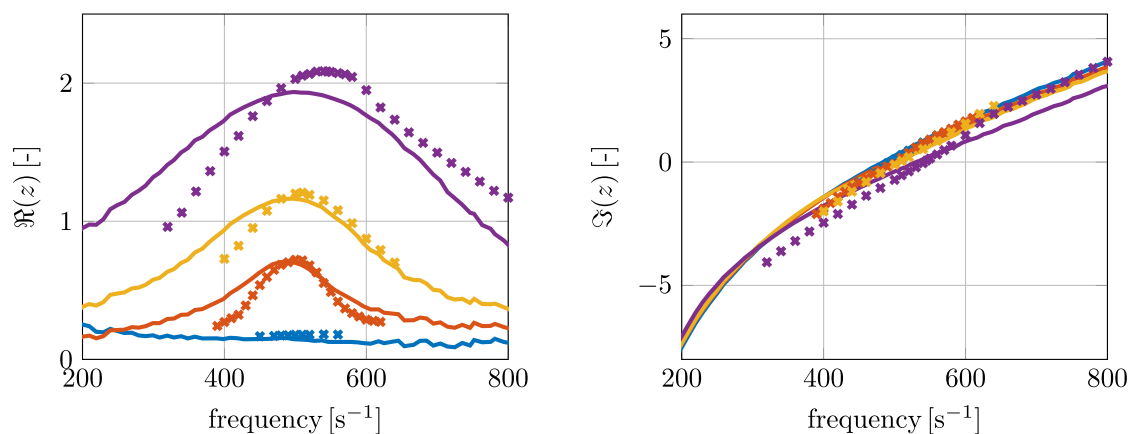
Appendix B. Graphs for test cases HR2, HR3, and HR4

In this section, the graphs for the test case HR2, HR3, and HR4 are provided. For each test case, the graphs are assembled in one figure. Subfigure (a) contains the reflection coefficient for the estimated LLNFN models and from experiment. Subfigure (b) shows the corresponding impedance. For HR2 and HR3, the experimental data is taken from Hersh et al. [5] for total SPLs of 75 dB (●), 120 dB (●), 130 dB (●), and 140 dB (●). The empirical data for HR4 have been provided by Temiz² in a setup as in [32]. The measurements have been adjusted such that the voltage at the microphone closest to the sample has been set to a fixed value. Dependent on the frequency, this results in total SPLs at the sample from (89.8–95.4) dB (●), (119.5–121.8) dB (●), and (125.7–127.7) dB (●). The evaluation of the model was adjusted to these values with interpolation for the intermediate points. Subfigure (d) shows the estimated impedance describing function from a SPL ranging from 80 dB (bluish) to 140 dB (reddish) in steps of 5 dB (Figs. B.1–B.3).

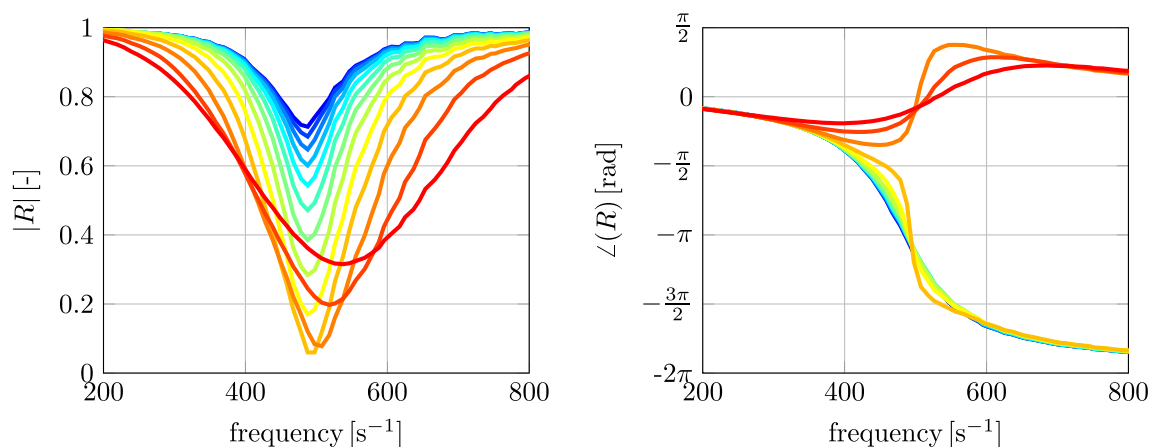
² Private communication by M.A. Temiz, Technische Universiteit Eindhoven, Department of Mechanical Engineering, Eindhoven, The Netherlands.



(a) Reflection coefficient.

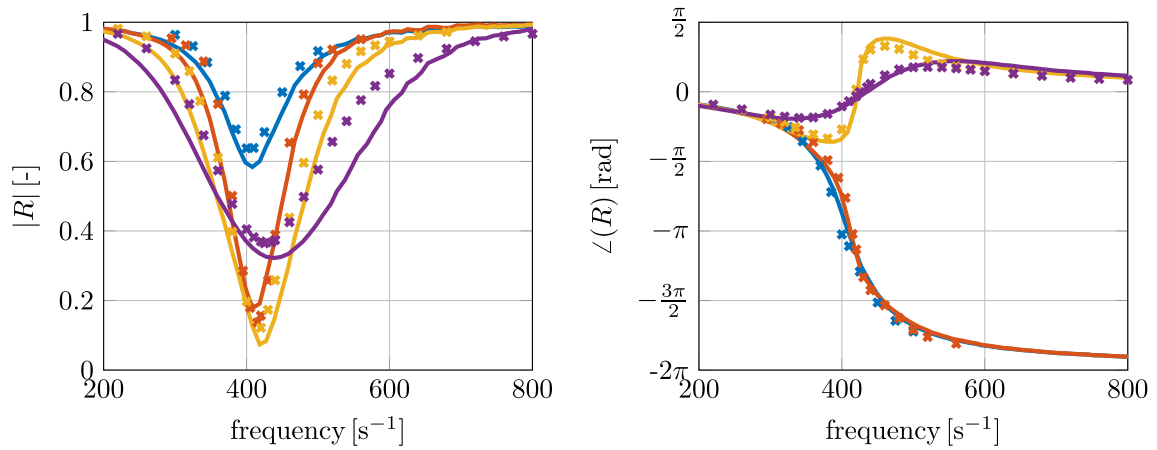


(b) Impedance.

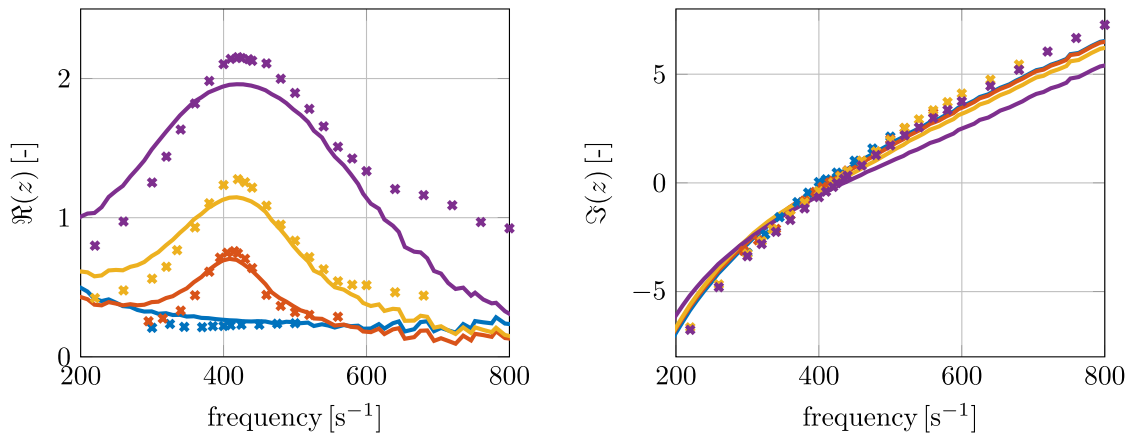


(c) Describing function for the reflection coefficient for a SPL from 80 dB to 140 dB.

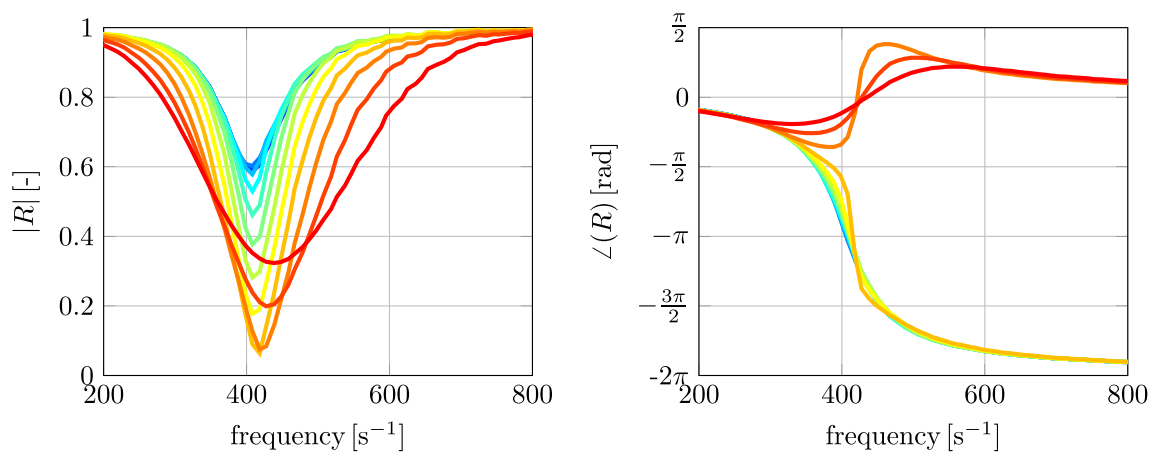
Fig. B.1. Estimated reflection coefficients (Subfig. (a)) and impedance (Subfig. (b)) for HR2 in comparison to measurements from Temiz [32] and a describing function for the reflection coefficient for a SPL from 80 dB to 140 dB (Subfig. (c)).



(a) Reflection coefficient.

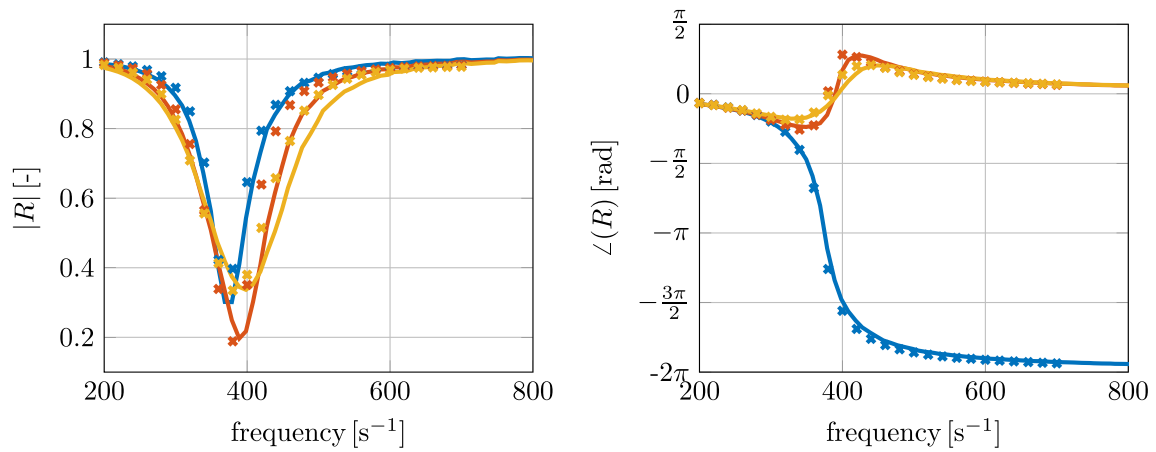


(b) Impedance.

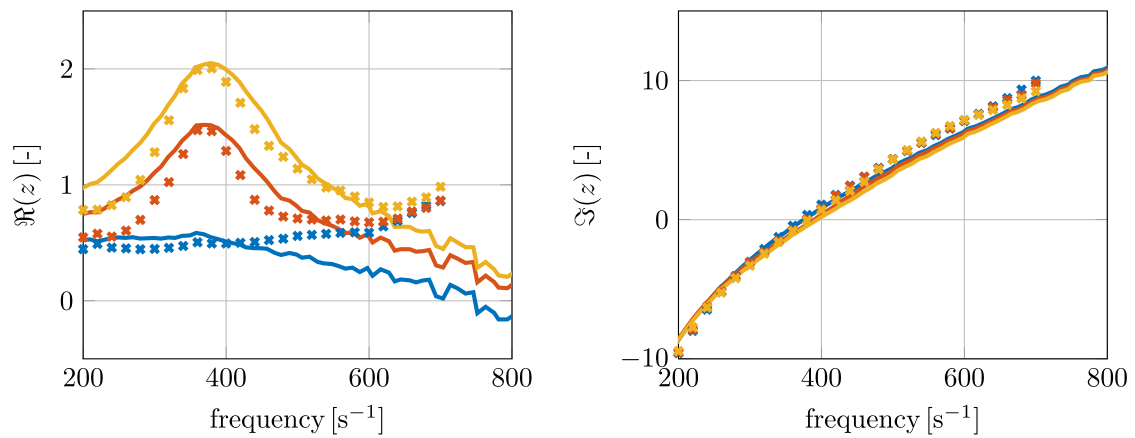


(c) Describing function for the reflection coefficient for a SPL from 80 dB to 140 dB.

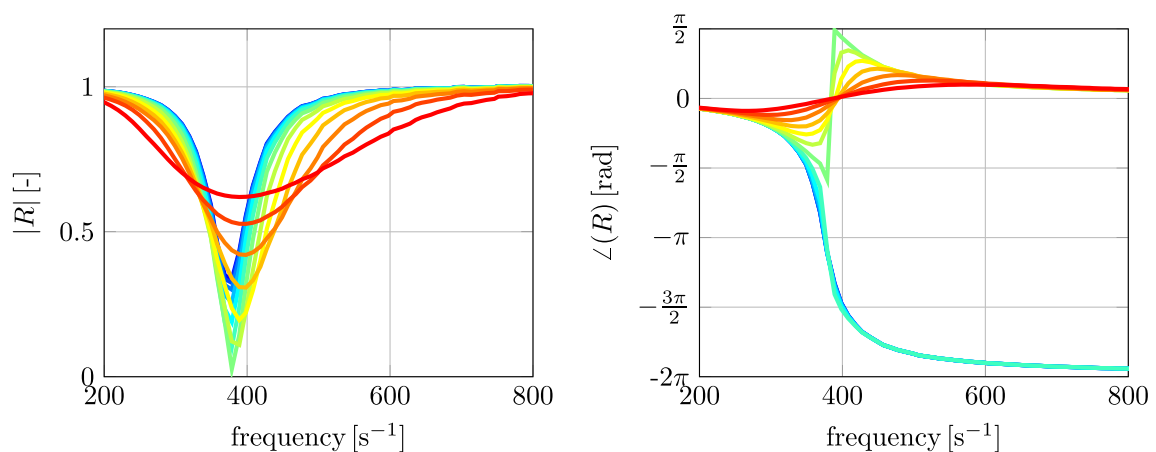
Fig. B.2. Estimated reflection coefficients (Subfig. (a)) and impedance (Subfig. (b)) for HR3 in comparison to measurements from Temiz [32] and a describing function for the reflection coefficient for a SPL from 80 dB to 140 dB (Subfig. (c)).



(a) Reflection coefficient.



(b) Impedance.



(c) Describing function for the reflection coefficient for a SPL from 80 dB to 140 dB.

Fig. B.3. Estimated reflection coefficients (Subfig. (a)) and impedance (Subfig. (b)) for HR4 in comparison to measurements from Temiz [32] and a describing function for the reflection coefficient for a SPL from 80 dB to 140 dB (Subfig. (c)).

References

- [1] The Jet Engine, 5th edition, Rolls-Royce Ltd., Derby, U.K., 1996.
- [2] V. Bellucci, P. Flohr, C.O. Paschereit, Numerical and experimental study of acoustic damping generated by perforated screens, *AIAA J.* 42 (8) (2004) 1543–1549, <http://dx.doi.org/10.2514/1.9841>.
- [3] L.J. Sivian, Acoustic impedance of small orifices, *J. Acoust. Soc. Am.* 7 (2) (1935) 94–101, <http://dx.doi.org/10.1121/1.1915795>.
- [4] U. Ingård, S. Labate, Acoustic circulation effects and the nonlinear impedance of orifices, *J. Acoust. Soc. Am.* 22 (2) (1950) 211–218, <http://dx.doi.org/10.1121/1.1906591>.
- [5] A.S. Hersh, B.E. Walker, J.W. Celano, Helmholtz resonator impedance model, part 1: nonlinear behavior, *AIAA J.* 41 (5) (2003) 795–808, <http://dx.doi.org/10.2514/2.2041>.
- [6] U. Ingard, Nonlinear distortion of sound transmitted through an orifice, *J. Acoust. Soc. Am.* 48 (1A) (1970) 32–33, <http://dx.doi.org/10.1121/1.1912106>.
- [7] A. Cummings, Transient and multiple frequency sound transmission through perforated plates at high amplitude, *J. Acoust. Soc. Am.* 79 (4) (1986) 942–951, <http://dx.doi.org/10.1121/1.393691>.
- [8] K. Förner, J. Tournadre, P. Martínez-Lera, W. Polifke, Scattering to higher harmonics for quarter wave and Helmholtz resonators, *AIAA J.* 55 (4) (2017) 1194–1204, <http://dx.doi.org/10.2514/1.J055295>.
- [9] P.G. Serrano, G. Gabard, P.B. Murray, R.J. Astley, Non-linear interaction of multiple tones on perforated liners, in: Proceedings of the 22nd AIAA/CEAS Aeroacoustics Conference, Lyon, France, 2016. <http://dx.doi.org/10.2514/6.2016-2790>.
- [10] E. J. Rice, A Model for the Acoustic Impedance of a Perforated Plate Liner with Multiple Frequency Excitation, Technical Report NASA-TM-X-67950, E-6636, NASA, 1971. URL (<https://ntrs.nasa.gov/archive/nasa/casi.ntrs.nasa.gov/19720004979.pdf>).
- [11] D.-Y. Maa, Potential of microperforated panel absorber, *J. Acoust. Soc. Am.* 104 (5) (1998) 2861–2866, <http://dx.doi.org/10.1121/1.423870>.
- [12] H. Bodén, Acoustic characterisation of perforates using non-linear system identification techniques, in: Proceedings of the 13th AIAA/CEAS Aeroacoustics Conference (28th AIAA Aeroacoustics Conference), Rome, Italy, 2007. <http://dx.doi.org/10.2514/6.2007-3530>.
- [13] H. Bodén, Non-linear system identification techniques for determination of the acoustic properties of perforates, in: Proceedings of the 21st AIAA/CEAS Aeroacoustics Conference, AIAA Aviation, Dallas, TX, USA, 2015. <http://dx.doi.org/10.2514/6.2015-3266>.
- [14] C.K.W. Tam, H. Ju, M.G. Jones, W.R. Watson, T.L. Parrott, A computational and experimental study of resonators in three dimensions, *J. Sound Vib.* 329 (24) (2010) 5164–5193, <http://dx.doi.org/10.1016/j.jsv.2010.06.005>.
- [15] C.K.W. Tam, K.A. Kurbatskii, K.K. Ahuja, R.J. Gaeta, A numerical and experimental investigation of the dissipation mechanisms of resonant acoustic liners, *J. Sound Vib.* 245 (3) (2001) 545–557, <http://dx.doi.org/10.1006/jsvi.2001.3571>.
- [16] C.K.W. Tam, H. Ju, B.E. Walker, Numerical simulation of a slit resonator in a grazing flow under acoustic excitation, *J. Sound Vib.* 313 (3–5) (2008) 449–471, <http://dx.doi.org/10.1016/j.jsv.2007.12.018>.
- [17] S. Mendez, J.D. Eldredge, Acoustic modeling of perforated plates with bias flow for Large-Eddy simulations, *J. Comput. Phys.* 228 (13) (2009) 4757–4772, <http://dx.doi.org/10.1016/j.jcp.2009.03.026>.
- [18] Q. Zhang, D.J. Bodony, Numerical investigation and modelling of acoustically excited flow through a circular orifice backed by a hexagonal cavity, *J. Fluid Mech.* 693 (2012) 367–401, <http://dx.doi.org/10.1017/jfm.2011.537>.
- [19] Q. Zhang, D.J. Bodony, Effects of the turbulent grazing flow over the impedance prediction of a single-orifice Helmholtz resonator, in: Proceedings of the 22nd AIAA/CEAS Aeroacoustics Conference, American Institute of Aeronautics and Astronautics, Lyon, France, 2016. <http://dx.doi.org/10.2514/6.2016-2729>.
- [20] W. Polifke, Black-box system identification for reduced order model construction, *Ann. Nucl. Energy* 67C (2014) 109–128, <http://dx.doi.org/10.1016/j.anucene.2013.10.037>.
- [21] K. Förner, W. Polifke, Aero-acoustic characterization of Helmholtz resonators in the linear regime with system identification, in: 22nd International Congress on Sound and Vibration (ICSV22), Florence, Italy, 2015. URL (http://iiaav.org/archives_icsv_last/2015_icsv22/content/papers/papers/full_paper_596_20150401121136373.pdf).
- [22] O. Nelles, *Nonlinear System Identification*, Springer Berlin Heidelberg, Berlin, Heidelberg, 2001 URL \diamond .
- [23] R. Babuška, H. Verbruggen, Neuro-fuzzy methods for nonlinear system identification, *Annu. Rev. Control* 27 (1) (2003) 73–85, [http://dx.doi.org/10.1016/S1367-5788\(03\)00009-9](http://dx.doi.org/10.1016/S1367-5788(03)00009-9).
- [24] J.J. Keller, E. Zauner, On the use of Helmholtz resonators as sound attenuators, *Z. Angew. Math. Phys.* 46 (1995) 297–327, <http://dx.doi.org/10.1007/BF01003552>.
- [25] H. Bodén, L. Zhou, An experimental study of the effect of flow and high level acoustic excitation on the acoustic properties of perforates and orifices, in: Proceedings of the 20th International Congress on Sound and Vibration (ICSV20), Bangkok, Thailand, 2013.
- [26] U. Ingard, On the theory and design of acoustic resonators, *J. Acoust. Soc. Am.* 25 (6) (1953) 1190–1197, <http://dx.doi.org/10.1121/1.1907235>.
- [27] M.A. Temiz, J. Tournadre, I. Lopez Arteaga, A. Hirschberg, Non-linear acoustic transfer impedance of micro-perforated plates with circular orifices, *J. Sound Vib.* 366 (2016) 418–428, <http://dx.doi.org/10.1016/j.jsv.2015.12.022>.
- [28] OpenFOAM Foundation, OpenFOAM (Version 2.3.0) [software]. URL (<http://www.openfoam.com/>).
- [29] T. Poinso, S.K. Lele, Boundary conditions for direct simulation of compressible viscous flows, *J. Comp. Phys.* 101 (1) (1992) 104–129, [http://dx.doi.org/10.1016/0021-9991\(92\)90046-2](http://dx.doi.org/10.1016/0021-9991(92)90046-2).
- [30] J. Tournadre, K. Förner, W. Polifke, P. Martínez-Lera, W. Desmet, Determination of acoustic impedance for Helmholtz resonators through in-compressible unsteady flow simulations, *AIAA J.* 55 (3) (2017) 790–798, <http://dx.doi.org/10.2514/1.J055337>.
- [31] S. Föller, W. Polifke, Advances in identification techniques for aero-acoustic scattering coefficients from Large Eddy simulation, in: Proceedings of the 18th International Congress on Sound and Vibration (ICSV18), vol. 4, Rio de Janeiro, Brazil, 2011, pp. 3122–3129.
- [32] K. Förner, M.A. Temiz, W. Polifke, I. Lopez Arteaga, A. Hirschberg, On the non-linear influence of the edge geometry on vortex shedding in Helmholtz resonators, in: Proceedings of the 22nd International Congress on Sound and Vibration (ICSV22), Florence, Italy, 2015. URL (http://iiaav.org/archives_icsv_last/2015_icsv22/content/papers/papers/full_paper_1341_20150325133515128.pdf).
- [33] A.K. Tangirala, *Principles of System Identification: Theory and Practice*, CRC Press, Boca Raton, Florida, USA, (ISBN 9781439895993), 2014 (URL \diamond).
- [34] K.J. Keesman, *System Identification. Advanced Textbooks in Control and Signal Processing*, Springer, London, London, 2011 (URL \diamond).
- [35] S. Jaensch, W. Polifke, On the uncertainty encountered when modeling self-excited thermoacoustic oscillations with artificial neural networks, in: Proceedings of the International Symp. on Thermoacoustic Instabilities in Gas Turbines and Rocket Engines, GTRE-006, Garching, Germany, 2016.
- [36] S. Jaensch, C. Sovardi, W. Polifke, On the robust, flexible and consistent implementation of time domain impedance boundary conditions for compressible flow simulations, *J. Comput. Phys.* 314 (2016) 145–159, <http://dx.doi.org/10.1016/j.jcp.2016.03.010>.
- [37] P. Murray, P. Ferrante, A. Scofano, Manufacturing process and boundary layer influences on perforate liner impedance, in: Proceedings of the 11th AIAA/CEAS Aeroacoustics Conference, Monterey, California, USA, 2005. <http://dx.doi.org/10.2514/6.2005-2849>.